

CEURS 2023



CIVIL ENGINEERING UNDERGRADUATE RESEARCH SYMPOSIUM

November 2023



PROCEEDINGS

ISSN 3021-6737

**PROCEEDINGS OF THE
CIVIL ENGINEERING UNDERGRADUATE
RESEARCH SYMPOSIUM
(CEURS) - 2023**



**DEPARTMENT OF CIVIL ENGINEERING
FACULTY OF ENGINEERING
UNIVERSITY OF PERADENIYA
SRI LANKA**

**DEPARTMENT OF CIVIL ENGINEERING
FACULTY OF ENGINEERING
UNIVERSITY OF PERADENIYA
SRI LANKA**

**PROCEEDINGS OF THE CIVIL ENGINEERING UNDERGRADUATE
RESEARCH SYMPOSIUM
CEURS 2023**

Editor: MMSGT De Silva

Cover Artwork: HJSH Jayaweera

Copyright © The Faculty of Engineering, University of Peradeniya, Sri Lanka.

Individual authors retain copyright in their own contributions.

First published in September 2023 by The Faculty of Engineering, University of Peradeniya, Sri Lanka.

ISSN 3021-6737

All rights reserved. No part of this publication may be reproduced, stored in a retrieval system, transmitted in any form or by any means, electronic, mechanical photocopying, recording or otherwise without the permission of the editorial board.

The editor and the Faculty of Engineering of the University of Peradeniya Sri Lanka are not responsible for any errors or views expressed in the articles as these are the responsibility of the individual contributors.

**PUBLISHED BY,
DEPARTMENT OF CIVIL ENGINEERING,
FACULTY OF ENGINEERING,
UNIVERSITY OF PERADENIYA,
SRI LANKA.**



Message from the Dean, Faculty of Engineering

It is with great pleasure I write this message to the proceedings of the Civil Engineering Undergraduate Research Symposium (CEURS) 2023.

First of all, I would like to congratulate the academic staff, students, and non-academic supporting staff of the Department for carrying out this high-quality research work under a challenging ground situation, mainly due to the economic downturn.

The fact that out of the 101 publications in indexed journals by the faculty members during the year 2023, 61 are with the authorship of the members of the Department is a testimony to the quality of the work. I am aware that a substantial portion of this research work is resulted from the Undergraduate Research work. I would also like to take this opportunity to thank Prof. J.J. Wijetunge, the Head of the Department of Civil Engineering for identifying this as a high priority and sphere heading the work.

At present the focus of the University is to encourage “multi-disciplinary type” research and therefore, it will be prudent that some of the research work highlighted in this proceeding can be conducted with collaborations between members of the other departments of the faculty and also with the other faculties of the University, during the next phase. That will certainly make develop a strong network between faculty members and it will be easy to secure funding from local and overseas organizations.

Finally, I sincerely wish that some of this research will move to the next step of product or process development through the facilities available at the faculty and university level such as ETIC, BLIITO, MuNIC, etc, so that the economy of the country is going to benefit from our research efforts.

Dr. U.I. Dissanayaka
Dean / Faculty of Engineering,
University of Peradeniya.



Message from the Head, Department of Civil Engineering

I am delighted to send this message as the Head of the Department for the Proceedings of the Civil Engineering Undergraduate Research Symposium (CEURS) - 2023.

The Department of Civil Engineering is pleased to compile and publish in this volume, subsequent to review, a collation of selected extended abstracts of research performed by final-year undergraduate students specializing in civil engineering during the academic year 2023/24. The research project spanning across two semesters being a key component of their final year of study, enables the students to acquire valuable training under the supervision of our highly-qualified and -experienced academic staff not only on research methods but also on reviewing literature and effective technical writing while enhancing logical thinking and reasoning as well as analytical skills.

Whilst congratulating the students for publishing their research outcomes, I also take this opportunity to appreciate the valuable guidance and training in systematic research provided to them with considerable dedication by the academic staff members of the department. Let me also very much appreciate the reviewers for their important contributions during the thorough review process which is also an important and integral part of vital training and experience for the students in publishing research.

Finally, I thank the editor, Dr Gouri De Silva, and her team for their time and effort in compiling the proceedings of the research symposium as an open-access digital publication thereby enabling the dissemination of the research findings to the entire world.

Prof. J. J. Wijetunge
Head / Department of Civil Engineering,
Faculty of Engineering,
University of Peradeniya.



Editorial Note

As the editor, I am delighted to present the Proceedings of the Civil Engineering Undergraduate Research Symposium (CEURS 2023). This compilation features peer-reviewed extended abstracts that showcase the research outcomes of our final-year undergraduate students from the Department of Civil Engineering. CEURS 2023 includes 32 extended abstracts spanning a wide range of research topics, including Hydraulics and Water Resources Engineering, Environmental Engineering, Materials and Structural Engineering, Transportation and Traffic Engineering, Geotechnical Engineering, and Construction Management. I believe this publication highlights our students' research capabilities and provides an excellent platform for them to engage with the broader research community and discuss their valuable findings.

This publication would not have been possible without the continuous guidance, support, and encouragement from Dr. U.I. Dissanayaka, Dean of the Faculty of Engineering, and Prof. J.J. Wijethunga, Head of the Department of Civil Engineering. I extend my sincere gratitude to them for their leadership throughout this process. I'm also deeply appreciative of the Tokyo Cement Group for their unwavering financial support in facilitating research activities within the department.

I would like to extend special thanks to Ms. E.M.Y.C. Ekanayake and Mr. T.D.B. Koralegedara for their editorial assistance and to Mr. H.J.S.H. Jayaweera for his creative contributions to the cover design and other graphic elements. Finally, I extend my deepest gratitude to all the academic staff members of the Department of Civil Engineering and to the students, whose collaborative research efforts have made this publication possible.

Dr. M.M.G.T. De Silva

Editors of CEURS 2023

Department of Civil Engineering

Faculty of Engineering

University of Peradeniya

Table of Contents

Geotechnical and Transportation Engineering

01. Shredded Rubber for Partial Replacement of Ballast in Rail Track Applications 03
Thanusikan C., Mathynushan E., and Navaratnarajah S.K.
02. Strength and Swell Characteristics of Expansive Road Subgrade Stabilized with Novel Fly Ash Based One-Part Geopolymer 07
Jayawardane K.R.H., Rangana K.S.S., Nasvi M.C.M., and Kurukulasuriya L.C.
03. Strength and Swell Characteristics of Expansive Road Subgrade Stabilized with Novel Rice Husk Ash Based One-Part Geopolymer 11
Krishnalojan I., Sivasithamparam A., Nasvi M.C.M., and Kurukulasuriya L.C.
04. Influence of Gradation on Shear Behavior of Railway Ballast Material 15
Tharmarajah R., Amalan M., and Navaratnarajah S.K.
05. Prediction of Geotechnical Properties of Expansive Soil Stabilized with Fly Ash Using Artificial Neural Network 19
Kirushanthan K., Thigitharan T., and Nasvi M.C.M.
06. Relate Soil Permeability to Particle Size and Porosity 23
De Zoysa D.N.R., Ravindu K.J.A., and Udakara D.de S.
07. Comparison of Predictive Models for Soil-Gas Diffusivity 27
Iddamalgoda I.P.T.H., Wickramarachchi M.N., and Chamindu D.T.K.K.

Material and Structural Engineering

08. Enhance the Seismic Performances of Concrete Filled Steelbox Columns by Improving Confinement Effect: A Numerical Approach 33
Alahakoon A.M.Y.D., Malalage V.P., and Jayasinghe J.A.S.C.
09. Seismic Performance of Steel Hollow Building Column Under Combined Fire and Cyclic Loading: A Coupled Thermo-Mechanical Numerical Approach 37
Kanakarathna Y.P.K.M.W.N., Jayasooriya J.A.R.D., and Jayasinghe J.A.S.C.

10. Stress Analysis and Rehabilitation of Ancient Stupas in Sri Lanka 41
Buddhika H.A.D.S., Shanaka K.D.A., and Wijesiri M.N.M.
11. Development of Detailed Numerical Modal of Women Upper Torso for Garment Requirement 45
Jayaneththi J.K.P.S., Wickramasuriya B.Y., and Jayasinghe J.A.S.C.
12. Development and Characterization of Sustainable Mortar with Sugarcane Bagasse Ash 49
Naweendra J.A.L.N., Udayanga R.G.I., and Buddika H.A.D.S.
13. Improving the Accuracy of Numerical Predictions of Wind Interactions with Rectangular Tall Buildings 53
Hemachandra K.R.T., Herath H.M.N.M., and Wijesundara K.K.
14. Shear Strength of Plain Concrete Made of Recycled Polypropylene Waste Plastic as a Partial Replacement of Coarse Aggregate (A comparison between Experimental, Analytical & Numerical Approaches) 57
Thilakarathna, K.G.D.I.H., Weragama, W.A.R.U., and Bandara, C.S.
15. Effect of Resource Planning on Construction Project Delays 61
Ranathunga K.E., Wijesinghe K.M.U.M., and Dissanayake P.B.G.
16. Evaluation of Flexural and Shear Performance of Steel-Concrete Composite Beams with Flexible Shear Connectors 65
Ramyalal, W.P.N.A., Bandara, K.G.K.A., and Dammika, A.J.
17. Investigation of Dynamic Characteristics of PSC Girders and Predicting Base Line Damping Characteristics of PSC Bridges 69
Wickramarathna W.G.G.K., Perera M.T.D., and Dammika A.J.
18. Load Capacity Assessment of Dapped-End Beams with Critical Shear Span to Depth Ratios 73
Weerasekara L.C., Jayashani W.P.M., and Yapa H.D.,
19. Feasibility Investigation of Foam Concrete for Wall Panels 77
Kavinda E.A.V., Wijesinghe K.A.K., and Bandara S.

20. Chloride Penetration of Concrete Containing High-Volume Supplementary Cementitious Materials 81
Nilakshi L.M.S., Rajapaksha M.Y.S.K., and Pathirana C.K.

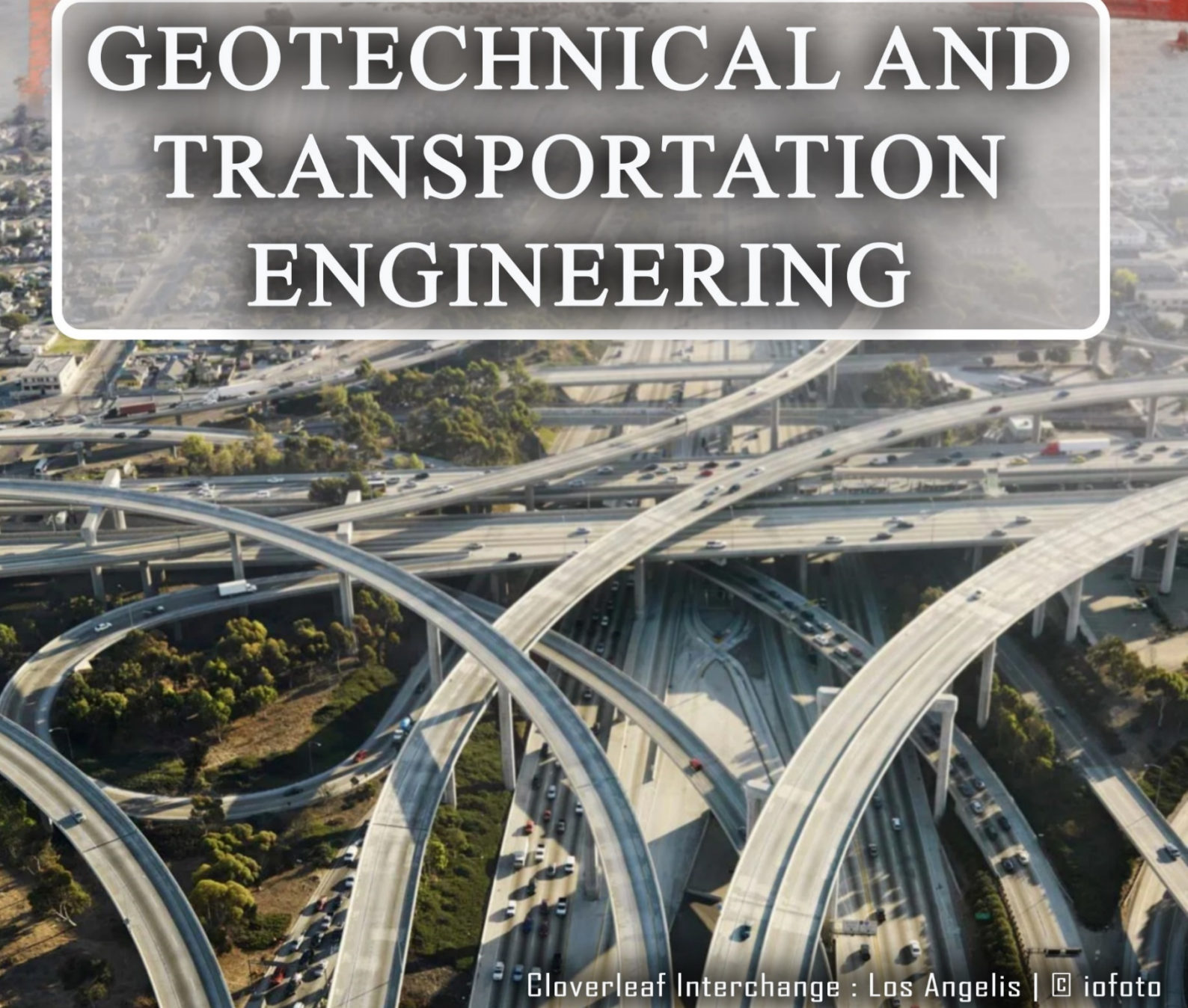
Water and Environmental Engineering

21. Application of HEC-HMS Model on Event-Based Simulation in Kalu Ganga 87
Kamburugamuwa S.W., Netthikumara N.K.Y., and Nandalal H.K.
22. Analyzing and Forecasting Rainfall Trends in Kirindi Oya River Basin 91
Withanage P.N.S., Wijeratne, P.W.G.R.S., and Nanayakkara, K.G.N.
23. Application Of Universal Soil Loss Equation to Mountainous Areas in Kalu Ganga Basin 95
Nethkalani K.A., Samarasinghe T.D.B. and Nandalal H.K.
24. Evaluating Clogging Effect in Vertical Flow Constructed Wetlands 99
Sachinika.W.A.T., Panagoda.H.A., and Weerakoon.G.M.P.R.
25. Comparison Of SARIMA and ANN Models for Forecasting Streamflow Data of the Nilwala River 103
Tharangani K.K.A., Dilshan V.P. and Nandalal K.D.W.
26. Modeling Of Hydrodynamic Processes of Membrane Based Treatment System Using Artificial Neural Network 107
Punchihewa K.G.G., Dissanayake D.M.N.D., and Nanayakkara K.G.N.
27. Hydraulic Modelling of Membrane Filtration Using Computational Fluid Dynamics 111
Pathiranage D.S., Sandaruwan G.P.C., and Nanayakkara K.G.N.
28. Investigate The Effect of Sustainable Stormwater Management in An Urban Catchment 115
Abeykoon G.A.M.H.K., Dunukara D.A.M.D., and Gunawardana W.C.T.K.

29. Impact of River Bathymetric Models on River Hydrodynamic Simulations 119
Banadara W.M.J.J., Hemakumara H.N.S., and Neluwala N.G.P.B.
30. Rainfall Trend Analysis in Mi-Oya River Basin 123
Wickramaratne L.T., Hasaranga H.J.S. and De Silva M.M.G.T.
31. Estimation of Water Level Using Satellite Data 127
Nawoda J.M.I., Madumalsha A.A.D.C., and Neluwala N.G.P.B.
32. Identification of the Most Critical Parameter for Wastewater Treatment Using STOAT Software 131
Wijewickrama W.S.C., Wimalarathne P.G.S.N., and Rathnayake R.M.L.D.



GEOTECHNICAL AND TRANSPORTATION ENGINEERING



Shredded Rubber for Partial Replacement of Ballast in Rail Track Applications

Thanusikan C.*, Mathynushan E., and Navaratnarajah S.K.

Department of Civil Engineering, Faculty of Engineering, University of Peradeniya, Sri Lanka

*kumar.sikan1997@gmail.com

Keywords: Ballasted track, Crumb rubber, Numerical simulation, Shredded rubber

Abstract

Railway transportation, a widely adopted mode globally, relies heavily on ballast materials to support tracks and ensure structural stability. Traditional choices like crushed stone, gravel, and slag dominate due to their cost-effectiveness and technical merits. However, prolonged exposure to cyclic loading and environmental factors alters their properties. Shredded rubber presents advantages such as durability, shock absorption, noise reduction, and sustainability. The research focuses on determining the optimal shredded rubber percentage as a weight-based replacement for ballast. Large-scale direct shear experiments were conducted, varying normal stress conditions. However, for this particular experiment, the loading was limited to 60kPa, to provide essential parameters. Subsequently, discrete element method simulations predict these parameters. The study recommends incorporating 10-15% shredded rubber by weight to mitigate peak shear stress and dilation effects, resulting in a notable 52-57% reduction in ballast breakage and enhanced durability for rail track applications.

1. Introduction

The railway transportation system is increasingly demanding, with ballasted tracks being a traditional mode of transportation. Ballast performance depends on the mechanical behavior of the ballast material, which can deteriorate due to repetitive loading and environmental conditions. Shredded rubber is derived from recycling automotive and truck scrap tires. This study aims to combine shredded rubber with ballast particles to reduce ballast degradation and noise, making it a cost-effective and environmentally friendly solution in the railway transportation system. In numerical analysis, the discrete element method (DEM) is used in rail track applications to simulate particle behavior in ballast materials. DEM allows for the analysis of particle interactions, settlement, deformation, and track degradation under different loading conditions. This helps

engineers optimize ballast design, assess track performance, and evaluate maintenance strategies, contributing to the development of efficient and sustainable rail track systems. In this study numerical models were developed to simulate the load test of rubber intermixed with ballast using DEM by scanning and importing rubber and ballast particles.

2. Literature review

The main functions of railway ballast are to facilitate the drainage of water from the track bed and mitigate the stresses resulting from train loads on the underlying layers. Ballast movement during long-term train loadings can cause settlement and stiffness changes, reducing strength. Techniques such as elastic inclusions like rubber mats, tire-derived aggregates, and polyurethane-based inclusions improve railway ballast serviceability (Esmaeili et al., 2016). Guo et al., (2022) propose a cost-effective and environmentally friendly solution of mixing crumb rubber with ballast particles derived from shredded waste tires, which has been proven to effectively reduce ballast degradation and noise. Gong et al. (2019) conducted large-scale direct shear tests on specimens of 500-350 mm in size and found that boundary effects can be ignored if the chamber dimension to particle size ratio is greater than 7-8%. The tests were conducted at three normal loads and stress levels. Ballast and TDA (Tyre Derived Aggregates) were mixed, and a sinusoidal load was applied for a compacted state. The study suggests that 10% rubber content provides the optimum solution.

Numerical models aid in studying complex systems, allowing researchers to analyse variables, conduct simulations, and explore potential outcomes through DEM. Guo et al., (2019) performed direct shear tests (DSTs) on the rubber-protected ballast (RPB) and built a DST model and a three-sleeper track model with the DEM. 'PFC2D' is utilized in this study. The primary components used to simulate ballast particles are discs, which are often insufficiently accurate to accurately represent the natural

characteristics of railway ballast (Indraratna et al., 2014). The bonded particle model (BPM) is a method used to model irregular particle shapes, focusing on clumps or clusters. Clumps are rigid particles that remain unbreakable despite large forces applied. Clusters, on the other hand, are less rigid particles that can break if the force exceeds a defined threshold value. Both models have been widely used in studies.

3. Methodology

3.1 Experimental method

For this study, ballast particles were collected from Gampola Railway Unit, and the required amount of rubber particles was collected from Jaffna. Particle size distribution was selected with four different size ranges: 19-25, 25-37.5, 37.5-50, and 50-63 mm as shown in Figure 1.



Figure 1: Ballast Particle size ranges

Subsequently, the samples underwent washing and drying to eliminate impurities. After obtaining the necessary samples from the previously separated four different-sized ballast samples, they were colour-coded with three different colours to distinguish the three layers within the samples for testing. This colouring process was essential due to the presence of three distinct layers in the DST apparatus. Following the painting, the particles were systematically numbered as 1, 2, 3, and 4, facilitating the differentiation of the four size ranges of particles. This procedural step played a crucial role in conducting breakage analysis. For the preparation of rubber samples, the collected rubber particles were cut according to the particle size distribution, and they were separated as shown in Figure 2. Then considering the proposed percentages by weight rubber particles were mixed with ballast as shown in Figure 3.



Figure 2: Rubber Particle size ranges

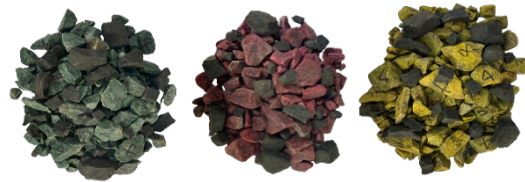


Figure 3: Prepared mixture of samples

For the test, already designed large-scale direct shear test apparatus was used. The apparatus has a circular shear plane and can accommodate a 400 mm diameter and 300 mm height test specimen. The shear plane was maintained at 150 mm height, allowing the sample to separate into two equal portions using top and bottom cylinders with 150 mm depth. The top cylinder movement was restricted, while the bottom cylinder was displaced laterally at a constant rate of 4 mm/min using a hydraulic jack. A lever-arm system was used to apply normal stress (60 kPa) through the top loading plate, which rested on the test sample and moved vertically throughout the test. The reaction force on the top cylinder during shearing was measured by the load cell, while the lateral displacement of the bottom cylinder was measured by Linear Variable Differential Transducers (LVDT). Data from the load cell and two LVDTs were recorded from the data logger. Figure 4 shows the large-scale direct shear test apparatus setup with connected load cell and LVDTs.



Figure 4: Large-scale direct shear test apparatus

3.2 Numerical analysis

The ballast and rubber particles are granular materials, therefore continuum modelling methods like the finite element technique or the finite difference method cannot capture realistic particle features like movements, morphology, and deterioration. DEM models, in comparison, can show both the characteristics and the behaviours of the particles at the mesoscopic level (such as contact force chains, accelerations, and displacements). Since the DEM has proven to be a useful tool for railway ballast simulation and has been successfully employed in

numerous research, numerical simulation with DEM models is used in this study.

3.2.1 Particle generation

The shape of the aggregate is crucial in numerical modelling to simulate the behaviour of angular ballast aggregates and rubber particles. A library of CAD templates for variously shaped ballast and rubber particles was produced using 3D scanning, representing each size range of ballast and rubber in accordance with the particle size distribution. The novel method is to construct the nearly realistic shape of ballast and rubber particles in DEM utilizing CAD templates of the original ballast and rubber particles. Overlapping (unbreakable) spheres were used to represent the four various size ranges of ballast and rubber, four chosen ballast and rubber particles were created. Figures 5 and 6 show the generated ballast and rubber particles using overlapping method.

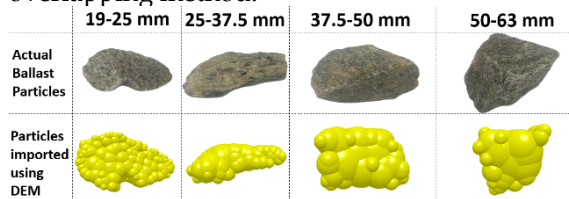


Figure 5: Unbreakable particle shapes of ballast

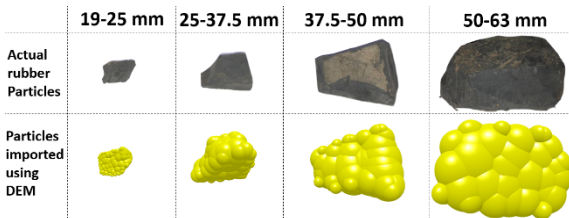


Figure 6: Unbreakable particle shapes of rubber

3.2.2 Large-scale direct shear test model

The test apparatus was modelled according to the actual dimensions using steel material as shown in Figure 7. The top cylinder is stationary, and the bottom cylinder is movable in the shearing direction with a constant strain rate of 4 mm/min. The top-loading plate is used to apply normal stresses on the samples during the test.

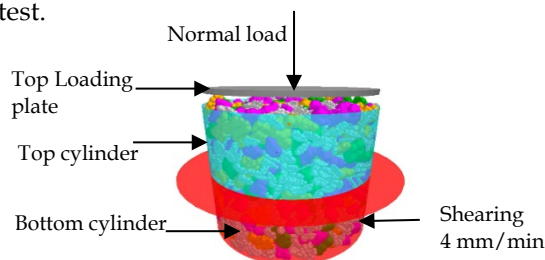


Figure 7: DEM of Large-scale direct shear test

3.2.3 Simulation and validation

The particles were injected into the cylinder according to the selected particle size distribution. The loading was applied after particle was filled. The numerical model was calibrated and validated using experiments involving five types of interactions (ballast-ballast, ballast-rubber, ballast-steel, rubber-steel, rubber-rubber). The model was initially calibrated for ballast interactions, then adjusted for rubber interactions and checked with multiple mixes. The process was completed to ensure accuracy and consistency in the model.

4. Results and Discussion

4.1 Experimental Results

Figure 8 shows the comparison of shear stress varying with shear strain for the normal stress of 60 kPa. As expected, the peak shear stress value is reduced with the increasing rubber percentages because rubber is typically less rigid and has lower shear strength compared to traditional ballast materials. As the rubber content increases, it can act as a softer material between the ballast particles, leading to decreased interparticle friction and, consequently, reduced shear strength.

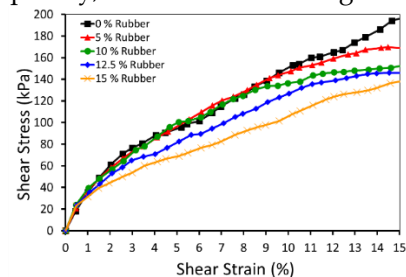


Figure 8: Comparison of Shear Stress vs Shear Strain for 60 kPa Normal Stress.

Figure 9 shows the variation of vertical strain with shear strain for the normal stress of 60 kPa. The positive vertical strain represents the upward movement of the loading plate, indicating the particles' dilation, while the negative vertical strain indicates the particles become compressed (dense) during the shear process. Normally, while doing the test with 0% rubber (only ballast), because of the angularity and hardness of the ballast material, the ballast particles roll on top of each other, which makes the dilation effect more prominent. But when the ballast particles are intermixed with the rubber, the overall sample compressibility is increased, so the dilation effect is somewhat reduced, and with the increasing rubber content, the compression gets higher.

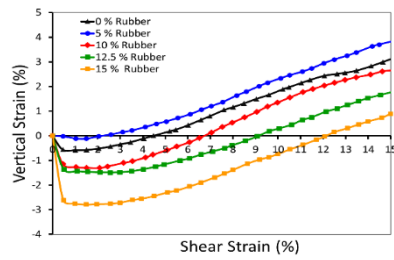


Figure 9: Comparison of Vertical Strain vs. Shear Strain for 60 kPa normal stress.

Figure 10 shows how the Ballast Breakage Index (BBI) and peak shear stress vary with different rubber percentages. Breakage occurred, especially at high normal stress during direct shear tests (DSTs), significantly influencing the mechanical behavior and durability of the track. Increasing rubber content decreased BBI as rubber particles are more deformable and less brittle than traditional ballast materials. This reduction in brittleness, accompanying higher rubber percentages, leads to less ballast particle breakage during loading and deformation, consequently lowering peak shear stress values.

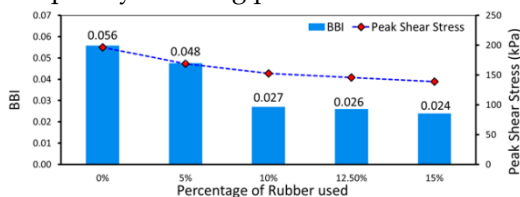


Figure 10: Comparison of BBI and Peak Shear Stress with percentage of Rubber

4.2 Numerical Analysis Results

Figure 11 shows the validation of numerical results with 0% rubber (ballast only) and 10% rubber for the normal stress of 60 kPa.

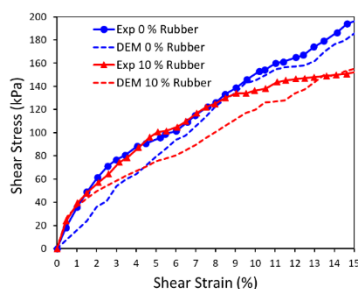


Figure 11: Validation of shear stress vs. shear strain results of both experiment and numerical (DEM) analysis under 60 kPa normal stress.

Figure 12 shows the comparison of experimental and numerical analysis results for the applied normal stress of 60 kPa. After validation the numerical model was run for different percentages of rubber intermixed with ballast particles.

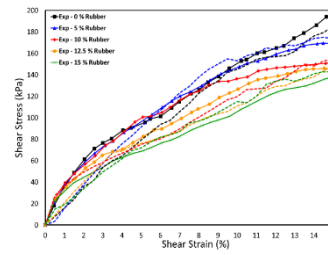


Figure 12: Comparison of shear stress vs. shear strain results of both experiment and numerical (DEM) analysis under 60 kPa normal stress.

5. Conclusions

The study on the impact of rubber content on ballast mixtures found that increasing the rubber content reduces peak shear stress. Incorporating 10-15% shredded rubber significantly reduced ballast breakage by 52-57%. These findings, supported by DEM simulations and laboratory tests, suggest that the optimal rubber content range is 10-15%, balancing shear stress reduction and improved durability in ballast mixtures. While the increase in rubber percentage leads to overall compression, the interaction of rubber particles with ballast during sliding and rolling allows more compression and reduces dilation. However, due to time constraints, the laboratory tests were limited to 60 kPa normal stress. To determine the friction angle for various rubber contents, further tests at additional normal stresses are required. This work is ongoing as part of the overall project plan.

References

- Esmaeili, M., Zakeri, J.A., Ebrahimi, H. and Khadem Sameni, M. (2016) 'Experimental study on dynamic properties of railway ballast mixed with tire derived aggregate by modal shaker test', *Advances in Mechanical Engineering*, 8(5), p. 168781401664024. Available at: <https://doi.org/10.1177/1687814016640245>.
- Gong, H., Song, W., Huang, B., Shu, X., Han, B., Wu, H. and Zou, J. (2019) 'Direct shear properties of railway ballast mixed with tire derived aggregates: Experimental and numerical investigations', *Construction and Building Materials*, 200, pp. 465-473. Available at: <https://doi.org/10.1016/j.conbuildmat.2018.11.284>.
- Guo, Y., Zhao, C., Markine, V., Jing, G. and Zhai, W. (2020) 'Calibration for discrete element modelling of railway ballast: A review', *Transportation Geotechnics*, 23, p. 100341. Available at: <https://doi.org/10.1016/j.trgeo.2020.100341>.
- Indraratna, B., Ngo, N.T., Rujikiatkamjorn, C. and Vinod, J.S. (2014) 'Behavior of Fresh and Fouled Railway Ballast Subjected to Direct Shear Testing: Discrete Element Simulation', *International Journal of Geomechanics*, 14(1), pp. 34-44. Available at: [https://doi.org/10.1061/\(ASCE\)GM.1943-5622.0000264](https://doi.org/10.1061/(ASCE)GM.1943-5622.0000264).

Strength and Swell Characteristics of Expansive Road Subgrade Stabilized with Novel Fly Ash Based One-Part Geopolymer

Jayawardane K.R.H.*, Rangana K.S.S., Nasvi M.C.M., and Kurukulasuriya L.C.

Department of Civil Engineering, Faculty of Engineering, University of Peradeniya, Sri Lanka

* e17141@eng.pdn.ac.lk

Keywords: One-part geopolymer, Fly ash, Unconfined compressive strength

Abstract

Expansive soils pose challenges in road construction due to volumetric changes and limited bearing capacity. Ordinary Portland Cement (OPC) is popular for stabilization, but its sustainability is hindered by greenhouse gas emissions. Alkali-activated geopolymers, which can be one-part or two-part, have gained attention as sustainable binders. This study aims to assess the strength and swell characteristics of a fly ash-based, one-part geopolymer (OP-G) stabilized road subgrade. A series of 16 Unconfined Compressive Strength (UCS) specimens were tested with various binder/dry soil and solid NaOH/fly ash ratios to determine the optimal mix for OP-G stabilization, with a comprehensive cost analysis. Based on both cost and UCS, the optimum OP-G formulation occurred at a binder/dry soil ratio of 0.2 and a NaOH/fly ash ratio of 0.1. The study supports the use of fly ash-based OP-G for stabilizing the expansive road subgrade.

1. Introduction

Expansive soil is problematic due to its low shear strength, high swelling, and shrinkage. Soil stabilization improves its structural capacity through physical and chemical methods. Physical methods alter soil properties, while chemical methods modify soil properties by adding active materials. Chemical stabilization is popular due to cost benefits and control over setting and curing times. Ordinary Portland Cement (OPC), a popular soil stabilization binder, is becoming unsustainable due to global greenhouse gas emissions.

Alkali-activated binders (AAB) are a promising solution to calcium-based stabilizer problems. Davidovits (2015) highlights that the use of AABs instead of traditional stabilizers can significantly reduce greenhouse gas emissions (GHG), ranging from 70 to 90%. Alkali-activated geopolymers have emerged as a promising alternative to traditional cement, offering

potential benefits for various applications. Geopolymers are divided into two types: one-part and two-part, based on the alkali activator used, with two-part geopolymers (TP-G) using liquid activators and one-part geopolymers (OP-G) using solid activators.

Despite the advantages of using one-part geopolymers, such as simplified transportation, reduced costs, and improved safety, the number of studies conducted on this specific application is limited, hindering a comprehensive understanding of their efficacy and potential. Therefore, there exists a significant knowledge gap regarding the utilization of one-part geopolymers in soil stabilization.

2. Literature review

Researchers have explored the use of alkali-activated fly ash-based OP-G for stabilizing expansive soils. Tesanasin et al., (2022) studied the use of alkali-activated fly ash-based OP-G for stabilizing marginal lateritic soil. They found that the optimal dosage of solid NaOH (NH) in flake form was 20% or less. The analysis of cost and CO₂ emission of OP-G and TP-G stabilized materials revealed that TP-G had higher CO₂ emissions and lower costs for samples stabilized with OP-G. Zheng et al., (2021) suggested using OP-G as a binder for stabilizing soft clay instead of OPC. The geopolymer binder was created by mixing water with a solid source material, ground granulated blast furnace slag, FA, and a solid NH activator. The study found that UCS values increased with FA content up to 10% and reduced with further addition. The geopolymer-stabilized clay achieved a higher UCS than clay stabilized with OPC.

3. Methodology

3.1 Sample Collection

The soil sample was obtained from the Hettipola area in Mahiyanganaya (Coordinates of 7.543038, 80.914474). Fly ash (FA) was collected

from the Lakwijaya coal power plant in Norochcholai.

3.2 Characterization Testing

The expansive soil sample was classified after conducting the following laboratory tests.

Table 1: Characterization Testing

Test	Result
Sieve and hydrometer analysis (BS 1377: Part 2: 1990)	Particle size distribution
Atterberg limit tests (BS 1377: Part 2: 1990)	Index properties
Standard proctor compaction test (BS 1377: Part 2: 1990)	Maximum dry density (MDD) & Optimum moisture content (OMC)
Specific gravity test (BS 1377: Part 4: 1990)	The specific gravity of soil
Swell pressure test (BS 1377: Part 5: 1990)	Swell pressure
Unconfined compressive strength (UCS) test (BS 1377: Part 7: 1990)	UCS

3.3 Mix Optimization

The optimized mix parameters for OP-G have been extracted from the relevant literature.

Table 2: Mix Optimization Parameters

Mix Parameter	Values
B/S (mass ratio)	0.2, 0.25, 0.3 and 0.35 (Wu et al., 2021)
NH/ FA (mass ratio)	0.1, 0.15, 0.2 and 0.25 (Wu et al., 2021, Zheng et al., 2021)

To determine the optimal mix for OP-G stabilization in terms of strength and cost, a series of 16 UCS specimens were casted with variations in binder (FA + NaOH)/ dry soil (B/S) ratio and solid NaOH/ FA (NH/FA) ratio. The mix optimization parameters are given in Table 2. The optimum one-part geopolymer

stabilized soil sample was found based on UCS test results and cost per unit volume of stabilized soil.

3.3.1 Sample Preparation

Two mixing methods were followed when preparing the stabilized soil samples.

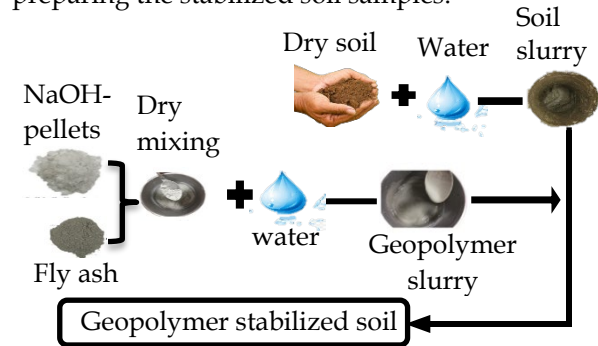


Figure 1: Mixing method 1

According to method 1, the soil-slurry was first made through mixing the dry soil mass with the prescribed amount of water. Secondly, geopolymer-slurry was prepared by mixing the dry source material (i.e., FA and solid NH) and water. Thirdly, the geopolymer-slurry was added into the soil-slurry to prepare the geopolymer stabilized soil slurry (see Figure 1). But this mixing method addressed an issue related to the geopolymer binder's inadequate mixing with the soil slurry (see Figure 2). It was due to the flocculation of the geopolymer binder before achieving thorough mixing with the soil. Consequently, it was decided to exclusively employ mixing method 2 (see Figure 3) for the preparation of all OP-G-stabilized soil samples.



Figure 2: The flocculation of geopolymer binder before being combined with the soil

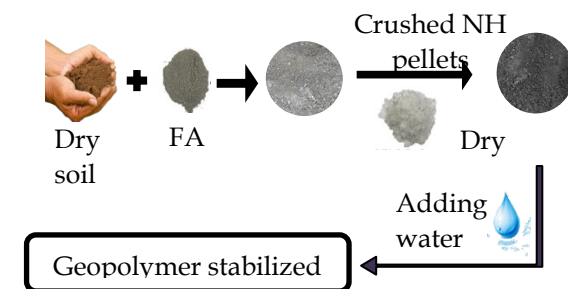


Figure 3: Mixing method 2

In accordance with mixing method 2, the soil was mixed with FA for an approximate duration of 5 minutes to ensure proper mixing. Following this, crushed solid NH pellets were mixed with the soil mixture, with the mixing process continuing for an additional 8 minutes. The next step involved the addition of the required quantity of water, taking into account both the soil and geopolymer binder. The soil, FA, and solid NH mixture underwent a thorough mixing with the water to achieve a homogenous consistency (see Figure 3). Flocculation of geopolymer binder was avoided using this method as shown in Figure 4.



Figure 4: Properly mixed geopolymer binder and soil

To obtain total water amount needed for each sample, three different cases were trialled.

- Case 1: Weight of water for the soil slurry = Total dry soil weight x OMC
- Case 2: Total weight of water = Total weight of solids x OMC
- Case 3: Total weight of water = Total weight of solids x 1.2OMC

Table 3: UCS results of the trial run

B/S	NH/FA	CASE 01	CASE 02	CASE 03
		Method 1 (UCS/ MPa)		
0.2	0.15	0.19	0.4	0.25

Based on UCS results obtained, case 2 was selected to prepare all the samples.

3.3.2 Testing of OP-G samples

The UCS of prepared OP-G stabilized samples was measured using a motorized machine, capable of applying axial compression to the specimen at a suitable rate of displacement. The test process was based on BS 1377-Part 7:1990. The actual rate of platen displacement was maintained at 0.1 mm/min. The UCS of cured samples was measured at 7 days, and the

reported UCS values are averages of 3 test specimens.

3.3.3 Optimization of the mix based on UCS and cost

The optimum OP-G stabilized soil sample was found based on UCS test results and cost per unit volume of stabilized soil. A comprehensive cost analysis, focusing solely on manufacturing expenses, was conducted for all samples. The overall utility for each sample was calculated considering UCS and cost/UCS assigning the same weights for both responses.

4. Results and discussion

4.1 Characterization test results

Table 4: Results of characterization testing

Properties	Values
Specific gravity	2.67
Liquid limit (%)	55
Plastic limit (%)	29
Plasticity index (%)	26
Maximum swell Pressure (kPa)	163.7
Maximum swell percentage (%)	4.7
UCS (MPa)	0.32
MDD (kN/m ³)	14.91
OMC (%)	23.8

4.2 UCS results

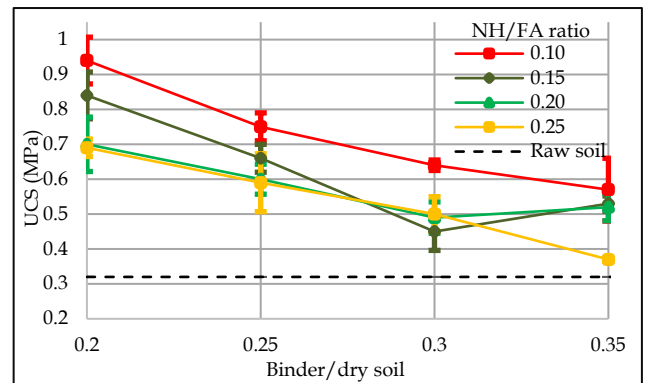


Figure 5: The variation of 7-D UCS with NH/FA ratios

Figures 5 and 6 show the UCS of OP-G stabilized soil at different NH/ FA ratios and B/S ratios. According to Figure 5, the optimum B/S ratio was found as 0.2.

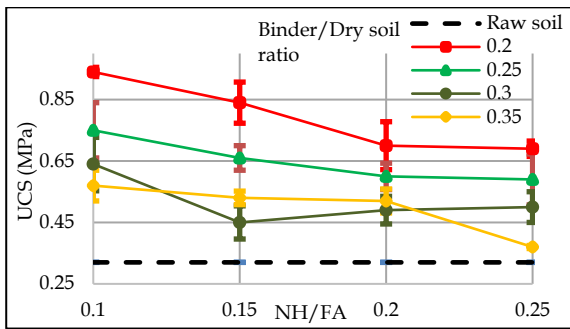


Figure 6: The variation of 7-D UCS with B/S ratios

According to Figure 6, the optimum NH/FA ratio was found as 0.1.

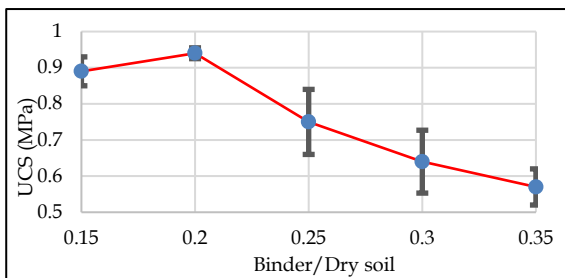


Figure 7: The variation of 7-D UCS with NH/FA ratio for optimum B/S ratio (0.2)

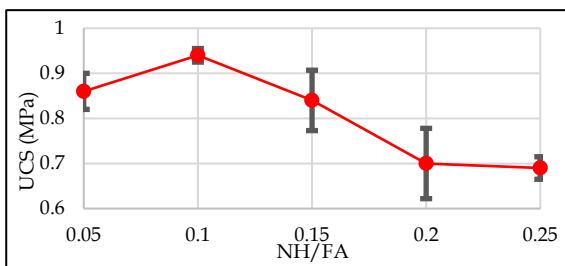


Figure 8: The variation of 7-D UCS with NH/FA ratio for optimum NH/FA ratio (0.1)

The highest UCS was found in the mix with a B/S ratio of 0.2 and solid NH/FA ratio of 0.1 in which the UCS value reached 0.94 MPa at 7 days curing time. According to Figure 7, the UCS values of stabilized soil increased to an optimum and again decreased with the increasing of NH/FA ratio. This indicated that higher or lower NH content would not improve the mechanical properties of expansive clay. The increase in UCS was due to the formation of N-A-S-H gels from polymerization reactions. The decrease in UCS with NH/FA higher than 0.1 was because of the heat generation of NH which led to expansion and cracking (Tesanasin et al., 2022). According to Figure 8, the UCS values of

stabilized soil increased to an optimum and again decreased with the increasing B/S ratio. This indicated that when the FA was beyond a certain amount, it also would perform negative impact on early UCS values of stabilized soil high strength due to a higher proportion of unreacted FA particles.

4.3 Optimized mix based on UCS and cost

According to the overall utility calculated for each sample considering UCS and cost/UCS, all mixes were ranked. The optimum mixing proportion of OP-G stabilized soil was found to be a B/S ratio of 0.2 and a solid NH/FA ratio of 0.1 based on both UCS and cost/UCS.

5. Conclusion

- For high UCS value, the optimum sample mixing method and optimum water content are premixing the dry ingredients first before adding water and OMC respectively.
- The highest UCS was found in the mix with binder/ dry soil (B/S) ratio of 0.2 and solid NaOH/ fly ash (NH/FA) ratio of 0.1 in which the UCS value reached 0.94 MPa at 7 days curing time.
- In this paper, the optimum mixing proportion of OP-G stabilized soil was found to be a binder/ dry soil (B/S) ratio of 0.2 and solid NaOH/ fly ash (NH/FA) ratio of 0.1 based on both UCS and cost/UCS.
- The fly ash-based one-part geopolymer can be used to stabilize expansive road subgrades.

References

- Tesanasin, T., Suksiripattanapong, C., Van Duc, B., Tabyang, W., Phetchuay, C., Phoo-ngernkham, T., Sukontasukkul, P. and Chindaprasirt, P. (2022) 'Engineering properties of marginal lateritic soil stabilized with one-part high calcium fly ash geopolymer as pavement materials', *Case Studies in Construction Materials*, 17, p. e01328. Available at: <https://doi.org/10.1016/j.cscm.2022.e01328>.
- Wu, J., Min, Y., Li, B. and Zheng, X. (2021) 'Stiffness and strength development of the soft clay stabilized by the one-part geopolymer under one-dimensional compressive loading', *Soils and Foundations*, 61(4), pp. 974-988. Available at: <https://doi.org/10.1016/j.sandf.2021.06.001>.
- Zheng, X. and Wu, J. (2021) 'Early Strength Development of Soft Clay Stabilized by One-Part Ground Granulated Blast Furnace Slag and Fly Ash-Based Geopolymer', *Frontiers in Materials*, 8, p. 616430. Available at: <https://doi.org/10.3389/fmats.2021.616430>.

Strength and Swell Characteristics of Expansive Road Subgrade Stabilized with Novel Rice Husk Ash Based One-Part Geopolymer

Krishnalojan I.*, Sivasithamparam A., Nasvi M.C.M., and Kurukulasuriya L.C.

Department of Civil Engineering, Faculty of Engineering, University of Peradeniya, Sri Lanka

* e17171@eng.pdn.ac.lk

Keywords: Alkali-activated binders, One-part geopolymer, Rice husk ash, UCS

Abstract

Expansive soil poses challenges for road subgrade due to its restricted bearing capacity and volumetric fluctuations with water during climate change. Common chemical stabilization techniques, like ordinary Portland cement, contribute to greenhouse gas emissions. Geopolymer has gained interest due to its low environmental impact. However, a Two-Part Geopolymer (TP-GP) has drawbacks. One-Part Geopolymer (OP-GP) mixes, known as "just add water" mixes, are recommended. This study analyses the swell characteristics and strength of OP-GP stabilized road subgrade based on Rice Husk Ash (RHA). A series of Unconfined Compressive Strength (UCS) specimens were cast with changes in (RHA + NaOH) /dry soil (B/S) ratios (0.10 to 0.35) and solid NaOH/RHA (NH/RHA) ratios (0.10 to 0.25) to identify the ideal mix for OP-GP stabilization. A thorough cost analysis was conducted for each sample, focusing on manufacturing and transportation costs. The best OP-GP formulation was found at a (B/S) ratio of 0.2 and an NH/RHA ratio of 0.15.

1. Introduction

Expansive soil is problematic because of the presence of clay minerals like montmorillonite. (Maheepala et al., 2022). Expansive soil damage, exacerbated by industrial waste amendments, incurs an annual global repair cost surpassing that of natural disasters, reaching \$7 billion. Ground improvements involve physical and chemical methods to improve load-bearing capacity, soil erosion resistance, and control soil heave. Chemical stabilization is popular due to its cost-effectiveness and control over curing and setting times. OPC is the most commonly used binder for soil stabilization. However, the International Energy Agency revealed that global PC production contributes to 8% of global CO₂ emissions, resulting in around 2.2 billion tons of CO₂ emissions. Ca-based stabilizers contribute to energy-intensive production,

greenhouse gas emissions, and soil stabilizer system misplacement due to leaching, forming carbonation shrinkage cracks with excess CO₂. Alkali-Activated Binders (AAB) are being diagnosed as a distinctly promising answer to tackle the issues related to calcium-based stabilizers. Geopolymers are inorganic, amorphous, and three-dimensional polymeric chains formed between alumina-silicate materials. The adoption of AABs as a substitute for regular stabilizers can lead to a terrific discount on greenhouse fuel (GHG) emissions, ranging from 70 to 90%. Geopolymers can be categorized into two distinct types: one-part and two-part. The differentiation lies in the phase of the alkali activator employed. The TP-GP employs liquid alkali activators, whereas the OP-GP uses solid alkali activators. Despite the disadvantages of using TP-GP, such as the complexity of mixing, short pot life, complexity of handling, and sensitivity to environmental factors, one-part geopolymers are preferred in soil stabilization.

The total annual RHA production would be approximately 0.1 million tons per year in Sri Lanka. Currently, RHA does not have any commercial use in Sri Lanka, leading to its frequent disposal in landfills, thereby causing wide scale environmental pollution. If OP-GP is used with RHA, then it would be a sustainable alternative for cement soil stabilization. Therefore, aim of this research is to analyse strength and swell characteristics of expansive road subgrade stabilized with novel RHA based OP-GP.

2. Literature review

Maheepala. et al., (2022) conducted a review on expansive soil stabilization. It was found that the incorporation of precursors in the range of 15-20%, alkaline molarities between 5 and 10 M, along with strong alkalis (NaOH or KOH), Ca-rich additives, and discrete fibers could enhance the stabilization performance with respect to UCS, swell, and durability. Tesanasin et al., (2022) conducted research on the properties of Marginal Lateritic Soil (MLS) with one-part high calcium fly ash geopolymer. Beyond 20%

NaOH, UCS and indirect tensile strength reduced due to the heat generation of NaOH which led to expansion, microcracking, shortening of setting time, early precipitation of the geo polymer products and reduction of strength.

3. Methodology

3.1 Sample Collection

The soil sample was collected from Wilgamuwa, Central Province, Sri Lanka. (7°32'34.9"N 80°54'52.1"E). The RHA was brought from Divulapitiya rice mill and chemical components such as NaOH and Na₂SiO₃ were brought from the local market in Colombo, Sri Lanka.

3.2 Characterization Testing

The classification of an expansive soil sample was determined by performing laboratory tests such as sieve and hydrometer analysis (BS 1377: Part 2: 1990), Atterberg limit tests (BS 1377: Part 2: 1990), standard proctor compaction test (BS 1377: Part 2: 1990), specific gravity test (BS 1377: Part 4: 1990), swell pressure test (BS 1377: Part 5: 1990) and UCS test (BS 1377: Part 7: 1990).

3.3 Mix Optimization

With the help of the literature, mix optimization parameters as given in Table 1 were selected. A series of 16 UCS specimens were cast with different binder (RHA + NaOH)/ dry soil (B/S) ratios and solid NaOH/ RHA (NH/RHA) ratios to determine the optimal mix for OP-G stabilization in terms of strength.

3.4 Sample preparation and curing

The method used to prepare the OP-GP stabilized expansive soil sample is described in Figure 1. Soil mix was prepared by mixing raw soil with the prescribed amount of water by following the method adopted by Wu et al., (2021). Thereafter, geopolymer mix was prepared by mixing RHA, and NaOH with the prescribed amount of water. Immediately both mixes were mixed to prepare the geopolymer stabilized soil mix.

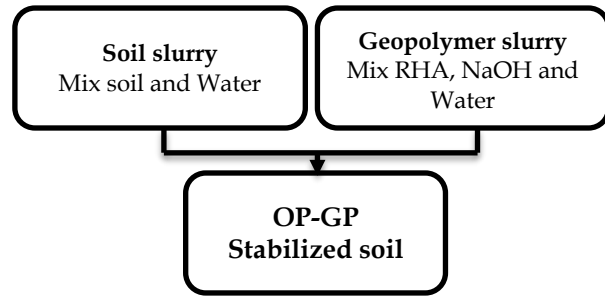


Figure 1: Sample preparation method

Mix Parameter	Values	Reference
B/S (by weight ratio)	0.1, 0.15, 0.2, 0.25, 0.3	Wu et al., 2021
NH/ RHA (by weight ratio)	0.1, 0.15, 0.2, 0.25	Wu et al., 2021, Zheng et al. 2021

Table 1: Mix Optimization for OP-GP

The required quantity of water was added, taking into account both the soil and geopolymer binder. The soil, RHA, and solid NH mixture underwent a thorough mixing with the water to achieve a homogenous consistency. Three different mixing water contents (Cases 1 to 3) were trialled to obtain the optimum water content for high UCSs.

Case 1: Total weight of water = Total weight of solids x OMC

Case 2: Total weight of water = Total weight of solids x 1.2 OMC

Case 3: Total weight of water = Total weight of solids x 1.4OMC

Stabilized samples were fully wrapped using cling wrap and cured under room temperature for 7 days.

3.5 UCS Test for OP-GP Samples

In compliance with BS 1377-Part 7:1990 standards, a motorized machine was utilized to measure the UCS of OP-GP stabilized samples. The platen displacement rate was kept constant at 1 mm/min. Three test specimens were excluded from the mould to determine UCS values, which guaranteed a standard deviation of less than 10% of the average strength after seven days.

3.6 Mix optimization of OP-GP

The optimal OP-GP stabilized soil sample was chosen by evaluating UCS test results and the cost per unit volume of stabilized soil. A thorough cost analysis, specially concentrating on manufacturing and transportation expenses, was carried out for all samples. The overall utility of each sample was calculated, taking into account UCS and cost/UCS, with weights of 0.3 and 0.7 assigned to both responses, respectively.

4. Results and Discussion

4.1 Characterization test results

The results of the raw soil characterization are given in Table 2. Based on the characterization results, this soil is classified as clay of high plasticity (CH).

Table 2: Results of characterization testing of expansive soil

Properties	Values
Specific gravity	2.67
Liquid limit (%)	55
Plastic limit (%)	29
Plasticity index (%)	26
Soil classification (USCS)	CH
Maximum swell Pressure (kPa)	163.7
Maximum swell percentage (%)	4.7
UCS (MPa)	0.32
MDD (kN/m ³)	14.91
OMC (%)	23.8

4.2 UCS results

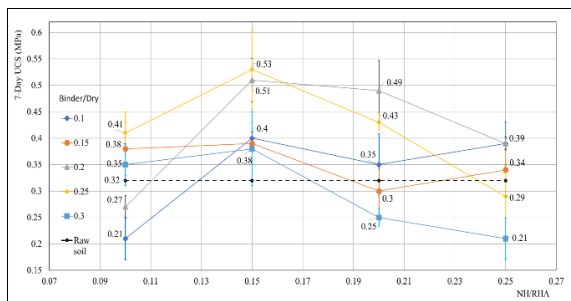


Figure 2: The variation of UCS with NH/RHA ratios

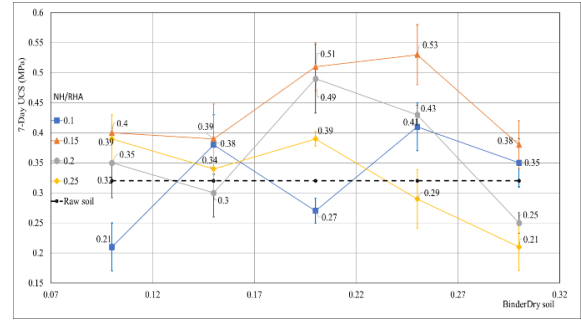


Figure 3: The variation of UCS with B/S ratios

Figures 2 and 3 shows the variation of UCS of OP-GP stabilized soil with NH/RHA and B/S respectively. According to Figures 2 and 3, the optimum B/S ratio and NH/RHA ratio for higher UCS were found to be 0.25 and 0.15.

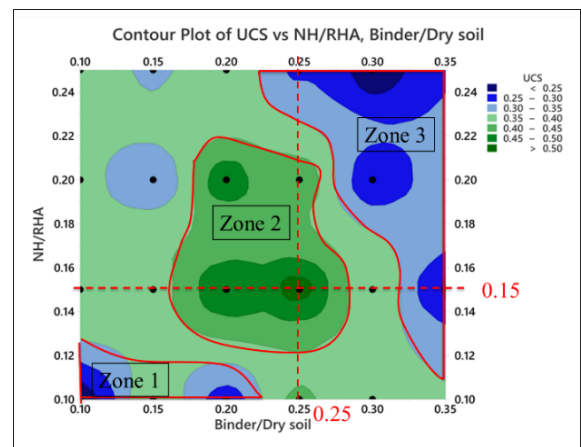


Figure 4: Contour plot for 7-D UCS with B/S and NH/RHA

A contour plot was developed to show the variation of UCS with B/S and NH/RHA. As depicted in Figure 4, three zones were identified as follows: zone 1: High amount of water content zone, zone 2: Optimum UCS zone, zone 3: High amount of geopolymer binder zone.

Figure 5 shows the variation of UCS with NH/RHA for constant B/S and Figure 6 shows the variation of UCS with B/S for constant NH/RHA.

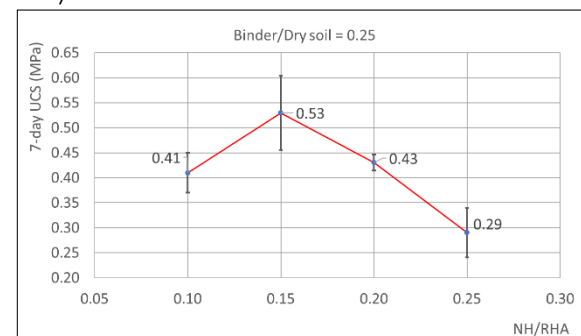


Figure 5: The variation of UCS with NH/RHA

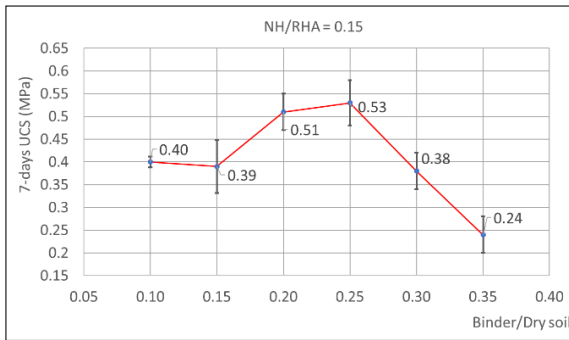


Figure 6: The variation of UCS with B/S

The mixture reached a UCS value of 0.53 MPa after 7 days of curing. It can be seen from Figure 5 that as the NH/RHA ratio increases, the UCS value of stabilized soil increases to the optimal value and then decreases again. The increase in UCS is due to the polymerization reaction to form C-A-S-H gel. The decrease in UCS of NH/RHA above 0.15 is due to expansion because of the heat generation of NaOH, and therefore micro-cracking. It can be seen from Figure 6 that as the B/S ratio increases, the UCS value of stabilized soil increases to the optimal value and then decreases again. The initial increment might be due to the quantity of RHA that could induce pozzolanic reaction and form cementitious compounds that have a strength increase, while the additional amount of RHA could act as unbounded particles, forming weak bonds between the soil and the cementitious compounds formed (Pushpakumara et al., 2022).

4.3 Optimized mix based on UCS and cost

Table 3: Utility results of top 5 samples of OP-GP

Binder/Dry soil	NH/RHA	Response		Overall Utility (U)	Rank
		Cost/UCS (USD/MPa/m ³)	UCS (MPa)		
0.20	0.15	52.25	0.51	6.43	1
0.10	0.15	36.93	0.40	6.39	2
0.25	0.15	59.91	0.53	6.26	3
0.20	0.20	69.41	0.49	5.70	4
0.15	0.10	38.58	0.38	6.13	5

All blends were ranked based on the overall benefit calculated for each sample, taking into account UCS and cost/UCS. The utility results of the top five samples (out of 16 samples) are shown in Table 3.

5. Conclusions

Following conclusions were drawn based on the findings (B/S=binder/dry soil, NH=NaOH). The samples with 1.4 OMC exhibited the highest UCS and were found to be free of surface cracks when compared to both OMC and 1.2 OMC samples. Highest UCS were found at OP-GP with B/S = 0.25 and NH/RHA = 0.15. The lowest cost/UCS were found at OP-GP with B/S = 0.2 and NH/RHA = 0.15 which has the lowest total cost and third highest UCS out of all samples. That is the optimum OP-GP stabilized sample based on both UCS and cost.

References

- Maheepala, M.M.A.L.N., Nasvi M.C.M., Robert D.J., (2022) 'A comprehensive review on geotechnical properties of alkali activated binder treated expansive soil', Journal of Cleaner Production, 363, p. 132488
- Murmu, A.L., and Patel, A. (2020) 'Studies on the Properties of Fly Ash-Rice Husk Ash-Based Geopolymer for Use in Black Cotton Soils', International Journal of Geosynthetics and Ground Engineering, 6(3).
- Pushpakumara, B. H. J., & Mendis, W. S. W. (2022) 'Suitability of Rice Husk Ash (RHA) with lime as a soil stabilizer in geotechnical applications', International Journal of GeoEngineering, 13(1).
- Tesanasin, T., Suksiripattanapong, C., Van Duc, B., Tabyang, W., Phetchuay, C., Phoo-ngernkham, T., Sukontasukkul, P., & Chindaprasirt, P. (2022) 'Engineering properties of marginal lateritic soil stabilized with one-part high calcium fly ash geopolymer as pavement materials', Case Studies in Construction Materials, 17, e01328.
- Wu, J., Min, Y., Li, B., & Zheng, X. (2021) 'Stiffness and strength development of the soft clay stabilized by the one-part geopolymer under one-dimensional compressive loading', Soils and Foundations, 61(4), 974–988.
- Zhang, H. Y., Liu, J. C., & Wu, B. (2021) 'Mechanical properties and reaction mechanism of one-part geopolymer mortars', Construction and Building Materials, 273, 121973.

Influence of Gradation on Shear Behavior of Railway Ballast Material

Tharmarajah R., Amalan M.*, and Navaratnarajah S.K.

Department of Civil Engineering, Faculty of Engineering, University of Peradeniya, Sri Lanka

*mamalan1909@gmail.com

Keyword: Ballast, Breakage, Dilation, DEM, Gradation, Shear strength

Abstract

The ballast layer in railway track infrastructure undergoes deformation and degradation from moving train loads and environmental changes. To enhance track performance and cut maintenance costs, it is imperative to study ballast shear behaviour and degradation under diverse loading conditions. This study investigates the influence of gradation on the shear behaviour of railway ballast materials. The research methodology involves laboratory testing of ballast samples with different gradations. Shear strength parameters are determined using Large-scale direct shear tests. The study uses three gradations of particle sizes and distributions commonly found around and within the Indian upper and lower limit gradation standard. Furthermore, a numerical model was developed to study the influence of ballast gradation and investigate the influence of vertical stress by carrying out a parametric study with different normal stresses.

1. Introduction

The ballast layer, the largest component in the track system, transfers loads from sleepers to the underlying layers and provides rapid drainage. Over time, ballast materials break and become fouled, affecting track performance and longevity. The shear strength of the ballast provides lateral confinement and resistance to maintain the geometry of the track structure. The shear behavior of ballast varies with different factors. Ballast gradation is one such factor that affects shear strength. The particle size distribution of ballast is not the same for all countries. It varies considering the subgrade properties, load application, climate, the strength of the parent rock, etc. Gradations are selected mainly by considering the strength and drainage properties of the ballast layer. Researchers studied the shear behavior of the ballast by conducting large-scale direct shear tests and triaxial tests. In Sri Lanka, ballast particle sizes ranging from 19 to 63 mm are used in rail tracks. There is no unique gradation used

in Sri Lankan tracks rather Indian ballast gradation is used. Therefore, this study mainly focuses on understanding the effect of different gradations on the shear behavior of the ballast used in the rail tracks in Sri Lanka.

2. Literature review

The shear behavior of railway track ballast plays a critical role in ensuring the stability and performance of tracks, impacting safety and operational efficiency (Indraratna, 2016). Key factors affecting shear behavior include particle size distribution, angularity, compaction, moisture content, and confining pressure (Danesh et al., 2018). The particle size distribution (PSD), void ratio, and degree of saturation are intricately tied to ballast behavior (Indraratna et al., 2005). The ideal gradation should balance drainage benefits with higher strength and reduced settlement, as suggested by Guo et al., (2022). The uniformity coefficient (C_u) is crucial, with larger values associated with higher shear strength. Global ballast specifications vary with different countries adopting various crushed rock particles based on quality and availability (Anbazhagan et al., 2012). Degradation can lead to the accumulation of fines, reducing drainage, causing water retention and track settlement (Danesh et al., 2018). In terms of shear resistance breakage indices, such as the ballast breakage index (BBI), indicate increased breakage under higher stress (Venuja et al., 2023).

While many studies stress the importance of factors like ballast gradation, shear behavior, and degradation in railway tracks, Sri Lanka lacks specific standards for ballast gradation, and there haven't been many studies on how different gradations affect shear behavior. Current research aims to explore the impact of different ballast gradations on the shear behavior of ballast used in Sri Lanka. This study specifically focuses on conducting large-scale direct tests with three different ballast gradations to suit the unique conditions of the Sri Lankan railway system.

3. Methodology

3.1 Laboratory test using large-scale direct shear test

In this study, ballast material was collected from the Ambepussa quarry. Property tests were conducted according to the accepted standards. Then the ballast was washed, dried, and sieved using 19, 25, 37.5, 50, and 63mm sieves to separate particles into required size ranges for the direct shear test. The main aim of this study is to analyze the effect of gradation on the shear behavior of railway ballast. For that, three gradations were chosen considering Indian gradation limits as shown in Figure 1. Indian gradation limits are considered in this study as it is adopted in Sri Lankan rail tracks. Here PSD A1 is in between the upper and lower limits of Indian standards which is normally adopted in Sri Lankan rail tracks. PSD A2 is obtained by increasing the percentage of particles between 19 - 37.5 mm size ranges, beyond the upper limit. On the other hand, PSD A3 is obtained by increasing the percentage of particles between 37.5 - 63 mm size ranges.

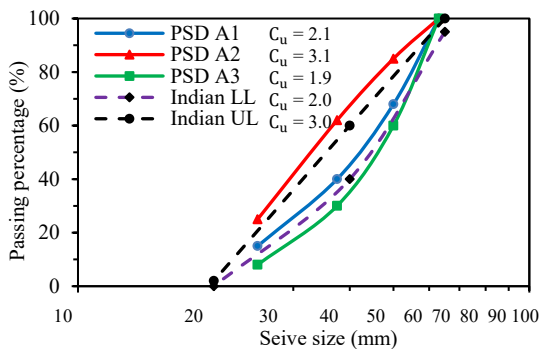


Figure 1: Different Particle Size Distribution

The test specimen was prepared based on the gradation, which was selected for the test. According to the required density of 1549 kg/m³ and the volume of the apparatus, the required mass of ballast was calculated. Then according to the selected gradation, the inclusion of particle size range was considered. Particles were filled into the apparatus in three layers. Before filling, particles were coloured (different colours for three layers as shown in Figure 2) and numbered (different numbers for different size ranges) to identify the breakage easily. With different colours, it could be easy to identify at which layer maximum breakage occurs, and with the numbers, it can be identified which size range particles are broken.



Figure 2: Coloured particles for three layers

Particles were filled into the large-scale direct shear test apparatus in three layers. Each layer was compacted manually using a rubber-padded vibratory hammer to obtain field density. Figure 3 shows the large-scale direct shear test apparatus used for the experiment. These are some pressures in ballast under various static and dynamic loading conditions. The pressure can be higher if the heavy engines are used, however, the laboratory testing apparatus has some limitations. Three different normal stresses were selected as 30 kPa, 60 kPa, and 90 kPa. Constant horizontal shear was applied manually using a hydraulic jack as 4 mm/min in the bottom cylinder.

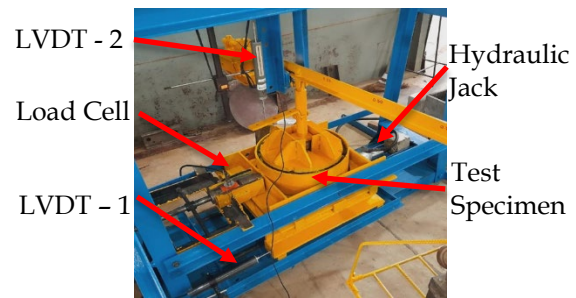


Figure 3: Large-scale direct shear test apparatus

Firstly, three different gradations were tested for one common normal stress, 60 kPa. Then PSD 1 and PSD 3 gradations were tested for 90 kPa normal stress. All tests were done until 15% shear strain ballast was reached.

3.2 Numerical modelling using DEM

Discrete Element Method (DEM) is one of the leading approaches in numerical analysis. Since ballast particles are granular angular particles, DEM was chosen for this study. Particle shape is one of the key factors, which decides the mechanical behaviour of ballast particles, and real ballast particles were scanned in 3D using a scanning device and imported as multi-sphere clump particles to the DEM software (EDEM). Then the particles were generated according to the selected gradation. The following Figure 4 illustrates the modelled experimental setup with generated particles.

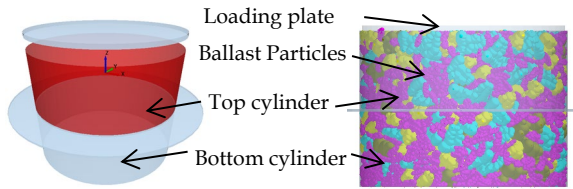


Figure 4: DEM model of shear test

4. Results and discussion

4.1 Experimental results

Shear stress and strain were calculated using the shear load and horizontal displacement data obtained from the data logger. Figure 5 shows the shear stress and vertical strain variation for different PSDs for 60 kPa normal stress. As expected, inclusion of larger size particles shows some significant effect on shear behaviour. Shear increased with the inclusion of larger-sized particles. In contrast, dilation decreased due to the void increasing with the inclusion of large-size particles.

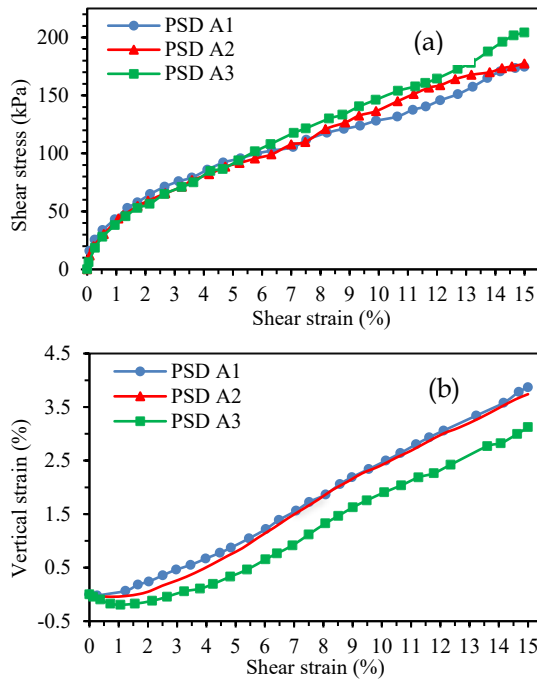


Figure 5: (a) Shear stress and (b) vertical strain variation with shear strain for 60 kPa normal stress

Then the normal stress was increased to 90 kPa and the test was done for PSD A1. As expected, shear stress was increased with normal stress as shown in Figure 6.

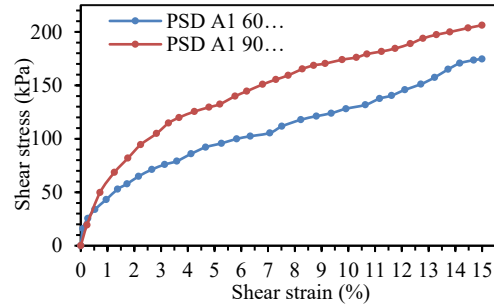


Figure 6: Shear stress variation with shear strain

Results obtained for the Ambepussa (A) material were compared with the results obtained for the ballast collected from Gampola (G) (Venuja et al., 2023). The Ambepussa ballast showed higher shear resistance than the Gampola ballast particles. Figure 7 shows the comparison of the results.

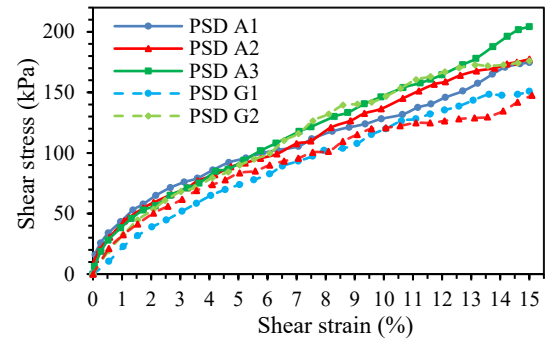


Figure 7: Shear stress vs shear strain for different gradations under 60 kPa normal stress

Breakage was analysed using BBI method (Indraratna et al., 2005). Comparatively higher breakage occurred in the middle layer, because of shear was applied in the middle layer. Considerable breakage was observed in the top layer, because normal stress was applied in top layer zone. As expected, inclusion of larger particles decreased the breakage, and with increasing normal stress breakage also increased. Figure 8 shows the breakage results for different gradations.

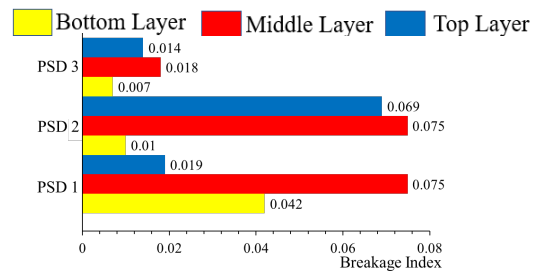


Figure 8: Breakage results under 60 kPa normal stress

4.2 Numerical analysis results

By changing the coefficients of restitution, static friction, and rolling friction at ballast-ballast contact and ballast-steel contact, an acceptable agreement between experimental shear variation and numerical shear variation was obtained for PSD A1 under 60 kPa normal stress. Using these calibrated coefficients, the same model was run for the other two gradations. Numerical results were obtained and compared with experimental results as shown in Figure 9. An acceptable agreement was observed in this comparison. Then the normal stress had been changed to 30 kPa and 90 kPa and simulation was done for PSD A1. Figure 10 shows the obtained results.

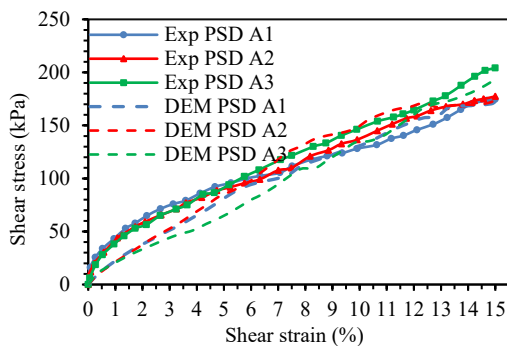


Figure 9: Comparison of shear stress vs shear strain results of both experiment and numerical analysis under 60 kPa normal stress

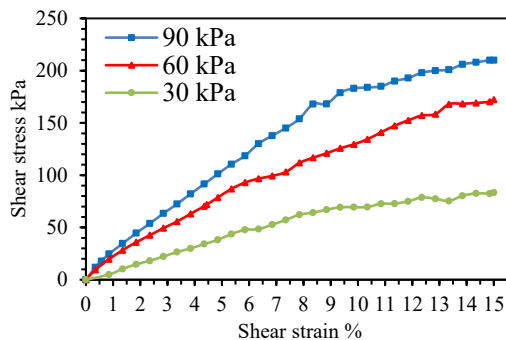


Figure 10: Comparison of shear stress vs shear strain for PSD A1

5. Conclusion

This research elaborates on the effect of particle size distribution on the shear behavior of ballast. For that, three different gradations were chosen, and large-scale direct shear tests were conducted. In addition to this, numerical simulation using DEM was carried out. Shear stress increased with increasing normal stress. In contrast, dilation is reduced due to the high compaction of materials. The presence of a

higher number of larger particles resulted in higher shear strength. The shear behavior of the ballast changes with gradation. High shear strength was obtained for the gradation with a higher number of larger-size particles. Numerical results showed acceptable agreement with the experimental results. So, the validated model can be used to conduct parametric studies under higher normal stresses. In terms of gradation, the selected new gradation PSD A3 shows better in resisting shear and reducing ballast breakage. So, further extending the same study for the permeability behavior will guide to find a good gradation limit.

References

- Anbazhagan, P., Bharatha, T.P. and Amarajeevi, G. (2012) 'Study of Ballast Fouling in Railway Track Formations', *Indian Geotechnical Journal*, 42(2), pp. 87-99. Available at: <https://doi.org/10.1007/s40098-012-0006-6>.
- Danesh, A., Palassi, M. and Mirghasemi, A.A. (2018) 'Effect of sand and clay fouling on the shear strength of railway ballast for different ballast gradations', *Granular Matter*, 20(3), p. 51. Available at: <https://doi.org/10.1007/s10035-018-0824-z>.
- Guo, Y., Marikine, V., & Jing, G. (2022) 'Railway ballast' In Elsevier eBooks (pp. 295-317).
- Indraratna, B., Sun, Y. and Nimbalkar, S. (2016) 'Laboratory Assessment of the Role of Particle Size Distribution on the Deformation and Degradation of Ballast under Cyclic Loading', *Journal of Geotechnical and Geoenvironmental Engineering*, 142(7), p. 04016016. Available at: [https://doi.org/10.1061/\(ASCE\)GT.1943-5606.0001463](https://doi.org/10.1061/(ASCE)GT.1943-5606.0001463).
- Indraratna, B., Lackenby, J. and Christie, D. (2005) 'Effect of confining pressure on the degradation of ballast under cyclic loading', *Géotechnique*, 55(4), pp. 325-328. Available at: <https://doi.org/10.1680/geot.2005.55.4.325>.
- Venuja, S., Navaratnarajah, S.K., Bandara, C.S. and Jayasinghe, J.A.S.C. (2023) 'Experimental and Numerical Study on the Shear-Strain Behavior of Ballast with Different Gradations', in R. Dissanayake, P. Mendis, K. Weerasekera, S. De Silva, S. Fernando, C. Konthesingha, and P. Gajanayake (eds) *ICSBE 2022*. Singapore: Springer Nature Singapore, pp. 245-254. Available at: https://doi.org/10.1007/978-981-99-3471-3_18.

Prediction of Geotechnical Properties of Expansive Soil Stabilized with Fly Ash Using Artificial Neural Network

Kirushanthan K.*, Thigitharan T., and Nasvi M.C.M.

Department of Civil Engineering, Faculty of Engineering, University of Peradeniya, Sri Lanka

*kirukamales1998@gmail.com

Keywords: Artificial Neural Network (ANN), Expansive soil, Fly ash, Sensitivity analysis, Soil stabilization

Abstract

Expansive soils are considered as problematic soils since they exhibit high swelling and shrinking when exposed to changes in moisture content. Chemical stabilization involves the addition of additives which mitigates these issues by reducing volume changes and enhancing strength. Determining the Geotechnical engineering properties of the stabilized soils is crucial for analysis and design. However, traditional laboratory experiments are time-consuming, costly, and energy-intensive. For these reasons, novel analytical methods can be used in order to predict the geotechnical properties of stabilized expansive soils. This study addresses these limitations by developing predictive models to determine the geotechnical properties (Optimum Moisture Content (OMC), Maximum Dry Density (MDD), and Unconfined Compressive Strength (UCS)) of expansive soil stabilized with Class F fly ash (FA) using Artificial Neural Network (ANN) in PYTHON. Drawing from a comprehensive dataset, the models were trained and validated, achieving high R^2 values ($R^2=0.951$, $R^2=0.911$ for OMC; $R^2=0.989$, $R^2=0.901$ for MDD; $R^2=0.993$, $R^2=0.915$ for UCS_{28d}). Sensitivity analysis highlights the substantial influence of natural soil OMC (45%) and MDD (46%) in their respective models, while the fly ash/soil ratio (41%) emerges as a key parameter for the UCS model.

1. Introduction

Expansive soil is a type of soil that expands when it absorbs water and shrinks when it dries. This expansion and contraction can cause damage to structures built on expansive soils. Expansive soil at shallow depths and other poor ground conditions are common problems faced in geotechnical engineering, and these problematic soils pose enormous challenges to the proposed infrastructural development (Das et al., 2010). Most often, the option of soil replacement is not economical, and there is a need to perform some form of ground

improvement or stabilization prior to construction. Soil stabilization may be done chemically or mechanically, depending on the peculiarity of the problem at hand. However, the treatment of most expansive soils will involve the use of chemical stabilization which involves adding chemical agents to the soil to modify its properties. Irrespective of the method used, it becomes imperative to investigate the performance of such stabilized soils using key parameters of the soil such as Unconfined Compressive Strength (UCS), Maximum Dry Density (MDD), Optimum Moisture Content (OMC), California Bearing Ratio (CBR), Plasticity index (I_p), Liquid Limit (LL), Plastic Limit (PL), etc (Chew et al., 2004; Eyo et al., 2020). Such geotechnical engineering properties of the stabilized soils are required in the analysis and design, and however conducting a large number of laboratory experiments to find the geotechnical properties is time-consuming, incurs high costs, and is energy intensive. For these reasons, novel analytical methods can be used in order to predict the geotechnical properties of stabilized expansive soils. Most of the time, these parameters are influenced by several variables leading to a multi-variable problem for which researchers have used several statistical methods to analyse, investigate, and model trends using laborious mathematical processes (Jeremiah et al., 2021). There are several analytical tools and techniques in the literature, such as artificial neural networks (ANNs) (Leong et al., 2018) multivariable regression (MVR) (Adhikari et al., 2019), genetic programming (Leong et al., 2018), etc. Among these techniques, ANN reflects the behaviour of the human brain, it allows computer programs to recognize patterns and solve common problems in the fields of machine learning and deep learning.

There is only limited study available to predict the geotechnical properties of expansive soil stabilized with FA by using Novel analytical methods. So, this study aims to predict the geotechnical properties of expansive soils

stabilized with Class F Fly ash (FA) by using an artificial neural network (ANN).

2. Literature Review

Smith et al., (2018) have conducted a comprehensive study on the use of fly ash as a soil stabilizer. The research highlighted a significant improvement in soil strength and a reduction in expansive soil behaviour when treated with fly ash. This finding underscores the potential of fly ash as a promising agent for stabilizing expansive soils. The authors concluded that the introduction of fly ash in soil stabilization experiments resulted in a notable enhancement of soil strength and a reduction in expansive soil behaviour.

Jones and Brown, (2016) have explored the application of Artificial Neural Networks (ANNs) in geotechnical engineering, specifically in modelling soil behaviour. The study demonstrated the efficacy of ANNs in capturing intricate relationships within expansive soils. This insight supports the utilization of ANNs as a valuable tool for predicting geotechnical properties in soil stabilization projects. The authors concluded that machine learning techniques, particularly ANN can be useful in estimating the strength properties of stabilized expansive soils.

Brown and Taylor (2019) have investigated the use of ANNs in predicting the compressive strength of expansive soils treated with different stabilizers, including fly ash. The study showcased the effectiveness of ANNs in modelling the complex relationships involved in soil stabilization, contributing to the advancement of predictive modelling in geotechnical engineering. The authors concluded that using Artificial Neural Networks (ANNs) can yield a better solution to predict compressive strength in expansive soils treated with different stabilizers.

3. Methodology

3.1 Data collection and treatment

An extensive compilation of databases containing results from numerous experimental studies were undertaken. The required data for the development of the three artificial neural network (ANN) models are optimum moisture content (OMC), Maximum Dry Density (MDD), and 28-day Unconfined Compressive Strength (UCS). The amount of data needed depends on

several factors, such as the complexity of the problem, the size of the input space, and the number of parameters in the model. As a rule of thumb, it is often recommended to have a sufficiently large dataset that provides a representative sample of the underlying population or distribution (Touzet et al., 1992). So, it was decided to collect data as much as possible but not less than 50 for each set.

It is important to remove outliers from the collected data and Cook's Distance method was used to remove the outliers from the collected data. Cook's distance D_i of observation k is given in Equation 1 (Jeremiah, et al., 2021).

$$D_i = \frac{\sum_{i=1}^n (\hat{y}_i - \hat{y}_{i(k)})^2}{pMSE} \quad (1)$$

where \hat{y}_i is the i^{th} fitted response value; $\hat{y}_{i(k)}$ is the i^{th} fitted response value when the fit excludes observation k ; MSE is the mean squared error; and p is the number of coefficients in the regression model.

3.2 ANN model Development

ANN models for OMC, MDD and UCS were developed by using PYTHON language. The input and output parameters of the developed ANN models for OMC, MDD and 28-day UCS are shown in the Figure 1.

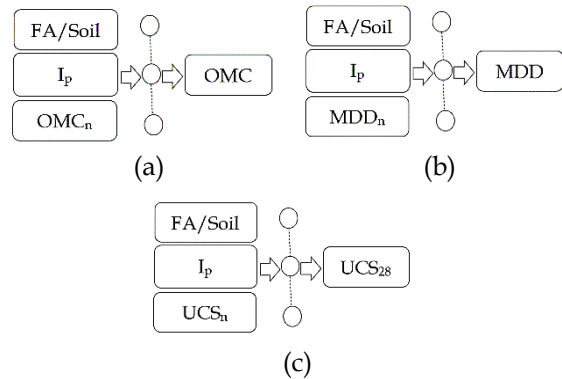


Figure 1: Input parameters used for ANN models: (a) OMC Model, (b) MDD Model, and (c) UCS Model.

In order to obtain statistically consistent training and testing data, the division of data for the ANN model is carried out where 70% of the experimental data were used for training the model and 30% for testing the ANN model (Gunasekara et al., 2020). As a part of pre-processing, the input and output variables were normalized to fall in the range $[-1, 1]$ to make the

learning rate high and to have consistency while training of ANN model. The ReLU function was used as the activation function in the development phase of ANN models.

The number of neurons in the hidden layer was varied to find the optimum architecture. The performance of the ANN model was reported in terms of three statistical parameters namely, coefficient of determination (R^2) and root mean square error (RMSE). The optimum architecture of ANN models was characterized by a high R^2 value and low RMSE value.

4. Results and discussion

The architecture of the developed ANN models is shown in Figure 2. The model architecture consists of three hidden layers and the number of neurons in the 1st, 2nd and 3rd hidden layers were 256, 128, and 32 respectively. The final model architecture is in the form 3-256-128-32-1. The number of epochs used for MDD, OMC, and UCS models were 150, 200, and 200 respectively as these numbers provided a better performance in predicting the output parameters of the respective models.

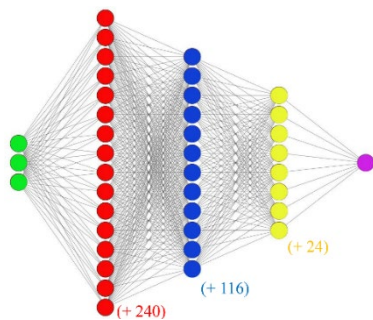
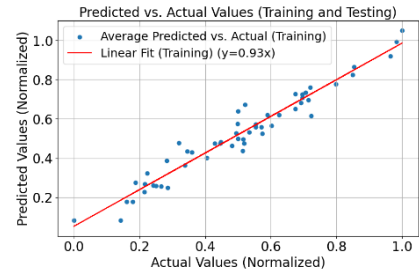


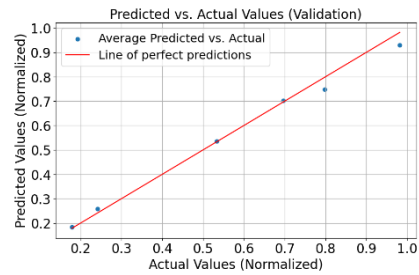
Figure 2: Architecture of developed ANN models (OMC, MDD and UCS).

4.1 MDD model

Model training and validation plots for the MDD model are shown in Figure 3. According to Figure 3, the training data set has high performance compared to the validation and target data sets. The R^2 values for the training and validation data sets are 0.989 and 0.901 respectively. The root mean square errors (RMSE) for the training and validation data sets are 0.030 and 0.162 respectively.



(a)

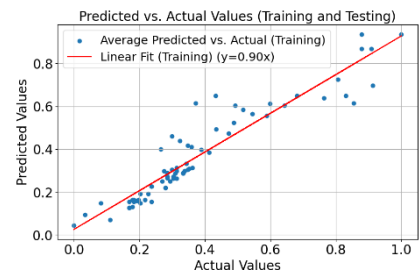


(b)

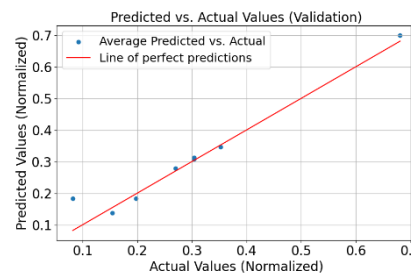
Figure 3: Coefficient of determination (R^2) values of MDD – ANN model (a) Training and (b) Validation

4.2 OMC model

Model training and validation plots for the OMC model are shown in Figure 4. According to Figure 4, the training data set has high performance compared to the validation and target data sets. The R^2 values for the training and validation data set are 0.951 and 0.911 respectively. The root mean square error (RMSE) for the training and validation data set are 0.037 and 0.196 respectively.



(a)

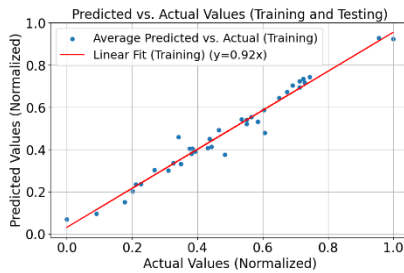


(b)

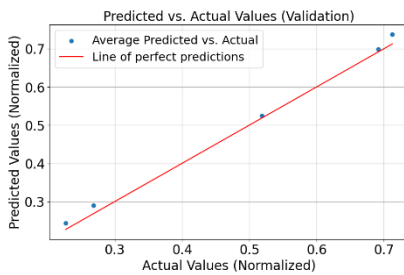
Figure 4: Coefficient of determination (R^2) of OMC – ANN model (a) Training and (b) Validation

4.3 UCS model

Figure 5 shows the model training and validation plots for the UCS model. According to Figure 5, the training data set has high performance compared to the validation and target data sets. The R^2 values for the training and validation data set are 0.993 and 0.915 respectively. The root mean square error (RMSE) for the training and validation data set are 0.017 and 0.271 respectively.



(a)

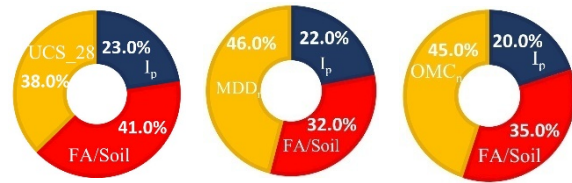


(b)

Figure 5: Coefficient of determination (R^2) values of UCS – ANN model (a) Training and (b) Validation.

4.4 Sensitivity analysis

Correlation matrix method (Leong et al., 2018) was used to find the input variable contribution to the model and the obtained sensitivity plots for the three developed ANN models are shown in Figure 6. According to Figure 6, the sensitivity ranks OMC of the natural soil as the most influential parameter (45%) followed by FA/Soil ratio (35%), and I_p (20%) is a less influential parameter for the OMC model. In the MDD model, MDD of the natural soil is the most influential parameter (46%) followed by FA/Soil ratio (32%), and I_p (22%) is a less influential parameter. In the UCS model FA/Soil ratio is the most influential parameter (41%) followed by UCS of natural soil (38%) and I_p (23%) is a less influential parameter for the UCS model.



UCS

MDD

OMC

(a)

(b)

(c)

Figure 6: Sensitivity analysis plots of developed (a) UCS, (b) OMC and (c) MDD models.

5. Conclusions

Artificial Neural Network (ANN) can be used to predict the unconfined compressive strength (UCS), maximum dry density (MDD), and optimum moisture content (OMC) of the expansive stabilized with fly ash (FA). It was verified that all proposed models were successfully trained and validated where the optimum architecture of the developed models is 3-256-128-32-1 for all three models (OMC, MDD, and UCS). Developed models show a reasonable predictive ability towards new data, suggesting that the models can be used as an alternative for conducting experimental studies to predict geotechnical properties of FA-stabilized expansive soil. Sensitivity analysis showed that OMC (45%) and MDD (46%) of the natural soil are the most influential parameters for the OMC model and MDD model respectively, whereas FA/Soil ratio (41%) is the most influential parameter for the UCS model. It is also recommended that using more data to develop the model gives a more accurate model.

References

Brown, C., & Taylor, D. (2019) 'Predicting Compressive Strength of Expansive Soils Treated with Various Stabilizers, Including Fly Ash, Using Artificial Neural Networks', *Geotechnical Engineering Journal*, 22(4), 87-102.

Jones, A., & Brown, R. (2016) 'Application of Artificial Neural Networks in Modeling Soil Behavior: Focus on Expansive Soils', *Geotechnical Journal*, 18(3), 45-58.

Smith, A., Johnson, B., & Williams, C. (2018) 'Impact of Fly Ash on Soil Stabilization: Experimental Analysis', *Journal of Geotechnical Engineering*, 25(2), 123-1.

Relate Soil Permeability to Particle Size and Porosity

De Zoysa D.N.R.*, Ravindu K.J.A., and Udakara D.de S.

Department of Civil Engineering, Faculty of Engineering, University of Peradeniya, Sri Lanka

* nilanrangana96@gmail.com

Keywords: Permeability, Porosity, Soil particle size

Abstract

In the field of geotechnical engineering, understanding the porosity, permeability, and particle size of the soil is essential for a variety of construction and environmental applications. This study investigates the relate soil permeability to particle size, and porosity. Normally to determine soil permeability it is required to carry out the permeability test for the respective soil samples. But after understanding the relationship among permeability, porosity, and particle size, it will be easier to determine soil permeability by using particle size and porosity values of soil. The objective of the study is to find a relationship among permeability, porosity, and particle size. The study is limited to 9 different samples due to time constraints. Sieve analysis test, Hydrometer test, Compaction test, Specific gravity test and falling head test were performed to determine the D_{10} , D_{30} , D_{60} , Porosity and Permeability values of each sample. RStudio software is used for the analysis of the results. Finally, a relationship is obtained to calculate permeability using porosity, D_{10} , D_{30} , and D_{60} values. By considering residual standard error and R squared value, the model without intercept was selected as the best model. The validity of the model was checked by plotting the graph between actual permeability values versus estimated permeability values. From the graph accuracy of the test was confirmed. The equation derived as the result is, k (mm/s) = $9.239 \times 10^{-2} \times n - 13.76 \times (D_{10}) - 7.926 \times 10^{-2} \times (D_{30}) - 1.249 \times 10^{-3} \times (D_{60})$.

1. Introduction

Soil permeability is the ability of soil to allow water or other liquids to pass through it. It is a measure of how quickly and easily water can move through the soil. It can be influenced by the size of soil particles and porosity. Soil permeability plays a significant role in groundwater flow, soil compaction, drainage, and nutrient transport within the soil profile. Understanding the factors controlling soil

permeability is crucial for effective land management, agricultural practices, and environmental conservation efforts. Coarse-grained soils with larger particles generally exhibit higher permeability due to their larger pore spaces, allowing for increased fluid flow (Fredlund and Rahardjo, 1993; Hillel, 2004). On the other hand, fine-grained soils with smaller particles tend to have lower permeability due to smaller pore sizes and increased compaction (Bear, 1972; Gee and Or, 2002). Similarly, higher porosity generally leads to increased permeability as there are more interconnected pore spaces available for fluid flow (Petersen and Luxmoore, 1982). The objective of this study is to find out how porosity and particle size effect on soil permeability.

2. Literature Review

There were some pioneering works that laid the foundation to understand these relationships between soil permeability, porosity, and particle size values. Hazen, A. (1892) conducted experiments to investigate the effect of particle size on the permeability of granular materials. The Hazen model, proposed by Allan Hazen, provides an empirical formula to estimate the coefficient of permeability based on the effective grain size of the soil.

$$k = C_H D_{10}^2 \frac{\rho g}{\mu} \quad (01)$$

k : Permeability (m/s)

C_H : Shape constant

D_{10} : Effective particle size

The Hazen model does not explicitly consider the influence of porosity on permeability. The Carman-Kozeny equation (or the Kozeny-Carman equation) is a relation to calculate the pressure drop for laminar flow through a packed bed of solids. It was originally developed by Kozeny in 1927 (McCabe et al. 2005). The original Kozeny-Carman equation assumes a constant porosity, which may not be accurate in

all cases. Therefore, modification factors are used with the kozeny equation.

$$k = \alpha \frac{\phi^3}{(1-\phi^2)} \times \frac{S}{d^2} \quad (02)$$

$$k = n \frac{\phi^3}{(1-\phi^2)} \times \frac{S}{d^2} \quad (03)$$

ϕ : porosity of the media

d : particle diameter

S : constant for particle shape

α, n : porosity constants

Costa (2006) conducted a re-examination of the permeability-porosity relationship by revisiting the Kozeny-Carman equation and introducing a fractal pore-space geometry assumption.

$$k = C_c \frac{\phi^m}{(1-\phi)} \quad (04)$$

C_c : Kozeny coefficient

k : Permeability

ϕ : Porosity

m : Archie exponent

Dehghanian Kaveh* and Hakan Murat Soysal (2019) investigated the correlation between the particle size and permeability of sands.

$$k = 1.9235D_{10}^2 - 7.4194D_{10} + 7.1451 \quad (05)$$

(Relationship between permeability and D_{10} particle size)

According to this polynomial function D_{10} effect on permeability can be calculated (Kaveh Dehghanian and Hakan Murat Soysal (2019). Chilingar (1964) explored the intricate relationship between porosity, permeability, and grain-size distribution of sands and sandstones. Chilingar's study emphasized that the porosity of sands and sandstones is influenced by the arrangement, packing, and size distribution of grains within the material. However, it couldn't find any relationship equation to prove that there is a relationship between particle size, porosity, and permeability

3. Methodology

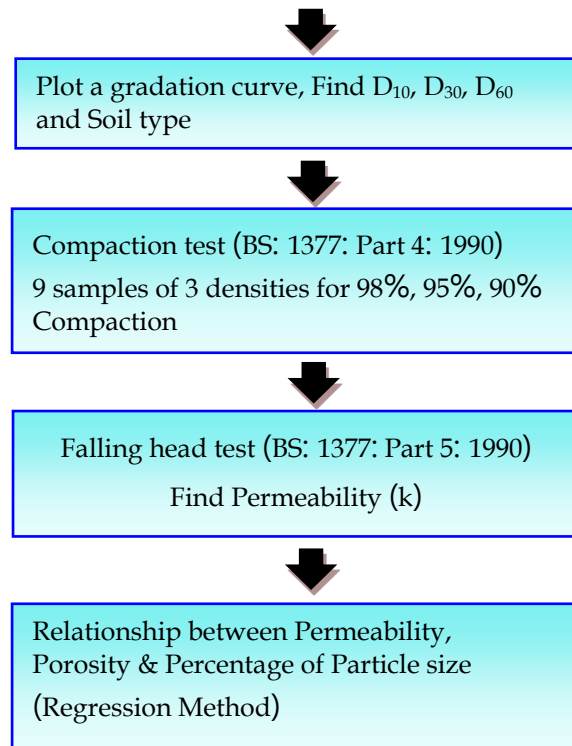
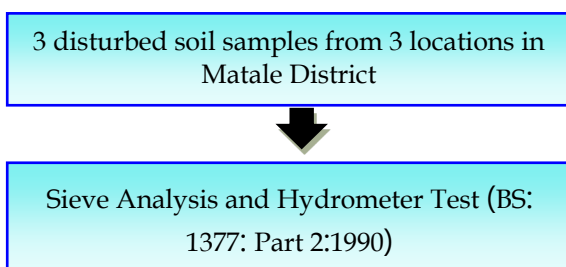


Figure 1: Methodology Flow Chart

4. Results and Discussion

According to the particle size distribution curve, all the collected soil samples were classified as Silty Sand, as per the British Soil Classification System. Rstudio software was used to analyse the obtained test results and to develop the relationship among permeability, particle size, and porosity of the collected soil samples. The results obtained for different degrees of compaction are shown in the following Table 1.

Table 1: Porosity and degree of compaction of samples

Sample	Degree of Compaction	Porosity (n)
01	98%	0.381
	95%	0.345
	90%	0.325
02	98%	0.356
	95%	0.320
	90%	0.299
03	98%	0.397
	95%	0.364
	90%	0.343

In every sample porosity values decreased when the degree of compaction increased.

Table 2: permeability and degree of compaction of samples

Sample	Degree of Compaction		
	90%	95%	98%
1	2.613×10^{-6} m/s	0.973×10^{-6} m/s	0.051×10^{-6} m/s
2	9.036×10^{-6} m/s	2.374×10^{-6} m/s	0.871×10^{-6} m/s
3	11.570×10^{-6} m/s	9.370×10^{-6} m/s	7.170×10^{-6} m/s

In every soil sample permeability decreases when degree of compaction increased.

4.1 Relationship between permeability and particle size

The following relationship is obtained considering an intercept.

$$k = -3.259 \times 10^{-2} + 2.996 \times (D_{10}) + 6.177 \times 10^{-1} \times (D_{30}) \quad (06)$$

k: Permeability(mm/s)
 D₁₀: Particle size 10% smaller
 D₃₀: Particle size 30% smaller

R² value = 0.556
 Residual Standard Error = 2.917×10^{-6}

However, it can be seen that there was no relation to D₆₀. Further analysis is carried out with no intercept, and the obtained relationship is:

$$k = -8.206 \times (D_{10}) - 4.149 \times 10^{-1} \times (D_{30}) - 1.410 \times 10^{-2} \times (D_{60}) \quad (07)$$

R² value = 0.7921
 Residual Standard Error = 2.917×10^{-6}

which gives a better relationship than the previous with an improved root mean square value of around 0.8

4.2 Porosity - Permeability relationship

The following result was obtained considering an intercept.

$$k = -2.899 \times 10^{-2} + n \times 9.742 \times 10^{-2} \quad (08)$$

R² value = 0.392
 Residual Standard error = 3.413×10^{-6}

R² Value of this equation is less than R² values of previous 2 equations. So, further analysis is carried out and obtained relationship is:

$$k = n \times 1.462 \times 10^{-2} \quad (09)$$

R² value = 0.5914
 Residual standard Error = 2.917×10^{-6}

R² value is higher than the with intercept equation from a significant amount of 0.2.

4.3 Permeability, Porosity, D₁₀, D₃₀, D₆₀ relationship

The following result was obtained considering an intercept.

$$k = -2.886933 \times 10^{-5} + 9.239061 \times 10^{-5} \times n - 3.834775 \times 10^{-3} \times (D_{10}) - 1.0036594 \times 10^{-4} \times (D_{30}) \quad (10)$$

R² value = 0.9318
 Residual Standard Error = 1.446×10^{-6}

It can be seen that there was no relation to D₆₀. Further analysis is carried out with no intercept, and the obtained relationship is:

$$k = 9.239 \times 10^{-2} \times n - 13.76 \times (D_{10}) - 7.926 \times 10^{-2} \times (D_{30}) - 1.249 \times 10^{-3} \times (D_{60}) \quad (11)$$

R² value = 0.9489
 Residual Standard Error = 1.446×10^{-6}

Considering all the obtained relationships equation (11) has the highest R² value and the lowest residual standard error value.

4.3 Actual Permeability Vs. Estimated permeability

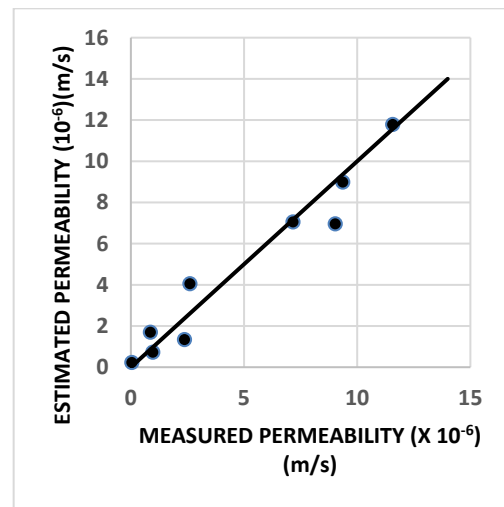


Figure 2: variation between measured permeability vs. estimated permeability

Figure 2 shows the variation between the predicted and measured values of permeability. Predicted values based on the derived relationship (equation (11)). For the comparison only used the test results obtained during the study, as there were no such data found in the literature.

5. Conclusions

This research aimed to investigate the intricate interplay between permeability, porosity, and particle size. The study involved a comprehensive analysis of sieve analysis, compaction test, and permeability test according to standard methods. The results give relationships between permeability and porosity, permeability-porosity, and particle size. It gives an estimated equation with the residual standard error which can use for calculate permeability of any sample after doing the sieve analysis test and compaction test. RStudio software was used to obtain the relationship as:

$$k=9.239 \times 10^{-2} \times n - 13.76 \times (D_{10}) - 7.926 \times 10^{-2} \times (D_{30}) - 1.249 \times 10^{-3} \times (D_{60})$$

According to the particle size distribution curve, all the collected soil samples were Silty Sand. Therefore, this equation is validated for the Silty Sand Soil Type.

However, it is essential to acknowledge the limitations of this study. Only 9 samples were used to get those results. By increasing the number of samples and conducting more laboratory tests can increase the accuracy of the results and by changing the soil types can get an equation, suitable for any type of soil samples. But the process remains the same.

In conclusion, the correlation between permeability, porosity, and particle size established in this research contributes to the growing body of knowledge in geotechnical engineering. The implications extend beyond the laboratory, offering practical insights that can inform decision-makers, researchers, and practitioners alike. This study represents a step forward in unravelling the complexities of fluid flow in porous media, setting the stage for continued advancements in civil and geotechnical engineering.

References

BS EN 1377-2, 1990, "Methods of Test for Soils for Civil Engineering Purposes. Part 2: Classification Tests." British Standards Institution, Milton Keynes, UK.

Chilingar, G.V. (1964) 'Relationship Between Porosity, Permeability, and Grain-Size Distribution of Sands and Sandstones. PP.71–75. Available at : [https://doi.org/10.1016/s00704571\(08\)70469-2](https://doi.org/10.1016/s00704571(08)70469-2).

Costa, A. (2006) 'Permeability-porosity relationship: A reexamination of the Kozeny-Carman equation based on a fractal pore-space geometry assumption', *Geophysical research letters*, 33(2).

Dehghanian, K. and Soysal, H.M. (2019) 'A Case Study on the Correlation between Size and Permeability of the Sands', 1(1), pp.1–8.

Göktepe, A.B. and Sezer, A. (2010) 'Effect of particle shape on density and permeability of sands', *Proceedings of the Institution of Civil Engineers-Geotechnical Engineering*, 163(6), pp.307–320.

Tang, Y., Wei, H., Chen, Y., Huang, B. and Zhang, S. (2023) 'Modeling of permeability for granular soils considering the particle size distribution', *Granular Matter*, 25(2), p. 35. Available at: <https://doi.org/10.1007/s10035-023-01323-0>.

Comparison of Predictive Models for Soil-Gas Diffusivity

Iddamalgoda I.P.T.H.*, Wickramarachchi M.N., and Chamindu D.T.K.K.

Department of Civil Engineering, Faculty of Engineering, University of Peradeniya, Sri Lanka

* e17118@eng.pdn.ac.lk

Keywords: Gas migration, Greenhouse gas emissions, Soil gas diffusivity

Abstract

The study investigates the role of soil-gas diffusivity in gas migration for soil aeration and greenhouse gas emissions. Despite century-long research on predictive soil-gas diffusivity models, reviews comparing classical and the most recent predictive models are limited. The research aims to understand the relationships between soil parameters and gas diffusion, guiding model selection for specific soil characteristics. The methodology involved a comprehensive literature review, followed by a review of existing predictive models and their applications. Reference soil-gas diffusivity measurements on selected sandy soils and diffusivity data from the literature on different soil types were used to evaluate the models. Statistical analysis was performed to compare the models' performance and determine the most accurate ones for specific soil textures and structures. The findings indicate that the Troeh model showed the best performance, offering higher accuracy. The Density Corrected and WLR-Marshall models also demonstrated commendable performance. Findings contribute to practical applications in soil science and environmental studies, paving the way for future research.

1. Introduction

Soil gas diffusivity (D_p/D_o , gas diffusion coefficients in soil and in free air, respectively) plays an important role in diffusion-controlled gas migration, necessary for soil aeration and greenhouse gas emissions. Through this study, a diverse array of predictive models for soil-gas diffusivity is assessed, seeking the most suitable ones for distinct soil textural and structural variations. This involves an extensive literature review, identifying key soil parameters influencing gas diffusion. Subsequently, various predictive models, spanning from the earliest to the latest, are scrutinized alongside their applications. Reference measurements in selected sandy soils, coupled with soil data from the literature, are employed for evaluation. Statistical analysis was carried out to compare

and select the best predictive model for different applications.

2. Literature review

With Buckingham (1904) making the first breakthrough in gas diffusivity modelling by introducing a simple, power-law model as follows (01), many number of models have been introduced by researchers up to the present.

$$\frac{D_p}{D_o} = \varepsilon^2 \quad (01)$$

where D_p/D_o is the soil gas diffusivity and ε is the air-filled porosity.

Penman (1940) introduced a simple linear model for gas diffusivity that takes the following form.

$$\frac{D_p}{D_o} = 0.66\varepsilon \quad (02)$$

Call (1957) made modifications to the Penman model by incorporating the assumption that 10% of the total soil volume was composed of isolated, inactive air-filled pores and introduced the following form.

$$\frac{D_p}{D_o} = A(\varepsilon - \varepsilon_0)^n \quad (03)$$

where ε_0 is the threshold are content, A and n are model parameters.

Millington and Quirk introduced two consecutive models in 1960 and 1961 by incorporating the total porosity (Φ) as a parameter in their models. The Millington and Quirk (1960) model takes the following form:

$$\frac{D_p}{D_o} = \frac{\varepsilon^2}{\Phi^3} \quad (04)$$

while Millington and Quirk (1961) can be presented as follows.

$$\frac{D_p}{D_o} = \frac{\varepsilon^{10}}{\Phi^2} \quad (05)$$

where Φ is the total porosity.

Troeh et al. (1982) introduced a new model combining advantages of commonly used linear and curvilinear equations as follows (06).

$$\frac{D_p}{D_o} = \left(\frac{s-u}{1-u} \right)^v \quad (06)$$

where s is the air porosity, u and v are model parameters.

Moldrup, Olesen, Gamst et al., (2000) enhanced the Marshall (1959) model by incorporating water-induced effects, with the Water-Induced Linear Reduction (WLR-Marshall) model, for sieved repacked soils.

$$\frac{D_p}{D_o} = \varepsilon^{1.5} \left(\frac{\varepsilon}{\Phi}\right) \quad (07)$$

The WLR term describes term (ε/Φ) describes the effects of changing pore shape and configuration in wet soil compared with dry soil at the same air-filled porosity.

Chamindu Deepagoda et al., (2010) developed the density-corrected model by analysing a diverse range of intact soils with varying densities from existing literature.

$$\frac{D_p}{D_o} = 0.1[2\left(\frac{\varepsilon}{\Phi}\right)^3 + 0.04\left(\frac{\varepsilon}{\Phi}\right)] \quad (08)$$

Deepagoda et al., (2011) extended the above model including interdependent model parameters which are functions of Φ .

$$\frac{D_p}{D_o} = 0.5\Phi\left(\frac{\varepsilon}{\Phi}\right)^{2+1.38\Phi} \quad (09)$$

Moldrup et al., (2013) developed a structure dependent, water induced linear reduction (SWLR) model by adapting WLR-Marshall (2000) model and introducing a media complexity factor (C_m) in the dry media term of the model as follows:

$$\frac{D_p}{D_o} = \varepsilon^{(1+C_m\Phi)} \left(\frac{\varepsilon}{\Phi}\right) \quad (10)$$

Lakshani at al., (2022) developed a novel air-saturation-dependent exponential (ASEX) gas diffusivity model to model D_p/D_o in relation to soil air saturation taking the following form:

$$\frac{D_p}{D_o} = \frac{D_{p,dry}}{D_o} \exp\left[\ln\alpha\left(\frac{1-S_a}{S_a}\right)\right] \quad (11)$$

Where S_a is the air saturation and α is the diffusivity at half air saturation relative to the diffusivity at complete soil air saturation.

3. Methodology

3.1 Soil Data

To investigate the soil-moisture effects on soil gas diffusivity and compare the selected model performance, soil and gas diffusivity data was collected from literature for testing eleven predictive gas diffusivity models. The selected soils belong to different geographical origins such as Sri Lanka, New Zealand, Japan, Denmark, Poland, and the United States, representing agricultural soils. They consist of different soil types including mainly sand, silt, clay and types of loam (sandy loam, sandy clay loam, and silt loam). They also represent both intact and sieved-repacked soils which demonstrate different soil structural status.

3.2 Reference Measurement

In addition to soil data taken from the literature, 6 sand samples (3 fine grained sand samples and 3 coarse grained sand samples) were collected for carrying out a reference measurement. Soil samples were packed in metal cores to a density

of 1.8 g/cm³. Then they were saturated for 24 hrs and subjected to a stepwise evaporation to obtain different moisture contents. At each moisture content, gas diffusivity was measured using one chamber diffusion apparatus which was introduced by Taylor (1949) and further developed by Schjønning (1985). The gas diffusion chamber was flushed with 100% N₂ to remove all O₂ inside the chamber. The sample was then opened to the atmosphere, allowing atmospheric air to enter the chamber through the soil sample. The increasing concentration of O₂ inside the chamber was continuously measured using the high-resolution oxygen sensor attached to the chamber wall. Gas diffusion (D_p) was calculated using the method proposed by Taylor (1949).

3.3 Statistical Analysis

For the comparison of the model performance, Root Mean Square Error (RMSE) and Bias were used. RMSE provides a measure of how well a model's predictions align with the actual observed values. It is given by the following formula (12).

$$RMSE = \sqrt{\frac{1}{n} \sum_{i=1}^n (d_i)^2} \quad (12)$$

The bias evaluates whether a model overestimates (positive bias) or underestimates (negative bias) the observations. It is given by the following (13) formula.

$$Bias = \frac{1}{n} \sum_{i=1}^n (d_i) \quad (13)$$

The model that showed the minimum RMSE and bias was to be selected as the best predictive model for the selected applications.

4. Results and Discussion

The detailed statistical analysis for model performance with Root Mean Square Error (RMSE) and Bias is given in Table 1.

According to the results, except for Peradeniya agricultural soil, all the other soils identified the Penman (1940) model as the least accurate model, with a significant overprediction. Except for Danish soil, almost all the other soils were well predicted by the Troeh model. Notably, the The density Corrected model exhibited superior performance with minimum RMSE and bias, specifically for Danish soil, a result aligned with its original development and calibration using the corresponding Danish soil dataset. Overall, Troeh (1982) model made an accurate prediction and statistically outperformed the other models with minimum RMSE and Bias. This superior

performance is attributed to the calibration of model parameters u and v , which ensures minimal RMSE and bias.

Table 1: Selected gas-diffusivity model performance in terms of RMSE and Bias

Model		Buckingham	Penman	Penman-Call	MQ ^a 60	MQ ^a 61	Troeh	WLR ^a -Marshall	DC ^a	GDC ^a	SWLR ^a	ASEX ^a
Geographic Origin												
Sri Lanka	RMSE	0.0605	0.0651	0.0425	0.0421	0.0553	0.0343	0.0411	0.1012	0.0773	0.0402	0.0480
	Bias	-0.0428	0.0513	-0.0147	0.0202	-0.0306	0.0001	-0.0190	-0.0853	-0.0639	-0.0199	-0.0321
Denmark	RMSE	0.0193	0.0930	0.0392	0.0506	0.0184	0.0101	0.0269	0.0073	0.0111	0.0302	0.0310
	Bias	0.0132	0.0869	0.0209	0.0373	0.0068	-0.0007	0.0165	0.0002	0.0057	0.0198	0.0186
Japan	RMSE	0.0473	0.0792	0.0337	0.0412	0.0455	0.0338	0.0314	0.0730	0.0604	0.0348	0.0336
	Bias	-0.0291	0.0720	0.0060	0.0294	-0.0257	0.0006	-0.0112	-0.0589	-0.0471	-0.0076	-0.0124
New Zealand	RMSE	0.0126	0.0633	0.0332	0.0162	0.0207	0.0125	0.0144	0.0229	0.0204	0.0154	0.0166
	Bias	-0.0031	0.0550	-0.0110	0.0045	-0.0153	-0.0023	-0.0081	-0.0166	-0.0148	-0.0097	-0.0107
Poland	RMSE	0.0397	0.1285	0.0668	0.0895	0.0505	0.0260	0.0560	0.0385	0.0333	0.0557	0.0505
	Bias	0.0278	0.1242	0.0582	0.0746	0.0175	0.0005	0.0369	-0.0137	0.0023	0.0355	0.0375
United States	RMSE	0.0279	0.0895	0.0337	0.0788	0.0695	0.0274	0.0550	0.0511	0.0408	0.0566	0.0298
	Bias	-0.0129	0.0851	0.0191	0.0501	-0.0003	0.0082	0.0110	-0.0441	-0.0267	0.0143	0.0056
SL-Experiment	RMSE	0.0144	0.0608	0.0393	0.0329	0.0181	0.0150	0.0154	0.0149	0.0120	0.0265	0.0238
	Bias	-0.0125	0.0493	-0.0167	0.0170	-0.0054	0.0016	-0.0012	-0.0052	-0.0061	0.0095	0.0079

^aMQ – Millington and Quirk model, WLR – Water-induced Linear Reduction model, DC – Density Corrected model, GDC – Generalized Density Corrected model, SWLR – Structure-dependent Water-induced Linear Reduction model, ASEX – Air saturation-dependent Exponential model

Figure 1 shows the scatter plot comparison of Troeh model for all the soil types considered in this study.

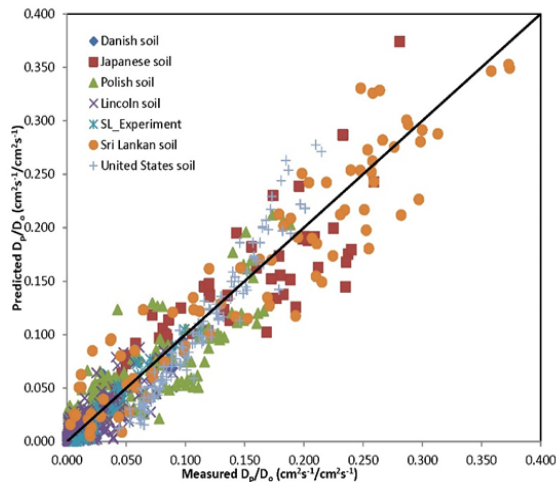


Figure 1: Scatter plot comparison of measured and predicted data using Troeh model (Eq. 6)

The optimization of model parameters (u , v) of Troeh model, results in unique u , v values for each dataset to minimize RMSE. Table 2 shows the optimized u , and v values for the considered soil types.

Table 2: Model parameters of Troeh (1982) model for the selected soil types

Troeh Model: $\frac{D_p}{D_0} = \left(\frac{s-u}{1-u}\right)^v$			
Soil Type	u	v	
Sri Lankan (Peradeniya) soil	0.04	2.13	
Danish soil	0.08	1.49	
Japanese soil	0.00	1.98	
New Zealand soil	0.00	2.35	
Polish soil	0.07	1.44	
United States soil	0.00	1.96	
Sri Lankan soil (experimental)	Coarse	0.00	1.84
	Fine	0.00	1.82

5. Conclusions

In this study, the performance of various soil-gas diffusivity models, ranging from the earliest to the newest, was assessed using soil data from different geographical regions. Experimental data, along with literature-based soil gas diffusivity data, were compared with eleven

existing models. Among all the models considered, the Troeh (1982) model emerged as highly accurate, statistically outperforming other models with minimum Root Mean Square Error (RMSE) and Bias. The Troeh model is noteworthy as its parameter u signifies a gas percolation threshold, aligning with percolation theory and establishing a solid theoretical foundation. However, a drawback lies in the requirement of two parameters known a priori for its predictions, necessitating calibration with limited measured data to optimize its use. Overall, Troeh model remains promising due to its theoretical underpinning. Additionally, the Density Corrected model (08) demonstrated superior performance for Danish soils, having been developed and calibrated against the same data set, further emphasizing its effectiveness in this context.

References

- Buckingham, E. (1904) 'Contributions to our knowledge of the aeration of soils', *Bur. Soil Bull* (Vol. 25). Washington, DC: U.S. Gov. Print. Office.
- Call, F. (1957) 'Soil fumigation. V.—Diffusion of ethylene dibromide through soils', *Journal of the Science of Food and Agriculture*, 8(3), pp.143-150.
- Deepagoda, T.C., Moldrup, P., Schjønning, P., Jonge, L.W.D., Kawamoto, K. and Komatsu, T. (2011) 'Density-corrected models for gas diffusivity and air permeability in unsaturated soil', *Vadose Zone Journal*, 10(1), pp.226-238.
- Deepagoda, T.C., Moldrup, P., Schjønning, P., Kawamoto, K., Komatsu, T. and de Jonge, L.W. (2011) 'Generalized density-corrected model for gas diffusivity in variably saturated soils', *Soil Science Society of America Journal*, 75(4), pp.1315-1329.
- Lakshani, M.M.T., Chamindu Deepagoda, T.K.K., Hamamoto, S., Elberling, B., Fu, W., Yang, T., Fan, J., Ma, X., Clough, T., Smits, K.M. and Parameswaran, T.G. (2022) 'A new exponential model for predicting soil gas diffusivity with varying degree of saturation', *Vadose Zone Journal*, 22(1), p.e20236.
- Millington, R.J. and Quirk, J.M. (1960) 'Transport in porous media. p. 97-106. FA Van Beren et al.(ed.) *Trans. Int. Congr. of Soil Sci.*, 7th, Madison, WI. 14-24 Aug. 1960. Vol. 1. Elsevier, Amsterdam.
- Millington, R.J. and Quirk, J.P. (1961) 'Permeability of porous solids', *Transactions of the Faraday Society*, 57, pp.1200-1207.
- Moldrup, P., Deepagoda, T.C., Hamamoto, S., Komatsu, T., Kawamoto, K., Rolston, D.E. and de Jonge, L.W. (2013) 'Structure-dependent water-induced linear reduction model for predicting gas diffusivity and tortuosity in repacked and intact soil', *Vadose Zone Journal*, 12(3).
- Moldrup, P., Olesen, T., Gamst, J., Schjønning, P., Yamaguchi, T. and Rolston, D.E. (2000) 'Predicting the gas diffusion coefficient in repacked soil water-induced linear reduction model', *Soil Science Society of America Journal*, 64(5), pp.1588-1594.
- Moldrup, P., Olesen, T., Komatsu, T., Schjønning, P. and Rolston, D.E. (2001) 'Tortuosity, Diffusivity, and Permeability in the Soil Liquid and Gaseous Phases', *Soil Science Society of America Journal*, 65(3), pp. 613-623. Available at: <https://doi.org/10.2136/sssaj2001.653613x>.
- Penman, H.L. (1940) 'Gas and vapour movements in the soil: I. The diffusion of vapours through porous solids', *The Journal of Agricultural Science*, 30(3), pp.437-462.
- Schjønning, P. (1985) 'A laboratory method for determination of gas diffusion in soil', *Beretning. Statens Planteavltsforsog* (Denmark).
- Schjønning, P., Eden, M., Moldrup, P. and de Jonge, L.W. (2013) 'Two-chamber, two-gas and one-chamber, one-gas methods for measuring the soil-gas diffusion coefficient: Validation and inter-calibration', *Soil Science Society of America Journal*, 77(3), pp.729-740.
- Taylor, S.A. (1950) 'Oxygen diffusion in porous media as a measure of soil aeration', *Proceedings, Soil Science Society of America*, 1949, 14, pp.55-61.
- Troeh, F.R., Jabro, J.D. and Kirkham, D. (1982) 'Gaseous diffusion equations for porous materials', *Geoderma*, 27(3), pp.239-253.



STRUCTURAL AND MATERIALS ENGINEERING



Enhance the Seismic Performances of Concrete Filled Steelbox Columns by Improving Confinement Effect: A Numerical Approach

Alahakoon A.M.Y.D.*, Malalage V. P.*, and Jayasinghe J. A. S. C.

Department of Civil Engineering, Faculty of Engineering, University of Peradeniya, Sri Lanka

* e17007@eng.pdn.ac.lk | e17204@eng.pdn.ac.lk

Keywords: Concrete-filled steel tubes, Confinement effect, Cyclic loading, Finite element model

Abstract

Highway piers are essential in elevated roadways, and they are widely used in industrialized nations. Therefore, designing piers that can withstand severe seismic loadings is crucial, especially in regions where earthquakes are common. The goal of this study is to alter the stiffener arrangements of concrete-filled steel box columns (CFST) in order to increase their strength, ductility, and energy absorption capacity and hence enhance their overall performance by enhancing the confinement effect. A comprehensive finite element model of CFST columns with stiffeners was developed and validated using past experimental data. Results revealed that the T arrangement of stiffeners shows an increment in confinement effect which results in the enhancement of the lateral performance of the column. Further enhancement of the confinement was obtained by changing the flange to web ratio (L_f/L_w) of the stiffeners. Finally, the obtained force-displacement curves were compared to investigate the effect of confinement and it was revealed that the cross-section having the ratio of $L_f / L_w = 2.0$ (flange to web length ratio) performs better than the other cross-sectional arrangements in strength and for the energy absorption capacity, while $L_f / L_w = 1.0$ is the best arrangement for the ductility.

1. Introduction

In the early 1900s, there were severe bridge collapses due to the insufficient strength of the piers against earthquakes. Because of that, structural engineers and researchers are more interested in the different structural elements, which provides adequate strength with enhanced ductility. Therefore concrete-filled steel tubes (CFST) are becoming much more popular in the civil engineering field due to their performance compared to other hollow steel and RC piers.

The aim of this study is to enhance the lateral performance of CFST by improving the confinement of the concrete by changing the stiffener arrangements. Experimental tests are

found to be very expensive and the results are inadequate to make exact conclusions. Due to this reason, this study is mainly focused on the numerical procedure.

In this study, a few parameters will be mainly considered to check the effect of confinement, and some of them are; stiffener arrangement and stiffener length. The confinement effect of the CFST will be mainly focused in this study. Also, an analysis will determine how the increased confinement will influence the CFST's strength, ductility, and energy absorption capacity.

2. Literature Review

After the hugely impacted earthquakes, such as Hyogo-ken Nanbu earthquake (Kitada, et al., 2003), researchers have been studying more about the seismic behaviour of hollow steel box piers. It is necessary to retrofit the existing steel bridge piers not satisfying the design standard and having inadequate ductility. Therefore, past studies indicated several methods to improve the lateral seismic performances of the steel hollow bridge piers. The use of steel sections with infilled concrete is one of these methods. (Ge et al., 1996).

Many studies have been carried out to improve the confinement effect of the CFSTs. Enhanced confinement for the concrete can improve the strength, ductility, and energy capacity. Some past studies present a systematic computational analysis of the confinement effect in hollow sections, using parameters such as concrete dilation and confining pressure. The strength enhancement of confined concrete is empirically related to the maximum average lateral confining pressure (σ_{lat}) and this confining lateral pressure imposed by the steel depends on the depth to thickness ratio. The value of lateral confining pressure can be obtained by the empirical equations. When concrete is subjected to laterally confining pressure, the uniaxial compressive strength f'_{cc} and the corresponding strain ϵ'_{cc} are much higher than those of unconfined concrete (Hu, et al., 2003). Under the axial compression, the steel tube is subjected to

biaxial stress state in the hoop and axial direction, and the hoop stress component provides confinement for the inner concrete. And also, there are many external methods to improve the confinement effect as well. However, in this study, confinement is increased by introducing different stiffener arrangements to the steel column.

3. Methodology

A FE model for a partially concrete-filled steel box column was created in ABAQUS and it was validated with the past experimental result by Ge and Usami, (1996). Table 1 shows the properties of the FE model which was used for validation. The experimental setup is shown in Figure 1 and the cyclic loading pattern is shown in Figure 2. Then, a series of analysis were conducted by varying the stiffener arrangement and observing the effect on the confinement of the CFST column, and studying how the confinement will affect the ductility, strength, and energy absorption capacity.

Table 2: Material properties

Properties	Values
Density of concrete (tonnes/mm ³)	2.4e ⁻⁹
Yield stress of steel	308 MPa
Young’s modulus of steel	211GPa
Ultimate stress of steel	455 MPa
Poisson’s ratio of steel	0.27
Young’s modulus of concrete	25.5 GPa
Poisson’s ratio of concrete	0.165

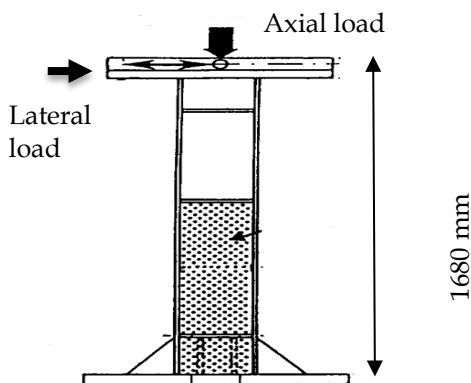


Figure 1: Experimental setup (Ge and Usami, 1996)

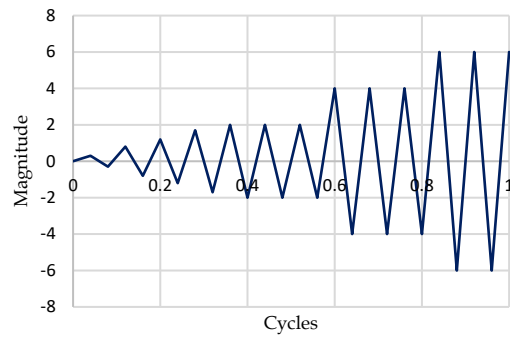


Figure 2: Cyclic loading for testing setup (Ge and Usami, 1996)

4. Results and Discussion

4.1 Validation models

Figure 3 shows the load-displacement envelope curve by joining peak points of the numerical and experimental results for the stiffeners with concrete model (Ge and Usami, 1996). Figure 4 shows the comparison of the envelope curves in 3 validated models. CFST with stiffeners model has the significant enhancement in strength, ductility and load bearing capacity.

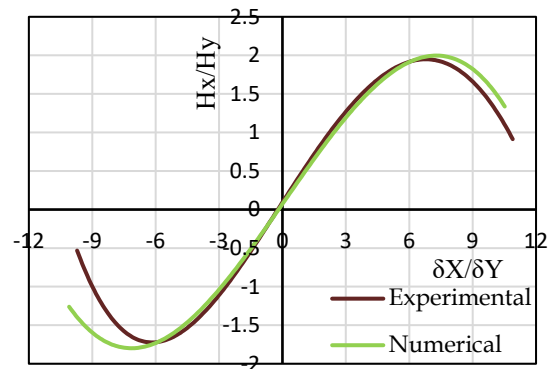


Figure 3: Validation of numerical model: CFST with stiffeners

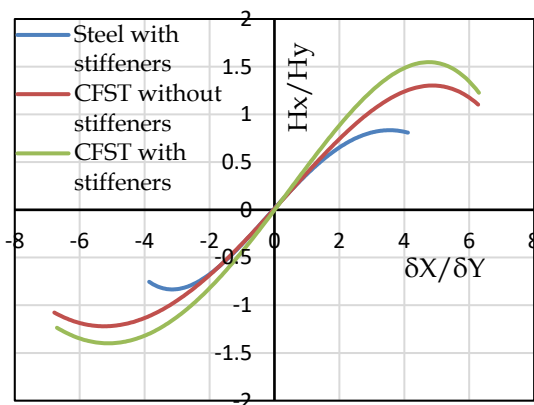


Figure 4: Envelope curves of the three different validated models

4.2 Parametric study

After the validation of the CFST model, the parametric study was conducted to see the

effects of (a) stiffener length (L_w / L_p), (b) stiffener arrangement, and (c) L_f/L_w on the confinement of the CFST column. Figure 5 shows the parameters on the cross section.

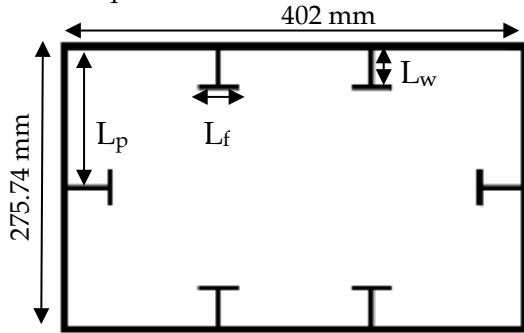


Figure 5: Parameters on the cross section

This section provides the results of the influence of parameter adjustments on concrete section principal stresses through a parametric study. Initially, the L_w/L_p ratios were systematically altered to 0.2, 0.26, and 0.34 as shown in Figure 6. Subsequent analysis involved the modification of the stiffener arrangement, providing an examination of stress distribution in cross sections (refer to Figure 8). Lastly, the effects of principal stress, arising from variations in the L_f/L_w ratio, were analysed in the context of a T-shaped stiffener arrangement, which demonstrated better confinement effects compared to alternative arrangements (see Figures 10 and 11). Figures 7, 9, and 12 present envelope curves for each case mentioned above, offering a comprehensive understanding of how the strength and ductility were enhanced by the increased confinement of the concrete.

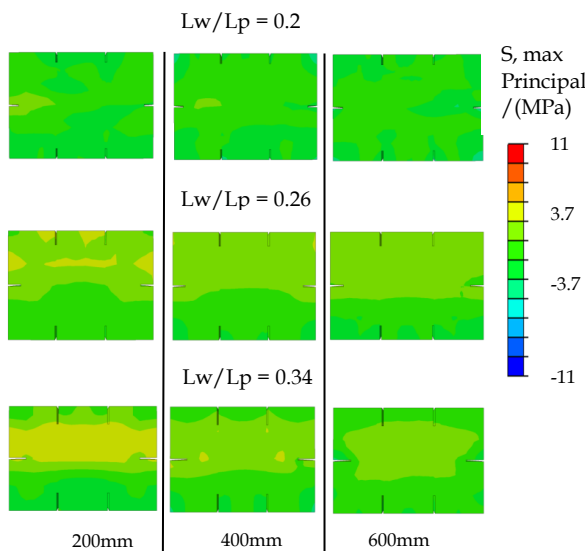


Figure 6: Variation of stresses for different L_w/L_p ratios

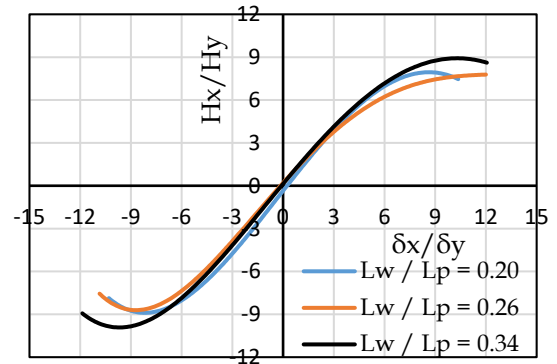


Figure 7: Envelop curves (different L_w/L_p ratios)

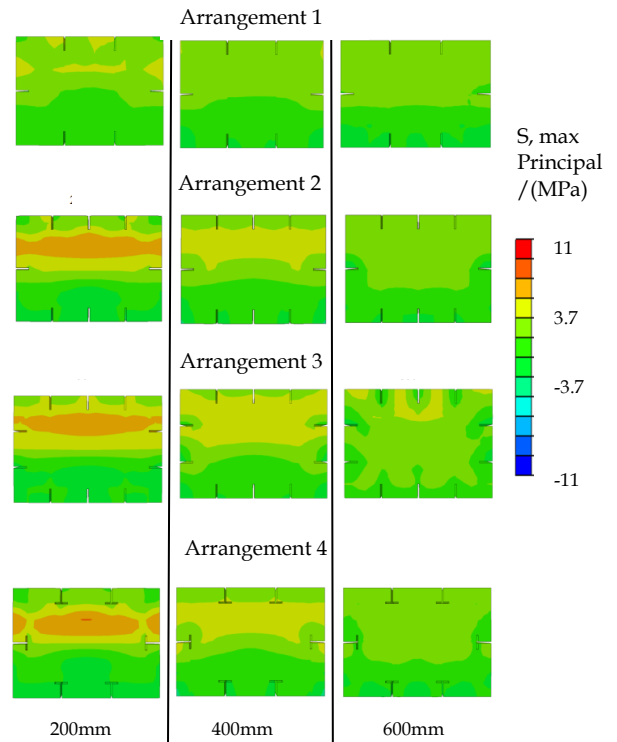


Figure 8: Variation of stresses for different stiffener arrangements

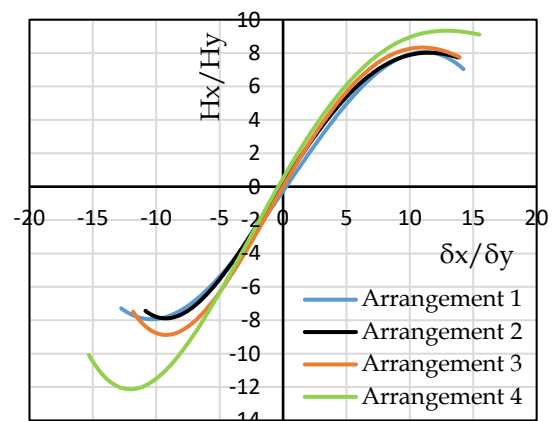


Figure 9: Envelop curves (different stiffener arrangements)

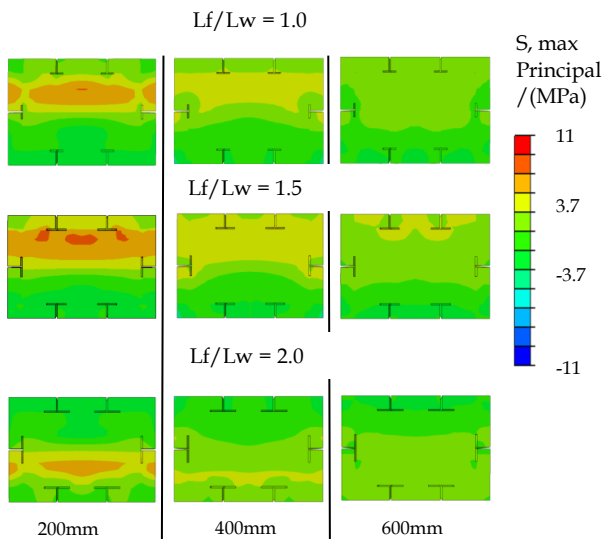


Figure 10: Variation of stresses for different L_f/L_w ratios (changing L_f)

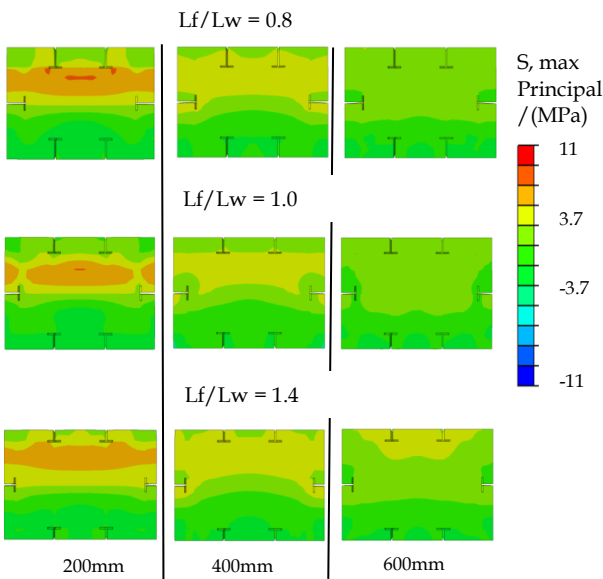


Figure 11: Variation of stresses for different L_f/L_w ratios (changing L_w)

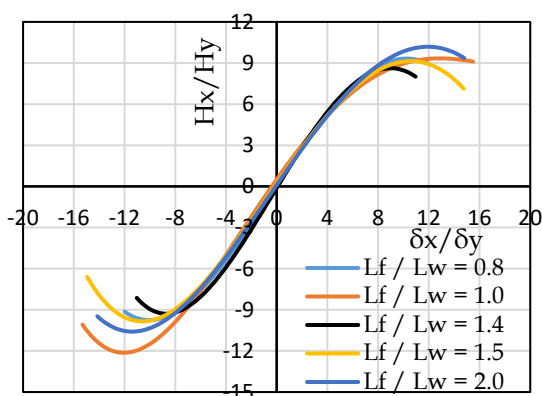


Figure 12: Envelop curves (different L_f/L_w ratios)

Figure 12 shows that the $L_f/L_w = 2$ has the highest strength and the maximum ductility.

5. Conclusions

- The maximum principal stress exhibits a gradual increase with the rising L_w/L_p ratio. Notably, the L_w/L_p ratio of 0.2 demonstrates an early enhancement in maximum strength. However, it is important to note that this ratio comes with a trade-off, as the ductility is lower in comparison to the $L_w/L_p = 0.34$ and 0.26.
- Stiffener arrangement 4 exhibits the highest H/H_y (lateral strength to yield lateral strength ratio), and maximum ductility μ_m due to the large confinement effect spread over the stiffeners.
- Further, modifying the L_f/L_w ratio in arrangement 4 results in additional improvements in confinement in the concrete. Specifically, $L_f/L_w = 2.0$ yields the highest H/H_y and maximum energy absorption capacity. Whereas, $L_f/L_w = 1.0$ achieves the maximum ductility.
- Considering the overall effect, $L_f/L_w = 2.0$ gives the best cross-sectional arrangement for the strength and for the energy absorption capacity. And $L_f/L_w = 1.0$ is the best arrangement for the ductile criteria.

References

Ge, H. and Usami, T. (1996) 'Cyclic tests of concrete-filled steel box columns', Journal of structural engineering, 122(10), p1169-1177.

Usami, T. and Ge, H. B. (1994) 'Ductility of concrete-filled steel box columns under cyclic loading', J. Struct. Eng. ASCE, 120(7), p2021- 2040.

Seismic Performance of Steel Hollow Building Column Under Combined Fire and Cyclic Loading: A Coupled Thermo-Mechanical Numerical Approach

Kanakarathna Y. P. K. M. W. N.*, Jayasooriya J. A. R. D.*, and Jayasinghe J. A. S. C.

Department of Civil Engineering, Faculty of Engineering, University of Peradeniya, Sri Lanka

* e17151@eng.pdn.ac.lk | e17135@eng.pdn.ac.lk

Keywords: CFD-FEM, Cyclic loading, Fire, Seismic performance, Steel hollow column

Abstract

This study presents a method to assess the structural response of steel hollow columns under combined fire and cyclic loading, using CFD fire simulations and FE analysis with ABAQUS. Validation studies confirm the model's accuracy in capturing fire and cyclic loading effects. Parametric analyses explore variations in width-to-thickness (b/t) and slenderness (λ) ratios, revealing significant reductions in seismic performance. Specifically, reducing the b/t ratio under fire conditions decreased maximum ductility, strength, and energy absorption capacity by 65%, 28%, and 44%, respectively. Increasing the slenderness ratio (λ) under fire conditions led to reductions of 32%, 40%, and 67% in these metrics.

1. Introduction

This study evaluates the performance of steel hollow box columns in buildings under simultaneous fire and cyclic loading, focusing on strength and ductility. Fire scenarios are simulated using Fire Dynamics Simulator (FDS), and Finite Element (FE) analysis is performed with ABAQUS. Adiabatic surface temperatures from fire simulations are transferred to the ABAQUS model using FDS2FEM. The modelling and analysis are validated with experimental data from Kamikawa et al. (2006). A parametric study assesses the seismic performance of steel hollow columns by varying the slenderness ratio (λ) and width-to-thickness ratio (b/t).

2. Literature review

Several studies have investigated the impact of non-uniform fire on steel structures. Chen et al., (2022) introduced a framework to transfer boundary information from a CFD-based fire model to a thermo-mechanical FEM model, avoiding the use of less accurate temperature curves and simplifying fire environments. Earthquakes or dynamic loads often occur

simultaneously with fires, as seen in the Loma Prieta (1989), Northridge (1994), and Kobe (1995) earthquakes. The combined damage from multiple disasters, such as fire and earthquake, is greater than from a single disaster alone.

3. Methodology

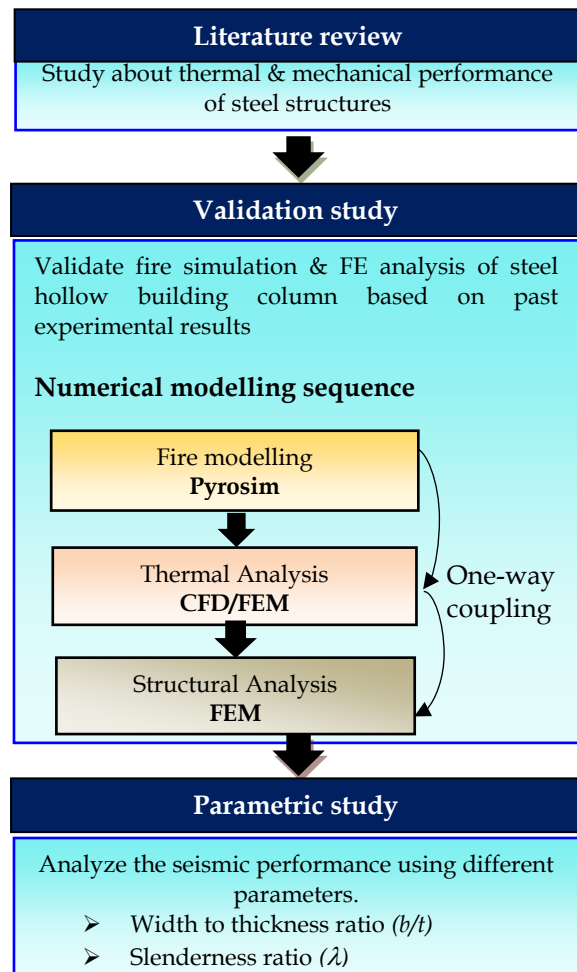


Figure 1: Methodology

Figure 1 shows the steps of the methodology of this study. The sequence starts with fire modelling using Pyrosim. After the fire simulation, thermal boundary conditions are converted into heat flux using the FDS2FEM tool. This heat flux is then mapped onto the FE

model using the node-set boundary file (NSET-BNDF) approach. Finally, thermal and mechanical analysis is conducted using ABAQUS.

3.1 Behaviour of steel structures

Studying the thermal and mechanical performance of steel elements under simultaneous fire and cyclic loading is crucial, as material properties deteriorate under thermal loading. Therefore, need to consider temperature-dependent material properties for the simulations.

3.2 Numerical modelling and Validation

Numerical simulation of fire modelling using *Pyrosim* software is validated using past experimental data (Kamikawa et al., 2006). Thermal analysis and mechanical analysis of the ABAQUS model are also validated using the same experimental data (Kamikawa et al., 2006). Table 1 shows details of the experiment test.

Table 3: Details of experimental testing

Element	STKR400 hollow
Column dimensions	0.1 m x 0.1 m, 3.2 mm thk.
Yield stress	2 N/mm ²
Tensile strength	400 N/mm ²
Density	7850 kg/m ³
Burner fuel type	Propane
Burner dimensions	0.3 m x 0.3 m
Heat release rate	52.5 kW

3.3 Parametric study

The seismic parameters such as ductility, strength, and energy absorption capacity of steel hollow building columns under simultaneously applied fire and cyclic loading were investigated by changing the width to thickness ratio and slenderness ratio. In this study, seismic parameters are compared at room temperature (25°C) and under fire conditions using hysteretic curves

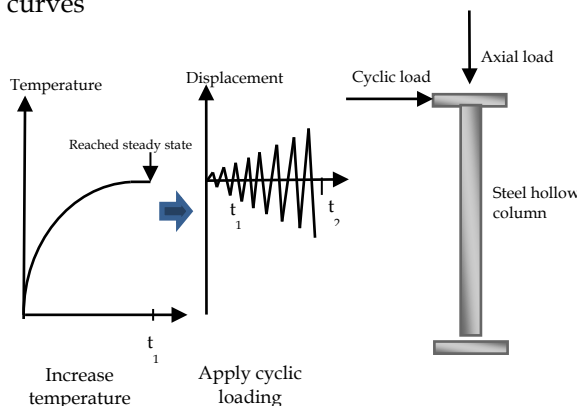


Figure 2: Steps of parametric study

For the parametric study same fire loading having 52.5 kW fire intensity is applied. After reaching the temperature into steady state symmetric cyclic loading and axial load are applied as shown in Figure 2. Table 2 presents the material properties of steel columns for the parametric study. According to Table 3 and Table 4, seismic parameters are checked by changing the b/t ratio and change slenderness ratio (λ).

Table 2: Details of material properties

Element	Steel square hollow
Column dimensions	0.1 m x 0.1 m
Steel type	Hot-rolled
f_y	206 N/mm ²
f_u	400 N/mm ²
ν	0.3
E	200000 N/mm ²

Table 3: Parameters of the column (Fixed slenderness ratio (λ) and change b/t ratio)

λ	H (height)	t (thickness)	b/t
0.27	1.6 m	3.2 mm	31.25
		4.0 mm	25.00
		5.0 mm	20.00
		6.3 mm	15.87

Table 4: Parameters of the column (Fixed b/t ratio and change slenderness ratio (λ))

t (thickness)	b/t	H (height)	λ
3.2 mm	31.25	1.6 m	0.27
		2.0 m	0.34
		2.4 m	0.40

4. Results and Discussion

4.1 Validation of Fire modelling

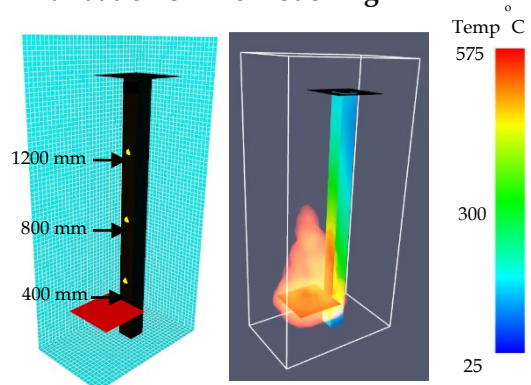


Figure 3: Pyrosim model and result visualization

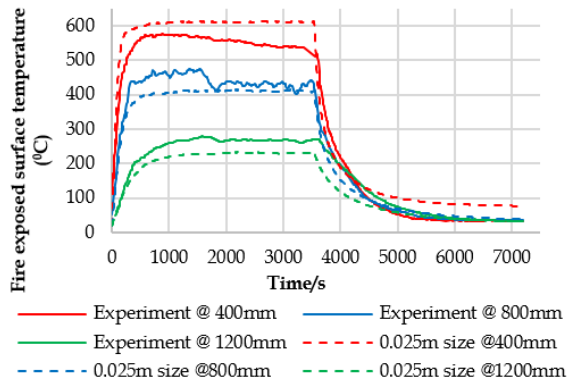


Figure 4: Comparison between *FDS* results and experimental results

Figure 3 shows the *Pyrosim* model and results visualization of the fire model. The variation of fire-exposed surface temperature with time for 3 heights is shown in Figure 4. It is clearly visible that 0.025 mm *FDS* mesh size results converge with experimental results.

4.2 Validation of FE analysis

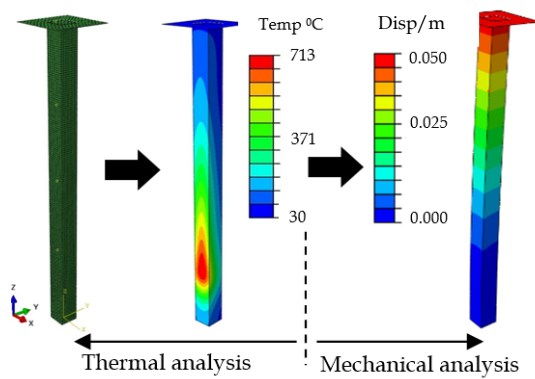


Figure 5: Result visualization of FE analysis

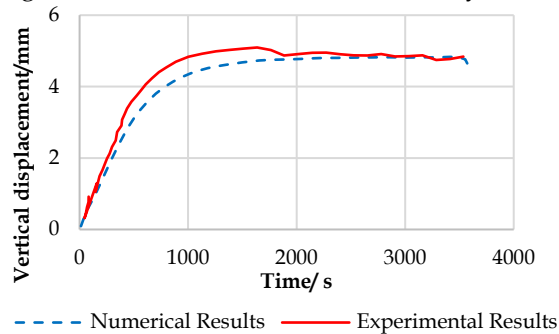


Figure 6: Comparison of vertical displacement between FE results and experimental results

Results visualization of FE analysis is shown in Figure 5 and numerical results of FE analysis converge with experimental results due to self-weight and fire loading (see Figure 6).

4.3 Parametric study

- Results when fixed slenderness ratio (λ) and change b/t ratio as shown in Table 3

Figure 7 shows the lateral load-lateral displacement envelope curves at room temperature (25 °C) and under fire conditions for different b/t ratios. Figure 8 represents the cumulative energy absorption capacity for both conditions when changing the b/t ratio. According to Figure 9, maximum seismic parameters decrease with changing b/t ratio.

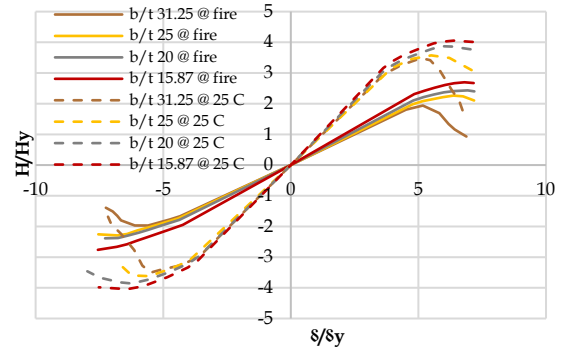


Figure 7: Envelope curves for different b/t ratio

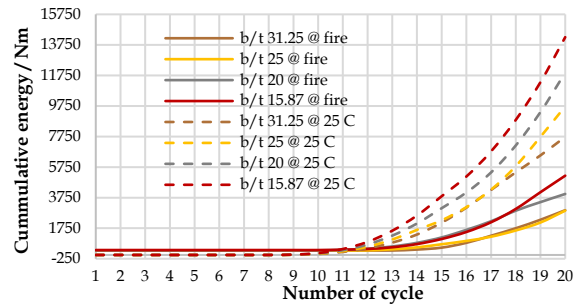
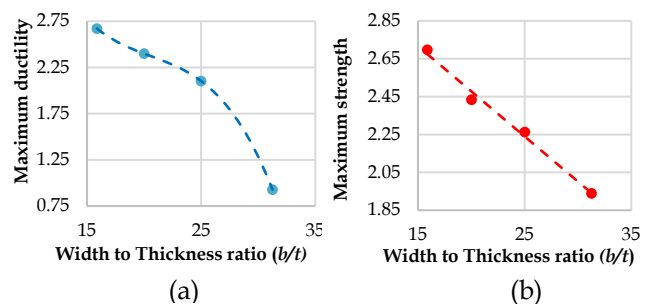
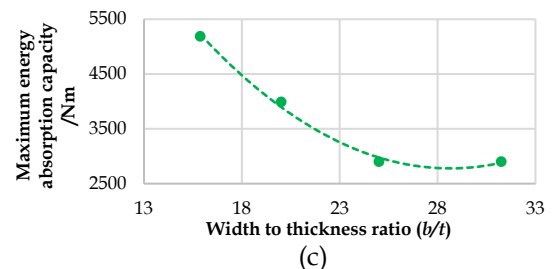


Figure 8: Cumulative energy curves for different b/t ratio



(a)

(b)



(c)

Figure 9: Results for different b/t ratios: (a) Maximum ductility, (b) Maximum strength and (c) Maximum energy absorption capacity

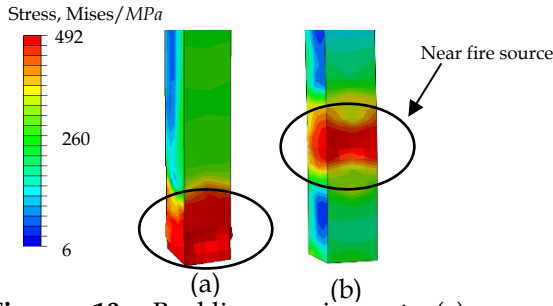


Figure 10: Buckling region at (a) room temperature and (b) under fire

Figure 10 shows the buckling region near the fire source under fire conditions and the buckling region at room temperature (25 °C) below the 1/3 height of the column in each model of the parametric study.

- Results when fixed b/t ratio and change slenderness ratio (λ) as shown in Table 4

Figure 11 shows the lateral load-lateral displacement envelope curves at room temperature (25 °C) and under fire conditions for different slenderness ratios (λ). Figure 12 represents the cumulative energy absorption capacity for both conditions when changing the slenderness ratio (λ). According to Figure 13, maximum seismic parameters linearly decrease with changing slenderness ratio (λ).

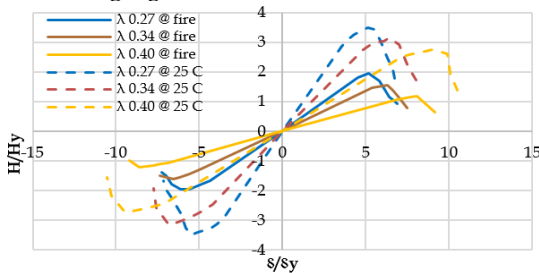


Figure 11: Cumulative energy curves for different slenderness ratios (λ)

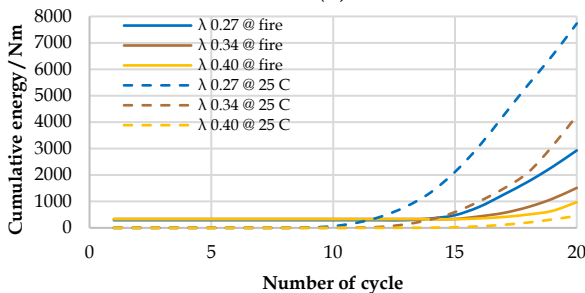


Figure 12: Cumulative energy curves for different slenderness ratios (λ)

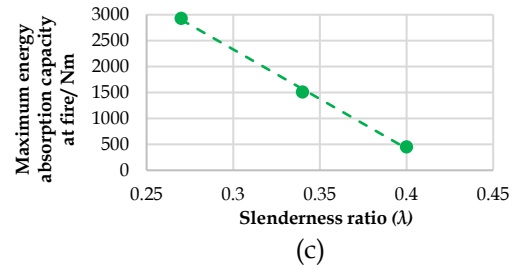
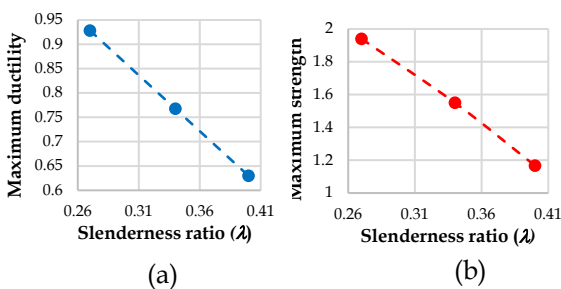


Figure 13: Results for different λ ratios: (a) Maximum ductility, (b) Maximum strength, and (c) Maximum energy absorption capacity

5. Conclusions

In this study seismic performance of steel hollow building columns under simultaneously combined fire and cyclic loading was observed by changing the b/t ratio and λ . Based on the results of the study, the following conclusions are made;

- When increasing b/t ratio around 50%, maximum seismic parameters such as ductility, strength, and energy absorption capacity represent noteworthy reductions 65%, 28%, and 44% under fire conditions and 55%, 13%, and 45% at room temperature (25 °C) respectively.

- When increasing the slenderness ratio around 50%, maximum seismic parameters such as ductility, strength, and energy absorption capacity represent a noteworthy reduction 32%, 40%, and 67% under fire conditions and 23%, 20%, and 94% at room temperature (25 °C) respectively.

- For each b/t ratio at room temperature (25 °C), maximum ductility and strength reduces by 30% to 50%, and energy absorption capacity is reduced by 60% to 75% when exposed to fire. Also, for each slenderness ratio at 25 °C, maximum ductility, and strength reduces by 45% to 60% and energy absorption capacity reduces by 50% to 55% when exposed to fire.

References

Kamikawa, D., Hasemi, Y., Yamada, K. and Nakamura, M. (2006) 'Mechanical response of a steel column exposed to a localized fire', In Proc., 4th Int. Workshop on Structures in Fire, Univ. of Aveiro, Aveiro, Portugal, p225-234.
 Chen, Q. and Jiang, Y. (2022) 'Performance Evaluation of Reinforced Concrete Columns under Simultaneously Combined Fire and Cyclic Loads', Buildings, 12(7), p1062.

Stress Analysis and Rehabilitation of Ancient Stupas in Sri Lanka

Buddhika H.A.D.S., Shanaka K.D.A.*, and Wijesiri M.N.M.

Department of Civil Engineering, Faculty of Engineering, University of Peradeniya, Sri Lanka

** shanaka.kda@gmail.com*

Keywords: Ancient mortar, Bricks, Brick masonry walls, Mechanical properties

Abstract

Stupa structures have been technically analysed to some extent, especially as a means of base knowledge for conservation purposes. The essential strength properties in engineering such as compressive strength, tensile strength, and modulus of elasticity play a crucial role. This study focuses on determining the compressive strength of mortar, bricks, and brick masonry walls. Additionally, flexural strength tests and water absorption tests were conducted on bricks. The investigation extends to understanding the behaviour of brick masonry walls under both in-plane and out-of-plane loadings. The study is conducted experimentally on samples generated for rehabilitation works at the Jetavana stupa in Anuradhapura, Sri Lanka.

1. Introduction

Stupas in Sri Lanka are monumental structures built to honor Lord Buddha. However, over time all these ancient stupas had fallen into ruins. There is a dedicated conservation program underway in Sri Lanka to preserve and protect the remaining stupas. Understanding the distribution of forces within stupas is essential for their preservation and restoration. The assumption of homogeneity was commonly made when analysing stupas. However, there is a lack of research that considers the real composition of a stupa, which consists of multiple zones made of different materials, resulting in a non-uniform structure. Valuable insights can be gained regarding its structural behaviour by considering the varied composition of a stupa's dome. To further enhance the accuracy of the analysis, laboratory experiments can be conducted to determine the mechanical properties of the different materials comprising the stupa. A deeper understanding of the structural characteristics and behaviour of non-homogeneous stupas can be achieved by undertaking this research.

2. Literature review

The stupas experience different types of stress and strain over time, caused by things like expansion, water absorption, and roots affecting the structure, weakened bricks, and foundation settling. It is important to determine the mechanical properties of materials to analyze the stress distribution of the stupa.

The primary construction material of a stupa is burnt clay bricks, with various sizes used for different components of the structure. The bricks used in ancient stupas are much larger than modern bricks. This higher sand content could be attributed to the greater strength observed in ancient bricks according to Ranaweera et al. (2006).

The ancient stupas were constructed using a unique clay slurry mortar called "navanita clay". As this substance is very soft, it fills the air gaps between the two bricks and ensures a tight fit. The plasticity of the clay allowed for significant movement within the brickwork without causing any fractures to the individual bricks.

The studies examined several mixtures consisting of different proportions of slaked lime, rice-husk ash, termite mound clay, ground burnt clay tile fragments, and water to evaluate their soaked and dry strengths. Mix 5 was found to be the typical choice for conservation purposes. The mix proportions by volume of the slaked lime, rice-husk ash, termite mound clay, and ground burnt clay tile fragments are 1:1:2:2 respectively

3. Methodology

The main objective of this study is to assess the structural strength of stupas under various loading conditions.

Mechanical properties of brick units, ancient masonry mixes, and brick masonry under in plane and out of plane loading are important factors for the study.

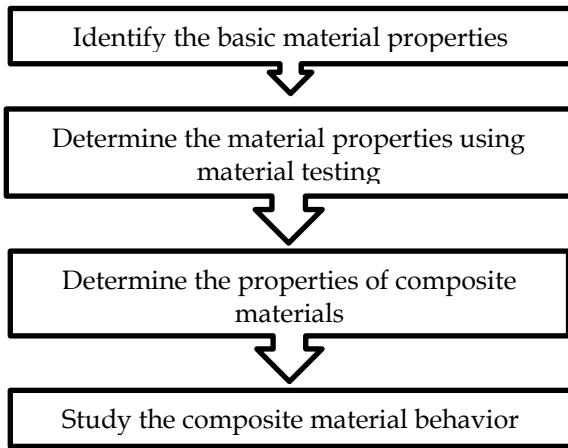


Figure 1: Flow chart of methodology

3.1 Testing of mortar

The mortar used in the study was formulated based on the findings from the existing literature. When it comes to testing there may not be a specific testing method available in established standards such as ASTM. It is necessary to adapt and modify existing testing procedures. Test specimens were prepared using Navanita clay and subjected to an applied force to determine their compressive strength.



Figure 2: Compressive strength test for mortar

3.2 Testing of stupa bricks

The mechanical properties of the burnt bricks were determined through the use of compressive and flexural strength tests. The compressive strength of bricks was tested adhering to the guidelines provided by ASTM C67.

The three-point loading test is a common method used to determine the flexural strength of bricks. This test assesses how well a brick can withstand bending forces. The load is increased at a constant rate until the brick specimen fails.



Figure 3: Flexural strength test

Young's modulus test involves the use of strain gauges and a load cell. Strain gauges are attached properly along the opposite sides where the strain of a brick specimen is to be measured. The load cell measures the applied force. Data acquisition software provided readings that could be used to create a stress-strain curve.



Figure 4: Test setup for Young's Modulus test

The water absorption test of the burnt bricks can be conducted following the BS EN 772-11 procedure. The dry densities of the burnt bricks can be determined following the BS EN 771-1 procedure.

3.3 Testing of brick masonry

In-plane and out-of-plane loading tests on brick masonry walls are crucial for assessing the structural behavior of the stupa under different conditions. These tests help to ensure that the brick masonry wall can safely support the applied loads, preventing collapse or excessive deformations.



Figure 5: In-plane loading test



Figure 6: Out-of-plane loading test

4. Results and Discussion

4.1 Introduction

Inside the ancient stupa, natural changes such as deformations, expansions, and settlements take place. Understanding the mechanical properties of Clay mortar, Bricks, and Composite materials is vital for studying these occurrences.

4.2 Mortar Compressive Strength Test

Two trial mixes were prepared, with the only variation being the water contents as indicated in Table 1.

Table 1: Mix proportions for Trial mixes

Mix id	Mix proportions by volume				
	Lime powder	Rice-husk ash	Roof-tile Powder	Termite Clay	Water
Mix 01	1	1	2	2	2
Mix 02	1	1	2	2	1.67

Compression tests for two trial mixes were conducted after 7, 28, and 90 days.

Table 2: Compressive strength test results for mortar

Mix id	Compressive Strength (kPa)		
	7 day	28 day	90 day
Trial mix 01	836.4	1085.7	714.8
Trial mix 02	1334.9	1794.7	1180.6

After 28 days, the compressive strength was higher than that at 7 days. However, at 90 days, the compressive strength was less than the strength observed at 7 days. The reason could be that curing was not conducted under realistic conditions, resulting in moisture loss over time. The cubes were exposed to a dry environment.

4.3 Brick Compression Test

Three brick samples were utilized, and the average compressive strength of these samples was 11.96 MPa.

Table 3: Compressive strength test results for bricks

Condition	Compressive strength (MPa)
Dry	11.96
Soaked	11.48

4.4 Brick Flexural Strength Test

Table 4 represents the values obtained for the flexural strength of brick specimens. All three specimens are nearly the same.

Table 4: Flexural strength test results

Brick No.	F (N)	f_t (Mpa)	Average f_t (Mpa)
1	311.5	0.486	0.482
2	290.4	0.478	
3	299.3	0.482	

4.5 Young's Modulus of Elasticity of Brick

Young's modulus was calculated from the slope of the linear elastic region of the curve. From figure 10 the average Young's modulus of bricks was obtained as 4.75 GPa.

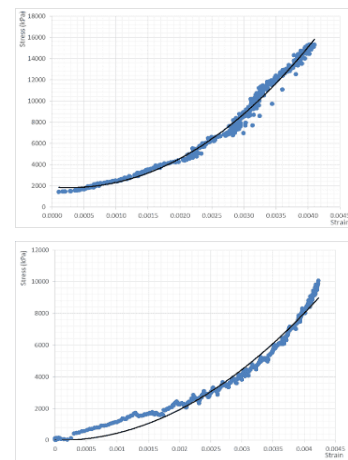


Figure 7: Stress-strain curves for two brick samples

4.6 Water absorption and dry density

Table 5 represents the values obtained for the water absorption and dry density of brick specimens. Three brick specimens were tested.

Table 5: Experimental values of water absorption and dry density

Property	Experimental value
Water absorption (%)	10.2
Density (kg/m ³)	1779.7

4.7 Out-of-Plane Loading for Composite Wall

A graph illustrating the relationship between displacement and applied force can be plotted as shown in figure 8.

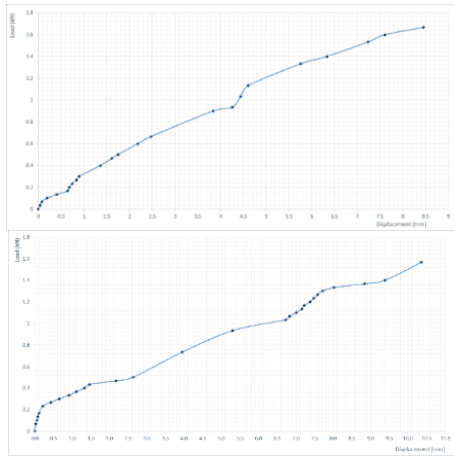


Figure 8: Load-displacement curves of walls

Based on the analysis of both graphs, it is observed that the maximum deflection reached approximately 10 mm, coinciding with a failure force of approximately 1.6 kN. Both graphs showed a significant initial load increase for minimal displacement, likely due to material stiffness, friction, preload, and boundary effects. The sudden load increase at 1.1 kN in both figures aligns with the mortar's compressive strength at 1.2 kN, hinting at material response and potential deformation or failure initiation, causing a rapid load rise. The observed cracking pattern reveals that some of the brick has developed a crack, causing the mortar to yield. Under the lateral load, the brick wall attempted to accommodate it through slip deformation between bricks and masonry. Since mortar only exists between horizontal joints, the initial failure mode was brick masonry slipping. It's important to note the absence of mortar between vertical joints, allowing for free movement. As the load increased, the masonry wall couldn't handle the lateral deformation solely through slip. Consequently, once the wall reached a maximum horizontal displacement, bricks at the wall's center developed vertical cracks under lateral loading. It's noteworthy that these brick cracks originated from the wall's bottom, likely due to frictional boundary conditions at the wall base, contrasting with the free boundary conditions at the top of the wall.

4.8 In-Plane Loading for Composite Wall

Two wall segments were employed for the testing, and an average displacement vs. load graph was generated, depicted in Figure 9. The calculated stiffness, derived from the load-displacement curve in Figure 14, stands at 15.27 kN/mm.

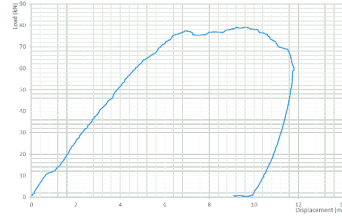


Figure 9: Load-Displacement curve of wall

Bricks crack before mortar due to varying material properties. Bricks, with higher compressive strength, resist compression but are prone to tension-induced cracking due to lower tensile strength. Mortar, more deformable, doesn't crack immediately. Bonding between them and mortar's support might delay brick cracking until a critical point.

5. Conclusions

- Optimum mortar was identified by preparing various trial mixtures according to the given proportions in the literature.
- This study reveals that adjusting mix proportion or modifying ingredient materials has the potential to unveil a superior mortar composition.
- Investigate the composite material behaviour of the combination of bricks and mortar under various loading conditions and observe the crack patterns.
- Finite element model can be developed using the obtained material properties and composite wall properties to simulate the structural behaviour of the stupa.

References

Peiris, K., Jayawardana, C., Wijesinghe, S. (2010) 'Engineering Features of Ancient Stupa Structure: A Review Based on Jethavana Vihara', Engineer - Vol. XXXIII, No. 02, pp. [59-69], The Institute of Engineers, Sri Lanka.

Ranaweera, M.P. and Abeyruwan, H. (2006) 'Materials used in the construction, conservation, and restoration of ancient stupas in Sri Lanka', Proceedings of the second International Congress on Construction History, Cambridge, England, March 29-April 2, 2006.

Development of Detailed Numerical Modal of Women Upper Torso for Garment Requirement

Jayaneththi J.K.P.S.*, Wickramasuriya B.Y., and Jayasinghe J.A.S.C.

Department of Civil Engineering, Faculty of Engineering, University of Peradeniya, Sri Lanka

* e17126@eng.pdn.ac.lk | e17393@eng.pdn.ac.lk

Keywords: Biomechanics, CAD modelling, FE analysis, Female upper torso, Hyper elastic material models, Sports bra design

Abstract

This study develops a detailed numerical model of the female upper torso to optimize garment design, particularly sports bras. The model utilizes finite element analysis (FEA) and incorporates hyper-elastic material properties to simulate tissue behavior under dynamic conditions. By examining the effects of breast volume, stiffness, and running dynamics, the research highlights the need for precise and adaptable garment elements to ensure comfort and support during physical activities.

1. Introduction

The goal of this research project was to create a numerical simulation that would allow Finite Element Analysis (FEA) to be used to analyse response in the upper torso of women under dynamic loading. The project includes a thorough literature analysis with an emphasis on Finite Element Modelling, CAD modelling, and 3D scanning of the upper thoracic anatomy of women. Mooney-Rivlin hyper-elastic models are used in the Finite Element Analysis to describe the nonlinear behaviour of the tissues in the upper torso of women. The dynamic model takes into account the system of flexible upper torsos in women and a rigid thorax, as well as tissue deformation while running. Utilizing vertical dynamic load functions in CAD modal analysis allows for the assessment of running-induced effects on breast area displacement. The study highlights how important it is to comprehend the upper torso biomechanics of women in order to create sports bras that are supportive and relaxing.

2. Literature review

The review of the literature dives into important details that are necessary for the numerical simulation of the upper torso mechanics in women. It focuses on three primary areas: CAD modelling, the creation of Finite Element Models (FEA), and 3D scanning with tools such as the EinScan-Pro handheld scanner. Using hyper-elastic models such as Mooney-Rivlin, Yeoh, and

polynomial models, Finite Element Analysis helps to understand the mechanical behaviour of women upper torso tissues (Liang et al., 2019). The review also emphasizes difficulties in validating models of the upper torso in women because of data scarcity, variability among subjects, uncertainty in model parameters, and the need for essential simplifications (Sun et al., 2019). Generally, research on women's upper torso biomechanics has laid the groundwork for the advancement of sports bra design.

3. Methodology

Three steps make up the process used to create a biomechanical model of a woman's upper torso: In Stage 01, the main objectives were scanning, CAD model creation, and a thorough literature analysis to comprehend upper torso anatomy. This covered the creation of 3D scanned CAD models as well as the investigation of hyper-elastic material models.

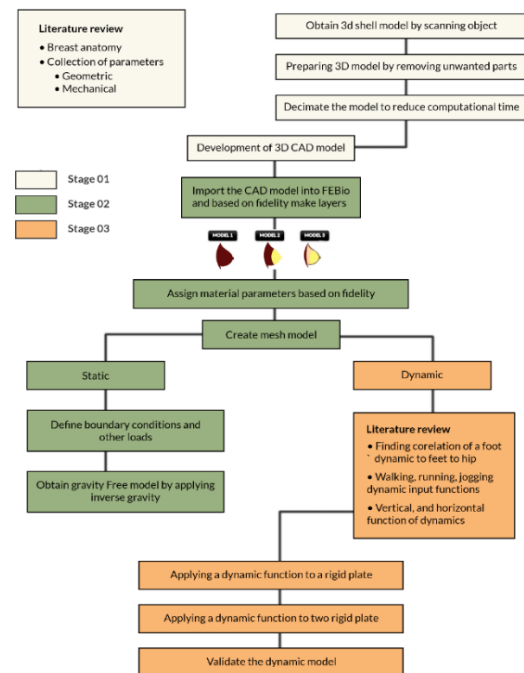


Figure 1: Methodology

Stage 02 entailed creating two CAD models that are more detailed, ranging in fidelity from low

to high, and include various material characteristics for the tissue layers. The FEBio program was used to complete material assignment. In the second stage inverse gravity method was used to create the gravity-free model, which is essential for precise biomechanical simulations. After that, analysis was conducted for both static and dynamic situations for various dynamic functions. Figure 1 shows the methodology of the research.

3.1. Development of CAD model

A methodical procedure was used in the methodology to create a 3D CAD model of the woman's upper torso. First, the upper torso of a lady dummy's physical attributes were recorded in three dimensions using the portable 3D scanner EinScan Pro as shown in Figure 2(a). Next, the Blender software cleaned up the 3D model, made sure it was accurate, and turned it into a solid model as shown in Figure 2(b). After that, a mesh model was created using Meshmixer software, which includes surface smoothing, cleaning, and refining for additional analysis. The mesh model's resolution is gradually decreased in order to maximize computer power, balancing the need to retain relevant detail with the need for computational efficiency. That finalized model is shown in Figure 2(c).

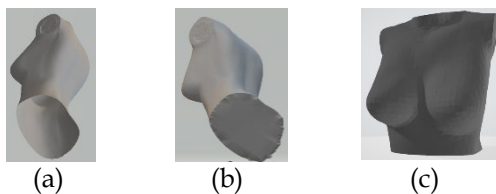


Figure 2: CAD modeling: (a) scanned raw 3D model, (b) cleaned 3D solid model obtained using Blender software, and (c) refined 3D CAD model using Meshmixer software

3.2. Layered models based on fidelity

The development of models involved a progressive increase in fidelity to capture the biomechanical behavior of the woman's upper torso comprehensively.

Model 1 which is shown in Figure 3(a) employs a low-fidelity approach, treating the entire CAD model as a single material for analysis under static and dynamic conditions. Model 2 which is shown in Figure 3(b) introduces a detailed model by dividing the CAD model into a rigid thorax and a flexible woman's upper torso, offering a more accurate representation of

skeletal and soft tissue allowing for a detailed analysis of each component's specific mechanical properties and behaviors.

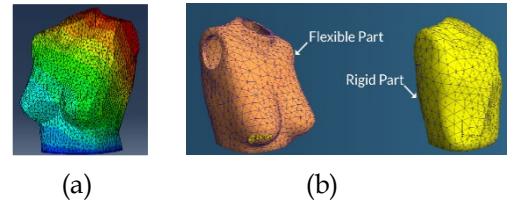


Figure 3: Fidelity of models: (a) low fidelity and (b) high fidelity

3.3. Gravity-free model development using inverse gravity method

The difficulty of integrating realistic gravity-induced stresses into a scanned 3D model of a woman's upper torso was addressed by the process of creating a free gravity model. The model's preserved distorted shape has no stress when it was imported into CAD software. An inventive solution to this problem was to apply an inverse gravity effect to bring the model's original shape back. After that, the model was exported as a .odb file with stress-free mesh data. Gravity effects are added when the .odb file is reimported, enabling a comparison of distorted shapes.

These are the steps for obtaining a gravity-free model:

- Step 1: Import the CAD model
- Step 2: Apply inverse gravity
- Step 3: Export as .odb file and reopen

3.4. Dynamic Analysis

The dynamic function in Eq. (1) was derived from a graph in the research paper Cheuk et al. (2021), which quantifies dynamic vertical breast displacement, crucial for seamless molded bra design. The graph is shown in Figure 4.

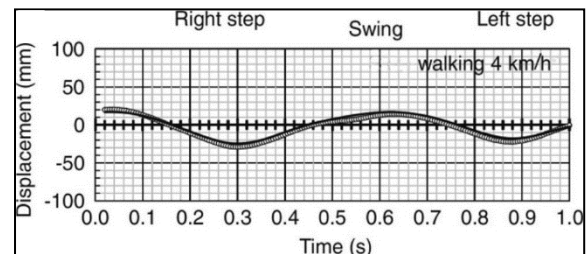


Figure 4: Reference data set used to develop the dynamic function (Cheuk Wing Lee et al., 2021)

$$D_{\text{vertical}} = 22.0375 \cos(627.178 t) - 6.353 \quad (1)$$

The dynamic function development involves analyzing vertical hip displacement (D_{ver}) data

during running. Parameters such as amplitude (A), frequency (f), decay rate (b), and baseline displacement (C) were identified from the dataset, with a maximum displacement of 23 mm. This concise process captured the key steps in creating the dynamic function from the provided dataset and developed function is in Eq. (2)

$$D_{\text{vertical}} = A \cdot \cos(2\pi f t) e^{-bt} + C \quad (2)$$

Where,

- D_{vertical} - Vertical dynamic displacement
- A - Amplitude of the displacement (Eq. (3))
- t - Time
- f - Frequency of displacement function
- b - Decay rate of the impact due to the treadmill surface characteristics
- C - Baseline displacement at the foot during treadmill running

$$A = k W P H \quad (3)$$

Where:

- K - Constant. = $1.85E^{-03}$
- W - Weight of the subject
- P - Tissue percentage
- H - Height

4. Result and Discussion

4.1 Inverse gravity simulation

The inverse gravity simulation incorporates the Mooney-Rivlin material model with parameters $C1 = 0.5 \text{ MPa}$, $C2 = 0.5 \text{ MPa}$, and a density of 1000 kg/m^3 . This model is applied to address deformation caused by gravity in scanned 3D models. The simulation involves restoring the model's unreformed shape by applying an inverse gravity effect, enhancing the accuracy of biomechanical predictions for women upper torso deformation scenarios as shown in Figure 5.

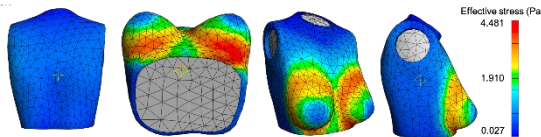


Figure 5: Inverse gravity simulation for static conditions

4.2 Parametric study

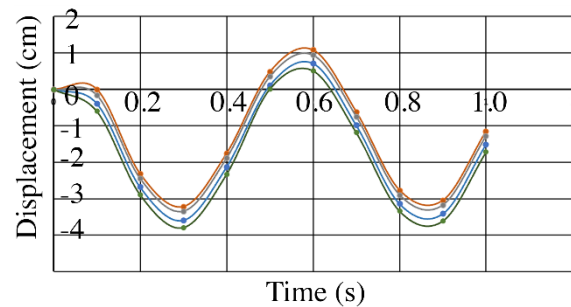
The parametric study involves a systematic exploration of breast biomechanics by varying key factors outlined in Table 1. Four distinct breast models are considered, differing in

volume, material properties (ranging from stiff to soft), running velocity (2.5 m/s to 5.5 m/s), and athlete height (155 cm to 185 cm). This comprehensive approach allows us to analyze the interactive effects of these parameters on breast displacement during running, providing valuable insights for optimizing sports bra design tailored to diverse physiological characteristics and activities. A summary of parametric study parameters is shown in Table 1.

Table 1: Parametric properties of 16 models

	Model 1		Model 2		Model 3		Model 4	
Volume (mL)	987		1192		1336		1546	
Material (kPa)	C_{10} = 9	C_{01} = 8	C_{10} = 7	C_{01} = 7	C_{10} = 5	C_{01} = 5	C_{10} = 3	C_{01} = 3
	Stiff		Mean 1		Mean 2		Soft	
Velocity (m/s)	2.5		3.5		4.5		5.5	
Height (cm)	155		165		175		185	

(1) The displacement-time graph shown in Figure 6 illustrates the dynamic behavior of breast models with varying volumes during a simulated running scenario. Smaller volumes exhibit minimal displacement, while larger volumes result in more pronounced oscillations. This information is crucial for understanding breast biomechanics and optimizing sports bra design for diverse breast sizes and activities.



- 987 ml
- 1192 ml
- 1336 ml
- 1546 ml

Figure 6: Time-displacement variation for different women's upper torso volumes

(2) The displacement-time graph shown in Figure 7 depicts the dynamic response of breast models with different material properties during simulated running. Softer materials show higher displacement, while harder materials exhibit reduced oscillations. Understanding these variations is essential for tailoring sports bra designs to provide optimal support and comfort based on individual preferences and activities.

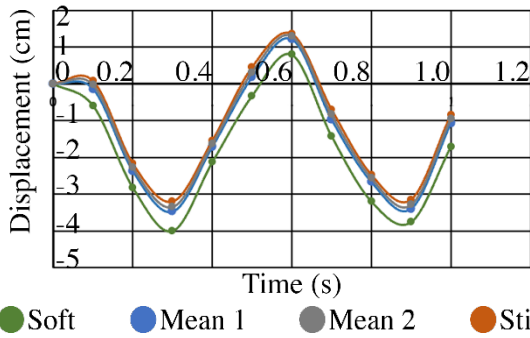


Figure 7: Time-displacement variation for different women's upper torso stiffnesses

(3) The displacement-time graph shown in Figure 8 depicts the dynamic responses of breast models at different running velocities. Varied speeds result in distinct displacement patterns. Notably, higher frequencies correlate with more substantial oscillations, indicating that running speeds directly influence breast movement. This insight is pivotal for sports bra design tailored to accommodate different running intensities and frequencies.

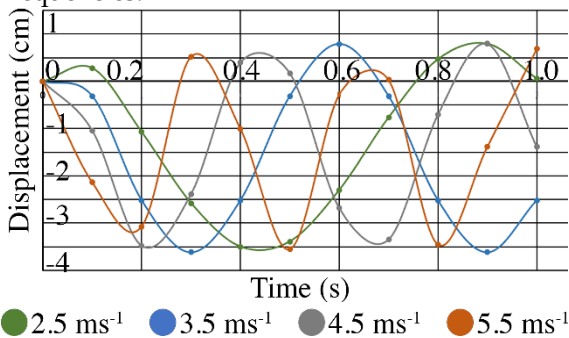


Figure 8: Time-displacement variation for different velocities

(4) The displacement-time graph in Figure 9 illustrates the dynamic response of breast models at varying athlete heights during simulated running. Higher athlete height correlates with increased breast displacement. This insight is crucial for designing sports bras that accommodate diverse body types, ensuring optimal support and comfort across different heights.

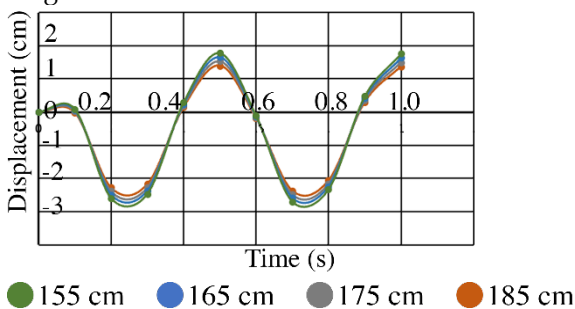


Figure 9: Time-displacement variation for different heights of athlete

5. Conclusions

The comprehensive study yields crucial insights for precise garment design. Conclusions reveal the inadequacy of simple models, emphasizing the necessity for detailed, adaptable garment elements addressing dynamic factors like breast volume, stiffness, and height variations.

(1) The study firmly proves that the simple model inadequately depicts women's upper torso behaviour. This highlights the urgent necessity for precise and comprehensive models to capture the complexities accurately.

(2) The advanced two-layer model, combining flexible and rigid components, accurately simulates women's upper torso actions in static and dynamic scenarios. This emphasizes the necessity of using such detailed models to capture female upper body biomechanics precisely.

(3) Breast volumes of 987 ml to 1546 ml cause 1.1 cm to 3.8 cm displacements in a woman's life stages. Adaptable garment parts are crucial for comfort. Dynamic adjustments for varying volumes are essential. Breast stiffness changes lead to 1.4 cm to 4 cm displacements. Specialized garment elements accommodating material variations ensure superior comfort. Higher velocities in activities increase cycles; quality damping materials in garments are vital. Heights of 155 cm to 185 cm result in 1.8cm to 2.8cm displacements, suggesting the potential for a single garment component to address variations across most heights.

References

- Liang, R., Yip, J., Yu, W., Chen, L. and Lau, N. M. L. (2019) 'Numerical simulation of nonlinear material behaviour: Application to sports bra design', *Materials & Design Journal*, 183, p108177.
- Sun, Y., Chen, L., Yu, W., Lau, N. and Jiao, W. (2019) 'Optimization method for the determination of Mooney-Rivlin material coefficients of the human breasts in-vivo using static and dynamic finite element models', *Journal of The Mechanical Behavior of Biomedical Materials*, 90, p615-625.
- Cheuk-wing Lee, Kit-lun Yick, Sun-pui Ng & Joanne Yip (2022) 'Analysis of dynamic vertical breast displacement for the design of seamless moulded bras', *The Journal of The Textile Institute*, 113(4), p637-646.

Development and Characterization of Sustainable Mortar with Sugarcane Bagasse Ash

Naweendra J.A.L.N., Udayanga R.G.I.*, and Buddika H.A.D.S.

Department of Civil Engineering, Faculty of Engineering, University of Peradeniya, Sri Lanka

* e17354@eng.pdn.ac.lk

Keywords: Compressive strength, Mortar, Workability, Sugar-cane bagasse ash, Sustainable

Abstract

This study explores Sugarcane Bagasse Ash (SCBA) as a partial substitute for ordinary Portland cement (OPC) in mortar production to mitigate greenhouse gas emissions. SCBA, an abundant agricultural waste, shows promising pozzolanic properties. Optimal SCBA content enhances mortar performance without compromising structural integrity. The research focused on the comprehensive characterization of SCBA, including chemical composition and pozzolanic properties. For this purpose, specimens containing 5, 10, 15, 20, and 25% SCBA in addition to a control specimen were prepared to assess the material's impact on key properties such as workability, and compressive strength of mortar at both 7 and 28 days. The results indicated that improvements in strength in mortar are observed as compared with the control sample when cement was replaced with bagasse ash at 5%. It was also found that the addition of SCBA in the replacement percentage reduced the workability. Implementing SCBA in mortar could transform construction practices towards sustainability.

1. Introduction

Cement is commonly used as a binder in mortar because it offers the necessary strength and durability. In more than 80 countries, Ordinary Portland Cement (OPC) is the most commonly used type of cement. A significant portion of CO₂ emissions comes from the production of cement; one ton of OPC produces one ton of CO₂, seriously degrading the environment. The primary oxide in OPC is carbon dioxide (CO₂), which is released when limestone (CaCO₃) is heated in the cement industry to produce calcium oxide (CaO). CO₂ is the primary cause of global warming. The CO₂ gas is roughly estimated at 5 to 7% by weight of the CO₂ emissions (total) and gases like CO₂ go into the atmosphere by the process of clinker manufacturing. In order to reduce or minimize the global warming problem, supplementary cementitious materials (SCM) are nowadays used as partial replacement of cement to

produce concrete of requisite strengths. Nowadays, a variety of agricultural wastes, including fly ashes and bagasse ash, are used to make affordable, eco-friendly concrete. In order to reduce the amount of expensive cement used in the manufacture of concrete mortar while maintaining the intrinsic qualities of concrete, several researchers have created substitute binders. Different cementitious materials like metakaolin, fly ash, slag, rice husk ash, silica fume, etc. have also been used as partial replacements for cement. Sugarcane Bagasse ash, an agricultural waste product has also been recently used as SCM in mortar mixes as a partial replacement of cement as it is cheap and makes the concrete sustainable. The compressive strength and other properties of concrete can be improved by the utilization of SCBA as agro waste pozzolanic SCM in the concrete industry.

Around the world, the total global production of sugarcane bagasse was found approximately 1661 million tons in the year 2009. In the year 2011, the total global production of sugarcane bagasse was estimated at 1794 million tons. The principal disposal methods for SCBA are dumping to landfill, or mixing with mill mud and returning to the cane field as a low-level fertilizer. Burning SCB at a sugar mill to produce co-generated heat and energy is what causes SCBA. A great deal of study has been done on the use of SCBA waste in the concrete industry; the majority of this research has been done on SCBA as a filler or as a substitute for cementitious materials. The pozzolanic property of SCBA gets improved due to the presence of less amount of carbon content, silica being in the amorphous state, and possessing a high specific surface area. However, the usefulness of SCBA as an SCM varies depending on the type of material used. The introduction of SCBA by partial replacement of cement in different proportions has shown improved concrete properties like the compressive strength of cement mortar at the hydration process. The microstructure characterization is practiced to perceive the presence of pozzolanic minerals

state and their forms present in SCBA using XRF, XRD, and SEM analysis. To ascertain the most efficient use of this waste source, it is crucial to assess the chemical and physical properties of each source of SCBA separately. This paper investigates the chemical and physical effects that local co-generation plant SCBA has on mortars.

2. Literature review

2.1 Chemical composition of SCBA

There is no fixed chemical composition for SCBA. Various research papers state different chemical compositions.

Table 1: Chemical composition of SCBA

Chemical components	Reddy, et al. (2015)	Travis et al. (2020)	José, et al. (2020)
SiO ₂	78.34	71.36	63.10
Fe ₂ O ₃	3.61	3.79	4.59
Al ₂ O ₃	8.55	11.2	7.56
CaO	2.15	6.83	8.28
MgO	-	1.56	4.54
Na ₂ O	0.12	-	1.24
K ₂ O	3.46	-	5.43
MnO	0.13	-	-
TiO ₂	0.50	-	-
P ₂ O ₅	1.07	-	2.13
LOI	0.42	-	3.10

So, it is clear that SCBA does not have a fixed chemical composition. There can be several reasons for this. Due to different methods of collecting SCBA, source of SCBA, and incineration method, the chemical composition of SCBA is not always the same.

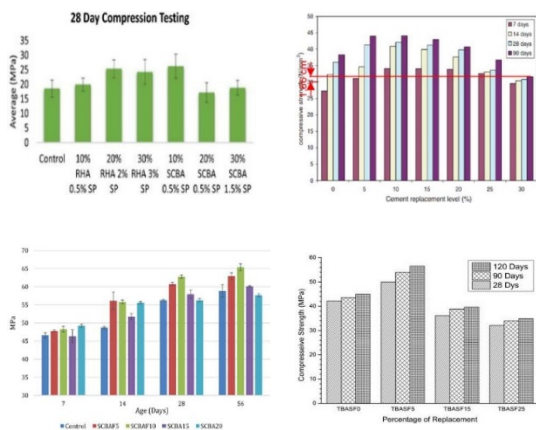


Figure 2: Variation of compressive strength with SCBA replacement, (a) Ganesan, et al. (2007), (b) Travis, et al. (2020), (c) Elisabeth, et al. (2017), (d) Santhosh, et al. (2020)

2.2 Durability properties of concrete with SCBA

According to the past literature, SCBA has been found to improve the durability of concrete by reducing chloride ion permeability, water absorption, and corrosion potential, and enhancing resistance to sulfate attack. These properties make it beneficial in marine, coastal, and sulfate-rich environments. Ganesan, et al. (2007) indicate that chloride permeability is considerably reduced by partial replacement of OPC with SCBA.

2.2.1 Chloride permeability

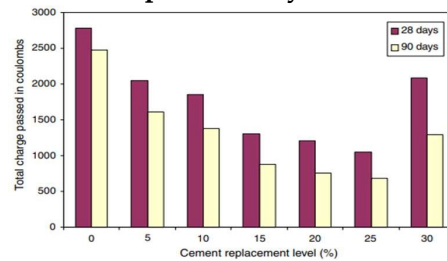
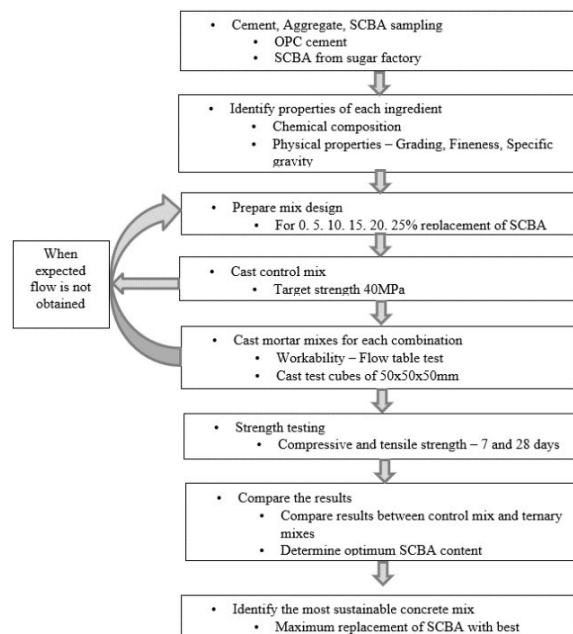


Figure 4: Variation of chloride permeability of concrete with SCBA according to Ganesan, et al. (2007)

Prinya, et al. (2020) mentioned that the pozzolanic reaction of the ingredients in SCBA is responsible for the enhancement of concrete's chloride resistance. The reason for this is that concrete containing SCBA had more hydration products, which allowed a larger quantity of chloride to be absorbed by the increased surface area of reaction products. In addition, the replacement of the high volume SCBA led to the production of finer pores and discontinuity of the pores, which led to reduced chloride permeability.

3. Methodology



4. Results and Discussion

Six mortar mixes were made by replacing cement with SCBA including a control (0%), 5%, 10%, 15% 20%, and 25% by mass while maintaining the water binder ratio the same (Tab4.1). The same amount of sand, water, and 2% superplasticizer were used to prepare all mixes.

Table 2: Mix proportions of cement-SCBA mortar

SCBA (%)	0	5	10	15	20	25
SCBA (g)	0	22.6	45.2	67.8	90.4	113
Cement (g)	452	429.4	406.8	384.2	361.6	339
Fine aggregate (g)	1244	1244	1244	1244	1244	1244
Water (ml)	198	198	198	198	198	198
2% SP (ml)	9	9	9	9	9	9

4.1 Effect of SCBA on Workability

In this study, two types of superplasticizers (SP) were used. Fig.4.1 shows the variations of flow values in different concrete mixes with different proportions of SCBA in mortar mixes with superplasticizer type 1 (Polycarboxylic-based admixture) and type 2 (Sulphonated naphthalene-based admixture). The superplasticizer dosage and water content were kept constant in all six mixes. The workability of concrete is observed to decrease with an increase in the percentage of SCBA. Thus, the addition of SCBA in the concrete mix results into increase in the water demand to attain the required workability of concrete. The superplasticizer type 2 gave a much higher flow value than superplasticizer type 1 in different SCBA replacement levels except in the control mix.

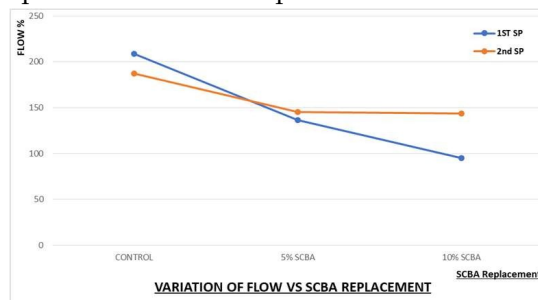


Figure 5: Variation of flow value at different proportions of SCBA.

The mortar mixes did not show a flow at 10% and 15% SCBA replacement levels with SP1 and

SP2 respectively. It may be due to the high water absorption capacity of SCBA. So, a water absorption test (4.2) was done for the SCBA. Then, prepare a new mix design by adding an additional water amount of 100% to mixes referring to test results. Fig.4.2 shows the variations of flow values of new mortar mixes (after adding additional water) for different proportions of SCBA replacement with superplasticizer type 2. The flow value of mortar mixed with additional water is observed increasing with increase in percentage of SCBA.

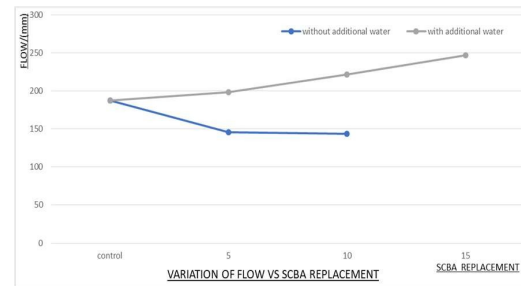


Figure 6: Variation of flow value at different proportions of SCBA after adding additional water.

4.2 Water absorption test

This test was carried out to measure the water absorption capacity of SCBA. Table 4.2 shows the test results. From that, it can be clearly seen that SCBA has a high water absorption capacity of 192%.

Table 3: Water absorption test results

Dry SCBA (g)	Wet SCBA (g)	Absorbed water (g)
2.125	6.975	4.850
2.145	6.278	4.133
2.304	6.093	3.789
2.426	6.958	4.532
2.391	7.020	4.629

4.3 Compressive strength

The results of average compressive strength (CS) at 7 days and 28 days for mortar mixes with SP1 as shown in Figure 4.3. It is evident from Figure that the CS of the control mix at 7 days is 28.86 N/mm² whereas the CS of mortar mix with 5% replacement at 7 days is 29.64 N/mm² respectively. Therefore, the CS of mortar mix at 5% replacement of cement by SCBA was observed almost similar to the control mortar mix. However, there was a gradual decrease in CS beyond 5% replacement of cement by SCBA at 7 days and from 5% replacement of cement at 28 days. The CS of the control mix at 28 days is 40.05 N/mm² whereas the CS of mortar mix with 5% and 10% replacement at 28 days are 38.45 N/mm², and 35.66 N/mm² respectively. It shows

that CS drastically reduced with the increase of cement replacement by SCBA. The reduction in compressive strength development especially at later stages due to the low reactivity of silica (SiO_2) and simultaneous reduction in CaO contents. This decrement of the strength for replacement of cement by SCBA may be due to inadequate adhesion of bagasse ash with the surface of aggregate and cement.

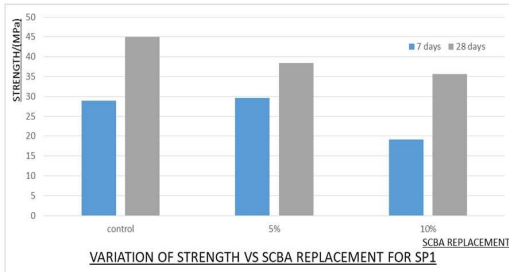


Figure 7: Variation of compressive strength for mortar mixes with SP1 at 7, 28 days

The Fig.4.4 shows the results of average compressive strength (CS) at 7 days for mortar mixes with SP2. It can clearly see that CS of all mortar mixes are reduced with increase of cement replacement by SCBA. The CS of the control mix at 7 days is 29.12 N/mm² whereas CS strength of 5%, 10%, and 15% replacement of cement by SCBA are 27.54 N/mm², 23.47 N/mm² and 17.71 N/mm² respectively. The 5%, 10%, and 15% of cement replacement show 5.4%, 14.8%, and 24.5% CS reduction respectively.

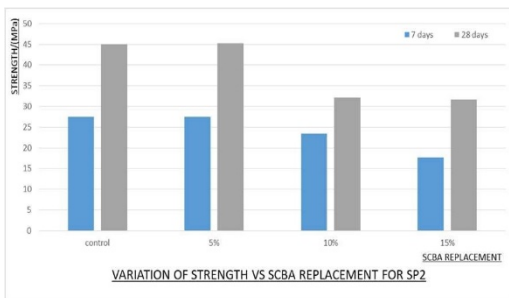


Figure 8: Variation of compressive strength for different mortar mixes with SP2 at 7 days

4.4 Effect of additional water

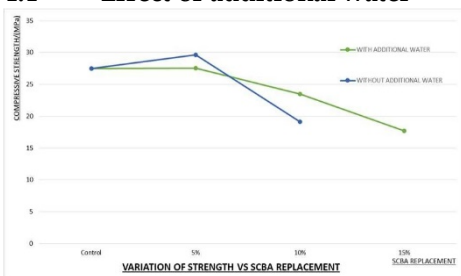


Figure 9: Variation of strength of mix with and without additional water.

Usually adding water into a mortar mix reduce its strength because it directly effects for the w/c ratio. But here such reduction could not detected.

5. Conclusions

Replacement of SCBA has reduced the workability of mortar. Superplasticizers can affect the workability and the strength irrespective of SCBA replacement. The strength of mortar with SCBA is initially increase with SCBA replacement but eventually decrease. Reduction of workability can be dealt with with additional water and maintain a reasonable flow. Such addition of water will not compromise the strength of the mortar considerably in fact it will improve the strength in high SCBA replacement by providing proper compaction.

References

- Prabhath, N., Kumara, B.S., Vithanage, V., Samarathunga, A.I., Sewwandi, N., Damruwan, H.G.H., Lewangamage, S. and Koswattage, K.R. (2023) 'Investigation of Pozzolanic Properties of Sugarcane Bagasse Ash for Commercial Applications', ACS omega, Available at: <https://doi.org/10.1021/acsomega.2c07844>.
- Jha, P., Sachan, A.K. and Singh, R.P. (2020) 'Agrowaste sugarcane bagasse ash (ScBA) as partial replacement of binder material in concrete', Materials Today: Proceedings, Available at: <https://doi.org/10.1016/j.matpr.2020.09.751>.
- Cordeiro, G.C., Toledo Filho, R.D., Tavares, L.M. and Fairbairn, E.M.R. (2012), 'Experimental characterization of binary and ternary blended-cement concretes containing ultrafine residual rice husk and sugar cane bagasseashes', Construction and Building Materials, [online] 29, pp.641–646.
- Ganesan, K., Rajagopal, K. and Thangavel, K. (2007) 'Evaluation of bagasse ash as supplementary cementitious material', Cement and Concrete Composites, [online] 29(6), pp.515–524. Available at: <https://doi.org/10.1016/j.cemconcomp.2007.03.001>.
- Arif, E., Clark, M.W. and Lake, N. (2017) 'Sugar cane bagasse ash from a high-efficiency co-generation boiler as filler in concrete', Construction and Building Materials, 151, pp.692–703. Available at: <https://doi.org/10.1016/j.conbuildmat.2017.06.136>.
- Jahanzaib Khalil, M., Aslam, M. and Ahmad, S. (2021) 'Utilization of sugarcane bagasse ash as cement replacement for the production of sustainable concrete - A review', Construction and Building Materials, 270, p. 121371. Available at: <https://doi.org/10.1016/j.conbuildmat.2020.121371>.

Improving the Accuracy of Numerical Predictions of Wind Interactions with Rectangular Tall Buildings

Hemachandra K.R.T.*, Herath H.M.N.M., and Wijesundara K.K.

Department of Civil Engineering, Faculty of Engineering, University of Peradeniya, Sri Lanka

* e17111@eng.pdn.ac.lk

Keywords: CAARC model, Inflow boundary conditions, LES, Structured mesh, Wind interactions

Abstract

As bluff bodies to wind flow, high-rise buildings experience flow separation and wake generation, which results in pressure differences. The objective of this study is to use the CAARC model and large eddy simulation to create a numerical model to simulate wind interaction with tall, rectangular buildings. To improve accuracy, the study uses a blocked mesh system with strategically placed finer and coarser meshes. The model was validated by numerical findings that were verified against wind tunnel tests. The study emphasizes how important it is to precisely simulate inflow boundary conditions because they have an impact on the pressure distribution on the windward side of the building.

1. Introduction

High-rise buildings have become a popular feature in worldwide, as they meet the growing needs and desires of urbanization within limited space. However, as buildings reach greater heights, the influence of wind around buildings becomes more pronounced. The accurate prediction of wind-induced responses on high-rise buildings provides a safe and occupational comfortable design for the construction. Conventional methods like code-based practices for predicting wind-induced responses are conservative and unreliable for modern complex buildings. Wind tunnel tests are widely adopted but have high costs and time consumption. With advancements in computational power and affordability, computational fluid dynamics (CFD) has gained popularity for fluid flow analysis.

Therefore, the main objective of this study is to develop a computationally optimized numerical model to simulate the wind interaction of rectangular tall buildings by employing the standard CARRC building.

2. Literature review

Numerous studies have been conducted to numerically simulate wind behavior around tall buildings, primarily using the Commonwealth Advisory Aeronautical Council (CAARC) building due to an experimental data base for that building to compare the numerical results. Techniques like Reynolds-averaged Navier-Stokes (RANS) and Large Eddy Simulation (LES) are used to accurately represent and predict turbulent flow phenomena. Zhang et al., (2015) have expressed LES is ideal for studying complex flows with significant unsteadiness, while RANS is used for simpler flow cases with computational efficiency.

The fluid domain must be discretized into meshes using RANS, LES, or other hybrid techniques to solve flow governing equations. Two types of meshes are used: structured and unstructured, but unstructured meshes have lower accuracy compared to structured meshes. Due to the simple geometry of the CAARC building and to obtain the most accurate results, Braun and Awruch (2009) and Koliyabandara et al. (2018) used the structured mesh for modelling the fluid domain while Huang et al. (2007), and Zhang et al. (2015) had used the unstructured mesh due to its advantages such as reducing the total number of nodes and ability to assemble freely within the computational domain. Alwis et al. (2022) utilized a strategic approach by dividing the fluid domain into multiple blocks with varying mesh sizes, instead of having a structured mesh throughout the computational domain with the same growth rate.

According to findings from Huang et al. (2007), the inflow velocity profile greatly affects the mean pressure coefficient distribution and the turbulence intensity profile affects the rms pressure coefficient distribution. Therefore, accurately modelling the inflow velocity profile and turbulence intensity profile are vital to obtain good correlation between numerical and experimental results.

3. Methodology

According to the conducted literature review, the methodology was set to develop a computationally optimized numerical model to simulate the wind interaction of buildings.

3.1 Modelling the Fluid Domain

The computational domain, the region around a building where a flow solution is required, was chosen as $34B \times 23B \times 2.75H$, in line with literature reviews. Here B is 30m and H is 183m.

This research focuses on the rigid analysis of a building, modeling it as a cavity within a domain. The computational domain is covered by four blocks with varying mesh sizes, increasing as blocks move away from the building boundary. Structured mesh is used for meshing all blocks, and the CUTCELL assembly technique in ANSYS FLUENT is adopted to avoid hanging nodes and maintain smooth transitions between block zones. Mesh refinement is considered for the leeward side of the building in the present study, as most eddies are formed on the leeward side.

3.2 Boundary Conditions

The computational domain, the region around a building where a flow solution is required, was chosen as $34B \times 23B \times 2.75H$, in line with literature reviews. Here B is 30m and H is 183m.

- 1) Inflow velocity profile is a form of power law as shown in equation (1) with $\alpha = 0.28$

$$\frac{u}{u_H} = \left(\frac{z}{z_H}\right)^\alpha \quad (1)$$

Where u_H is the wind speed at the building height which was 15 m/s in NEA (a) study.

- 2) No-slip boundary condition at the ground surface
- 3) Atmospheric pressure at the outlet
- 4) Zero normal velocity flux at the side walls and top surface which flow is parallel to the surfaces.

The fluctuating velocity algorithm was selected as Spectral Synthesizer which was available in ANSYS software. The Reynolds number was kept as 4.6×10^4 based on the building width B and u_H in present study.

The simulation was performed in a workstation having 32 CPUs and 64 GB of memory for 150s total duration with 0.1s time steps.

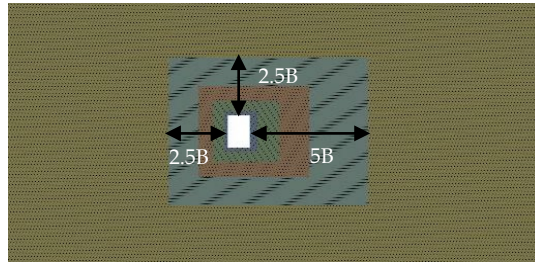


Figure 1: Plan view of mesh scheme 1

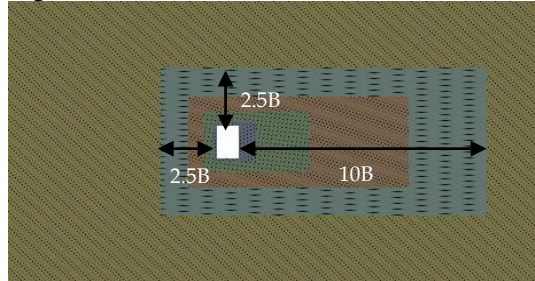


Figure 2: Plan view of mesh scheme 2

4. Results and Discussion

The mean pressure coefficients around the building perimeter at $2/3$ height of the building were compared with the wind tunnel test measurements. Results are plotted along the wall perimeter and values are established in the corners of the building according to the parameter called (x/L) as shown in Figure 3, where L is the perimeter of the building.

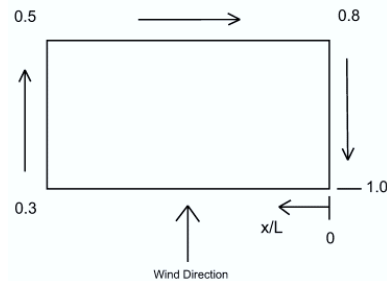


Figure 3: Variation of X/L along the building

4.1 Optimized computational domain

Mesh schemes 1 and 2 were simulated in ANSYS software and results were analysed to identify the optimized computational domain. Figures 4 and 5 show the mean pressure coefficient distribution around the building perimeter at $2/3$ height of the building for mesh schemes 1 and 2 respectively. Figure 6 represents the percentage deviation of the numerical results from experimental results.

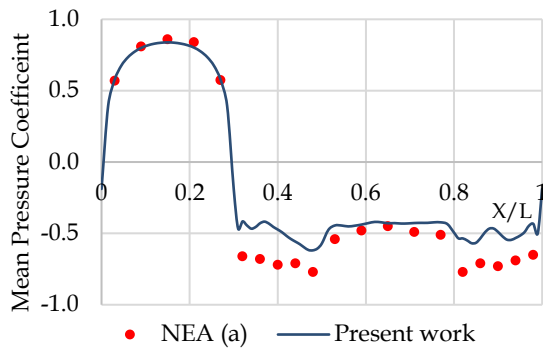


Figure 4: Mean pressure coefficient variation in mesh scheme 1

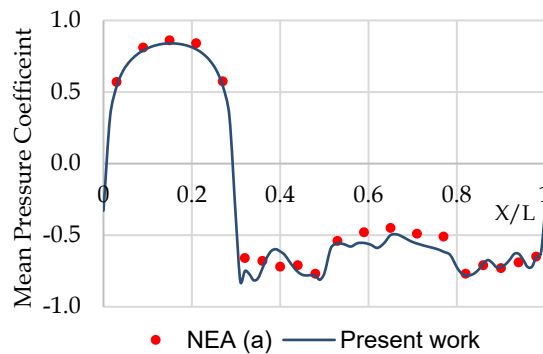


Figure 5: Mean pressure coefficient variation in mesh scheme 2

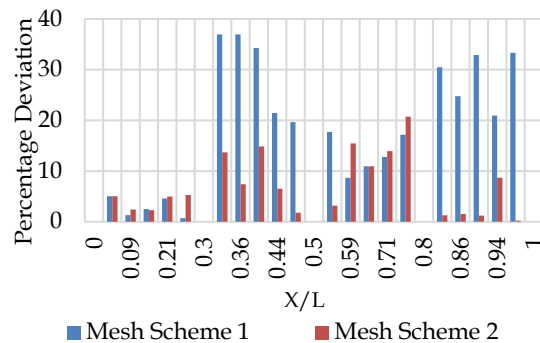


Figure 6: Percentage deviation of the mean pressure coefficient

The experimental results show that mesh scheme 2 has less deviation than mesh scheme 1, with a percentage deviation of less than $\pm 21\%$ while mesh scheme 1 has a percentage deviation of $\pm 37\%$. Although mesh refinement was done for the leeward side, Figure 6 shows the pressure result improvement on side walls instead of leeward side. The pressure results show improvement on side walls, with a percentage deviation of side wall pressure reduced from $\pm 37\%$ to $\pm 15\%$. This may be due to the free development of the boundary layer around the building. In mesh scheme 1, the mesh block dimensions on the leeward side are $B/3$, $2B/3$, $4B/3$, and $8B/3$, with a total leeward side length of $5B$, only focused on modelling the eddies within $5B$ distance from the building wall. This

restricts the development of the boundary layer on side walls. In contrast, mesh scheme 2 has leeward side blocks with dimensions of $2B/3$, $4B/3$, $8B/3$, and $16B/3$ with a total leeward side length is $10B$, solving the more turbulence in the leeward side, allowing the boundary layer to develop without restriction.

This can be further explained using Figures 7 and 8 which depict the streamline distribution at $2/3$ height of a building for mesh schemes 1 and 2, respectively. The boundary layer formed due to flow separation has a flattened shape in Figure 7, while Figure 8 shows a volume-up shape on both sides. This indicates a restriction for freely developing the boundary layer in mesh scheme 1 with corresponding leeward side mesh arrangement, indicating that leeward side mesh refinement significantly affects side wall pressure distribution. Furthermore, Figure 8 shows the asymmetric eddies formation on the leeward side which is the same as the actual scenario.

When comparing the mesh scheme 1 and 2, mesh scheme 1 provides a better prediction in leeward side pressure distribution with less than $\pm 18\%$ deviation. But mesh scheme 2 provides better prediction on side wall pressure distribution with less than $\pm 15\%$ deviation. Accurately predicting the side wall pressure distribution is important when studying phenomena like vortex shedding. Because vortex shedding causes the building movement across wind direction by resulting pressure difference on side walls. In that case, the use of mesh arrangement same as mesh scheme 2 will help to monitor the accurate prediction of wind induced forces on the structure.

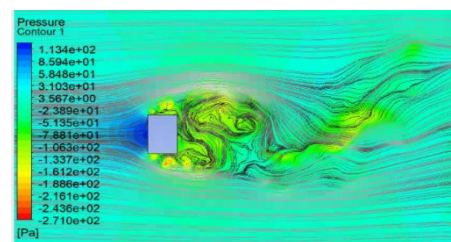


Figure 7: Streamlines distribution at $2/3$ height of the building in mesh scheme 1

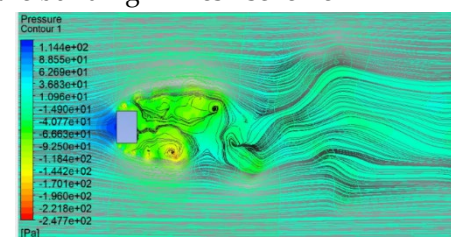


Figure 8: Streamlines distribution at $2/3$ height of the building in mesh scheme 2

4.2 Modelling the inflow velocity profile

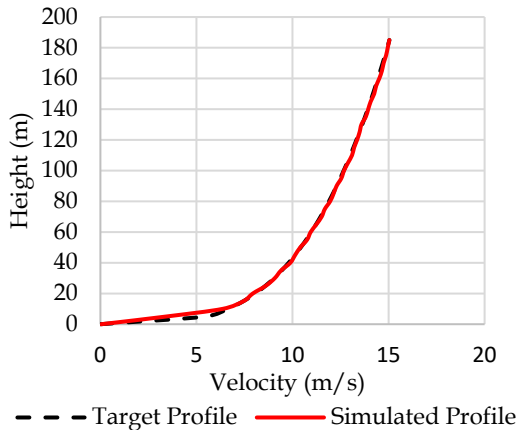


Figure 9: Target and simulated inflow velocity profile

Figure 9 shows a similarity between the target power law velocity profile and the simulated velocity profile, Huang et al. (2007) concluded that the mean velocity profile significantly influences the mean pressure coefficient on the building. Figure 6 shows similar behavior on the windward side for both mesh schemes, with a percentage deviation less than $\pm 5.5\%$ due to accurate modelling of the inflow velocity profile. Therefore, accurate simulation of the inflow velocity profile will help to obtain a more similar prediction to the actual scenario.

5. Conclusions

The study utilized a special mesh modelling method to optimize numerical simulations for investigating wind interaction around tall buildings. The following are the key findings from the current study.

- The modelling of inflow velocity profile similar to the experimental test was resulted with better correlation in windward side mean pressure coefficient distribution independent from time steps and durations that used and the leeward side mesh block arrangement which percentage error deviation was less than $\pm 5.5\%$. Therefore, accurately modelling the inflow velocity profile can be implemented as a check for this kind of simulation.
- The pressure distribution on the side walls of the building was highly sensitive for the extension of the mesh block on the leeward side since the extended arrangement allowed to freely develop the boundary

layer after flow separation. Therefore, the deviation of the pressure distribution on the side wall was reduced from $\pm 37\%$ to $\pm 15\%$ for mesh schemes 1 to 2.

- The study suggests that the mesh size in LES should be fine enough to solve over 80% of turbulence kinetic energy for accurate results. Improvements from mesh schemes 1 to 2 were confirmed, and the initial estimate for the mesh size in a block next to a building wall should be 1/5th of the integral length scale to model more than 80% of turbulence kinetic energy.
- The mesh arrangement in scheme 2 is crucial for analysing wind interaction under vortex shedding, as it accurately predicts pressure distribution on side walls. Block sizes from 1 to 4 should have minimum dimensions of $2B/3$, $4B/3$, $8B/3$, and $16B/3$, with a mesh gradient that needs to be approximately maintained as 2.0 to obtain the side wall pressure improvement.

References

- Alwis, V. A. U., Weeraratne, P. H. T. D. and Wijesundara, K. K. (2022) 'Rigid and Aeroelastic Analysis of Wind Induced Flow Behavior Around Unscaled Tall Buildings using Numerical Techniques', *Journal of Wind Engineering & Industrial Aerodynamics*.
- Braun, A.L. and Awruch, A.M. (2009) 'Aerodynamic and aeroelastic analyses on the CAARC standard tall building model using numerical simulation', *Computers & Structures*, 87(9-10), pp. 564-581.
- Huang, S., Li, Q.S. and Xu, S. (2007) 'Numerical evaluation of wind effects on a tall steel building by CFD', *Journal of Constructional Steel Research*, 63(5), pp. 612-627.
- Melbourne, W.H. (1980) 'Comparison of measurements on the CAARC standard tall building model in simulated model wind flows', *Journal of Wind Engineering and Industrial Aerodynamics*, 6(1-2), pp. 73-88.
- Zhang, Y., Habashi, W.G. and Khurram, R.A. (2015) 'Predicting wind-induced vibrations of high-rise buildings using unsteady CFD and Modal Analysis', *Journal of Wind Engineering and Industrial Aerodynamics*, 136, pp. 165-179.

Shear Strength of Plain Concrete Made of Recycled Polypropylene Waste Plastic as A Partial Replacement of Coarse Aggregate (A Comparison Between Experimental, Analytical & Numerical Approaches)

Thilakarathna, K.G.D.I.H.*, Weragama, W.A.R.U., and Bandara, C.S.

Department of Civil Engineering, Faculty of Engineering, University of Peradeniya, Sri Lanka

*hashanthilakarathna24@gmail.com

Keywords: Plain concrete, Plastic aggregates, Polypropylene waste, Shear strength

Abstract

This study inspects the potentialities of using polypropylene (PP) plastic waste as coarse aggregate in concrete. It mainly focuses on evaluating the shear strength of plastic aggregate concrete (PAC). The experimental work includes a varying percentage of PP as 10%, 20%, and 30% of the volume of natural coarse aggregate. PAC was weaker in both compression and shear than natural aggregate concrete (NAC). However, the relationship between push-off shear strength (f_{cu}) was similar and $v_{po} = 0.6 \sqrt{f_{cu}}$ for both PAC and NAC.

- The low modulus of elasticity of PPA and weak interfacial transition zone (ITZ) in PAC result in unfavorable effects on the shear strength.
- In general, concrete is a brittle material. With the incorporation of PPA, the strain bearing capacity increases, and a ductile behaviour was observed (Islam et al., 2022).
- According to BS EN 1992-1-1-2004 the shear strength of plain concrete can be determined as the concrete design strength in tension.

$$v_n = f_{cta} \quad (01)$$

V_n : nominal shear strength (MPa)

f_{cta} : design tensile strength (MPa)

1. Introduction

The PAC can result in reducing natural resource extraction while minimizing the cost and energy consumption of the plastic recycling process. According to previous studies, high-density polyethylene (HDPE), polyethylene terephthalate (PET), and polypropylene (PP) have the potential to be used as sustainable construction materials. Among them, PP is the plastic type, having the highest demand but the lowest recycling percentage. PP can be used in concrete as a fiber, a fractional substitution of natural coarse aggregate (NCA) or fine aggregate (FA), or as a percentage of cement mass. However, limited research has been done on PP as a NCA. The inferior properties of PP aggregates (PPAs) resulted in the reduction of the strength of PAC by comparing to NAC.

On the other hand, concrete shear strength is one of the critical parameters in structural design, because of its catastrophic nature. Further, the aggregate interlock is mainly governing the shear strength of plain concrete. Thus, this study focuses on assessing the shear strength of plain concrete with PPA.

2. Literature Review

3. Methodology

3.1 Experimental Program

In total, four batches were mixed, where different replacement levels of NCA with PPA were performed including 0%, 10%, 20%, and 30% volumetrically. Figure 1 shows the details of a push-off specimen. The specimen was 150 × 150 × 320 mm in dimensions. The nominal dimensions of the shear-transfer plane are 116 × 150 mm.

3.1.1 Materials

This study used ordinary Portland Cement (OPC) as the binding material. The cement was CEM type-I. The specific gravity was 3.15. Well-graded river sand was used as FA, and crushed rock as NCA. FA was with maximum size of 4.75 mm, a specific gravity of 2.65, and fineness modulus of 3.1. Crushed rock with a 12.5 mm maximum nominal size was used as NCA, where the specific gravity was 2.85.

A mechanically operated shredder as shown in Figure 2(a) was used to crush the waste plastic. PPA was irregular in shape, with sharp edges as shown in Figure 2(b), and had a specific gravity

of 0.89. The sieve analysis results were used to determine the particle size distribution and PPA satisfied the coarse aggregate limits of ASTM C33/C33M – 18 shown as in Figure 3.

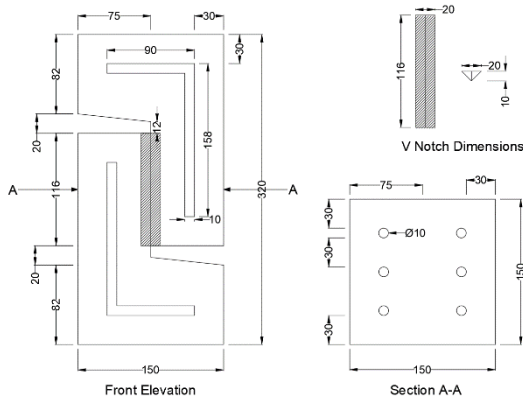


Figure 1: Details of the push-off model.

A water-reducing admixture was used to increase the workability of concrete with PPA. It was a polycarboxylic ether-based admixture. The specific gravity of the admixture was 1.20. It satisfied the standards of EN 934-2 and ASTM C494 Types A and F.



Figure 2: (a) Plastic shredder, (b) Shredded PP aggregates.

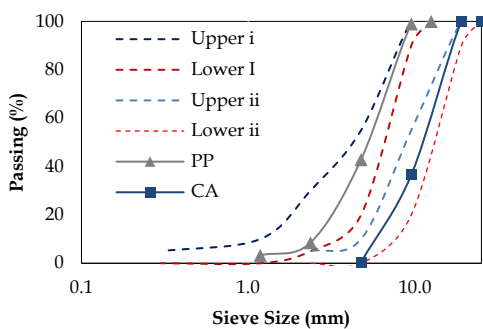


Figure 3: Particle size distributions.

3.1.2 Mix Proportions

The testing targeted producing concrete with a characteristic compressive strength of 25 MPa. The water/cement ratio was found to be 0.55. The mix proportioning followed the guidelines of ACI 211.1. Four concrete mixes were prepared and cast. Table 1 presents a summary of the mix

proportions. PP30 indicates 30% of NCA with PPA.

Table 01: Mix proportions of concrete per 1 m³.

Sample	W/C Ratio	Cement (kg)	Water (kg)	FA (kg)	CA (kg)	PP %	PP (kg)	Admixture (ml)
PP0	0.55	393	216	886	832	0	0	0
PP10					806	10	26	785
PP20					780	20	52	1180
PP30					754	30	78	1570

Per batch, five 100 mm cubes, four 150 mm cylinders, and three push-off specimens were cast for the determination of cube & cylinder compressive strengths (f_{cu} , f_{cy}) splitting tensile strength (f_{ct}), Modulus of Elasticity (E_{cm}) and push off shear strength (v_{po}). Three 100 mm cylinders were cast for the acquisition of stress-strain data. The push-off specimens were tested as shown in Figures 4(a) and 4(b). A centric compressive load was used at a rate of 0.5 kN/s for compressive tests while a rate of 3 N/mm²/s was used for the push off tests.

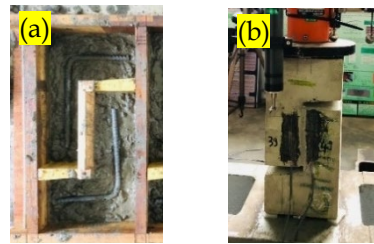


Figure 4: (a) Casting and (b) testing of push-off specimens.

3.2. Numerical Program

3.2.1 Cylinder Model

A concrete cylinder was modelled by using the dynamic explicit method in ABAQUS to investigate whether the CDP model can be used to simulate the behaviour of PAC. A set of input data are shown in Table 2.

3.2.2 Push off Model

ABAQUS was used to create a finite element model (FEM) to simulate the push-off tests. The simulation was involved with defining an accurate mesh to simulate direct shear failure through the shear-transfer plane. Then model was validated for both NAC and PAC by using experimental data. The hexahedral elements were used for FEM, with 5 mm fine mesh and 10 mm coarse mesh. 10 mm diameter steel bars were embedded into the concrete. This arrangement is shown in Figures 5(a) and 5(b).

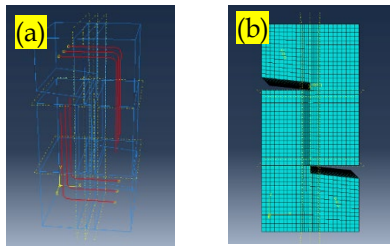


Figure 5: (a) Embedded reinforcements and (b) meshing for push-off model.

Concrete-to-steel bond was established using the embedded option. Steel connectors were linked to concrete bilinear elements through zero-interface elements. A 5 mm displacement load was applied as a line load at the top and a similar line was fixed in all the directions at the bottom.

Table 2: Material properties for PP30.

Properties	Values
Density of concrete (ton/mm ³)	2.2×10^{-9}
Young's modulus of concrete (GPa)	24.2
Poisson's ratio of concrete	0.2
Density of steel (ton/mm ³)	7.8×10^{-9}
Young's modulus of steel (GPa)	210
Poisson's ratio of steel	0.33
Yield stress of steel (MPa)	325

Note: Units as used for numerical models

Table 3: Summary of experimental results.

Batch	Slump (mm)	Wet Density (kg/m ³)	Hardened Density (kg/m ³)	f_{cu} (MPa) 28 day	$C_{R/N}$	f_{cy} (MPa) 28 day	E_{cm} (GPa)	f_{ct} (MPa)	v_{po} (MPa)	v_n (MPa)	$V_{R/N}$	$\beta_{po} = \frac{v_{po}}{\sqrt{f_{cu}}}$
PP0	85	2410	2398.6	44.62	1.0	35.70	32.99	2.76	4.22	1.9	1.0	0.6
PP10	75	2370	2339.1	38.17	0.9	30.90	29.86	2.44	3.73	1.7	0.9	0.6
PP20	75	2280	2263.2	35.96	0.8	28.40	28.09	2.34	3.60	1.6	0.9	0.6
PP30	85	2260	2199.6	30.90	0.7	24.70	25.22	2.06	3.38	1.4	0.8	0.6

4. Results & Discussion

4.1 Experimental Results & Discussion

A summary of the test results is given in Table 3. The reported ultimate strengths were average values calculated based on the measured ultimate applied loads and the actual dimensions of the concrete.

4.1.1 Workability

With increasing PP% slump has been reduced as shown in Figure 6. This is due to the non-uniform shape and sharp edges of PPA. The required workability was achieved with the addition of a super-plasticizer.

4.1.2 Compressive Strength (f_{cu})

As shown in Figure 7, with increasing PP%, the compressive strength decreases. It is due to the lower E_{cm} of PPA and the weak ITZ.

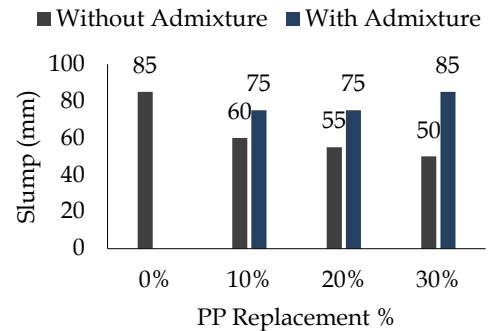


Figure 6: Variation in slump values of different concrete mixtures.

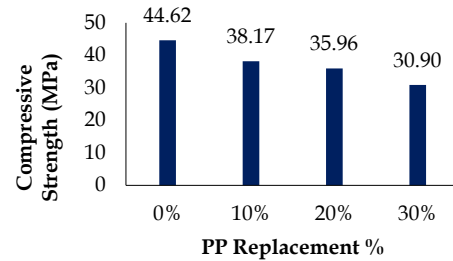


Figure 7: Variation in cube compressive strength of different concrete mixtures.

4.1.3 Stress Strain Behaviour

Figure 8 indicates PPA increases the strain bearing capacity of concrete. A ductile behaviour was observed for PAC.

4.1.4 Shear Strength (v_{po})

Table 3 shows, the use of PPA in concrete, decreased both the f_{cu} and v_{po} . For series PP30, the average $C_{R/N}$ was 0.7, while the average $V_{R/N}$ was 0.8. Figure 9 shows v_{po} is greater than v_n for both NAC and PAC. The average value of the normalized strength factor $\beta_{po} = 0.6$. Thus,

$$v_{po} = 0.6 \sqrt{f_{cu}} \quad (02)$$

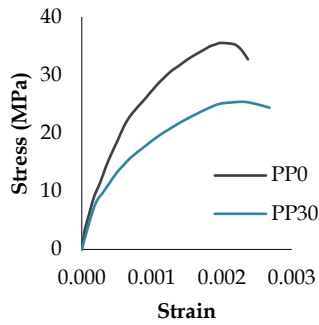


Figure 8: Stress strain behaviour for PP0 and PP30 mixtures.

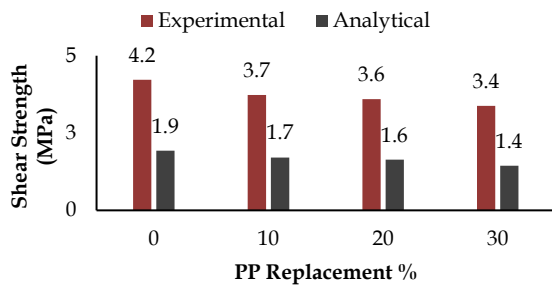


Figure 9: Variation of push-off shear strength of different concrete mixtures.

4.2 Numerical Results & Discussion

4.2.1 Validation of CDP Model for PAC

PP30 was used to validate the FEM model with experimental results as shown in Figure 10.

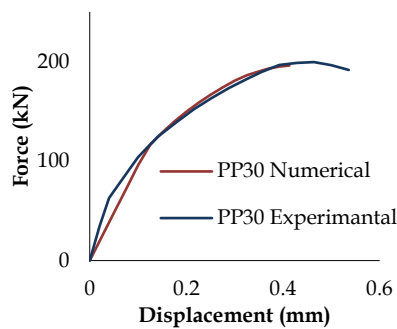


Figure 10: Cylinder model validation for PP30.

4.2.2 Validation of Push-off Model

PP0 was used to validate the push-off model as shown in Figure 11. Failure of the model occurred through the shear-transfer plane, like the experimental observations. Figure 12 indicates the failure pattern and the stress variation.

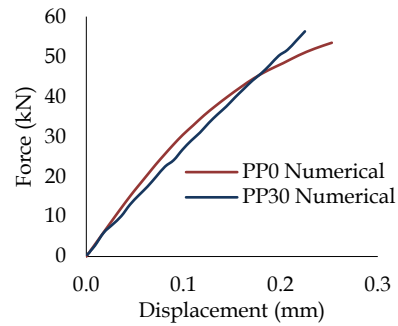


Figure 11: Push-off model validation for PP0.

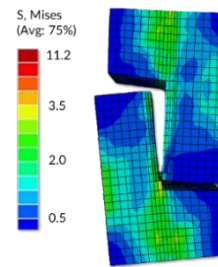


Figure 12: Stress variation and failure pattern of push-off model with PP0.

5. Conclusions

1. Slump value decreased up to 42% and compressive strength reduced by 30% with 30% of PP content.
2. PAC is weaker in shear relative to NAC. However, the cracks propagated along the ITZ, around the aggregates for both PAC and NAC.
3. Determination of shear strength of plain concrete by using BS EN 1992-1-1-2004 is more conservative for PAC.
4. The relationship $v_{po} = 0.6 \sqrt{f_{cu}}$ was equally suitable for NAC and PAC.
5. CDP model can be used for numerical simulation of PAC with PPA up to 30% replacement of NCA.

References

- Islam, M. J., Shahjalal, M., & Haque, N. M. A. (2022) 'Mechanical and durability properties of concrete with recycled polypropylene waste plastic as a partial replacement of coarse aggregate', *Journal of Building Engineering*, 54, 104597.
- Rahal, K. N., & Hassan, W. (2021) 'Shear strength of plain concrete made of recycled low-strength concrete aggregates and natural aggregates', *Construction and Building Materials*, 311, 125317.

Effect of Resource Planning on Construction Project Delays

Ranathunga K.E.*, Wijesinghe K.M.U.M., and Dissanayake P.B.G.

Department of Civil Engineering, Faculty of Engineering, University of Peradeniya, Sri Lanka

* e17273@eng.pdn.ac.lk

Keywords: Causes of delay, Construction industry, Relative importance index, Sri Lanka

Abstract

This study explores how resource planning affects construction project delays in Sri Lanka. It identifies key delay factors using the Relative Importance Index (RII) based on data from 60 industry respondents. Findings highlight material shortages, price fluctuations, and equipment issues as major contributors to delays. Recommendations are provided to enhance resource planning practices and minimize project delays effectively.

1. Introduction

This research study focuses on investigating the impact of resource planning on construction project delays in the Sri Lankan construction industry. Acknowledging the significant resources involved in construction, including manpower, materials, equipment, and finances, the study aims to contribute to project management practices improvement. The introduction provides an overview of key construction project components and emphasizes the importance of resource planning in efficiently allocating and managing these resources for timely project completion. The study also explores the repercussions of inadequate resource planning on project delays, addressing challenges faced by various stakeholders. Through a comprehensive review of past studies, the research aims to identify critical factors contributing to construction project delays in Sri Lanka and proposes practical recommendations for effective resource planning to minimize or eliminate these delays.

2. Literature Review

Several researchers have studied about the causes of construction project delays in different countries. The findings of such studies have been reviewed for this research.

2.1 Study Delay of Road and Bridge Construction Project in Yalimo Regency, Papua Province

This study in Yalimo Regency, Papua Province, examined road and bridge construction projects, addressing specific challenges like difficult terrain and limited materials. Using the Relative Index and Factor Analysis methods, it identified and ranked six key delay factors: Planning & Scheduling, Scope and Work Document, Organizational, Coordination, and Communication Systems, Resource Readiness/Preparation, Inspection and Control, and Other Factors. Common Factor Analysis helped assess dominant factors. Relative Index Analysis ranked these factors, offering valuable insights for improving project management in the region. The research included stakeholders from the Public Project Office, contractors, and consultants in five road projects and two bridge projects, with SPSS version 17 facilitating data analysis.

2.2 Resource Planning to Reduce Project Delays Sri Lankan Construction Industries

This study aimed to identify causes of delays in the construction industry with a focus on resource planning and suggest remedies. The research was confined to construction projects specifically in Sri Lanka.

The researchers utilized a questionnaire survey and interviews, involving a sample of 107 Sri Lankan construction projects. The questionnaire comprised three parts: respondent and organization details, resource-related causes of delays, and resource planning activities. The identified resource-based causes of delays were categorized into seven distinct groups.

The collected data was analysed using MS Excel to determine the relative importance of different causes of construction project delays. The Relative Importance Index (RII) was calculated using Likert's scale of five ordinal measures. The causes were ranked in each category based on their RII.

Key causes of delays in Sri Lankan construction projects included cost, technical, and human-related issues. Top 10 causes encompassed conflicts in subcontractor schedules, payment delays, financing difficulties, labour shortages, low productivity, subcontractor work delays, rework due to errors, subsurface challenges,

poor communication, and material delivery delays.

2.3 A Methodology for Ranking of Causes of Delay for Residential Construction Projects in Indian Context

Construction delays, and exceeding contract completion dates, have adverse effects on both owners and contractors, resulting in revenue loss, increased costs, and strained relationships. Various factors contribute to delays, including party performance, resource availability, environmental conditions, and contractual relations.

Researchers have identified numerous causes, categorized into groups, such as financial problems, design changes, and coordination issues. Two approaches, the Relative Importance Index (RII) and the Importance Index, were proposed to analyse and rank delay causes, utilizing Spearman's rank correlation coefficient for validation. Understanding these causes and their relative importance is crucial for developing effective strategies to mitigate delays and improve project outcomes. The Importance Index considers both frequency and severity, while the Frequency Index quantifies how often a factor occurs, and the Severity Index evaluates its seriousness. Spearman's Rank Correlation Coefficient assesses the strength and direction of relationships between different rankings in the context of construction delays.

2.4 An Assessment of the Factors Causing Delays on Building Construction Projects in Uganda

The study assessed schedule delays in Ugandan building construction projects. Four consultancy firms were selected from registered architectural firms. Key stakeholders from Kampala Capital City Authority were involved in four projects meeting specific criteria. A self-administered questionnaire identified 81 delay factors, categorized into consultant-related, contractor-related, client-related, and external factors. Respondents rated factors on a 5-point Likert scale, and data were analyzed using SPSS. The Relative Importance Index (RII) ranked attributes by perceived criticality. The study employed a comprehensive methodology, including firm selection, project identification, and questionnaire-based data collection, to determine the causes of schedule delays in Uganda.

In here delay factors were mainly considered under 4 types such as consultant related delay

factors, contractor related delay factors, client delay factors and external related delay factors.

The study investigated delay factors in Ugandan building construction projects, categorizing them into consultant-related, client-related, contractor-related, and external-related. Recommendations focused on effective handling of design changes, thorough site investigations, financial discipline, and clear communication among stakeholders.

3. Methodology

The methodology section will outline our process for investigating the impact of resource planning on construction project delays and proposing mitigation methods. This includes detailing the research design, participant selection from the Sri Lankan construction industry (covering project managers, site engineers, clients, and consultants in both building and road construction), and the distribution of a questionnaire based on a review of past studies. The statistical analysis techniques used to assess factors contributing to project delays were explained and how findings are synthesized was discussed. Recommendations were provided to improve resource planning practices in the construction industry, ensuring the rigor and validity of our research.

This study employed the "Relative Importance Index" (RII) to analyze questionnaire data. RII is a quantitative method that assesses the relative importance of factors based on participant responses, aiding in understanding their significance in relation to the research objective of determining the impact of resource planning on construction project delays.

The formula to calculate the RII is as follows:

$$\text{Relative Importance Index} = \frac{\sum (n_i * x_i)}{\sum N_i}$$

Here, $\sum (n_i * x_i)$ represents the sum of the weightings given by the respondents for each factor. The weightings are multiplied by the respective number of respondents for each response category, such as "Strongly Disagree" (n1), "Disagree" (n2), "May be" (n3), "Agree" (n4), and "Strongly Agree" (n5). A represents the highest weighting given to any factor, and N represents the total number of respondents multiplied by 5.

The RII value ranges from 0 to 1, with a higher value indicating a greater importance of the factor in contributing to construction project delays. Recommendations are suggested based on the insights gained from the data analysis, and case study and to mitigate construction

project delays associated with resource planning.

4. Results and Discussion

4.1 Questionnaire survey

The questionnaire survey was conducted using a Google form. 60 responses were received and these respondents were divided into three groups as follows.

- Client - 03
- Consultant - 13
- Contractor - 43
- Sub-contractor- 01

The Google form link was sent to 115 people and 60 responses were received.

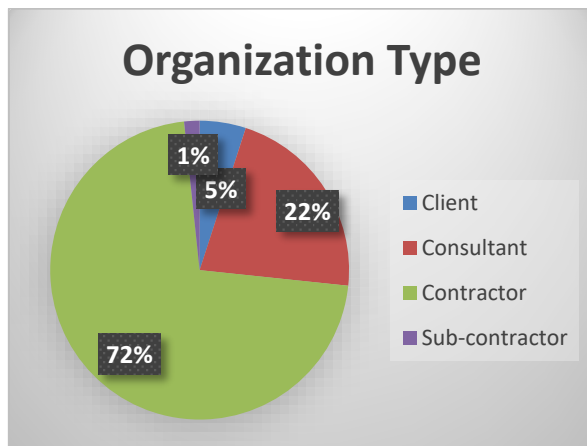


Figure 1: Percentages of respondents from each organization type

Table 1: Details about Respondents

Company Name	Organization Type	Project Name	No of responses
RDA	Consultant	2 flyover projects at slave islands	5
SEC	Consultant	Orugodawattha housing project	2
	Consultant	Makumbura housing project	1
CESL	Contractor	Construction of international gem and jewellery trade center, Ratnapura	2
	Contractor	Centre for liver disease	4
Tudawe Brothers (Pvt) Ltd	Contractor	Makumbura Housing Project	5
	Contractor	Celone Frontier Building project, Bambalapitiya.	3
	Contractor	Widening and improvements to	2

		Pasyala- Giriulla road section	
	Contractor	GPV lanka Factory construction	2
	Contractor	Bambalapitiya Site	2
Maga Engineering (Pvt) Ltd	Contractor	Flyover project at Baladaksha Mawatha	3
	Contractor	Ruwanpura Expressway	4
	Contractor	2 flyover project at slave islands	3
ICC	Sub Contractor	FOCT, airport hotel project	2
	Contractor	University of Jayawardenapura multipurpose building	3
Sathuta Builders(Pvt) Ltd	Contractor	Waters Edge 48 rooms project	3
Wkk engineering	Sub Contractor	Rehabilitation, maintenance and improvement of Warakapola - Pasyala road	2
Lakdhana vi Limited	Contractor	Sobadanavi 350MW RLNG Power Plant	1
WMB constructors	Contractor	JICA	3
	Contractor	improvements to Unduruwa road	1
Sinohydro cooperation limited	Contractor	Basnagoda reservoir project	1
Abdeen builders pvt ltd	Contractor	Colombo waste water project CMC	1
Access Engineering	Sub Contractor	Kohuwala flyover	3
Mahaweli Water Security Investment Program	Consultant	North Western Province Canal Project	2

A total of 60 responds from different groups working on a variety of initiatives were collected and are shown in the table. According to the responses RII values for all of those factors were calculated and ranked those factors according to the RII values. Here are the top 10 factors with their RII values.

1. Shortage of construction material (0.8233)
2. Fluctuation of prices (0.8167)
3. Fluctuations of material prices (0.8067)
4. Shortage of machines/equipment (0.7933)
5. Delay in interim bill payment (0.7867)
6. Frequent machines/equipment breakdown (0.7800)

7. Insufficient financial arrangement (0.7767)
8. Delays in decision making by client/consultant (0.7767)
9. Low efficiency of machines/equipment (0.7667)
10. Low efficiency of machines/equipment (0.7567)

4.2 Case study

Slave Island, a busy commercial hub in Sri Lanka, faces significant disruptions with over 100 daily closures at its level crossings on Justice Akbar Mawatha and Uttarananda Mawatha due to railway traffic. The resulting loss of more than 3 hours per day per crossing underscores the need for an integrated traffic solution to enhance the efficiency of development projects and railway plans in the area. The contractor of this project is Maga Engineering (Pvt) Ltd; the Consultant is RDA and funded by the Government of the Democratic Socialist Republic of Sri Lanka. The project period is 1 year.

After doing the case study, those 10 factors were found as the top 10 causes which caused to the delay of the flyover project.

- Fluctuations in material prices
- Shortage of construction material
- Issues regarding material suppliers
- Fluctuation of prices (overall)
- Delays in decision making by client or consultant
- Unskilled machines operators
- Shortage of machines/equipment
- Unavailability of new technical machines/equipment
- Delay in manufacturing materials
- Insufficient financial arrangement of the project

8 out of 60 responses of the research were taken from the flyover project at Slave Island. RII values for each and every 48 factors were calculated again using those 8 responses and ranked those factors. According to those rankings, those are the top 10 project delaying causes due to poor resource planning.

1. Fluctuations in material prices
2. Delay in manufacturing materials
3. Issues regarding material suppliers
4. Shortage of construction material
5. Fluctuation of prices (overall)
6. Shortage of machines/equipment
7. Unavailability of new technical machines/equipment
8. Issues regard to material suppliers

9. Abundance of hired machines
10. Difficulties in the site access

5. Conclusion

Following the questionnaire survey and the case study we have found that Fluctuations of material prices, Delay in manufacturing materials, Issues regard to material suppliers, Shortage of construction material, Fluctuation of prices (overall), Unskilled machines operators are the most commonly affected causes for the project delays.

Therefore, the following recommendations were suggested to minimize the impact of delays.

- Keep the inventory management system orderly.
- Create a backup plan in case there are unexpected material shortages.
- Negotiate solid pricing arrangements in long-term supplier contracts.
- Keep an eye on market developments and prepare for any price swings.
- Use adaptable budgeting techniques to account for changes in prices.
- Create a solid procurement plan that prioritizes quantity and timing.
- Purchase a backup equipment rental plan in case of overwhelming demand.
- Keep lines of communication open in order to quickly address any payment-related concerns.
- Send progress reports and updates on a regular basis to all stakeholders.
- To optimize equipment efficiency, give operators specialized training.

References

- Abbas, G. and Gidado, K. (n.d.). 'Causes of Project Delay in the Construction Industry in Afghanistan'.
- Amri, A.A.M.A. (2022) 'Delay Factors of Construction Projects in Oman', *Technium*, [online] 4(8), pp.1-10.
- Lanka, S. and P. Dissanayake (2015) 'Resource Planning to Reduce Project Delays Sri Lankan Construction Industries'.
- Parrangan, P., Rachman, R. and Tanijaya, J. (2021) 'Study Delay of Road and Bridge Construction Project in Yalimo Regency, Papua Province', *IJSET - International Journal of Innovative Science, Engineering & Technology*.

Evaluation of Flexural and Shear Performance of Steel-Concrete Composite Beams with Flexible Shear Connectors

Ramyalal, W.P.N.A.*, Bandara, K.G.K.A., and Dammika, A.J.

Department of Civil Engineering, Faculty of Engineering, University of Peradeniya, Sri Lanka

*e17271@eng.pdn.ac.lk

Keywords: steel-concrete composite beams, shear capacity, flexural capacity, degree of shear connectivity

Abstract

In the current design codes, the contribution of the concrete slab to the shear resistance of the steel-concrete composite (SCC) beam has been neglected. However, recent research indicates that the contribution of the concrete flange to shear resistance is substantial. The focus of the present study is a numerical investigation into the behaviour of an SCC beam equipped with stud shear connectors. A composite beam model was analysed under a four-point loading arrangement using the ABAQUS finite element platform and validated referring to the benchmarked experimental setup. Then, a parametric study was conducted, varying the degree of shear connectivity from 100% to 50% in 10% intervals referring to EN1994-1-1. The obtained results revealed that 20% of the total shear was attributed to the concrete slab while decrease in both flexural and shear capacity with the reduction in the degree of shear connectivity.

1. Introduction

Steel-concrete composite (SCC) beams combine the strength of steel with the compressive strength of concrete through shear connectors, facilitating composite action. This composite action enhances load capacity. Current design codes such as EN 1994-1-1, GB 50017 (2003), AISC 360-10 (2010), and AS 2327.1 (2003), neglect the concrete flange's contribution to shear resistance, assuming it's handled by the steel beam web alone. However, recent studies highlight the significant role of both the concrete flange and composite action in shear strength. In this study, a validated finite element model of a SCC beam was developed referring to an experimental study conducted by Jayakody et al. (2019) at the University of Peradeniya. Then a parametric study was conducted to investigate the effects of the degree of shear connectivity on the shear and flexural performance of SCC beams. The results of the parametric study were used to identify the contribution of concrete

flange to shear resistance SCC beams and the role of the degree of shear connectivity on the performance of SCC beams.

2. Literature Review

According to EN 1994-1-1, GB 50017 (2003), AISC 360-10 (2010), and AS 2327.1 (2003), the contribution from the concrete flange to shear resistance is neglected when designing SCC beams. It is assumed that the acting shear is resisted by the web of the steel beam alone. However, Vasdravellis and Uy (2014) and Men et al., (2023) shown that both the concrete flange and the composite action contribute significantly to the shear strength of a composite section and that the main factors that influence the shear capacity of a SCC beam are the slab thickness and the degree of shear connection.

In the research work of Chattopadhyay and Umamaheswari (2022), channel shear connector is considered to evaluate the flexural behaviour with the consideration of varying grades of steel section along with the degree of interaction and to compare the results with a different section of shear connectors. They showed that in full shear connection, deflection is less, and slip is lesser than in partial shear connection.

The concrete flange thickness of the beam, degree of shear connection, effective width of flange, and reinforcement ratio would contribute to the flexural and shear performance of the beam (Johnson and Willmington, 1972; Nie et al., 2004; Vasdravellis and Uy, 2014). Therefore, by studying significance of the contribution of these factors to the shear and flexure capacity of SCC beam, economical designs can be achieved.

3. Methodology

A finite element model of the SCC beam was developed in ABAQUS, and it was validated with the past experimental study conducted by Jayakody et al. (2019) at the University of Peradeniya. Figure 1 shows the schematic diagram of the experimental setup including the

cross-section details of the SCC beam. Table 1 shows the properties of the model. Once the model was validated, it was used to conduct a parametric study to study the shear and flexural performance of the beam by varying the degree of shear connectivity while keeping other properties unchanged.

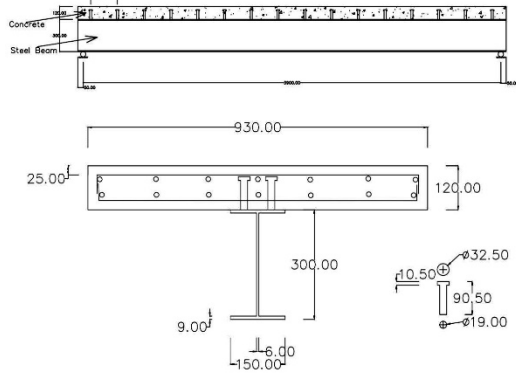


Figure 1: Schematic diagram of test setup and beam cross section

Table 4: Material properties

Details	Description	Value
Concrete	Density, kg/m ³	2400
	Elastic Modulus, GPa	32.92
	Poisson's ratio	0.15
	Yield strength, MPa	11.44
	Ultimate strength, MPa	38.94
	Ultimate strain	0.0035
Steel	Density kg/m ³	7,800
	Young's Modulus, GPa	205
	Poisson's ratio	0.3
	Yield strength, MPa	267
	Ultimate strength, MPa	431
	Ultimate strain	0.25
R/F	Density kg/m ³	7,800
	Young's Modulus, GPa	200
	Poisson's ratio	0.3
	Yield strength, MPa	519
	Ultimate strength, MPa	615
Studs	Density kg/m ³	7,800
	Young's Modulus, GPa	200
	Poisson's ratio	0.3
	Yield strength, MPa	476
	Ultimate strength, MPa	668
	Ultimate strain	0.2

In FE modelling, solid elements (C3D8R) were used to model the concrete flange and the shear studs. Shell elements (S4R) and Wire elements

(T3D2) were used to model the steel beam and reinforcement bars. This approach was also used by Men et al. (2023).

In material modelling, for concrete, non-linear concrete damage plasticity model was used and stress strain curve was developed using the method proposed by Carreira and Chu (1985, 1986). An isotropic hardening model associated with the Von-Mises plasticity criterion was employed for structural steel. The stress-strain curve for structural steel was modelled using a tri-linear curve. Rebars were modelled utilizing a bi-linear curve with a yield strength of 500 MPa and an ultimate strength of 670 MPa. Shear studs were modelled assuming a perfect elastic-plastic curve with a yield strength of 350 MPa.

4. Results and Discussion

4.1 Model validation

The load deflection curve for the mid span of the composite beam obtained from the FE model and experiment are compared in Figure 2 which depicts the validity of the FE model.

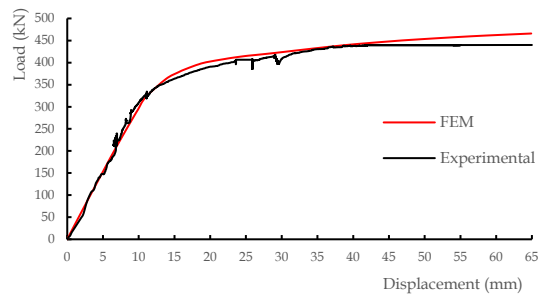


Figure 2: Load vs deflection at midspan of the SCC beam

4.2 Load-displacement variation

The load-displacement variation is depicted for the SCC beam at 100%, 90%, 80%, 70%, 60%, and 50% degree of shear connectivity in Figure 2. It can be observed that there is a reduction in load capacity when the degree of shear connectivity is reduced from 100% to 50%. Capacity reduction is shown in Table 2 in percentages for easy understanding.

4.3 Shear contribution of concrete flange and steel beam in SCC beam

Contributions from the concrete flange and steel beam at different degrees of shear connectivity levels were compared in Table 5. It can be observed that the shear capacity was reduced when the degree of shear connectivity was

Table 5: Shear contribution of concrete slab and steel beam.

Degree of shear connectivity	Total shear force	Shear reduction	Slab contribution	Steel beam contribution
100%	234.88	-	21.0%	79.0%
90%	231.38	1.49%	20.3%	79.7%
80%	225.72	3.90%	19.9%	80.1%
70%	219.82	6.41%	19.1%	80.9%
60%	211.36	10.01%	19.1%	80.9%
50%	207.62	11.60%	20.4%	79.6%

reduced. However, the shear distribution between the concrete flange and the steel beam is about 20% and 80% respectively in all cases. Reduction of shear capacity in SCC beam, concrete flange and steel beam are shown in Figure 4 to Figure 6 respectively.

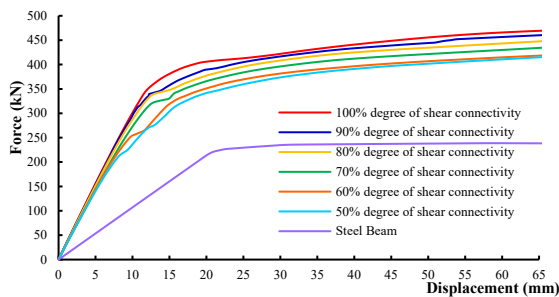


Figure 3: Load vs Displacement Behaviour

Table 6: Load capacity reduction vs degree of shear connectivity reduction

Degree of shear connectivity reduction	Load capacity reduction
10%	1.94%
20%	4.61%
30%	7.47%
40%	10.85%
50%	11.58%

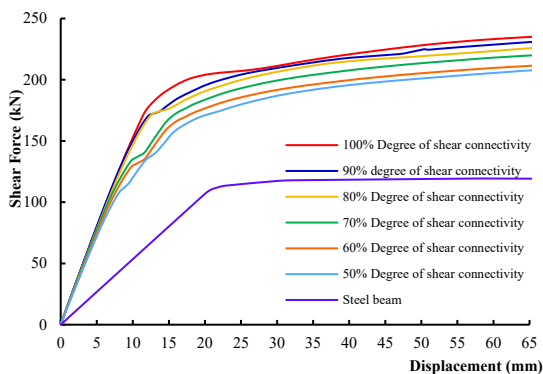


Figure 4: Shear vs Displacement Behavior of Composite Section

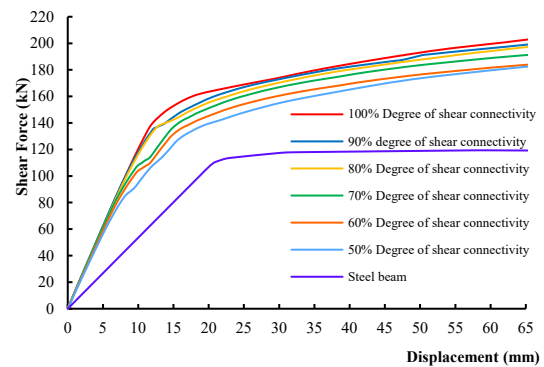


Figure 5: Shear vs Displacement in Steel beam

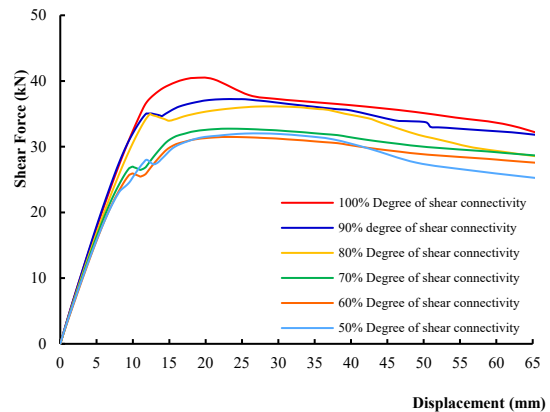


Figure 6: Shear vs Displacement in Concrete Flange

5. Conclusions

When the degree of shear connectivity is reduced, both the flexural and shear capacity of the SCC beam are decreased. This indicates that the degree of shear connectivity has a significant influence on the load-deformation behavior of the SCC beams. However, no significant increase in slip between the concrete flange and the steel beam is detected with varying degrees of shear connectivity. This implies the possibility of varying degrees of shear connectivity in SCC beams depending on the required performance level.

In all six cases, shear distribution between concrete slab and steel beam is about 20% and 80% of total shear.

Vasdravellis, G. and Uy, B. (2014) 'Shear Strength and Moment-Shear Interaction in Steel-Concrete Composite Beams', *Journal of Structural Engineering* [Preprint]. Available at: [https://doi.org/10.1061/\(asce\)st.1943-541x.0001008](https://doi.org/10.1061/(asce)st.1943-541x.0001008).

References

AISC Committee, (2010) 'Specification for structural steel buildings (ANSI/AISC 360-10)', American Institute of Steel Construction, Chicago-Illinois.

Carreira, D.J. and Chu, K.-H. (1985) 'Stress-Strain Relationship for Plain Concrete in Compression', *ACI Journal*, 82(6), pp. 797–804.

Carreira, D.J. and Chu, K.H. (1986) 'Stress-Strain Relationship for Reinforced Concrete in Tension.', *Journal of the American Concrete Institute*, 83(1), pp. 21–28. Available at: <https://doi.org/10.14359/1756>.

Chattopadhyay, S. and Umamaheswari, N. (2022) 'Numerical investigation of steel-concrete composite beams using flexible shear connectors', *AIMS Materials Science*, 9(5), pp. 668–683. Available at: <https://doi.org/10.3934/mat.2022041>.

EN, B., 1994. 1-1: 2004: Eurocode 4. Design of composite steel and concrete structures. General rules and rules for buildings. British Standards Institution, London.

Jayakody, J. A. N. N. et al. (2019) 'Experimental Investigation and Numerical Simulation of Behaviour of Steel-Concrete Composite Girders.

Johnson, R. and Willmington, R. (1972) 'Vertical shear in continuous composite beams.', *Proceedings of the Institution of Civil Engineers*, 53(2), pp. 189–205. Available at: <https://doi.org/10.1680/iicep.1972.5409>.

Men, P., Liang, B., He, W., Di, J., Qin, F. and Zhang, Z., (2023) 'Vertical shear resistance of noncompact steel-concrete composite girders under combined positive moment and shear', *Case Studies in Construction Materials*, 18, p. e01835. Available at: <https://doi.org/10.1016/j.cscm.2023.e01835>.

National Standards of the People's Republic of China (2003), Code for Design of Steel Structures (GB50017-2003) (English version), China Architecture & Building Press.

Nie, J., Xiao, Y. and Chen, L. (2004) 'Experimental Studies on Shear Strength of Steel-Concrete Composite Beams', *Journal of Structural Engineering*, 130(8), pp. 1206–1213. Available at: [https://doi.org/10.1061/\(ASCE\)0733-9445\(2004\)130:8\(1206\)](https://doi.org/10.1061/(ASCE)0733-9445(2004)130:8(1206)).

Standards Australia, (2003) AS/NZS 2327.1: 2003 Composite Structures: Simply Supported Beams.

Investigation of Dynamic Characteristics of PSC Girders and Predicting Base Line Damping Characteristics of PSC Bridges

Wickramarathna W.G.G.K.*, Perera M.T.D., and Dammika A.J.

Department of Civil Engineering, Faculty of Engineering, University of Peradeniya, Sri Lanka

* e17390@eng.pdn.ac.lk

Keywords: Mode shapes, Modal damping ratio, Natural frequency, PSC girders,

Abstract

Knowing the dynamic characteristics of individual pre-stressed concrete (PSC) girders is an advantage to get an idea about the dynamic characteristics and health monitoring of bridges built with PSC girders. This study consisted of an approach to identify dynamic characteristics in PSC girders by using experimental, numerical, and analytical approaches. In this study, field vibration measurements have been analyzed to obtain the experimental modal characteristics. Accordingly, dominant frequencies were identified through FFT, and damping characteristics were identified by referring to the decay curve. Seismosignal application and MATLAB were used for data processing and analysis. The dynamic characteristics of the PSC girders were numerically obtained by conducting modal analysis using the SAP2000 finite element package. Experimentally identified and numerically obtained dynamic characteristics of the PSC girders were compared. Experimental identifications reveal that PSC girders exhibit viscous damping behavior and the approach for predicting the damping characteristic of PSC girder bridges was discussed.

1. Introduction

Road bridge construction using Pre-stressed Concrete (PSC) girders is a common practice in the world for many decades. Early detection of the existence of damage is of utmost importance in these bridges to avoid catastrophic failures. Vibration-based damage detection approaches play an important role in this regard as damage indicators such as modal damping ratio is very sensitive to common defects such as cracks and reinforcement/tendon corrosion which lead to nonlinear dissipative characteristics. The identification of dynamic characteristics in PSC girders and bridges built with them is important in this process as baseline information is not available for most of such bridges in Sri Lankan context. Therefore, the

present study focuses on identifying dynamic characteristics of PSC girders experimentally and numerically at first while trying to establish a method to predict the damping characteristics of PSC girder bridges at their intact condition using the identified behaviour of PSC girders.

2. Literature Review

Knowing the dynamic characteristics of individual (PSC) girders is an advantage to get an idea about the dynamic characteristics and health monitoring of bridges built with PSC girders. Shahzad (2013) showed the sensitiveness of modal damping ratios and natural frequency by testing corroded and uncorroded RC beams and results were obtained by logarithmic discriminant method and curve fitting methods.

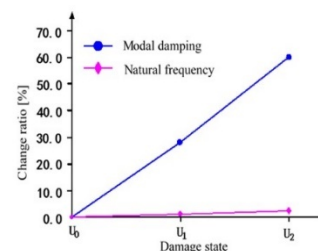


Figure 1: Variation of Natural Frequency and damping ratio with Damage Level (Shahzad et al, 2013)

Figure 1 clearly implies the sensitivity of two parameters and their behaviours against damage level.

Damping characteristics have a direct impact on the stability and safety of PSC girders and bridges. Khaleel et al., (1993) investigated damping properties of existing single-span pre-stressed concrete girder bridges with different service periods and highlighted their crucial role in reducing dynamic amplification and preventing excessive vibrations. Understanding the damping characteristics allows engineers to design and optimize PSC girders and bridges to ensure their stability, reduce the risk of dynamic instability, and enhance overall safety.

3. Methodology

The research is basically undergoing two main approaches namely experimental, and numerical modal identifications in order to identify modal parameters of the selected girders.

3.1 Selected girders

Six types of (PSC) girders which were cast and stored at State Development and Construction Cooperation (SD & CC) casting yard at Weragantota, Mahiyangana were selected. They include Bulb-T sections of lengths 9.5m, 11.5m, 13.5m, 16.5m, 19.0m and 25.0m. Cross sections of the PSC girders are shown in Figure 2.

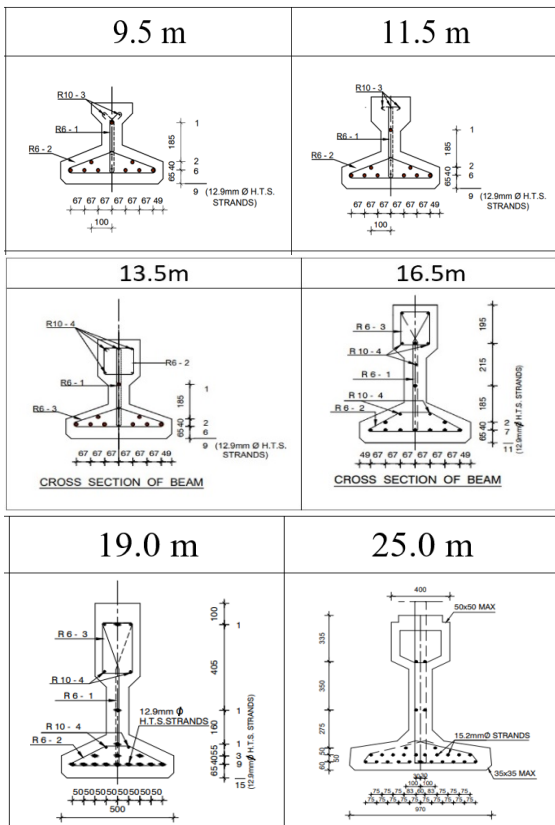


Figure 2: Cross section details of PSC girders

3.2 Experimental Modal Analysis

The experimental analysis consisted of measuring field vibrations and obtaining modal parameters, namely natural frequency, and modal damping ratio by processing those measured responses. Seismosignal application and MATLAB were used in vibration data processing. Three accelerometer sensor setups (Guralp Fortis, 0-200 Hz) were used to measure

the vibration responses of the PSC girders as shown in Figure 3. Sensors are fixed in A₁, A₂ and A₃ locations.

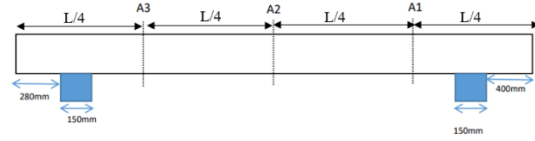


Figure 3: Sensor setup

An impact from the impact hammer was used to excite the PSC girder while acceleration sensors recorded the acceleration responses of the girder. At least five set of responses were measured from each beam and a sample record of the acceleration response of a 9.5 m length PSC girder is shown in Figure 4.

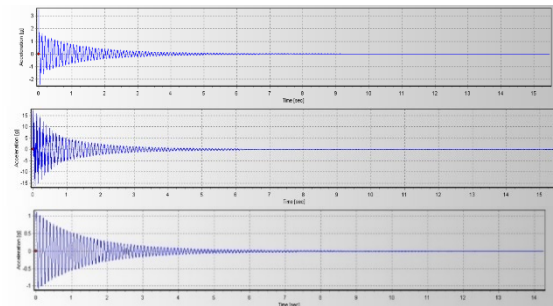


Figure 4: Acceleration responses of 3 Channels of 9.5 m length PSC girder

3.3 Numerical Modal Analysis

The numerical approach consisted of creating finite element (FE) models of studied PSC girders and identifying the dynamic characteristics of those girders by conducting modal analysis. A commercially available finite element package, SAP 2000 was used in this process. Solid elements were used for modeling the FE solid modal. The beam element and tendon element were used for modeling the FE beam modal. The natural frequencies and mode shapes of the girders were identified using FE solid models. The variations in natural frequencies were identified using the FE beam model under different percentages of pre-stress force losses. Fixed and pin support conditions were assigned in order to represent the support conditions.

4. Result and Discussion

Natural frequencies of two dominant vibration mode shapes, namely, the first symmetric vertical bending mode and the first asymmetric

vertical bending mode as shown in Figure 5 were identified through the modal analysis of each girder.

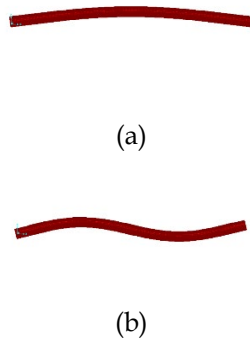


Figure 5: First symmetric vertical bending mode (a) and first asymmetric vertical bending mode (b).

Natural frequencies were experimentally identified by taking the Fast-Fourier Transformation (FFT) of measured acceleration responses. Modal damping ratios of the PSC girders were identified by applying the Logarithmic decrement technique using a response decay curve. A sample set of FFT outputs using the response for the 9.5 m PSC girder is shown in Figure 6.

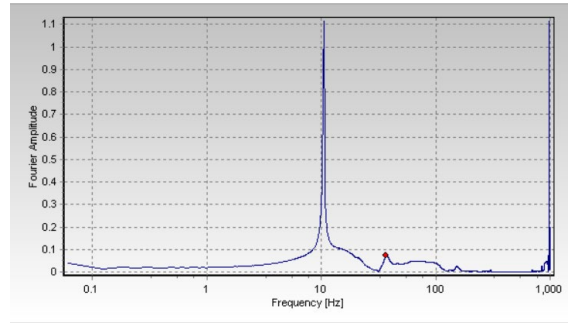
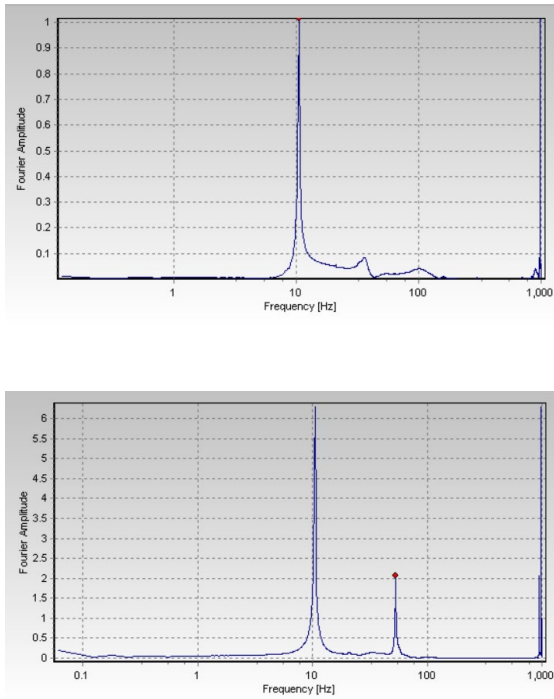


Figure 6: FFT outputs of 03 channels of 9.5m girder

The experimentally identified modal damping ratios of the PSC girders indicate its viscous damping behaviour as it can be seen in the figure. The summary of the numerical and experimental findings of modal parameter identifications is tabulated in Table 1. Experimentally identified parameters given in the table are the average values found from repeated test attempts.

Table 1: Numerical and experimental modal identifications of the PSC girders

Length	Mode	Natural Frequency (Hz)			Damping Ratio
		Experiment	Solid	Tendon	
9.5 m	Mode1	10.56	9.57	9.93	0.57
	Mode2	36.62	36.27	37.96	-
11.5 m	Mode1	8.48	7.78	7.86	0.70
	Mode2	30.88	29.84	30.65	-
13.5 m	Mode1	6.84	7.12	6.52	0.69
	Mode2	26.25	27.28	25.60	-
16.5 m	Mode1	6.71	5.73	5.79	0.68
	Mode2	26.87	22.13	22.73	-
19.0 m	Mode1	5.58	5.37	5.11	0.50
	Mode2	20.98	20.62	20.08	-
25.0 m	Mode1	5.16	4.99	4.11	0.51
	Mode2	18.49	19.25	15.84	-

No change in natural frequencies of the PSC girders with the loss of pre-stressing force as it is found from the numerical simulation. The variation of natural frequencies with a different percentage loss of pre-stressing force for the 9.5 m PSC girder is shown in Figure 7. This indicates that natural frequency is not a sensitive damage indicator to find invisible damages in PSC girders.

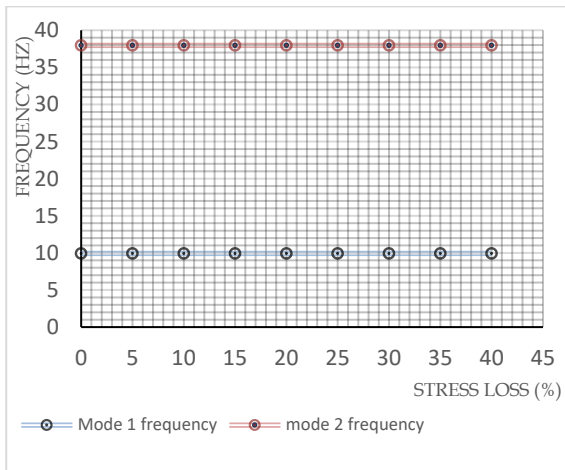


Figure 7: The variation of natural frequencies with different percentage loss of pre-stressing force for 9.5 m PSC girder

5. Conclusions

- Followed experimental and numerical approaches enable easy identification of dynamic characteristics of studied PSC girders.
- Experimental identifications reveal that PSC girders exhibit viscous damping behavior and average modal damping ratio of the First Vertical Bending mode vary in the range of 0.5% - 0.7 %.
- No change in natural frequencies was seen in PSC girders with the removal of pre-stressing forces using numerical simulation, evidence of the natural frequency is not a sensitive damage indicator for PSC girders or bridges.
- Tendency of viscous type damping behavior can be expected from the PSC girder bridges made out from similar girders at intact condition, and possible prediction of the damping ratio of the PSC bridges using the damping behavior of PSC girders need to be explored.

References

Atmaca, B., Ateş, Ş. and Günaydın, M. (2022) 'Analytical, numerical, and experimental determination of dynamic characteristics of prestressed concrete girders', *Journal of Structural Engineering & Applied Mechanics*, 5(1), pp. 1-12. Available at: <https://doi.org/10.31462/jseam.2022.01001012>.

Fernando, K.S.D.M., Dissanayake, D.M.C.D., Dharmasiri, M.A.K.M. and Dammika, A.J. (2020)

'Damage Detection and Condition Monitoring of Prestressed Concrete Bridges by using Vibration based Health Monitoring Techniques', *The Institution of Engineers, Sri Lanka*, Vol. LIII (No. 03), pp. pp. [91-100].

Khaleel, M.A. and Itani, R.Y. (1993) 'Safety evaluation of existing partially prestressed concrete girder bridges', *Computers & Structures*, 48(5), pp. 763-770. Available at: [https://doi.org/10.1016/0045-7949\(93\)90498-3](https://doi.org/10.1016/0045-7949(93)90498-3).

Shahzad, S., Yamaguchi, H., Takanami, R. and Asamoto, S. (2013) 'Detection of corrosion-induced damage in reinforced concrete beams based on structural damping identification', *Proceedings of the 13th East Asia-Pacific Conference on Structural Engineering and Construction*, EASEC 2013.

Acknowledgment

We would like to express our sincere gratitude to the service of the State Development and Construction Cooperation (SD & CC) Weragantota casting yard for facilitating to conduct vibration measurements of PSC girders.

Load Capacity Assessment of Dapped-End Beams with Critical Shear Span to Depth Ratios

Weerasekara L.C.*, Jayashani W.P.M., and Yapa H.D.

Department of Civil Engineering, Faculty of Engineering, University of Peradeniya, Sri Lanka

* *e17375@eng.pdn.ac.lk*

Keyword: Dapped-end beams, PCI design approach, shear span-to-depth ratio, shear strength

Abstract

The a/d and a_v/d_{eff} ratios are the key geometric parameters that affect the load carrying capacity of dapped-end beams (DEBs). It was observed that these parameters are not sufficiently considered in the popularly used design guidelines from the Prestressed Concrete Institute (PCI). This study investigated the sensitivity of these two parameters on the load capacity of DEBs. Existing experimental data was gathered, and an experimental investigation consisted of six DEBs was conducted such that a/d and a_v/d_{eff} varied in the ranges of 1.1 – 2.5 and 1.5 to 2.5 respectively. The concrete strength was maintained around 35 MPa and the orthogonal reinforcement configuration was implemented in the DEBs. The results indicated that the strength of the DEBs decreased with the increment of both a/d and a_v/d_{eff} ratios. It was also identified that, in order to ensure ductile behaviour, DEBs be designed such that a/d and a_v/d_{eff} ratios were at least 1.6 and 1.5 respectively. Using the available database, a modification factor to the PCI formulation was identified to cover the sensitivity of the two ratios. The mean of the V_{pred}/V_{exp} ratio before and after the modification was 2.05 and 1.27 respectively. The prediction accuracy of the result of the current experiments was also found to be high (mean =1.10, SD =0.05) with the incorporation of the introduced factor.

1. Introduction

Dapped-end beams (DEBs) were widely used in bridge construction in the past due to their cost-effectiveness, efficiency, and construction flexibility. The beams offer a unique space saving advantage by significantly reducing floor depth and overall building height. The load capacity assessment of DEBs with critical shear span to depth ratios is essential to ensure safety, prevent failures, optimize designs, and develop codes of practice and standards. The understanding of the behavior and limitations of these beams under different loading capacities is helpful when identifying potential failure modes and implementing appropriate analytical method to design modifications. The presence of

a highly stress-concentrated D-region in DEBs poses a challenge to their design, leading to cracking and potential structural issues. Various analytical methods, including those from the PCI code and Strut and Tie modelling, have been employed, each with its limitations. This investigation was conducted with the major objective of exploring the sensitivity of two critical shear span to depth ratios, namely a/d and a_v/d_{eff} (shear clearance to full depth ratio) towards the behaviour of the DEBs.

There is a high stress concentration at the re-entrant corner of DEBs due to the abrupt change in the depth of the beam. The cracks can appear near the disturbed (D) region due to high stress concentration and may lead to catastrophic failure. The amount of main nib reinforcement and the reinforcement layout type affect to the shear capacity of DEBs. Based on the layout of reinforcement, two approaches for designing reinforcement in DEBs can be distinguished: the UK type and the US type. (Desnerk et al., 2016)

Previous investigations found that, with the increase of the shear clearance to depth ratio (a_v/d_{eff}), the strength and stiffness of DEBs decrease (Aksoylu et al., 2023). Similarly, when the shear span-to-depth ratio (a/d) decreases, stiffness and the ultimate vertical load carrying capacity of dapped-ends increase (Lu et al., 2012). The combined effects of a/d and a_v/d_{eff} on a shear capacity have been investigated numerically too. The shear capacity was reduced using the approaches in the numerical results, which converge to a great extent with the experimental data by 92.46%. (Aksoylu et al., 2023)

The design of the D-region is complex due to the geometric discontinuity. Hence the conventional design methods cannot be used, and some alternative methods are used such as the PCI design handbook, strut and tie method, mechanism analysis, and kinematics-based model. The predictions obtained from the PCI approach is not affected by the variation of a_v/d_{eff} ratio for all a/d values. Hence the acceptable results cannot be obtained through the PCI method and that is underestimated

(Yang et al., 2011). The PCI approach recommended five potential failure modes to predict the shear capacity. The design equations given in the code are suitable only for cases where the shear span to depth ratio (a/d) is under 1.0.

2. Methodology

The research methodology was developed to establish a relationship between two governing parameters using a combination of experimental and analytical tools. Comparing accuracy, design potential, and validity towards experimental results, the most suitable analytical tool was selected and modified with suitable predictions. The experimental test database was collected based on the previous test results and experimental design was done. The effect of geometric parameters and the behaviour of DEBs was investigated through the experiment and results were compared with the modified analytical method.

3. Experimental Study

This experiment mainly considers the influence of critical geometric parameters. Six DEBs with different geometric parameters were tested under three-point bending. For the reinforcement arrangement, an orthogonal reinforcement layout was used according to the existing PCI design approach and the reinforcement details are shown in Figure 1.

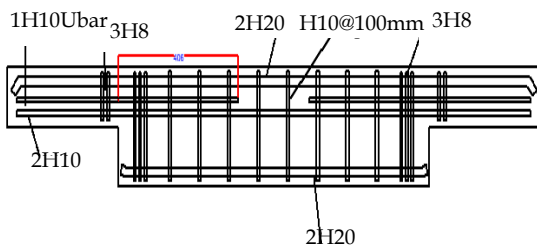


Figure 1: Reinforcement design and arrangement

3.1 Testing Procedure

The tests were conducted under static load with three-point bending. Four strain gauges were used at the critical locations and displacement was measured at the supports and the loading point using 3 displacement gauges. The expected first crack is at the re-entrant corner, therefore one strain gauge was placed at the middle of the hanger reinforcement, in the previous literature mentioned that, when

increasing the a/d ratio there is a need for vertical reinforcement in the nib region, to monitor that one strain gauge was placed at the mid-point of the vertical reinforcement in the nib. Another strain gauge was placed at the nib flexure reinforcement to investigate the flexure failure at the nib region. To study the full depth corner diagonal crack, another strain gauge was placed at the bottom point of the hanger reinforcement.

4. Analytical Predictions

4.1 PCI Design Handbook Predictions

According to the PCI Design Handbook, the smallest value of shear strengths calculated from the main 5 equations is taken as the predicted shear strength of DEBs.

4.2 The Proposed Modification

Considering the above limitations, the Geometric factor (δ) proposed represents the two critical geometric parameters. Test results of 25 DEBs were compiled from different experimental investigations carried out by previous literature to propose the geometric factor. Table 2 presents the comparison of existing and modified PCI approach predicted shear capacities of DEBs considered. The geometric factor shown in Eq. (1) and this concept can be used to estimate the shear capacity of DEBs with different ratios of a/d and a_v/d_{eff} .

$$V_u \propto \frac{1}{\left(\frac{a}{d}\right)^\alpha} \tag{a}$$

$$V_u \propto \frac{1}{\left(\frac{a_v}{d_{eff}}\right)^\beta} \tag{b}$$

Considering the above two relationships, Equation (1) can be obtained as the geometric factor (δ_1) to modified PCI design approach equations and δ_1 can be expressed as

$$\delta_1 = \frac{1}{\left(\frac{a}{d}\right)^\alpha \times \left(\frac{a_v}{d_{eff}}\right)^\beta} \tag{1}$$

Table 1: Geometric coefficient values for corresponding a/d parameter

Geometric coefficient	a/d range		
	$0.75 \geq a/d$	$0.75 < a/d \leq 1$	$a/d > 1$
α	0.5	3.3	-0.2
β	3.65	1.4	0.3

Specimen	a/d	a _v /d _{eff}	V _{dv,test} /(kN)	V _{dv,calc} /(kN)	V _{dv,test} /V _{dv,c} alc	V _{dv,calc} /(kN)	V _{dv,test} /V _{dv,ca} lc
1	0.56	0.78	561.00	157.28	3.57	525.97	1.07
2	0.59	0.78	705.00	175.94	4.01	573.22	1.23
3	0.59	0.78	713.00	179.59	3.97	585.10	1.22
4	0.54	0.78	599.00	175.94	3.40	599.17	1.00
5	0.54	0.78	642.00	179.59	3.57	611.59	1.05
6	0.89	0.78	360.00	157.28	2.29	328.47	1.10
7	0.83	0.78	513.00	175.94	2.92	462.61	1.11
8	0.81	0.78	521.00	179.59	2.90	511.78	1.02
9	0.83	1.00	291.00	157.05	1.85	290.46	1.00
10	0.85	1.00	351.00	175.94	1.99	300.81	1.17
11	0.85	1.00	392.00	179.59	2.18	307.04	1.28
12	1.2	1.53	313.00	267.37	1.17	244.07	1.28
13	1.19	1.53	236.00	195.08	1.21	194.52	1.21
14	1.5	1.67	346.00	256.15	1.35	256.69	1.35
15	1.2	1.53	362.00	267.37	1.35	244.07	1.48
16	1.51	1.68	248.00	212.48	1.17	197.50	1.26
17	1.5	1.67	308.00	276.29	1.11	256.69	1.20
18	1.5	1.67	346.00	276.29	1.25	256.69	1.35
19	1.2	1.53	469.00	373.10	1.26	340.60	1.38
20	1.2	1.53	492.00	373.10	1.32	340.60	1.44
21	1.51	1.68	352.00	318.54	1.11	296.08	1.19
22	1.5	1.67	344.00	276.29	1.25	256.69	1.34
23	2.1	1.96	37.50	20.91	1.79	19.81	1.89
24	2.1	1.67	35.00	21.51	1.63	21.41	1.63
25	2.1	1.67	34.50	21.69	1.59	21.58	1.60
				AVG	2.05	AVG	1.27
				SD	0.99	SD	0.22
				COV	0.48	COV	0.17

Table 2: Existing and modified PCI Design Handbook predicted shear capacities of DEBs

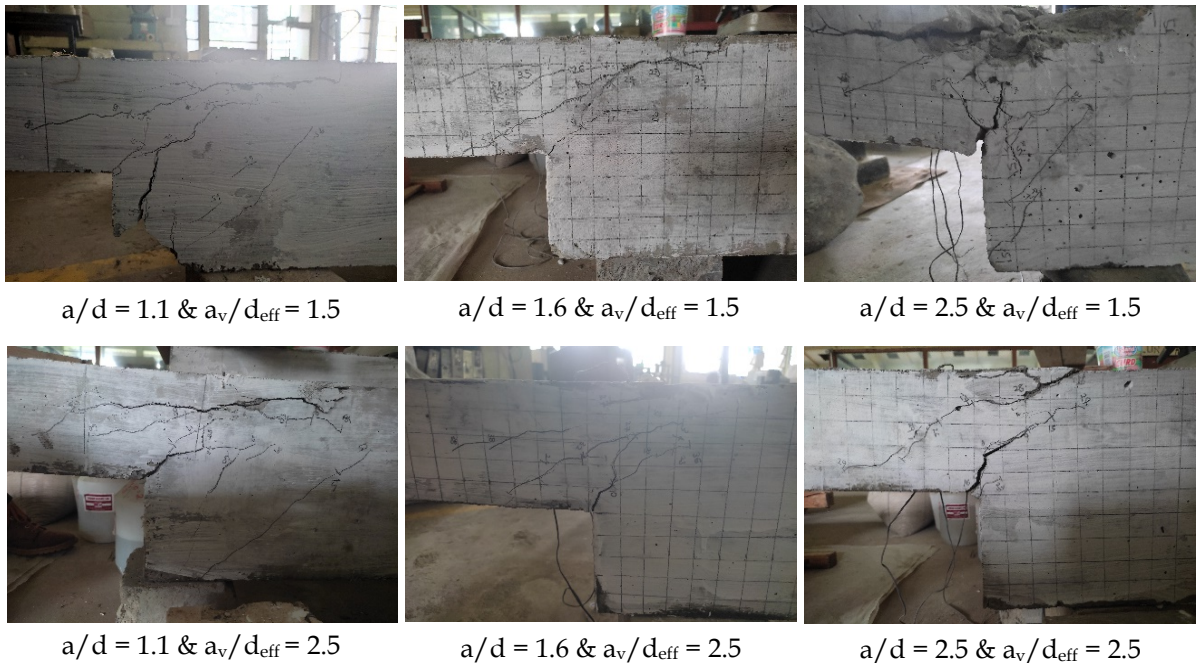


Figure 2: Crack patterns of each specimen

5. Results and Discussion

In the experimental study obtained the shear capacity of DEBs for each specimen is shown in Table 3. According to the results obtained from the experimental test, variation of displacement was plotted and that is shown in Figure 2.

Table 3: The shear capacity of DEBs

Specimen	f_c' (MPa)	a/d	a_v/d_{eff}	V_{test} (kN)
DEB 1	34.36	1.1	1.5	81.6
DEB 2	34.36	1.1	2.5	63.6
DEB 3	33.10	1.6	1.5	51.5
DEB 4	33.10	1.6	2.5	46.1
DEB 5	35.78	2.5	1.5	37.8
DEB 6	35.78	2.5	2.5	29.0

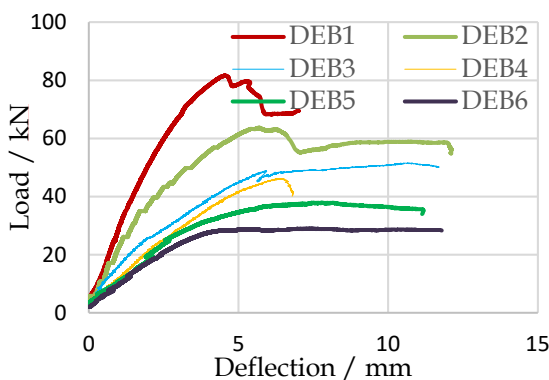


Figure 3: Variation of displacement with shear capacity

Figure 3 demonstrates the change in normalized load capacities for experimental study, and existing and modified PCI predictions. Figure 4 shows the crack patterns of each specimen during the test.

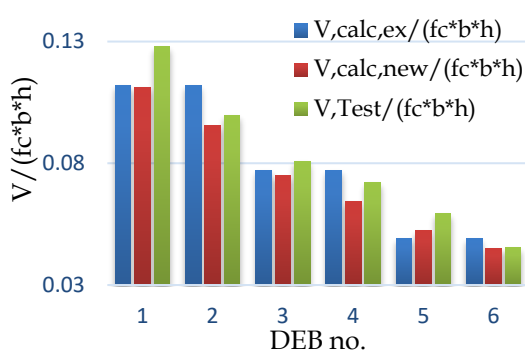


Figure 4: Variation of normalized shear force for experimental study

6. Conclusions

In this study, six reinforced concrete DEBs with different geometric parameter values were tested. Comparisons between the experimental results and the predictions show that the PCI code gave considerable underestimations.

Whereas the modified PCI design code was able to make reasonable predictions.

1. The existing PCI design approach is not sensitive to the a_v/d_{eff} parameter whereas the experimental database shows clearly that the DEB load capacity reduces with the increment of this particular ratio.
2. The modified PCI design formulation provided better accuracy and consistency in prediction of the DEB failure loads of the experimental results in the literature. The mean and COV of the V_{exp}/V_{pred} ratio were 1.27 and 0.17 respectively. Prior to the modification, the two statistical values were 2.05 and 0.48 respectively.
3. The shear strength of the tested DEBs increased with the decrease of both a/d (1.1 to 2.5) and a_v/d_{eff} (1.5 to 2.5) by 32.1% and 16.0% respectively.
4. The DEB behaviour became more ductile with the increment of two shear span to depth ratios. This observation was more prominent when a/d and a_v/d_{eff} ratios were more than 1.6 and 1.5 respectively. Furthermore, the nib flexure reinforcement became the most critical reinforcement element as the two ratios exceeded that particular threshold.

References

- Aksoylu, C., Özkılıç, Y.O. and Arslan, M.H. (2023) 'Experimental and numerical investigation of shear strength at dapped end beams having different shear span and recess corner length', In Structures (Vol. 48, pp. 79-90), Elsevier.
- Desnerck, P., Lees, J. and Morley, C. (2016) 'Impact of the reinforcement layout on the load capacity of reinforced concrete half-joints', Engineering Structures, 127.
- Lu, W.Y., Chen, T.C. and Lin, I.J. (2015) 'Shear strength of reinforced concrete dapped-end beams with shear span-to-depth ratios larger than unity', Journal of Marine Science and Technology, 23(4), p.5.
- PCI Design Handbook, Precast and pre-stressed concrete, Precast/ pre-stressed concrete institute, USA, 6th Edition, (2004)
- Acknowledgments**
- The support provided by the technical staff of the Materials laboratory/Engineering workshop of the University of Peradeniya and the financial support given by the Tokyo Cement PLC are highly appreciated.

Feasibility Investigation of Foam Concrete for Wall Panels

Kavinda E.A.V.*, Wijesinghe K.A.K., and Bandara S.

Department of Civil Engineering, Faculty of Engineering, University of Peradeniya, Sri Lanka

* e17160@eng.pdn.ac.lk

Keywords: Concrete Damage Plasticity model, Finite Element Analysis, Foam concrete, Wall panels

Abstract

This research addresses the limited understanding of the behaviour of foam concrete wall panels, aiming to study their material behaviour using numerical analysis. Foam concrete wall panels are common. The study begins by investigating the material properties of foam concrete through literature. Key parameters such as compressive strength, flexural strength, and modulus of elasticity were studied. A validated numerical model will be developed to simulate the behaviour of foam concrete wall panels. Through numerical analysis, valuable insights will be gained into the behaviour and performance of foam concrete wall panels. Furthermore, a comprehensive parametric study will be conducted to explore the effects of different design variables on the performance of foam concrete wall panels. Based on the results obtained from the numerical simulations and the parametric study, practical design guidelines and recommendations will be proposed. These guidelines will aim to optimize the use of foam concrete wall panels in construction projects. The outcomes of this research will contribute to advancing the knowledge and understanding of foam concrete wall panels.

1. Introduction

Foam concrete, a lightweight and sustainable construction material, is gaining attention for its reduced weight, thermal insulation, and easy handling. Despite studies on its mechanical and material properties, there is a gap in understanding foam concrete wall panels' specific performance. This research addresses the lack of literature on their behaviour as load bearing and non-load bearing elements. Assessing properties like density, compressive and flexural strength, and water absorption is crucial for determining structural integrity. Numerical simulations, such as finite element analysis, aid in predicting load capacity and deformation, guiding optimal design, and enhancing foam concrete

wall panel technology for practical applications.

2. Literature Review

Foam concrete is typically composed of Ordinary Portland Cement (OPC) or Rapid Hardening Portland Cement, along with additives like High Alumina and Calcium Sulfoaluminate. Fine aggregates, including fly ash, lime, crushed concrete, and recycled materials, are incorporated. The water-cement ratio ranges from 0.4 to 1.25 (Ramamurthy, et al., 2018) and the modulus of elasticity varies from 1 to 12 kN/m² for dry densities between 500 and 1600 kg/m³ (Jones and MacCarthy, 2005). Crucially, both flexural and compressive strengths rise with foam concrete density, making it a versatile material suitable for diverse construction applications.

Numerical simulation, notably Extended Finite Element Method (XFEM), is pivotal for understanding foam concrete wall panel behaviour. Limited literature exists, but studies on foam concrete beams and cubes confirm XFEM's effectiveness in analysing fracture behaviour, offering insights into crack propagation and failure modes (Ahmad et al., 2021).

The Concrete Damaged Plasticity (CDP) model proves valuable for numerical simulations of foam concrete due to its versatility in representing complex behaviours. CDP parameters of stress strain values for both compression and tension were obtained through tests (Goh et al., 2014).

3. Methodology

Figure 1 shows the general steps of the methodology of this study. To establish the accuracy of the numerical model, a dedicated model for a foam concrete notch beam with a 20mm notch size used in Ahmad et al., (2021) was developed as shown in Figure 2. By incorporating experimental data from the notch beam experiments conducted in (Ahmad et al., 2021), the numerical model was validated and refined.

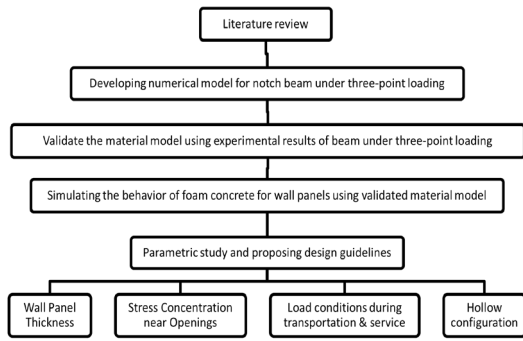


Figure 1: Flow chart of the methodology

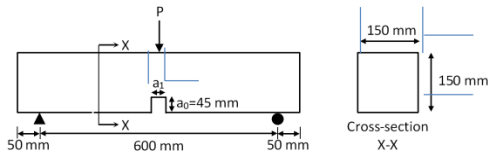


Figure 2: Geometry of the 20mm notch size beam

A finite element model for a foam concrete notch beam under three-point loading is created in ABAQUS and it is validated with the past experimental result by Ahmad et al., (2021). As material properties, the foam concrete density, Poisson's ratio, and Young's modulus are 1600 kg/m³, 0.2, and 12 GPa respectively. Table 1 shows the constitutive parameters used in the concrete damaged plasticity model for both the compressive and tensile behaviour of foamed concrete material. The parameters listed in Table 3 that are not measurable from the experiment mentioned in paragraph 2 above were taken using values from normal strength concrete (Abaqus 6.9, 2009, Jankowial & Lodygowski, 2005, Jason et al., 2004, Lee & Fenves, 1998, Mokhatar & Abdullah, 2012, Sourav Basak & Paul, 2012).

Table 1: Concrete damage plasticity properties of foam concrete

Concrete Damaged Plasticity (assumed)					
Dilatation Angle	Eccentricity	Initial biaxial/uniaxial ratio, σ_2/σ_1	K	Viscosity	
27°	0.1	1.16	1	0	
Compressive Behaviour from Experiment			Tension Behaviour from Experiment		
Yield stress f_c (Mpa)	Inelastic strain	Damage parameter, D	Yield stress f_t (Mpa)	cracking strain	Damage parameter, D
8.751	0	0	0.861	0	0
9.850	0.0017	0	0.776	0.00159	0.204
10.356	0.0033	0	0.605	0.00409	0.476
10.032	0.0041	0.215	0.518	0.00526	0.582
9.714	0.0047	0.337	0.431	0.00638	0.673
9.357	0.0055	0.456	0.345	0.00746	0.752
8.734	0.0066	0.577	0.259	0.00854	0.824
7.725	0.0078	0.682	0.173	0.00966	0.889
5.450	0.0127	0.862	0.086	0.01082	0.947
3.962	0.0194	0.934	0	0.01202	1

Once the numerical model was validated, a comprehensive parametric study on foam concrete wall panels was conducted.

4. Results and Discussion

4.1 Validation of the model

In Figure 3, envelop curves are formed by connecting the peak points of the experimental and numerical results obtained for the load-displacement curve. The figure reveals similarities between the peak point and corresponding failure displacement of the obtained result and the experimental result, though there are mismatches in the stiffness of the curve. Figure 4 shows the crack pattern of the validated notch beam.

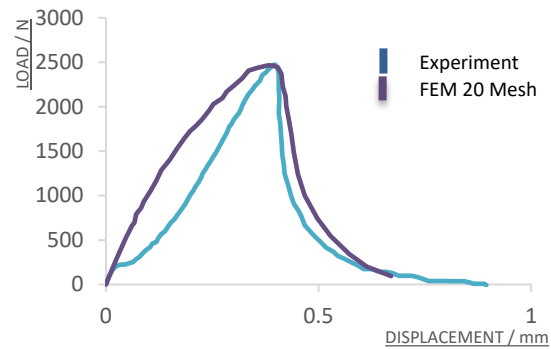


Figure 3: Comparison of experimental and Numerical envelope curves

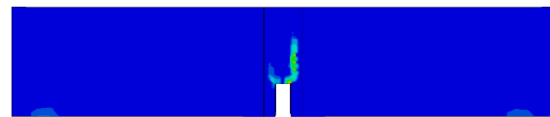


Figure 4: The crack pattern of the notch beam

4.2 Parametric study

After successfully validating the model of the foam concrete wall panel, a parametric study can be conducted to explore the effects of various parameters on the panel's behaviour and performance. This study involves systematically varying one or more input parameters while keeping others constant to observe their influence on the response of the wall panel. Parameters are wall panel thickness, stress concentration behaviour near openings, the choice between hollow or solid panels, and wall panel transportation and service condition. For the parametric study, the mesh size was chosen as 20mm as same as in the validated model.

Thickness - Varying wall panel thickness from 100 to 225 mm in simulations explores its impact on load capacity, as shown in Figure 5

while maintaining constant dimensions of 2400 x 600 mm.

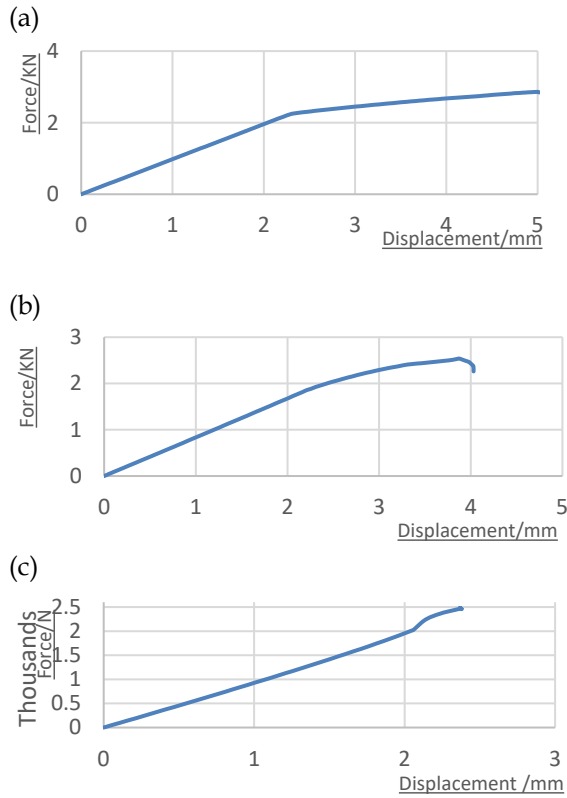


Figure 5: Force displacement curves for thicknesses of (a) 225mm, (b) 150mm, (c) 100mm

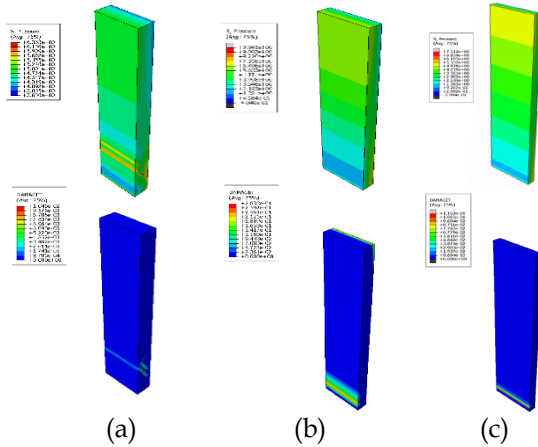


Figure 6: Pressure distribution and crack pattern wall panels having thicknesses of (a) 225mm, (b) 150mm, (c) 100mm

Hollow configuration - Comparing hollow and solid wall panels reveals insights into their structural behaviour. In Figure 7, 8, and 9 hollow panels, with radius of 25mm and 45mm for 225mm, 150mm, and 100mm configurations, offer benefits such as weight reduction, enhanced thermal insulation, and greater design flexibility.

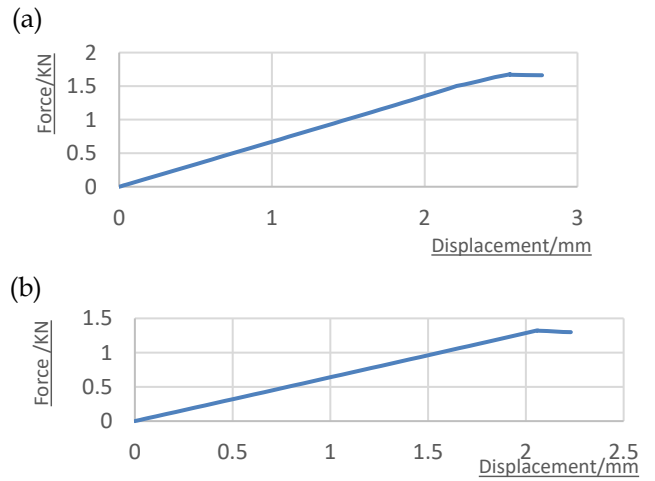


Figure 7: Force displacement curves for thickness of 225mm hollow radius (a) 25mm, (b) 45mm

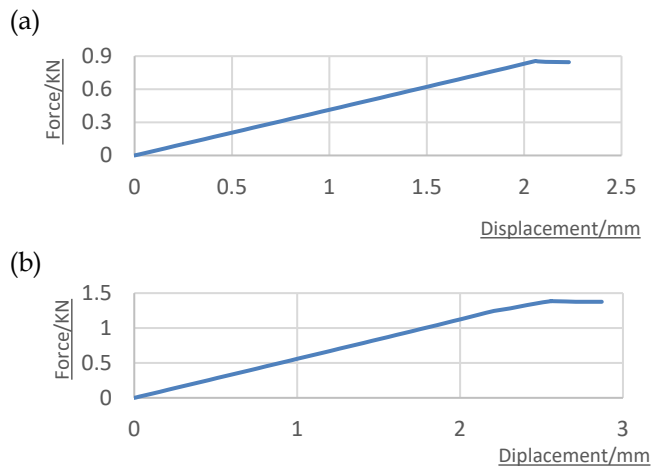


Figure 8: Force displacement curves for thickness of 150 mm hollow radius (a) 25mm, (b) 45mm

Wall panel transportation and service condition- The number of wall panels that can be stacked on top of each other without damage during transportation and service conditions should be checked. Starting with 5 panels and ending with 10 panels, slight cracks appeared in panels 9 and 10. Consequently, it can be concluded that 8 panels can be stacked safely on top of each other.

Table 2: Load applied on the bottom panel with the number of panels stacked on each other

Number of panels	Load apply on the bottom panel/(KN/m)
5	7.0
8	11.3
9	12.7
10	14

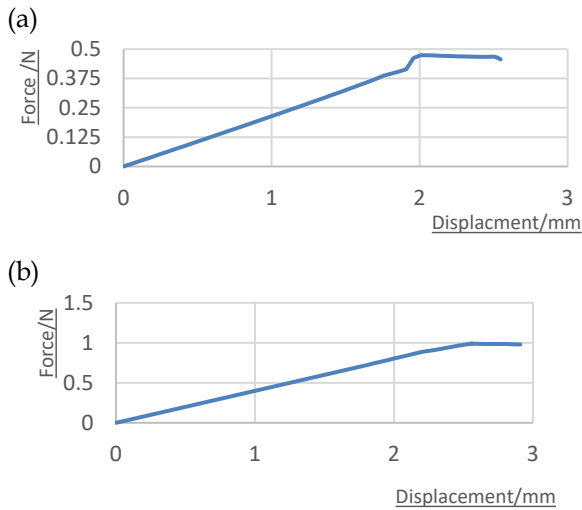


Figure 9: Force displacement curves for thickness of 100 mm hollow radius (a) 25mm, (b) 45mm

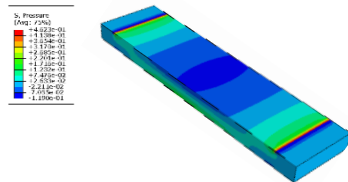


Figure 10: Pressure distribution for 8 panels

5. Conclusions

- The results suggest that foam concrete walls can be used as effective non-load-bearing partition walls.
- Increasing the cross-sectional area of foam concrete wall panels by 50% and 125% results in a proportional increase in their load-carrying capacity, with a corresponding improvement of approximately 3% and 16.3%.
- Depending on the density, thickness, and compressive strength of foam concrete wall panels, the maximum number of wall panels stacked together in transportation should be determined. For our selected compressive strength and $t=150\text{mm}$, 8 walls can be stacked together in transportation.

Table 3: Load carrying capacity reduction, void increment for each thickness

Thickness (mm)	Radius of a void (mm)	Void increment (%)	Load carrying capacity reduction (%)
225	25	9	41.7
	45	24	54.1
150	25	13	45.3
	45	35	66.4
100	25	20	59.8
	45	53	80.7

References

Ahmad, H.I.L.T.O.N., Sugiman, S.U.G.I.M.A.N., Jaini, Z.M. and Omar, A.Z. (2021) 'Numerical Modelling of Foamed Concrete Beam under Flexural Using Traction-Separation Relationship', Latin American Journal of Solids and Structures, 18.

Bhat, F.Z. and Kanni, S., FINITE ELEMENT ANALYSIS OF CONCRETE SPECIMEN. *Bone*, 5, p.10

Goh, W.I., Mohamad, N., Abdullah, R. and Samad, A.A.A. (2014) 'Compression test and finite element analysis of foamed concrete cube', Journal of Engineering and Technology (JET), 5(1), pp.1-10.

Huang, S., Hu, M., Huang, Y., Cui, N. and Wang, W. (2018) 'A new model for optimal mechanical and thermal performance of cement-based partition wall', *Materials*, 11(4), p.615.

Joda, S.A.A., Samad, A.A.A. and Mohamed, N. (2020) 'Numerical analysis of precast wall panels with openings', *International Journal of Sustainable Construction Engineering and Technology*, 11(2), pp.30-41.

Kozłowski, M., Kadela, M. and Gwozdź-Lason, M. (2016) 'Numerical Fracture Analysis of Foamed Concrete Beam Using XFEM Method', *Applied Mechanics and Materials*, 837, pp. 183–186. Available at: <https://doi.org/10.4028/www.scientific.net/AMM.837.183>.

Raj, A., Sathyan, D., & Mini, K. M. (2019) 'Physical and functional characteristics of foam concrete: A review', *Construction and Building Materials*, 221, 787-799.

Ramamurthy, K., Nambiar, E. K., & Ranjani, G. I. S. (2009) 'A classification of studies on properties of foam concrete', *Cement and concrete composites*, 31(6), 388-396.

Chloride Penetration of Concrete Containing High-Volume Supplementary Cementitious Materials

Nilakshi L.M.S.*, Rajapaksha M.Y.S.K., and Pathirana C.K.

Department of Civil Engineering, Faculty of Engineering, University of Peradeniya, Sri Lanka

** shanikanilakshi7291@gmail.com*

Keywords: Supplementary Cementitious Materials, Chloride Penetration, Strength, Fly Ash, Silica Fume

Abstract

Due to its coastal location, concrete structures in Sri Lanka, exposed to chloride ions, face durability issues. This study explores the impact of incorporating Supplementary Cementitious Materials (SCMs) like Silica Fume (SF) and Fly Ash (FA) on chloride penetration. Various mix designs were tested with different replacement levels of Ordinary Portland Cement (OPC) by SF and FA. Results showed that the 5SF+10FA mix achieved maximum compressive strength, surpassing the control sample by 5% at 28 days. The 10SF+30FA mix demonstrated the most significant reduction in chloride penetration, reaching a 62% decrease at 28 days and 87% at 42 days. Optimal results were observed in the 10SF+30FA mix, balancing chloride resistance and achieving target strength.

1. Introduction

Concrete, vital in construction, raises environmental concerns with its significant carbon emissions (Zhang et al., 2019). To mitigate this, SCMs are introduced, partially replacing cement while improving environmental impact and concrete properties.

Chloride attack compromises reinforced concrete by corroding embedded steel, leading to deterioration, cracking, and structural weakening. Factors like pore structure, and water/cement ratio influence chloride penetration over time. SCMs like SF and FA effectively minimize such penetration.

While studies have explored concrete with SF or FA individually, limited research exists on their combined use. This study experiments with eleven mixes, varying FA (0%-60%) and SF (0%-10%) to determine the optimal combination for enhanced chloride penetration resistance.

2. Literature Review

Various investigations have looked into the possibility of replacing OPC with SF and FA. The mix combination consisting of 12.5% SF and 5% FA demonstrated the maximum 28-day compressive strength (72.1 MPa) (Sanjeewa et al., 2017). Thushara et al., (2015) found that the maximum compressive strength (61.4 MPa) achieved consisted of 10% FA, in 28 days. Zhang et al., (2019) found that the highest 28-day compressive strength was achieved at 5% SF (25.45 MPa). Self-consolidating concrete (SCC) mixture with 40% FA replacement shows adequate compressive strength (33 MPa) at 28 days (Xin et al., 2014).

Chin et al., (2012) also found that compressive strength and chloride penetration vary according to the w/c ratio. Naleem & Rafat, (2012) found that increasing concrete temperature boosts tensile strength when mixed with fly ash but also increases chloride penetration, contrasting its beneficial impact at normal temperatures.

3. Methodology

3.1 Experimental Procedure

In the experimental procedure, eleven mix proportions were tested for workability, density, compressive strength, split tensile strength, and chloride penetration. The amounts of SF, FA, and OPC were varied while keeping the total mass of binder content constant at 385 kg/m³. The coarse aggregate, fine aggregate, and water mass were kept constant across all of the concrete mixes.

3.2 Material Testing

Materials were tested by BS, EN, and ASTM standards. The specific gravity of hydraulic cement was found to be 3.02 at 31 °C, the specific gravity of the coarse aggregate was found to be 2.77 and the specific gravity of fine aggregate was found as 2.63. The fine aggregate and coarse aggregate were analysed through

Table 1: Mix proportion

Sample No.	Sample	Water (kg/m ³)	Aggregate /(kg/m ³)		Cement (kg/m ³)	FA (kg/m ³)	SF (kg/m ³)
			Coarse	Fine			
S1	100 OPC (Control Sample)	225.00	867.35	893.03	384.62	-	-
S2	10FA+90OPC	225.00	867.35	893.03	346.15	38.46	-
S3	20FA+80OPC	225.00	867.35	893.03	307.69	76.92	-
S4	30FA+70OPC	225.00	867.35	893.03	269.23	115.38	-
S5	40FA+60OPC	225.00	867.35	893.03	230.77	153.85	-
S6	50FA+50OPC	225.00	867.35	893.03	192.31	192.31	-
S7	60FA+60OPC	225.00	867.35	893.03	153.85	230.77	-
S8	5SF+10FA+85OPC	225.00	867.35	893.03	326.92	38.46	19.23
S9	5SF+20FA+75OPC	225.00	867.35	893.03	288.46	76.92	19.23
S10	10SF+30FA+60OPC	225.00	867.35	893.03	230.77	115.38	38.46
S11	10SF+40FA+50OPC	225.00	867.35	893.03	192.31	153.85	38.46

sieve analysis, showing a well-graded shape of the gradation.

3.3 Mix Proportioning

A mix design for the control mix targeted for a strength of 30 MPa with no SF and FA was carried out, as a control sample in the DOE Manual for a slump of 60 –180 mm. The resulting mix proportions were 385 kg/m³ of cement, 867 kg/m³ of coarse aggregate, 893 kg/m³ of sand, and 225 kg/m³ of water. The ten mix combinations proposed for SF and FA are shown in Table 1.

The notation xSF, yFA stands for x% replacement of cement with SF and y% replacement of cement with FA both by weight. The mix combinations were categorized into six fly ash series, namely 10FA, 20FA, 30FA, 40FA, 50FA, and 60FA. For example, FA10 would stand for 10% of OPC replaced with FA. In each of the SF and FA series, 5SF+10FA, 5SF+20FA, 10SF+30FA, and 10SF+40FA are tested. The total mass of the binder material was kept constant at 385 kg/m³. The amounts of coarse aggregate, fine aggregate, and water were also kept constant in all of the mix combinations.

Cubes of size 150×150×150 mm³, cylinders of size 150 mm diameter and 300 mm height, and cylinders of diameter 100 mm and thickness of 50 mm specimens were cast and tested for their 28-day and 42-day, compressive strengths by ASTM C39/C39M, split tensile strength by ASTM C496 and rapid chloride penetration test by ASTM C1202 for 28-day. A slump test was carried out for all mix combinations by ASTM C143 guidelines and the variation of the workability was observed. The density for all mix combinations was tested according to Density ASTM C138/C138M.

4. Results and Discussion

Test results were analysed for workability, density, 28-day compressive strength and 42-day compressive strength, 28-day split tensile strength and 42-day split tensile strength, and 28-day chloride penetration.

4.1 Results for Workability and Density

Table 2 shows the workability and density results of eleven mixes including the control sample.

Table 2: Workability and density results

Sample	Slump (mm)	Density (kg/m ³)
S1	178	2.390
S2	156	2.381
S3	176	2.368
S4	173	2.340
S5	171	2.335
S6	144	2.332
S7	133	2.331
S8	110	2.330
S9	102	2.342
S10	85	2.350
S11	78	2.371

The values obtained for workability and density are illustrated in Figures 1 and 2.

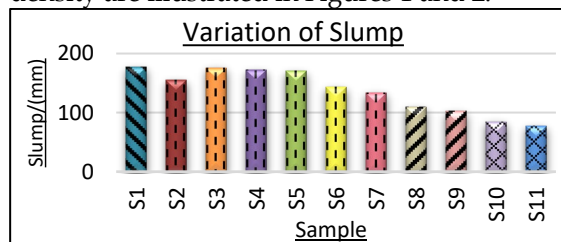


Figure 1: Workability results

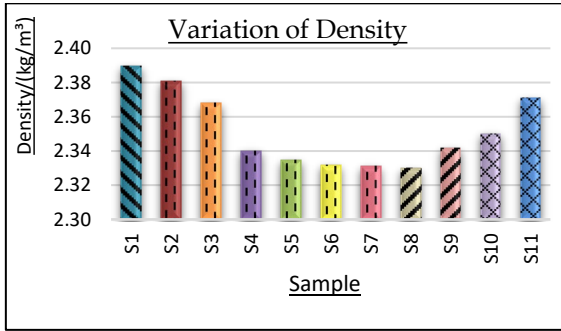


Figure 2: Density results

The control sample showed maximum workability and density. The 5SF+20FA mixture had minimum workability, while the 5SF+10FA sample had the lowest density. SCMs are finer than cement. Therefore, it absorbs more water, reducing workability.

4.2 Results of Compressive Strength and Split Tensile Strength

Table 3 shows the compressive strength and split tensile strength results of eleven mixes including the control sample for 28-day and 42-day.

Table 3: Strength results

Sample no.	Compressive Strength (MPa)		Tensile Strength (MPa)	
	28 days	42 days	28 days	42 days
S1	42.67	45.62	2.995	3.103
S2	42.98	44.88	2.410	2.471
S3	38.55	41.16	2.702	2.725
S4	32.84	38.75	2.234	2.773
S5	31.89	33.45	2.190	2.375
S6	20.53	25.51	1.303	1.877
S7	11.88	15.63	0.607	1.120
S8	45.40	47.25	2.817	3.153
S9	41.49	45.38	2.226	2.410
S10	32.74	38.09	2.089	2.551
S11	17.17	22.87	1.092	1.435

Figure 3 and Figure 4 show the variation of compressive and tensile strength of 28-day and 42-day.

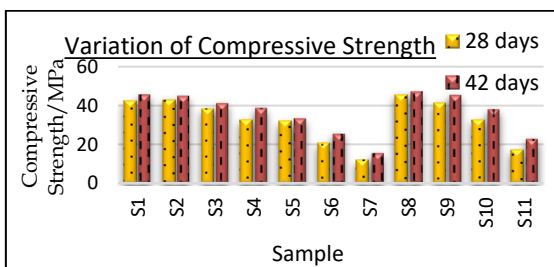


Figure 3: Compressive strength results

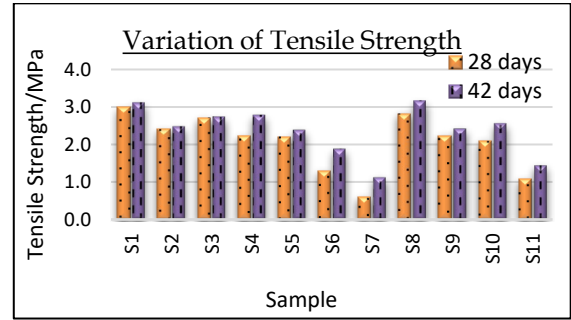


Figure 4: Split tensile strength results

Maximum compressive strength was taken by sample with 5SF+10FA mix. That is 5% higher than the control sample at 28 days. Only 5SF+10FA and 10FA samples passed the strength of the control sample. The 60FA sample achieved minimum compressive strength and it is 28% less than the control sample. After 42 days, compressive strength was increased in every sample. Compressive strength decreases with the proportion of FA and can be increased by adding SF to FA. SCMs refine concrete's pore structure through pozzolanic reactions, forming additional C-S-H, reducing porosity, and increasing strength.

Maximum tensile strength was achieved by the control sample at 28 days and the 5SF+10FA sample at 42 days. Minimum tensile strength achieved by the 60FA sample. However, all samples have approximately the same tensile strength, and with curing age, tensile strength was increased.

4.3 Results of the Chloride Penetration Test

Table 4 shows the 28-day chloride penetration test results and 5 shows the Chloride Ion Penetrability Classifications from ASTM C1202

Table 4: Chloride penetration test results

Sample no.	Charge Passed 28 days (coulombs)	Charge Passed 42 days (coulombs)
S1	5443	4937
S2	5349	4444
S3	3026	1253
S4	2391	1002
S5	2268	1768
S6	4923	3100
S7	5763	5249
S8	3894	2398
S9	2871	2010
S10	2073	636
S11	3137	2126

Table 5: Chloride ion penetrability classification from ASTM C1202

Charge Passed (coulombs)	Chloride Ion Penetrability
> 4000	High
2000-4000	Moderate
1000-2000	Low
100-1000	Very Low
< 100	Negligible

Figure 5, shows that the chloride penetration test results in coulombs.

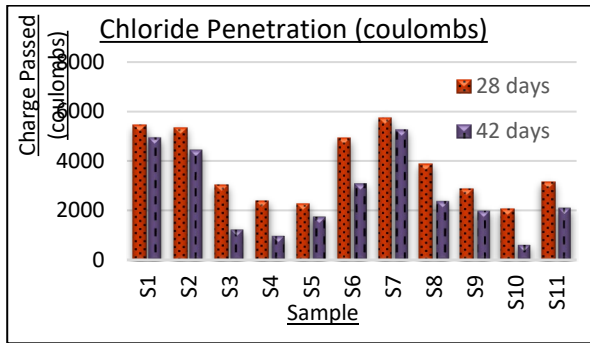


Figure 5: Chloride penetration test results

10SF+30FA sample achieved the minimum chloride penetration results. That is a 62% reduction from the control sample and it was in the moderate chloride ion penetration range. Chloride penetration significantly reduces with increasing FA content up to 40% and FA mix with SF. Improved particle packing reduces porosity and decreases chloride penetration.

5. Conclusions

This study investigated the behavior of chloride penetration, compressive and tensile strength, workability, and density for concrete mix with FA and SF. Based on the results of this experimental study, the following conclusions were found.

1. The control sample exhibited the highest workability, while the 5SF+20FA mixture showed the least.
2. Maximum density was observed in the control sample, and the 5SF+10FA sample demonstrated the minimum density.
3. 5SF+10FA mix exceeded control strength by 5% at 28 days. 60FA had 28% less strength. All strengthened at 42 days, and SF counteracted FA's strength decrease.
4. The control sample peaked in tensile strength at 28 days; 5SF+10FA excelled at 42 days. 60FA had the least strength, but overall, strength increased with curing age.
5. The control sample peaked in tensile strength at 28 days; 5SF+10FA excelled at

- 42 days. 60FA had the least strength, but overall, strength increased with curing age.
6. The 10SF+30FA mix reduced chloride penetration by 62% at 28 days and 87% at 42 days, showing effective resistance.
7. Best mix: 10SF+30FA, minimal chloride penetration, meets target strength.

References

Lee, C.-L., Huang, R., Lin, W.-T. and Weng, T.-L. (2012) 'Establishment of the durability indices for cement-based composite containing supplementary cementitious materials', *Materials & Design*, 37, pp.28-39. Available at: <https://doi.org/10.1016/j.matdes.2011.12.030>.

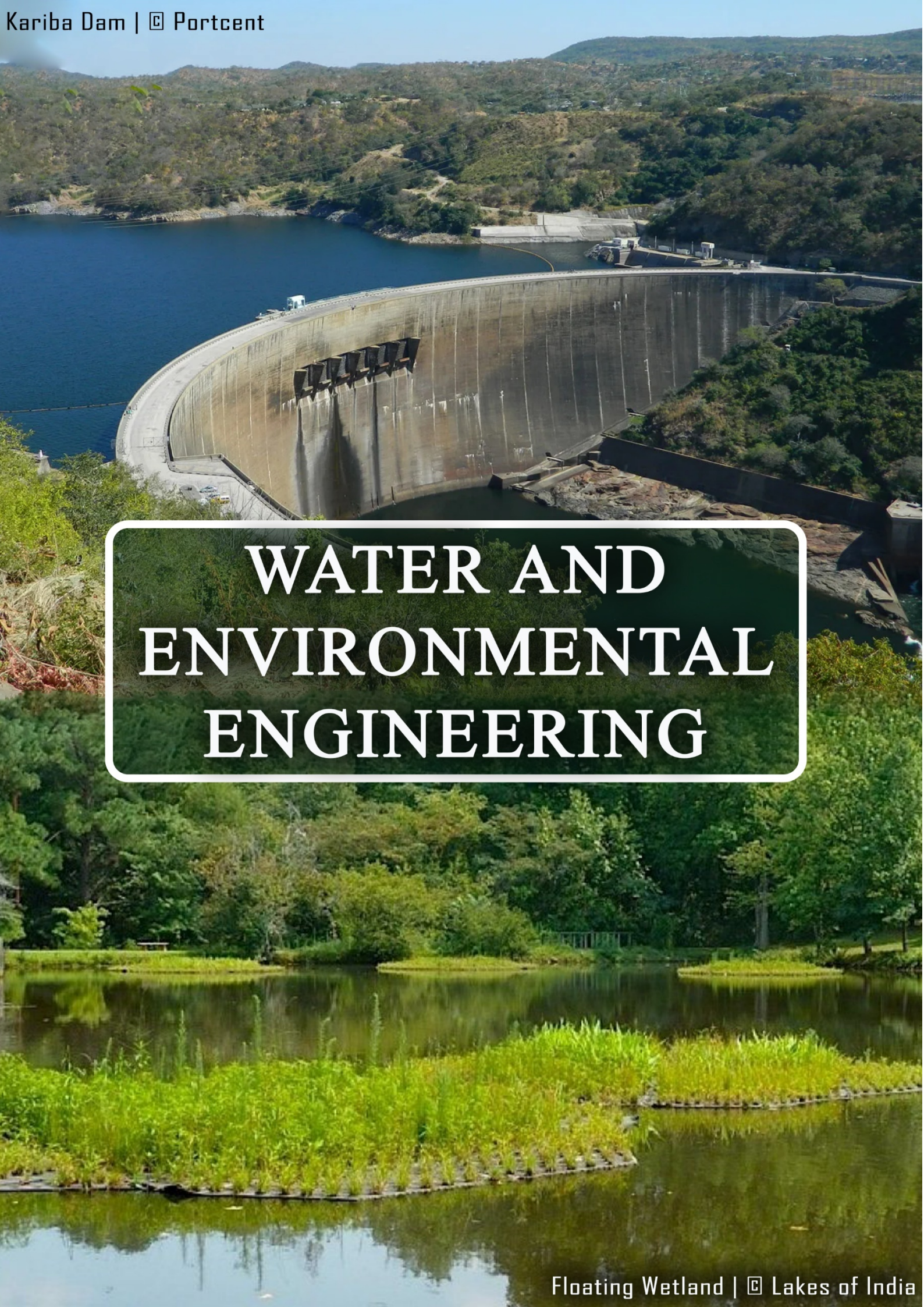
Pathak, N. and Siddique, R. (2012) 'Properties of self-compacting concrete containing fly ash subjected to elevated temperatures', *Construction and Building Materials*, 30, pp.274-280. Available at: <https://doi.org/10.1016/j.conbuildmat.2011.11.010>.

Priyadarshana, T., Dissanayake, R. and Mendis, P. (2015) 'Effects of Nano Silica, Micro Silica, Fly Ash and Bottom Ash on Compressive Strength of Concrete' *Journal of 37 Civil Engineering and Architecture*, 9(10). Available at: <https://doi.org/10.17265/1934-7359/2015.10.002>.

Sanjeeva, R.M.D.M., Pathirana, P.S.K. and Yapa, H.D. (2017) 'Mix Design Aspects of High-Performance Concrete Comprised of Silica Fume and Fly Ash. Engineer', *Journal of the Institution of Engineers, Sri Lanka*, 50(4), p.23. Available at: <https://doi.org/10.4038/engineer.v50i4.7272>.

Wang, X., Wang, K., Li, J., Garg, N. and Shah, S.P. (2014). Properties of self-consolidating concrete containing high-volume supplementary cementitious materials and nano-limestone. *Journal of Sustainable Cement-Based Materials*, 3(3-4), pp.245-255. doi <https://doi.org/10.1080/21650373.2014.954155>.

Zhang, Y., Zhang, J., Luo, W., Wang, J., Shi, J., Zhuang, H. and Wang, Y. (2019) 'Effect of compressive strength and chloride diffusion on life cycle CO2 assessment of concrete containing supplementary cementitious materials', *Journal of Cleaner Production*, 218, pp. 450-458. Available at: <https://doi.org/10.1016/j.jclepro.2019.01.335>.



WATER AND ENVIRONMENTAL ENGINEERING

Application of HEC-HMS Model on Event-Based Simulation in Kalu Ganga

Kamburugamuwa S.W.*, Netthikumara N.K.Y., and Nandalal H.K.

Department of Civil Engineering, Faculty of Engineering, University of Peradeniya, Sri Lanka

* e17150@eng.pdn.ac.lk

Keywords: Calibration and Validation, Event-based rainfall, HEC-HMS, Rainfall-runoff model,

Abstract

Rainfall-runoff modelling is a crucial tool for authorities dealing with flood risks, particularly for rivers like the Kalu Ganga in Sri Lanka, which is prone to frequent flooding. The Hydrologic Engineering Center's Hydrologic Modelling System (HEC-HMS- 4.10 version) proves invaluable for simulating and analysing rainfall-runoff dynamics. Event-based hydrological modelling reveals how a basin responds to an individual rainfall event, which is very important in predicting a flood. This study assesses six combinations of rainfall-runoff models using various hydrological models to determine the most effective one for the Kalu Ganga Upper catchment up to Ellagawa. Criteria such as rainfall type (Event), spatial process (Semi-lumped), model type (Empirical), and relevant parameters (Fitted parameters) are considered based on the acquired data for the selection of model combinations. Event-based rainfall of four gauging stations in Rathnapura district and discharge at Ellagawa gauging station corresponding to the period of 2018-2021 is used in the calibration and validation process in this study. The initial parameters are optimized, and it's observed that each model combination performs differently for each event. Among the selected combinations, the Initial Constant method paired with the Clark Unit hydrograph, the Recession base flow method with Lag, and the Muskingum method exhibit superior performance. The model evaluation shows Nash Sutcliff value as 0.98, RMSE as 0.1, and Percent bias as 0.16. Visual assessments and statistical indicators from the study demonstrate that the developed model reasonably predicts floods in the basin. As a result, it can serve as a valuable tool for flood prediction, offering forecasts for flood peaks and their timing with a reasonable degree of accuracy.

1. Introduction

A rainfall-runoff model is a mathematical representation or simulation of the hydrological processes that convert precipitation into runoff.

These models attempt to estimate how rainfall and other factors influence the excess water to be transported through a watershed or catchment. Hydrologic Engineering Center - Hydrologic Modelling System (HEC- HMS) is one of the hydrological models that has the capability of transforming rainfall into runoff. This research describes a case study of developing event rainfall-runoff modelling using HEC-HMS to Kalu Ganga basin up to Ellagawa which is a located in wet zone of Sri Lanka with high flood frequency and the goal is to employ six alternative model combinations available in HEC-HMS software to identify the best model for the Kalu Ganga Ellagawa basin for event-based.

2. Literature review

In the early nineteenth century, rainfall-runoff modelling was mainly limited to the use of empirical formulas or the logical method to transform rainfall into surface runoff. Since the introduction of computers in 1960, computational models such as HEC-HMS, MIKE, and SHE have been developed to aid with tasks (Vijaykumar Kherde, 2016). In terms of flood forecasting, mostly it is required for cities with many floods and heavy rainfall throughout the year (Nandalal & Ratnayake, 2010; Gunathilake, 2019).

The model performance is not always improving by catchment scaling if most of the subbasins have same properties (Kanchanamala et al.,2016). Furthermore, for the role of selecting model performance objective functions are used. For example, for a minimization problem, the Weighted Root Mean Square (WRMS) method is commonly used, and for a maximization problem, Nash Sutcliffe or Total Runoff Volume is commonly used (Jayadeera & Wijesekera,2019).

3. Methodology

The methodology of this research has followed to develop and identify a Suitable rainfall-runoff model for the Ellagawa sub-basin and summarized workflow shows in Figure 1.

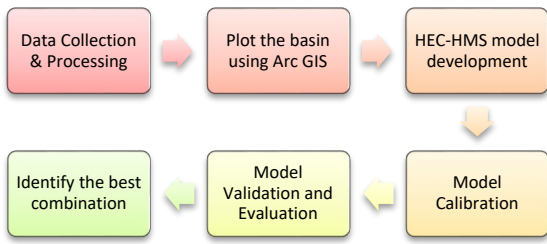


Figure 1: Methodology chart

3.1 Data collection and processing

Daily Rainfall data from 2017-2022 were purchased from the Department of Meteorology for the selected rain gauging stations at Ratnapura, Halwatura, Wellandura, and Allupola. Stream flow data for the same time were gathered from the Department of Irrigation from river gauging stations at Ratnapura and Ellagawa. Digital Elevation Model (DEM) and land use data were obtained from the Department of Survey.

The HEC-HMS model was calibrated and validated by identifying events where discharge maximum occurred after rainfall peaks as shown in Figures 2, and 3, excluding missing data spans. Then, Thiessen polygons were created using ArcGIS to calculate the catchment average rainfall in the Ellagawa sub-basin

accurately. Table 1 shows the durations of the events chosen for calibration and validation.

Table 7: Summary of the selected events

Event	Duration
Calibration Event 1	01/09/2021 - 12/09/2021
Validation Event 1	31/05/2018 - 07/06/2018
Validation Event 2	24/01/2018 - 31/10/2018
Validation Event 3	22/09/2021 - 30/09/2021

3.2 HEC HMS model development

After plotting the basin using Arc GIS, the map was imported to the HEC-HMS software to create watershed modelling components. The rainfall-runoff model in HEC HMS involves creating a basin model to convert atmospheric conditions into streamflow at specific locations in the Ellagawa watershed. The model is divided into sub-basins as shown in Figure 4 using GIS tools in HEC HMS software.

Three Hydrologic elements, Sub-basins, Reach, and Sink are connected in a dendritic network to represent the stream system in HEC HMS software as shown in Figure 5.

Table 2 presents the different combinations of HEC-HMS used in this study, here, the base flow method and the routine method remain the same for all selected combinations as the Recession method and Lag and Muskingum method respectively. The lag method is used in

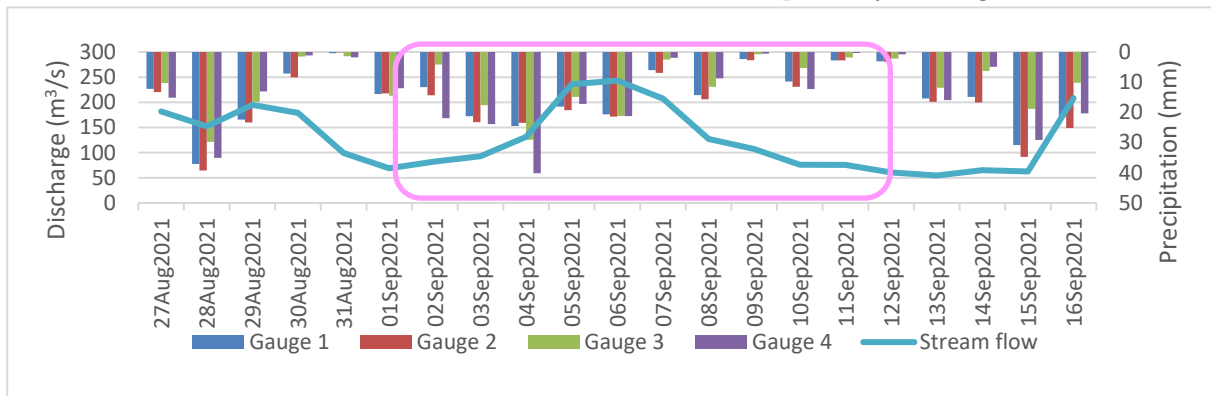


Figure 2: Calibration event (01/09/2021 - 12/09/2021)

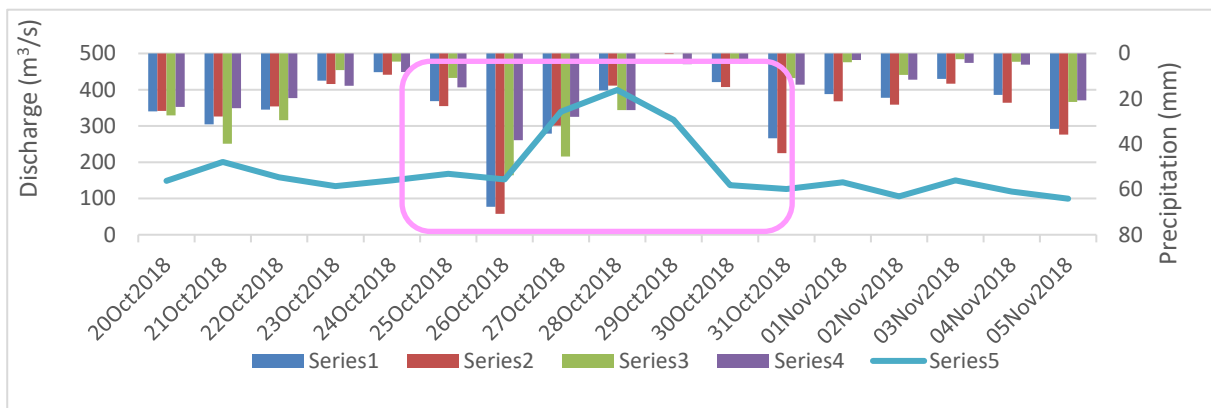


Figure 3: Validation event 2 (24/01/2018 - 31/10/2018)

steep slope areas, and the Muskingum method is used in mild slope areas in the Kalu Ganga. Model combinations are selected based on criteria such as rainfall type (Event), spatial process (Semi-lumped), model type (Empirical), and relevant parameters (Fitted parameters), compared.

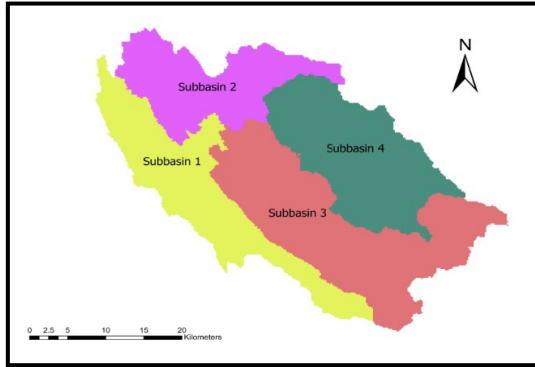


Figure 4: Sub-basins of Ellagawa watershed

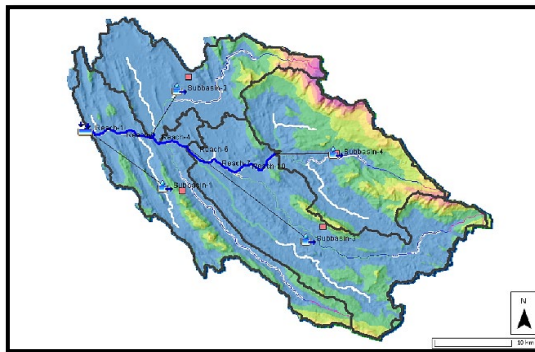


Figure 5: Hydrological elements represented in HEC HMS

Table 2: Different combinations adopted to simulate floods in the study

Combination	Direct runoff	Loss method
C1	Clark UH	Initial and constant method
C2	Snyder's UH	Initial and constant method
C3	SCS UH	Initial and constant method
C4	Clark UH	SCS curve No
C5	Snyder's UH	SCS curve No
C6	SCS UH	SCS curve No

4. Results and Discussion

4.1 Model Calibration

Model calibration is a process that involves changing the parameters of each model to find the best runoff hydrograph. Two methods used are simulation run and optimization run. In the simulation run, both observed and simulated hydrographs are compared, but the simulated hydrograph may not fit with the observed one.

Parameters are optimized in an optimization run to achieve more similar outputs. Model runoff was conducted for each rainfall event, with Nash Sutcliffe coefficients checked at each trial until near 1.00.

Table 3: Nash Sutcliffe value, RMSE value, and Percent bias for the calibration event

Combination	Nash-Sutcliff value	RMSE	Percent bias %
1	0.981	0.1	0.05
2	0.978	0.1	-0.06
3	0.978	0.1	0.16
4	0.98	0.1	-0.58
5	0.981	0.1	-0.65
6	0.98	0.1	-0.36

Figure 6 depicts the difference between observed and simulated hydrographs during the calibration event for combination 1. Variations for other combinations were discovered that were nearly identical to this variation.

4.2 Model Validation

After completing the calibration procedure, the model is ready for validation, where it's evaluated for correctness using identical objective functions and validation events for each combination.

Table 3,4,5,6 shows the Nash Sutcliffe, RMSE, and Percent bias values that yielded for each Calibration and Validation event through each model combination.

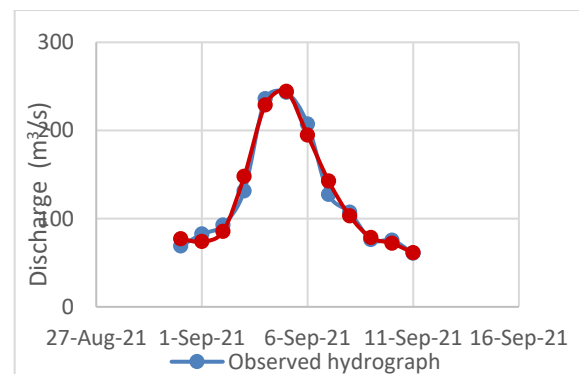


Figure 6: Combination 1 Observed discharge and simulated discharge graph

Table 4: Nash Sutcliffe value for validation events

Combination	V-event 1	V-event 2	V-event 3
1	0.940	0.531	0.857
2	0.905	0.528	0.831
3	0.936	0.692	0.904
4	0.894	0.784	0.836
5	0.890	0.773	0.827
6	0.628	0.704	0.833

Table 5: RMSE value for validation events

Combination	V-event 1	V-event 2	V-event 3
1	0.2	0.7	0.4
2	0.3	0.7	0.4
3	0.3	0.6	0.3
4	0.3	0.5	0.4
5	0.3	0.5	0.4
6	0.6	0.5	0.4

Table 6: Percent bias value for validation events

Combination	V-event 1	V-event 2	V-event 3
1	-3.64	15.30	-15.04
2	-2.54	15.11	-10.83
3	4.51	3.23	-4.42
4	-7.75	-14.19	-19.14
5	-8.36	-16.05	-19.14
6	6.12	-6.33	-15.68

4.3 Model Evaluation

HEC-HMS offers objective functions for model calibration, including Nash-Sutcliffe, RMSE, and Percent bias values, which can be used individually or combined to assess model performance. Out of all the combinations performed combination 3 shows the best performance. Figures 7, 8, and 9 show the validation results obtained for combination 3. According to the performance evaluation criteria, the ranking of the model combinations took place. For all the validation events model performance criteria were satisfied.

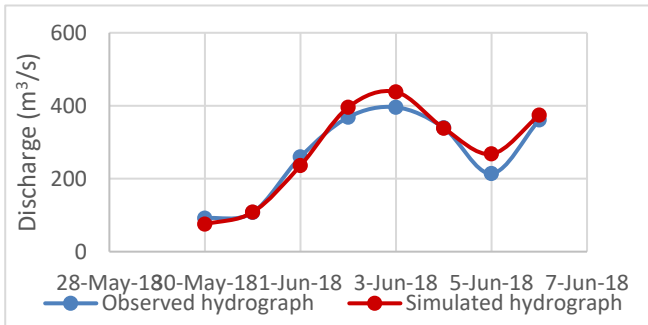


Figure 7: Observed and simulated hydrographs for Validation event 1- Combination 3

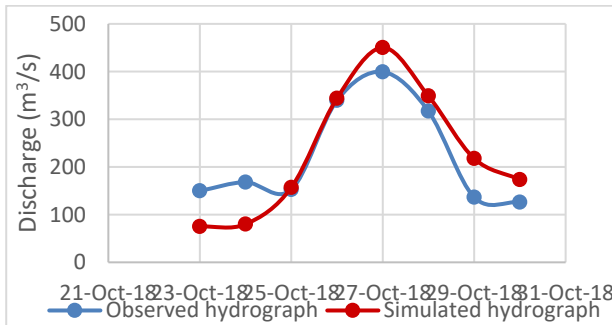


Figure 8: Observed and simulated hydrographs for Validation event 2- Combination 3

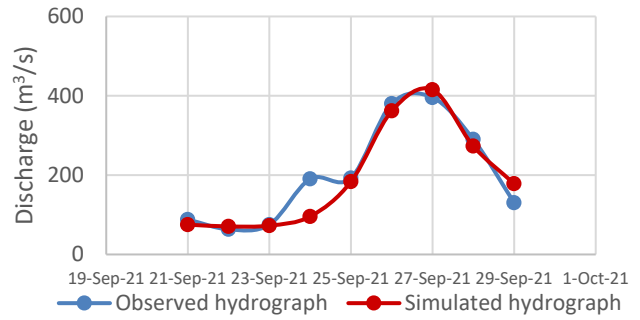


Figure 9: Observed and simulated hydrographs for Validation event 3- Combination 3

5. Conclusions

The study focused on identifying the optimal model combination for the Kalu Ganga basin up to Ellagawa using HEC-HMS 4.10, assessing six precipitation loss and runoff methods. The second validation event differs from the calibration event and the other two validation events in that it displays less rainfall for sub-basin 4 whereas the other events indicate maximum rainfall for sub-basin 4. The Initial constant technique performs well for validation events, but the SCS Curve Number method is better for the second validation event. The Curve Number approach, established for temperate conditions, may be inaccurate in tropical watersheds like the Kalu Ganga catchment, where rubber plantations and forests make up nearly half of the land use (Halwatura & Najim, 2013). Direct runoff techniques SCS UH, Clark UH, and Snyder UH show little variation. Based on the results, the Initial Constant technique was chosen as the loss method, the SCS Unit Hydrograph method as the transformation method, and the Recession method as the base flow method shows the best performance for the Kalu Ganga upper catchment area. Most studies traditionally use continuous rainfall in HEC-HMS for long-term water management, whereas our event-based hydrological modelling reveals basin responses to individual rainfall events, crucial for predicting floods in wet zone districts like Rathnapura.

References

Gunathilake, G.R.M.B., Panditharathne, P., Gunathilake, A.S. and Warakagoda, N.D. (2019) 'Application of HEC-HMS Model on Event-Based Simulations in the Seethawaka Ganga River, Sri Lanka', Scholar Journal of Applied Sciences and Research, 2(9), pp.32-40.

Halwatura, D. and Najim, M.M.M. (2013) 'Application of the HEC-HMS model for runoff simulation in a tropical catchment', Environmental Modelling & Software, 46, pp.155-162. Available at: <https://doi.org/10.1016/j.envsoft.2013.03.006>

Analyzing and Forecasting Rainfall Trends in Kirindi Oya River Basin

Withanage P.N.S., Wijeratne, P.W.G.R.S., and Nanayakkara, K.G.N.*

Department of Civil Engineering, Faculty of Engineering, University of Peradeniya, Sri Lanka

* nadeen@eng.pdn.ac.lk

Keywords: Artificial neural network, Forecasting, Innovative trend analysis, Mann-Kendall test, Rainfall trend

Abstract

Research in hydrology that focuses on identifying, detecting, and evaluating variability and rainfall trends is crucial for effective water resource planning and management. According to the reported literature, there is limited available literature on variability and rainfall trend analysis in the Kirindi Oya river basin, and no literature specifically focuses on rainfall forecasting. This study analyzed 31 years of rainfall data (1992-2022) from five rain gauge stations, employing various methods such as coefficient of variation, Mann-Kendall test, Sen's slope estimator, and innovative trend analysis. Findings showed a general rise in annual rainfall across stations, yet statistically insignificant trends. Forecasting using Long Short-Term Memory (LSTM) neural networks faced challenges in accurately predicting rainfall trends due to inherent study limitations. This research highlights the importance of studying rainfall variability for water resource management but acknowledges challenges in forecasting accurately for the Kirindi Oya basin

1. Introduction

Rainfall, as a form of precipitation, is the primary source of fresh water for all living beings and a fundamental component of Earth's hydrological cycle. Hence, changes in rainfall play a vital role in the environment, agriculture, and human health. Research on changes in rainfall occurrences is crucial for sustainable water resource management (Praveen et al., 2020). Therefore, variability and rainfall trend analysis hold significant importance in hydrology, climatology, and meteorology research across the globe. Furthermore, forecasting based on rainfall data would be helpful for decision-makers to determine water availability for agriculture, industry, and the general population. (Alahacoon & Edirisinghe, 2021).

2. Literature Review

In most studies, researchers have used statistical methods such as linear regression test, Mann-Kendall test (MK), Modified Mann-Kendall test (MMK), Sen's slope estimator (SSE), and Spearman rank correlation test (SR) for rainfall trend analysis and coefficient of variation (CV), precipitation concentration index (PCI), and standardized anomaly index (SAI) for rainfall variability. Statistical techniques, physical models, and machine learning (ML) models can be used to forecast hydro-climatic variability. Past studies (Dankwa et al., 2021; Rahman et al., 2017) have used statistical techniques like the autoregressive integrated moving average (ARIMA) model to perform precipitation forecasts, but these models show a limited ability to capture major nonlinear features of rainfall series (Perez-Alarcón et al., 2022). Therefore, machine learning (ML) has gained popularity for water management and rainfall prediction.

The importance of water resource planning and management in the Kirindi Oya basin has increased with the rise in population, climate change, and industrialization. (Abeysingha et al., 2017). According to the reported literature, there are limited studies on the variability and rainfall trend analysis of the Kirindi Oya river basin, and no literature was found related to the forecasting of rainfall in the basin.

2.1 Rainfall variability

The variability of rainfall is the extent of fluctuations or changes in the amount of rainfall over a specific period. Coefficient of variation (CV) is a widely used method to assess the variability of rainfall in reported literature (Nisansala et al., 2019).

$$CV = \frac{\sigma}{\mu} * 100 \quad (1)$$

2.2 Rainfall Trend Analysis

Rainfall trend analysis involves examining historical rainfall data to identify patterns and changes. Rainfall trend analysis methods can be

broadly categorized into statistical and graphical methods.

Graphical technique, the innovative trend analysis (ITA) is a simple technique developed by Sen that gives a qualitative rather than a quantitative analysis (Sen, 2012).

$$D = \frac{1}{n} \sum_{i=1}^n \frac{10(y_i - x_i)}{\bar{x}} \quad (2)$$

D is the ITA trend indicator, and a positive value for D indicates an increasing trend, whereas a negative value indicates a decreasing trend (Nisansala et al., 2019).

MK is a widely used non-parametric statistical test to determine climatic trends.

$$S = \sum_{i=1}^{n-1} \sum_{j=i+1}^n \text{sgn}(X_j - X_i) \quad (3)$$

$$\text{sgn}(X_j - X_i) = \begin{cases} +1, & > (X_j - X_i) \\ 0, & = (X_j - X_i) \\ -1, & < (X_j - X_i) \end{cases} \quad (4)$$

$$\text{Var}(S) = \frac{n(n-1)(2n+5) - \sum_{i=1}^m t_i(i)(t_i(i)-1)(2i+5)}{18} \quad (5)$$

$$Z_c = \begin{cases} \frac{S-1}{\sqrt{\text{Var}(S)}}, & S > 0, \\ 0, & S = 0, \\ \frac{S+1}{\sqrt{\text{Var}(S)}}, & S < 0, \end{cases} \quad (6)$$

A positive Z_c value indicates an upward trend, whereas a negative Z_c value indicates a downward trend time (Alahacoon & Edirisinghe, 2021).

SSE is usually combined with the MK test and can be used to identify the magnitude of the trend.

$$Q_i = \frac{x_j - x_k}{j - k} \quad (7)$$

When Q_i is positive, it means that there is an increasing trend. A negative value of Q_i reveals a decreasing or downward trend (Nisansala et al., 2019).

2.3 Rainfall Forecasting

ML models like Artificial Neural Network (ANN) have gained popularity in water-related studies due to their capability to capture

nonlinear and nonstationary patterns hidden in time series.

ANN is a computational model inspired by the structure and functioning of biological neural networks of the human brain. Among different types of architectures in ANN, LSTM is a widely used neural network for sequential data (Pérez-Alarcón et al., 2022).

3. Methodology

The Kirindi Oya River basin, located in Sri Lanka's dry zone's South-eastern part is an important source of irrigation for the dry zone downstream. It is one of the principal sources in the water distribution model for Weeravila tank cascade systems. Additionally, the upstream catchments and the mid-stream sub-catchment have a tendency to dry out. Therefore, studying hydro-climatic trends in the Kirindi Oya River basin is essential.

In this study, daily rainfall data spanning 31 years (1992-2022) from five rain gauge stations – Bandara Eliya State, Handapanagala, Lunugamwehera, Thissamaharama Irrigation, and Wellawaya – was considered. The data was purchased from the Department of Meteorology. Missing rainfall data within the selected period was filled using the normal ratio method, which estimates the missing values based on the average rainfall from nearby stations. To ensure data consistency, a double mass curve analysis was conducted, plotting cumulative rainfall data from the target station against reference stations to detect inconsistencies. The temporal variability was quantified using the CV. Trend analysis was performed using the MK test, SSE, and ITA to identify and quantify trends in the data. For forecasting future rainfall, the LSTM network was utilized due to its effectiveness in handling sequential data and capturing long-term dependencies in time series forecasting. Finally, the Nash-Sutcliffe efficiency (NSE) and the R-squared (R^2) were used to evaluate the model efficiency.

4. Results and Discussion

4.1 Variability of Annual Rainfall

Figure 1 displays the annual rainfall along with the corresponding five-year running mean, which is used to smooth the series, for five selected rain gauge stations from 1992 to 2022. Across all stations, the use of the five-year

running mean clearly illustrates varying trends in annual rainfall.

Table 1 shows the CV values of the annual rainfall of five stations. Handapanagala station has a high degree of variability, and the Lunugamwehera station has a Lower degree of variability while the other three stations have a moderate degree of variability. Most of the stations represented moderate CV, meaning all stations have homogenous characters in terms of precipitation variations.

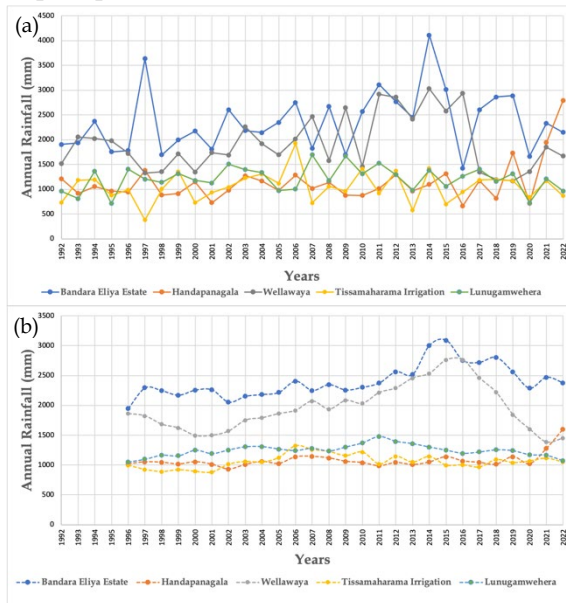


Figure 1: (a) Annual Rainfall Variation (b) Five-year running mean

Table 1: CV values

Station	CV (%)
Bandara Eliya Estate	25.25
Handapanagala	35.54
Wellawaya	28.37
Tissamaharama Irrigation	28.27
Lunugamwehera	19.96

4.2 Rainfall Trend Analysis

Table 2 presents the results of the MK test. According to the results, annual rainfall at 5 locations showed an upward trend, but none were significant ($p < 0.05$).

The MK test and SSE produce almost similar trends in all five stations. Nevertheless, the ITA method depicts a negative insignificant trend in Tissamaharama Irrigation station, in contrast to the upward insignificant trend suggested by the other two methods.

Table 3 demonstrates the Sen’s Slope for each station. The highest rainfall trend is seen in Bandara Eliya Estate.

Table 2: Summary of MK test

Station	Z
Bandara Eliya Estate	1.7676
Handapanagala	0.9178
Wellawaya	0.3739
Tissamaharama Irrigation	0.3739
Lunugamwehera	0.1020

Table 3: Summary of SSE test

Station	SSE (mm/year)
Bandara Eliya Estate	24.93
Handapanagala	5.37
Wellawaya	5.10
Tissamaharama Irrigation	3.37
Lunugamwehera	0.44

Table 4: D values of the ITA test

Station	D
Bandara Eliya Estate	1.61
Handapanagala	1.79
Wellawaya	1.35
Tissamaharama Irrigation	-0.12
Lunugamwehera	0.16

4.3 Forecasting

The time series comparison of actual and predicted values for the training data and the scatter plot of actual and predicted values for the training data with the R-squared value for Wellawaya are shown in Figure 2 and Figure 3, respectively. Both graphs indicate a weak correlation and limited predictive accuracy. The statistical measures used to validate the model forecast for Wellawaya Station, R^2 and NSE, were 0.42 and 0.38, respectively. These values confirm what is visually evident in Figure 2, clearly indicating that further improvement of the model is needed. However, due to certain limitations, additional improvements couldn't be implemented. These limitations are:

- The study's dataset is small, causing the LSTM model to overfit to noise and resulting in poor generalization to new data.
- Optimizing LSTM hyperparameters was a challenging task.
- LSTMs struggle with extreme events, and since the dataset includes such events, the model's performance is compromised.
- The study relies solely on a single input variable, rainfall, potentially limiting the model's predictive capacity by excluding other relevant variables.

The other four rain gauge stations show the same results as Wellawaya.

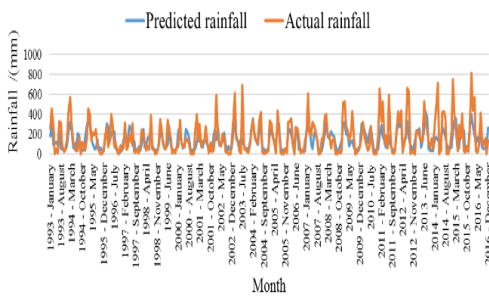


Figure 2: Comparison of actual and predicted monthly rainfall for the training data for Wellawaya.

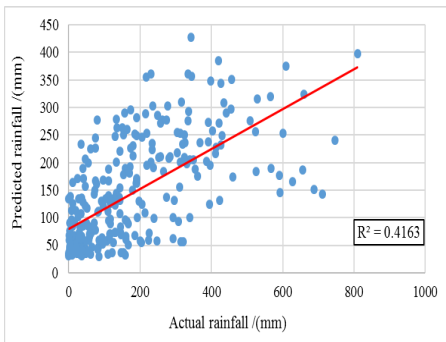


Figure 3: Scatter plot of actual and predicted rainfall for the training data with R^2 value for Wellawaya.

5. Conclusions

The findings indicate that only the Handapanagala station exhibits a high degree of variability, while the other stations show a moderate or lower degree of variability in annual rainfall. MK and SSE tests show comparable results for all five stations in annual rainfall trends. However, the ITA produced contrasting results for one station. In general, all five stations exhibit increasing trends in annual rainfall, although these trends are not statistically significant.

This study aimed to forecast rainfall trends for the next 10-year period (2023-2032) using an

LSTM Model. However, the study encountered several challenges and limitations. The insufficient dataset restrained the use of LSTMs, leading to overfitting and an inability to adapt to new data. The complexity of LSTMs, defined by multiple hyperparameters, added further challenges in determining the optimal configuration. Additionally, the model struggled with extreme events, and its sole reliance on rainfall as an input variable limited overall predictive reliability.

With these limitations and tests, the study suggests that a more reliable rainfall forecasting model could be developed with a larger dataset, careful hyperparameter adjustments, and consideration of other relevant variables.

Acknowledgments

The authors acknowledge the final support extended by the Tokyo Cement Company (Lanka) PLC and the University of Peradeniya to conduct the research and the support given by Dr. Damayanthi Herath, Department of Computer Engineering, University of Peradeniya.

References

- Abeysingha, N.S., Jayasekara, J.M.N.S. and Meegastenna, T.J., (2017) 'Stream flow trends in up and midstream of Kirindi Oya river basin in Sri Lanka and its linkages to rainfall', *Mausam*, 68(1), pp.99-110.
- Alahacoon, N. and Edirisinghe, M. (2021) 'Spatial variability of rainfall trends in Sri Lanka from 1989 to 2019 as an indication of climate change', *ISPRS International Journal of Geo-Information*, 10(2), p. 84. doi:10.3390/ijgi10020084.
- Nisansala, W.D.S., Abeysingha, N.S., Islam, A. and Bandara, A.M.K.R. (2019) 'Recent rainfall trend over Sri Lanka (1987-2017)'. *International Journal of Climatology*, 40(7), pp.3417-3435.
- Pérez-Alarcón, A., García-Cortés, D., Fernández-Alvarez, J.C. and Martínez-González, Y. (2022) 'Improving monthly rainfall forecast in a watershed by combining neural networks and autoregressive models'. *Environmental Processes*, 9(3), p.53.
- Praveen, B., Talukdar, S., Shahfahad, Mahato, S., Mondal, J., Sharma, P., Islam, A.R.M.T. and Rahman, A. (2020) 'Analyzing trend and forecasting of rainfall changes in India using non-parametrical and machine learning approaches', *Scientific Reports*, 10(1), p. 10342. Available at: <https://doi.org/10.1038/s41598-020-67228-7>.
- Şen, Z. (2012) 'Innovative Trend Analysis Methodology', *Journal of Hydrologic Engineering*, 17(9), pp. 1042-1046. Available at: [https://doi.org/10.1061/\(ASCE\)HE.1943-5584.0000556](https://doi.org/10.1061/(ASCE)HE.1943-5584.0000556).

Application of Universal Soil Loss Equation to Mountainous Areas in Kalu Ganga Basin

Nethkalani K.A.*, Samarasinghe T.D.B. and Nandalal H.K.

Department of Civil Engineering, Faculty of Engineering, University of Peradeniya, Sri Lanka

* e17223@eng.pdn.ac.lk

Keywords: Kalu Ganga Basin, Universal Soil Loss Equation, Soil Erosion

Abstract

The uneven terrain of the Kalu Ganga Basin accelerates soil erosion, necessitating a detailed understanding of erosion mechanics. This study uses the USLE and RUSLE models within a GIS framework, employing a Digital Elevation Model (30 m × 30 m), land use and soil maps, and 15 years of rainfall data. Findings show the basin experiences mild erosion, with annual rates of 0.19 t ha⁻¹ yr⁻¹ (USLE) and 0.21 t ha⁻¹ yr⁻¹ (RUSLE). Further, high erosion areas, are mainly found in Rathnapura and Kuruwita. The Meethitiya sub-basin has the highest erosion rate (31.10 t ha⁻¹ yr⁻¹), highlighting the necessity for focused conservation measures through proper land management practices.

1. Introduction

Soil erosion, driven by water, wind, gravity, and human activities, poses a significant environmental threat, intensified by agriculture, deforestation, and poor land management. This study estimates soil erosion rates in the steep, high-rainfall areas of the Kalu Ganga Basin up to Ellagawa in Sri Lanka using USLE and RUSLE models with ArcGIS. The goal is to quantify erosion and identify vulnerable areas for sustainable land management, water quality protection, and flood risk management, aiding targeted conservation to stabilize soil and maintain agricultural productivity.

2. Literature Review

The following section illustrates the calculation process for each factor of the USLE equation as outlined in the referenced literature.

2.1 R Factor

Sri Lankan research papers mostly have used the rainfall-erosivity relationship developed by Premalal (1986). The same equation has been used by Wijesundara et al., (2018) and Fayas et al., (2019).

$$R = \frac{(972.75 + 9.95 \times F)}{100} \quad (1)$$

F is the average annual rainfall (mm).

2.2 K Factor

To overcome time and cost limitations in field data collection, soil maps and soil data of the basin (Fayas et al., 2019) were used to ascertain soil distribution in the river basin area.

2.3 LS Factor

The slope gradient is important in water erosion, and the LS factor helps assess the soil erosion rates. For the L factor, the following equation was used. (Fayas et al., 2019; Belasri and Lakhouili, 2016)

$$L = \left(\frac{\text{flow accumulation} \times \text{resolution}}{22.1} \right)^m \quad (2)$$

m -Slope length exponent

For the S factor following equation has been identified as more suitable for the two models. (Fayas et al., 2019; Belasri and Lakhouili, 2016)

For the USLE model;

$$S = \frac{(\text{Sin Slope})^{1.3}}{0.0896} \quad (3)$$

For the RUSLE model;

$$\begin{aligned} S &= 10.8 \sin\theta + 0.03 \text{ for slope percent} < 9\% \\ S &= 16.8 \sin\theta - 0.50 \text{ for slope percent} \geq 9\% \end{aligned} \quad (4)$$

θ -Slope angle in degree

2.4 C Factor

Vegetation is vital for reducing water erosion, with the vegetation cover factor as the second most influential in controlling soil erosion risk.

For the USLE model;

To estimate this factor in USLE, studies use NDVI (Normalized Difference Vegetation Index) and regression models, correlating NDVI values from satellite images. (Belasri and Lakhouili, 2016)

$$C = e^{-(\alpha \times \frac{NDVI}{\beta - NDVI})} \quad (5)$$

Where α is 1 and β is 2.

For the RUSLE model;

In this model, C-factor values are determined based on land use and land cover maps, often relying on past studies in the respective countries, as seen in Sri Lankan literature, including Fayas et al., (2019).

2.5 P Factor

Soil conservation practices, aimed at preventing erosion, often adjust USLE estimates. The P factor map in this study for both models is derived from land use, land cover, and support factors, following the methodology of Belasri and Lakhouili, (2016) and Fayas et al., (2019)

3. Methodology

3.1 Data Collection

This study collected data from various sources. Rainfall records (2007-2022) from five gauging stations in the Kalu Ganga Basin were obtained from the Sri Lankan Department of Meteorology. The soil map was sourced from the Natural Resource Management Center in Peradeniya, and land use maps with DEM data came from the Department of Survey, Sri Lanka. Satellite imagery from the USGS Earth Explorer was used to integrate remote sensing data and calculate NDVI values.

3.2 The USLE and RUSLE Models

In the 1960s, Wischmeier and Smith (1978) developed the Universal Soil Loss Equation (USLE), a widely used model for predicting long-term erosion rates. The Revised Universal Soil Loss Equation (RUSLE) is an enhanced version, incorporating advancements for greater accuracy and applicability. While maintaining the foundation of the USLE, RUSLE introduces significant algorithmic changes for individual factor calculations, now computerized, expecting enhanced efficiency.

$$A = R * K * LS * C * P \quad (6)$$

- A - Average annual soil loss
- R - Rainfall runoff erosivity factor
- K - Soil erodibility factor
- LS - Slope length and steepness factor
- C - Land cover management factor
- P - Conservation practice factor

3.3 Methodological Flow Chart

Figure 1 indicates the detailed methodology of this research.

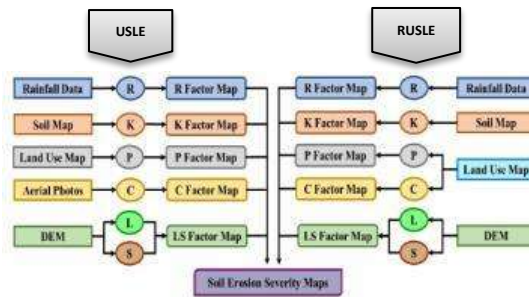


Figure 1: Methodology

4. Results and Discussion

4.1 R Factor Map

Table 1 shows the obtained average annual rainfall of five stations.

Table 8: Annual average rainfall

Rainfall Gauge Station	Average Annual Rainfall (mm)
Rathnapura	3745
Maliboda	4754
Halwathura	4137
Wellandura estate	2785
Allupola group	4677

Figure 2 was generated by using the above data, Equation (1), and the IDW interpolation method.

4.2 K Factor Map

Table 9: K values for different soil types

Soil	Erodibility (K)
Reddish brown earth	0.33
Alluvial soil	0.31
Steep rock land and lithosols	0.25
Red-yellow podzolic soil	0.22
Low humic gley soil	0.10
Bog & half bog soil	0.05

Table 2 shows K values for different soil types. Figure 3 was generated from the vector soil map using the ArcGIS Pro application.

4.3 LS Factor Map

A Slope map was created by using DEM. Figure 4 was generated from that slope map using Equation (2) and (3) for the USLE method. According to the RUSLE, the factor map was generated from that slope map using Equations (2) and (4).

4.4 C Factor Map

Table 3: C factor and P factor values for different land use types for Kalu Ganga basin

Type	Description	C	P
CCNTA	Coconut	0.54	0.6
CHENA	Chena	0.8	0.4
FRUSA	Forest	0.45	0.7
GRSLA	Grass Land	0.51	1.0
HOMSA	Home Garden	0.51	0.25

MRASHA	Marsh Land	0.3	1.0
PADDY	Paddy	0.43	0.15
RUBBER	Rubber	0.44	0.35
ROCKA	Rock	0.1	0
SCRBA	Scrub Land	0.6	0.1
STRMA	Streams	0.2	0
TANKA	Tanks	0.2	0
TEAA	Tea	0.57	0.35
OTHER	Other Cropland	0.73	1

According to the USLE, there used NDVI values for calculate C factor values. Figure 5 was created with the help of NDVI values and Equation (5). When considering the RUSLE method, Figure 6 was generated from the land use map and using specified C factor values in Table 3.

4.5 P Factor Map

Figure 7 was generated from the land use map and using specified P factor values in Table 3.

4.6 Soil Erosion Potential Maps

Using factor maps and Equation (6), soil erosion potential maps were generated (Figures 8 and 9) for the USLE and RUSLE models. Soil erosion rates were classified as per Tables 4 and 5, with additional details provided in these tables for sub-classes in USLE and RUSLE.

For further analysis, the study area is divided into sub-basins by considering tributaries. Figure 10 shows the divided sub-basins and Table 6 indicates how soil loss rates vary in those sub-basins.

Table 4: Estimated soil loss rate and area distribution according to the USLE model

Value (t ha ⁻¹ yr ⁻¹)	Soil Erosion Class	Area (km ²)	Area (%)
0 - 1	Slight Erosion	1343.51	93.95
1 - 5	Moderate Erosion	55.06	3.85
5 - 10	High Erosion	25.45	1.78
>10	Very high Erosion	6.01	0.42

Table 5: Estimated soil loss rate and area distribution according to the RUSLE model

Value (t ha ⁻¹ yr ⁻¹)	Soil Erosion Class	Area (km ²)	Area (%)
0 - 1	Slight Erosion	1335.93	93.42
1 - 5	Moderate Erosion	59.20	4.14
5 - 10	High Erosion	28.31	1.98
>10	Very high Erosion	6.58	0.46

Table 6: Estimated soil loss rate in selected sub-basins according to the RUSLE model

Sub Basin	Notation	Soil loss (Max) (t ha ⁻¹ yr ⁻¹)	Soil loss (Mean) (t ha ⁻¹ yr ⁻¹)
Mudunkotuwa	A	5.83	0.06
Millavitiya	B	15.76	0.21
Meehitiya	C	31.10	0.29
Kiribathgala	D	26.79	0.18
Rajasingama	E	23.26	0.15
Galathura	F	30.08	0.23

According to the above data Meehitiya sub basin has the maximum soil erosion rate in the basin. Rath Ganga, Bambarabotuwa Oya, and Denawak Ganga are the main tributaries located in this Meehitiya Sub Basin.

5. Conclusions

The soil erosion severity map developed using the USLE and RUSLE models with ArcGIS categorizes the basin into four severity levels. With mean annual soil erosion rates of 0.19 t ha⁻¹ yr⁻¹ (USLE) and 0.21 t ha⁻¹ yr⁻¹ (RUSLE), the majority experiences slight erosion. High erosion severity affects around 1.78% (USLE) and 1.98% (RUSLE) of the total basin, particularly impacting administrative divisions such as Kuruwita and Rathnapura.

Moreover, areas such as Dambuluwana, Gileemale-South, Ellagawa, Katepola, and Batewela exhibit notable erosion rates.

Minor disparities in erosion rates in the two models may be attributed to factors like cloud cover affecting NDVI values and infrequent land use map updates.

The sub-basin analysis further underscores that Meethitiya has the maximum soil erosion rate (31.10 t ha⁻¹ yr⁻¹) and the maximum mean soil erosion rate (0.29 t ha⁻¹ yr⁻¹).

Analyzing erosion in sub-basins is vital for effective land management and ecosystem preservation.

References

Belasri, A. and Lakhouili, A. (2016) 'Estimation of soil erosion risk using the universal soil loss equation (USLE) and geo-information technology in Oued El Makhazine watershed, Morocco', *Journal of Geographic Information System*, 08(01), pp. 98-107

Fayas, C.M., Abeysingha, N.S., Nirmanee, K.G.S., Samaratunga, D. and Mallawatantri, A. (2019) Soil loss estimation using RUSLE model to prioritize erosion control in Kelani River basin in Sri Lanka', *International Soil and Water Conservation Research*, 7(2), pp. 130-137.

Wijesundara, N.C., Abeysingha, N.S. and Dissanayake, D.M. (2018) 'GIS-based soil loss

estimation using RUSLE model: A case of Kirindi Oya River Basin, Sri Lanka', *Modeling Earth Systems and Environment*, 4(1), pp. 251-262.

planning (No. 537)', Department of Agriculture, Science and Education Administration.

Wischmeier, W.H. and Smith, D.D. (1978) 'Predicting rainfall erosion losses: a guide to conservation

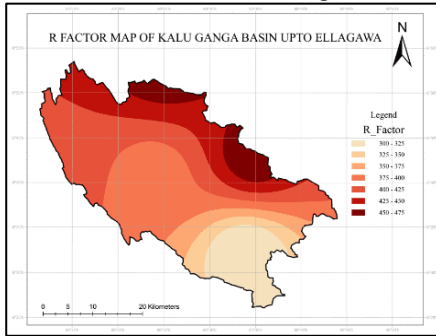


Figure 2: R factor map

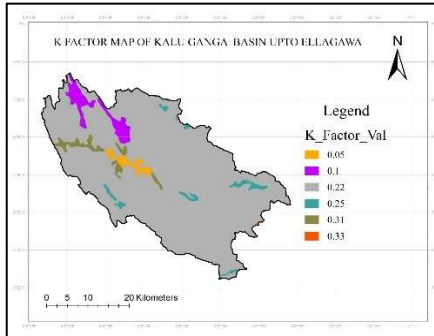


Figure 3: K factor map

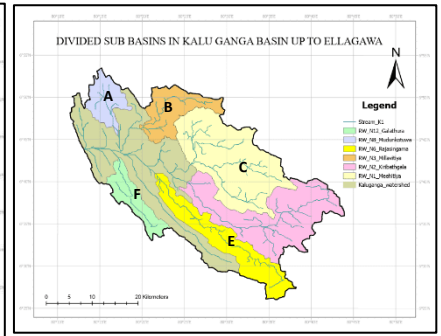


Figure 10: Divided sub-basins

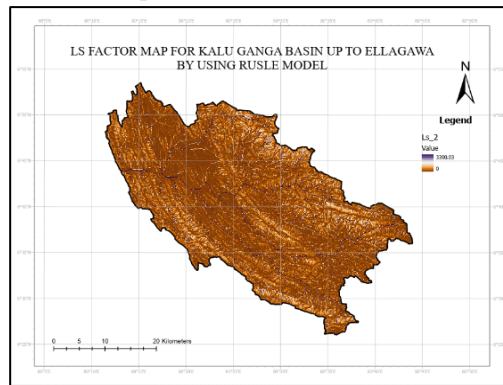
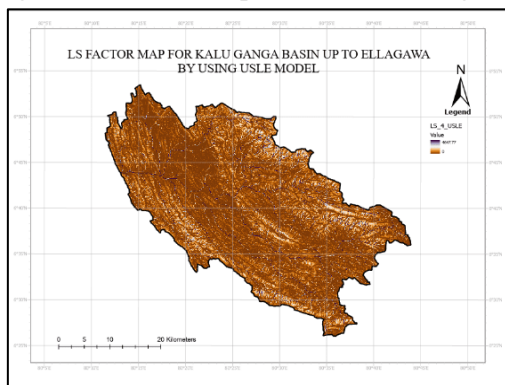


Figure 4: LS factor map for USLE and RUSLE models respectively

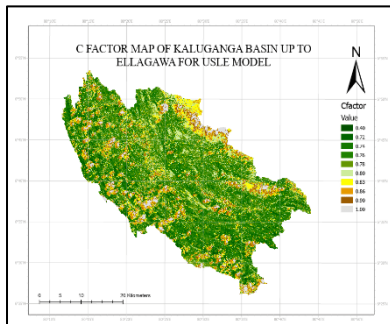


Figure 5: C factor map for the USLE model

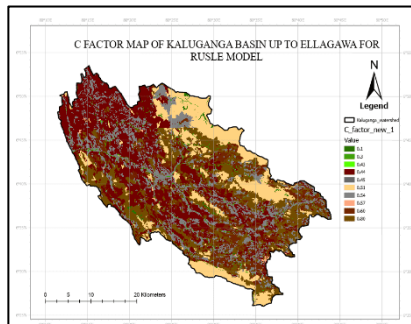


Figure 6: C factor map for the RUSLE model

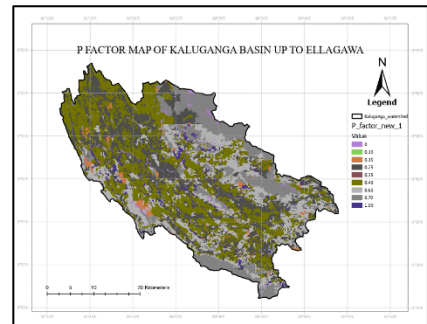


Figure 7: P factor map

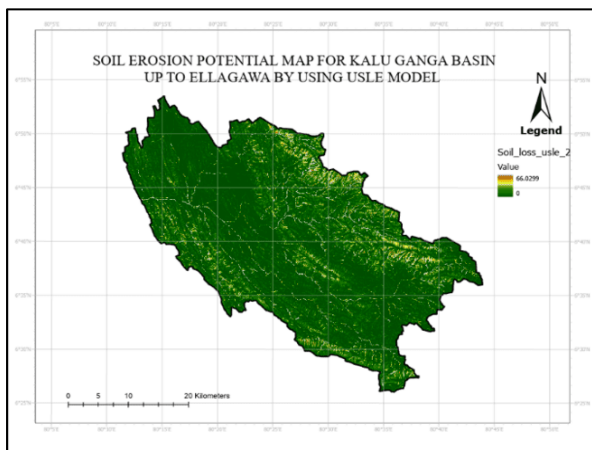


Figure 8: Soil erosion potential map for the USLE model

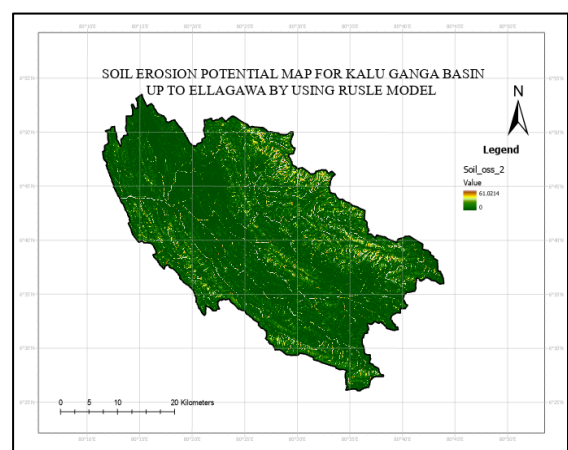


Figure 9: Soil erosion potential map for the RUSLE model

Evaluating Clogging Effect in Vertical Flow Constructed Wetlands

Sachinika.W.A.T.*, Panagoda.H.A.*, and Weerakoon.G.M.P.R.*

Department of Civil Engineering, Faculty of Engineering, University of Peradeniya, Sri Lanka

* e17299@eng.pdn.ac.lk, e17233@eng.pdn.ac.lk, prabhaw@eng.pdn.ac.lk

Keywords: Constructed Wetlands, Hydraulic Loading Rates, Wastewater

Abstract

Vertical Flow Constructed Wetlands (CW) are renowned for low cost and ecofriendly processes in wastewater treatment. This study methodically explored the impact of varying hydraulic loading rates (HLR) on VSSF CW performance. Utilizing three laboratory-scale experimental units planted with *Cyperus alternifolius*. The study reveals that HLR is a critical factor in determining VFCW performance and the clogging effect. Conversely, lower HLRs lead to underutilization of the wetland's capacity, resulting in subpar pollutant removal and resource inefficiency. This research enhances the relationship between HLR and pollutant removal in VSSF. For that 20cm/d, 35cm/d and 50cm/d HLR use in 3 units. According to our study, the best HLR for feed is identified as 20cm/d, which has the highest removal efficiency and lowest clogging observed. Considering cost efficiency HLR can further optimize between 20cm/d and 35cm/d.

1. Introduction

Vertical subsurface flow (VSSF) constructed wetlands (CWs) are recognized as a sustainable and cost-effective option for wastewater purification due to their high efficiency in pollutant removal. However, the most troublesome phenomenon in these wetlands was the clogging effect, which influenced treatment performance. Various studies came up with different methods to reverse and reduce this clogging effect for better performance. Out of these methods, controlling hydraulic parameters such as HLR was identified as a possible alternative to overcome the clogging effect in VSSF wetlands. Therefore, the aim of this study was to methodically explore the impact of varying HLR on VSSF CW performance and clogging effect, and the objectives of this study were to evaluate the impact of the HLR on the performance of VSSF wetlands, assess the occurrence of clogging concerning HLR in VSSF CWs, using three laboratory-scale CW units operating at three different HLRs of 20, 35, and 50 cm/day,

respectively. The analysis of collected data resulted in the unit operating at 20 cm/d being the best-performing considering the waste removal efficiency of the wetland. The clogging of these units indicated that the HLR is a critical factor, resulting in the 50 cm/d feeding unit being the most prone to clogging.

2. Literature review

Constructed wetlands (CWs) are human-made systems designed to harness the natural processes of wetland environments for wastewater treatment, (Vymazal, 2011). Today, they are recognized as reliable and sustainable wastewater treatment technologies. Major types include surface flow wetlands (SF) and subsurface flow (SSF) wetlands, with vertical subsurface flow (VSSF) CWs gaining prominence due to their resilience, smaller land footprint, and cost-effectiveness (Pucher and Langergraber, 2019).

However, CWs have drawbacks, including a large land footprint and the critical issue of clogging, which requires increased investment for operation and maintenance. Clogging, characterized by pore space obstruction, compromises the effectiveness of these systems, leading to hygienic problems and environmental issues (Fang et al., 2022). Various studies categorize clogging into external and internal blockages, influenced by factors like microbial proliferation, suspended solids buildup, and particle size distribution (Pucher and Langergraber, 2019). Detection methods include assessing reductions in hydraulic conductivity, porosity, and tracer tests (Hua et al., 2014; Wang et al., 2021).

To address clogging, early approaches involved substrate media replacement (Pucher and Langergraber, 2019), resting CWs for periods (Hua et al., 2014), solubilization treatments using solvents (Guofen et al., 2010) and oxygenation methods to prevent substrate clogging (Wang et al., 2021). Despite these advancements, drawbacks like the need for standby setups during resting periods, high-cost pretreatment, and potential plant damage persist. However, a novel approach involves

optimizing hydraulic loading to mitigate bio-clogging without chemical agents, preventing negative effects on CW performance and the environment (Tang et al., 2023). This study was to evaluate the effect of different HLR on the pollutant removal performance of VSSF CWs and then how different HLRs affect the clogging in VSSF wetlands.

3. Methodology

This experimental setup was kept in open air at normal sunlight conditions with 23 – 30 degrees centigrade temperature, at the University of Peradeniya, Sri Lanka. (33° 31' 43.8204" N and 112° 15' 50.0436" W.)

3.1 Experimental Setup

The experimental setup consists of three laboratory-scale vertical flow CWs units, prepared using Perspex tubes with a diameter of 30 cm and a total height of 105 cm. Each CW unit was filled with approximately 3 - 5 mm (Chips) granular media as the substrate up to 85cm, as shown in Figure 1. Each unit was planted with an Umbrella palm (*Cyperus alternifolius*) of a height of approximately 20 cm. The wastewater is fed to the top of each wetland unit, and treated wastewater is collected from the bottom with a raised outlet, allowing all three wetlands to be saturated to a depth of 60 cm. The experimental setup includes an overhead tank with an agitator.

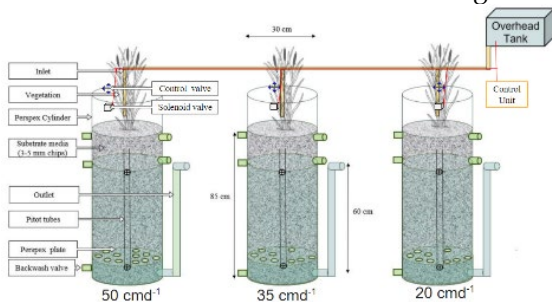


Figure 1: Experimental setup

3.2 Synthetic wastewater

Synthetic wastewater was prepared for 500L using 150g of sugar, 100g of urea, 20g of (NH₄) SO₄, 20g of MgSO₄, 11g of K₂HPO₄, 2g of MnSO₄.H₂O, 1g of NH₄Cl, 0.6g of FeCl₃ and 20g of septage from Gannoruwa treatment plant secondary treatment unit sludge then mixed with tap water.

3.3 Feeding arrangement and sample collection

Three wetland units were fed with tap water for two weeks to grow the wetland plants and to remove any impurities present. Then the system was fed with synthetic waste for another

week before collection of samples. The feeding was done at 20cm/d, 35cm/d, and 50cm/d HLR with the intermittent feeding control system, which fed the system for 5 min every 2 hours.

The samples were collected from one inlet and all three outlets to 500ml clean plastic bottles every Tuesday for 7 weeks, then tested for BOD, COD, TSS, Ammonium, Nitrate, Phosphate, and fecal coliform (FC). COD tests were carried out in alternative weeks. Head loss and plant height were measured weekly.

4. Results and discussion

Removal efficiencies (RE) for wastewater parameters were calculated as the percentage change in concentration from influent to the effluent using Eq (1), where C_i = concentration of the wastewater parameter in the influent and C_o = concentration of the same wastewater parameter in the effluent.

Removal efficiency,

$$\text{Removal efficiency (R}_E\text{)} = \frac{C_i - C_o}{C_i} \times 100\% \quad (1)$$

4.1 Organic matter

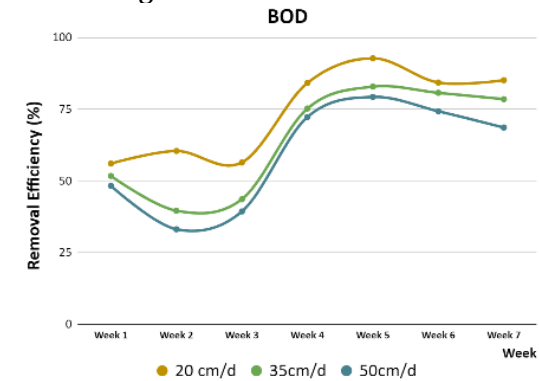


Figure 2: BOD removal efficiency

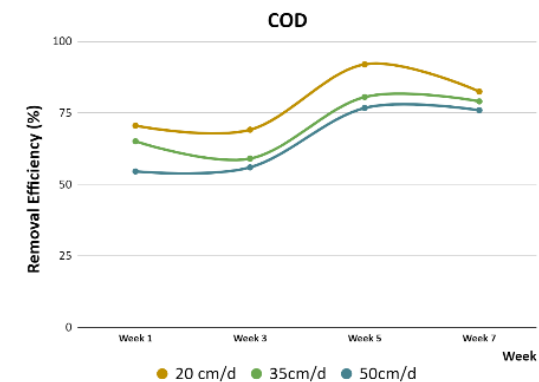


Figure 3: COD removal efficiency

As shown in Figure 2 and Figure 3, the removal efficiency of BOD and COD levels gradually increased over the period which could be due to filtration and settling of organic matter, and

bacterial degradation due to the growth of microorganisms. With time the microbial activity tends to increase with their nutrient uptake (Stefanaki et al.,2014), which is similar to the results of Ma Fei, (2010). This indicates high removal efficiency in the organic matter of these units. As shown in Figure 2 and Figure 3, the 20cm/d feeding unit has the overall highest removal efficiency.

4.2 Suspended solids

As shown in Figure 4, the RE of suspended solids increases over the period with the 20cm/d feeding unit with the highest RE. The main removal processes of TSS are gravitational settling and filtration (Stefanaki et al.,2014). Similar to BOD and COD removal efficiency, increasing TSS removal efficiency could also be due to bacterial decomposition.

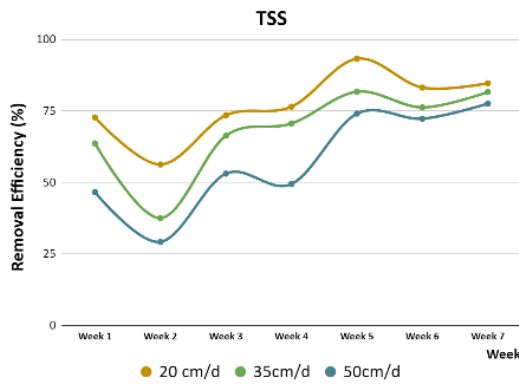


Figure 4: TSS removal efficiency

4.3 Nitrogen

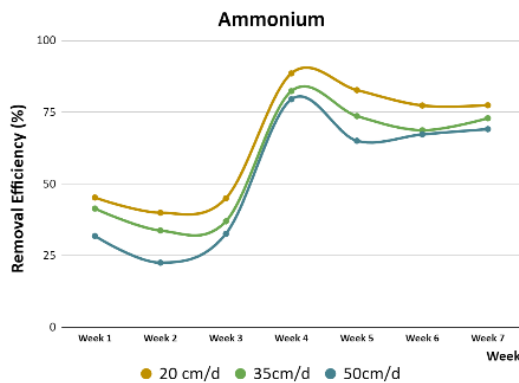


Figure 5: Ammonium removal efficiency

Nitrogen removal is one of the main removal processes in CW units. Nitrate and ammonium both are inorganic forms of nitrogen. When ammonium is taken up by plants and through the process of adsorption, some of the ammonium also turns to nitrates through the nitrification process (Vymazal et al., 2011). These nitrates are taken up by plants and microorganisms (assimilation). Therefore, these results indicate a possibility of ammonium turning into nitrate with time and taken up by

microorganisms. As shown in Figure 5 and Figure 6, the RE of ammonium increases over the period, and nitrate RE shows negative efficiency. This could be due to the increased nitrate due to nitrification. The results indicate better performance of the 20cm/d feeding unit similar to other parameters.

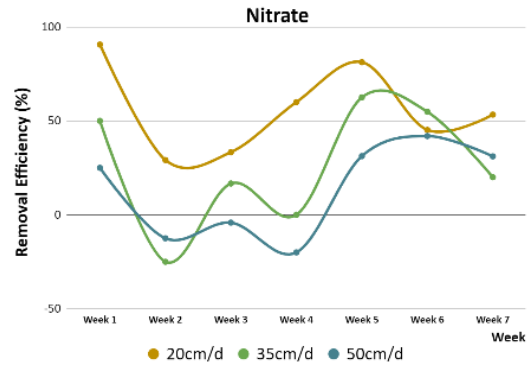


Figure 6: Nitrate removal efficiency

4.4 Phosphorus

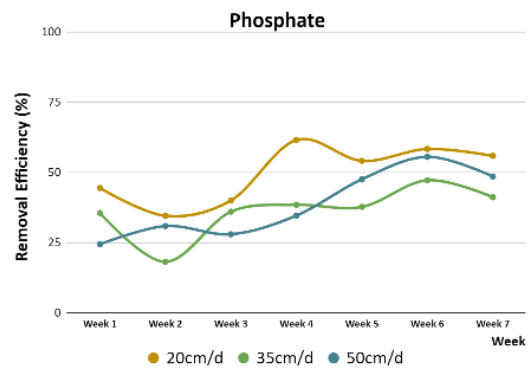


Figure 7: Phosphate removal efficiency

Dissolved organic P and insoluble organic and inorganic P must be converted into soluble inorganic forms, to be biologically consumed. Plants take up soluble reactive P to cover their growth needs and convert it to tissue P, while P is also sorbed to wetland substrate (Vymazal et al., 2011). As in Figure 7 the increased phosphate removal efficiency might be due to plant growth progresses and the number of plants within the units increases, the potential for plant assimilation and the formation of root zones with enhanced microbial activity. This can lead to more efficient removal of phosphate from the wastewater. Phosphate indicates better RE of 20cm/d feeding unit than the other two units as in Figure 7.

4.5 Fecal coliform

It is observed a range of FC removal efficiencies, from 50% to 90%, which is generally higher than other wastewater parameters, such as BOD, COD, nitrate, and phosphate. This could be due to FC bacteria being relatively fragile to removal through exposure to sunlight and UV

rays. Similar to other results 20cm/d feeding units have overall better RE than other units.

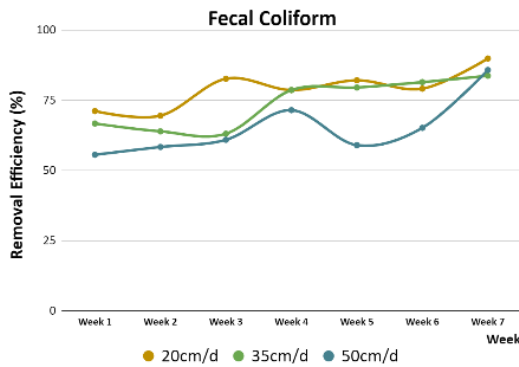


Figure 8: Faecal coliform removal efficiency

4.5 Head loss and plant growth

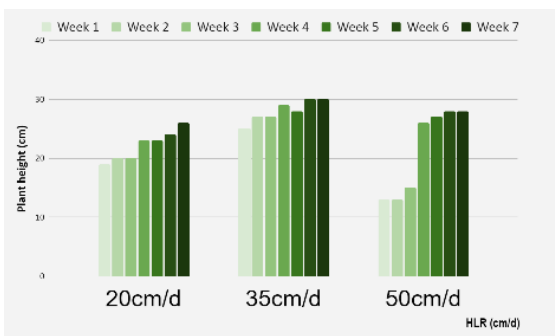


Figure 9: Plant Heights over the weeks

Table 1: Head loss values measured every week

Week	Head loss ($10^{-3} \times m$)		
	20cm/d	35 cm/d	50cm/d
Initial	0.0	0.0	0.0
4	0.0	1.0	0.0
5	0.0	1.5	0.5
7	2.0	3.0	3.0
8	2.0	4.0	4.0
9	3.0	4.0	5.0
10	4.0	5.0	5.0
11	4.0	5.0	6.0

Plant height can be used as a proxy for root depth. However, it is worth noting that there isn't a perfect correlation between the two. For example, a plant may be tall but have a shallow root system with granular conditions. Plant root depth in a CW has a multifaceted impact on treatment parameters, primarily by altering hydraulic characteristics, nutrient uptake, sedimentation, microbial activity, oxygen availability, and overall treatment efficiency. As in Figure 9 with the plant growth, the root system might have improved over time resulting in better nutrient uptake and filtering

processes. Head loss values in Table 1 indicate the 3 units have an incremental head loss with time, currently, they are at 4mm,5mm, and 6mm. The highest head loss is at the unit feeding at a rate of 50 cm/d. Which indicates it's the most prone to clogging.

5. Conclusions

This study's results indicate that the 20cm/d feeding unit is better than the other two units when considering the overall removal efficiency of BOD, COD, TSS, Ammonium, Nitrate and phosphate, and FC. When considering head loss measurements the 50cm/d feeding unit is the most prone to clogging.

References

Fang, Y., Kong, L., Zhang, P., Zhang, L., Zhao, H., Xiang, X., Cheng, S., Zhang, H., Ju, F. and Li, L. (2022) 'Fifteen-year analysis of XW clogging: A critical review', *Journal of Cleaner Production*, p.132755.

Guofen, H., Wei, Z., Lianfang, Z. and Yunhui, Z. (2010) 'Applying solubilization treatment to reverse clogging in laboratory-scale vertical flow constructed wetlands', *Water Science and Technology*, 61(6), pp. 1479-1487. Available at: <https://doi.org/10.2166/wst.2010.038>.

Hua, G., Zeng, Y., Zhao, Z., Cheng, K. and Chen, G., (2014) 'Applying a resting operation to alleviate bioclogging in vertical flow CWs: an experimental lab evaluation', *Journal of environmental management*, 136, pp.47-53.

Ma, F., Jiang, L. and Zeng, T. (2010) 'Reversing Clogging in Vertical-Flow Constructed Wetlands by Backwashing Treatment', *Advanced Materials Research*, 129-131, pp. 1064-1068. Available at: <https://doi.org/10.4028/www.scientific.net/AMR.129-131.1064>.

Pucher, B. and Langergraber, G. (2019) 'The state of the art of clogging in vertical flow wetlands', *Water*, 11(11), p.2400.

Stefanakis, A., Akrotos, C.S. and Tsihrintzis, V.A. (2014) 'Vertical flow CWs: eco-engineering systems for wastewater and sludge treatment', *Newnes*.

Tang, P., Chen, L., Zhang, W. and Zhou, Y., (2023) 'Bioclogging alleviation for CW based on the interaction among biofilm growth and hydrodynamics', *Environmental Science and Pollution Research*, 30(7), pp.18755-18763.

Vymazal, J. (2011) 'CWs for wastewater treatment: five decades of experience', *Environmental science & technology*.

Wang, H., Sheng, L. and Xu, J., (2021) 'Clogging mechanisms of CWs: A critical review', *Journal of Cleaner Production*, 295, p.126455.

Comparison of Sarima and ANN Models for Forecasting Streamflow Data of the Nilwala River

Tharangani K.K.A.*, Dilshan V.P. and Nandalal K.D.W.

Department of Civil Engineering, Faculty of Engineering, University of Peradeniya, Sri Lanka

* e17344@eng.pdn.ac.lk

Keywords: ANN, ARIMA, Comparison of ARIMA with ANN, Flow forecasting, SARIMA

Abstract

This study addresses the critical need for accurate streamflow forecasting in the Nilwala River basin, an area susceptible to water scarcity and flooding. Focusing on Pitabeddara and Urawa gauging stations, the research employs Artificial Neural Network (ANN) and Auto-Regressive Integrated Moving Average (ARIMA) methods to predict daily streamflow. Using historical rainfall data from Anningkanda station, SARIMA models (SARIMA (3,0,3)(2,1,1) for Pitabeddara and SARIMA (1,1,1)(1,1,1) for Urawa) are utilized for monthly predictions, while ANN models excel in daily forecasts. The study evaluates model performance using Root Mean Square Error (RMSE), Nash-Sutcliffe Efficiency (NSE), and Bias (BIAS), emphasizing ANN's effectiveness in enhancing daily streamflow prediction accuracy for effective water resource management.

1. Introduction

Accurate streamflow data is crucial for effective water resource management, particularly in river basins susceptible to water scarcity and flooding, such as the Nilwala River basin. Unfortunately, insufficient streamflow data in regions like this hinders comprehensive understanding and long-term management of water resources. The proposed research focuses on forecasting Nilwala River flow at Pitabeddara and Urawa gauging stations based on the Artificial Neural Network (ANN) technique and Auto-Regressive Integrated Moving Average (ARIMA) method to identify the most suitable forecasting method using daily streamflow data and daily rainfall data of Anningkanda station located in the upper catchment of the Nilwala River.

2. Literature Review

Several studies explore the effectiveness of different models in river flow forecasting. Cigizoglu (2003) utilized Autoregressive

Moving Average (ARMA) models to enhance artificial neural networks (ANNs) for monthly river flow predictions in an East Mediterranean region of Turkey. The incorporation of synthetic series improved ANN accuracy, particularly with periodic components. Kisi (2007) found that the Levenberg-Marquardt algorithm is the most efficient in terms of training time by developing ANN with different training algorithms. Valipour et al., (2012) highlighted that the ARIMA model is better than ARMA model since it makes time series stationary, and that ANN with sigmoid activity function gives a better performance.

3. Methodology

This study focuses on the Nilwala River Basin in the wet zone of Sri Lanka, known for its high annual rainfall. The basin experiences severe floods in the wet season due to intense upper-basin rainfall and faces significant drying in the dry season, affecting downstream irrigation needs. These fluctuations in streamflow timing impact flood patterns, water supply, agriculture, and drinking water purification.

Daily mean river discharge data from Urawa (Jan 2000-Dec 2020) and Pitabeddara (Jan 2000-Dec 2021) stations were sourced from the Department of Irrigation. Daily mean rainfall data from Anningkanda station (Jan 2000-Apr 2020) were obtained from the Department of Meteorology.

Missing discharge data were addressed using a linear regression method, utilizing nearby station data from the same river to estimate values due to insufficient correlation coefficients for direct in-filling.

3.1 Autoregressive Moving Average (ARMA) Models

The ARMA (p, q) model is foundational in time series analysis, expressed by Equation (1);

$$X_t = \phi_0 + \phi_1 X_{t-1} + \dots + \phi_p X_{t-p} + Z_t - \theta_1 Z_{t-1} - \dots - \theta_q Z_{t-q} \quad (1)$$

Here, 'p' and 'q' are autoregressive and moving average orders, ϕ_1 to ϕ_p are autoregressive coefficients, ϕ_0 is a constant term, and θ_1 to θ_q are moving average coefficients. The initial step involves selecting the 'p' and 'q' values by analysing autocorrelation and partial autocorrelation functions, crucial for time series modelling, aiding AR and MA order identification.

3.2 Autoregressive Integrated Moving Average (ARIMA) Models

The ARMA model is suitable for stationary time series data, but many real-world time series exhibit non-stationary characteristics with trends and seasonal patterns. To address this, the ARIMA model integrates three components autoregressive (AR), integrated (I), and moving average (MA) to model and capture underlying data patterns.

$$[1 - \sum_{i=1}^p \phi_i L^i](1 - L)^d X_t = [1 + \sum_{i=1}^q \theta_i L^i] \quad (2)$$

Equation (2) represents the ARIMA (p, d, q) model, where p, d, and q are integers denoting autoregressive, integrated, and moving average components respectively. The integrated component (d) involves differencing to achieve stationarity, typically set at d=1. When d=0, the model simplifies to an ARMA (p, q) model, suitable for stationary time series.

3.3 Seasonal Autoregressive Integrated Moving Average (SARIMA) Models

SARIMA extends ARIMA by handling time series with seasonal and non-seasonal elements, beneficial for datasets showing regular or seasonal patterns. It enhances efficacy by transforming data into a stationary state through differencing. The model, denoted as ARIMA (p, d, q)×(P, D, Q)S, incorporates non-seasonal and seasonal autoregressive, differencing, and moving average components, with 'S' representing the seasonal pattern's time span for robust forecasting.

3.4 Development of ARIMA Model

According to the literature, Due to unsatisfactory daily flow performance in ARIMA models, monthly data from 2000 to 2021 was used for Pitabeddara and Urawa stations. To develop ARIMA models, data series stationarity was confirmed through Autocorrelation and Partial Autocorrelation functions, revealing a stationary series with 12-month seasonality. Non-stationarity was

addressed through differencing or standardization if necessary.

3.5 Artificial Neural Network (ANN) Model

ANNs are brain-inspired models with interconnected neurons in layers. Input signals pass through neurons with activation and threshold functions, modified by weights. Training refines output based on defined data sets. There are different ANN techniques such as Feed Forward Neural Networks (FFNN), Convolution Neural Networks (CNN), Recurrent Neural Networks (RNN), etc. In this study, our focus was on the Feed Forward Network. A feedforward neural network (FNN) directs data from input to output, adjusting weights through backpropagation for accurate predictions in training.

3.6 Development of ANN Model

This study employed supervised learning with the Levenberg-Marquardt algorithm to train the neural network. This algorithm optimizes weights by minimizing the cost function, enhancing accuracy in streamflow predictions. One hidden layer was utilized, with a trial-and-error approach testing 1 to 10 neurons to determine the optimal configuration. Two approaches were explored in developing the ANN model.

1. Approach 1:
Daily flows were predicted using only considering past daily streamflow values as inputs.
2. Approach 2:
Daily flows were predicted using both past daily streamflow values and past daily rainfall values at Anningkanda stations as inputs.

3.7 Performance Evaluation

Performance evaluation in ANN and ARIMA models is a critical aspect of assessing how well the model is performing on the task. The evaluation is essential for determining the accuracy of the model, generalization capability, and its ability to make reliable predictions. In this study RMSE, NSE and BIAS are used for the evaluation and which are easy to understand.

4. Results and Discussion

4.1 Results and Discussion of the ARIMA Model

For Urawa and Pitabeddara stations, monthly flow modelling utilized data from January 2000 to August 2014 (2/3 of data), with validation conducted on monthly flow data from September 2014 to December 2021 (1/3 of data). Monthly flows served as inputs, and a seasonal coefficient was applied. The model selection involved assessing RMSE, NSE, and BIAS, with MINITAB analysing the fitted model using Mean Square (MS) to determine optimal matches based on the lowest MS value. Results are shown in Tables 4.1 and Table 4.2.

Table 4.1: Statistical parameters for Urawa station

(p,d,q)(P,D,Q)	RMSE	NSE	BIAS
SARIMA (1,1,1) (0,1,1)	45.845	0.315	2.510
SARIMA (1,1,1) (1,1,1)	45.798	0.317	1.214
SARIMA (1,1,0) (1,1,1)	45.865	0.315	-1.418

Table 4.2: Statistical parameters for Pitabeddara station

(p,d,q)(P,D,Q)	RMSE	NSE	BIAS
SARIMA (3,0,3)(2,1,1)	335.698	0.298	-17.100
SARIMA (2,0,2)(2,1,1)	337.500	0.290	-16.055
SARIMA (3,1,2)(2,1,2)	336.935	0.292	-14.522

The SARIMA model with parameters (1,1,1) (1,1,1) shows the best performance for Urawa station and (3,0,3)(2,1,1) shows the best performance for Pitabeddara station.

4.2 Results and Discussion of the ANN Model

In Approach 1, focusing solely on past streamflow data as input variables, the results were analysed across various neural network architectures. The number of nodes in the hidden layer was varied, and time lags of 1 day, 2 days, 3 days, and 4 days were considered for each network. Evaluation metrics, including RMSE, NSE, and BIAS, were observed for each case. Tables 4.3 and Table 4.4 present the outcomes for three different time lags trained under the best performing neural network

identified for the Pitabeddara and Urawa station respectively.

Table 4.3: Approach 1 for Pitabeddara station

Time lag	RMSE	NSE	BIAS
1 day (7 neurons)	4.064	0.955	0.552
3 days (5 neurons)	1.537	0.994	-0.624
4 days (5 neurons)	2.751	0.980	0.637

Table 4.4: Approach 1 for Urawa station

Time lag	RMSE	NSE	BIAS
2 days (10 neurons)	0.771	0.315	-0.007
3 days (9 neurons)	0.325	0.986	-0.175
4 days (10 neurons)	0.458	0.975	-0.081

In Approach 2, incorporating both past streamflow and rainfall data as input variables, results were analysed across diverse neural network architectures. The number of nodes in the hidden layer was adjusted, and time lags of 1 day, 2 days, 3 days, and 4 days were explored for each network. The evaluation metrics RMSE, NSE, and BIAS were observed for each case. Tables 4.5 and Table 4.6 display outcomes for three different time lags trained under the most effective neural network identified for the Pitabeddara and Urawa station respectively.

Table 4.5: Approach 2 for Pitabeddara station

Time lag	RMSE	NSE	BIAS
1 day (10 neurons)	6.752	0.970	-2.104
2 days (4 neurons)	5.068	0.983	-0.167
3 days (3 neurons)	10.918	0.921	-2.101

Table 4.6: Approach 2 for Urawa station

Time lag	RMSE	NSE	BIAS
2 day (9 neurons)	2.140	0.659	-0.031
3 days (8 neurons)	2.085	0.677	-0.151
4 days (7 neurons)	2.147	0.599	-0.034

According to the above results, it can be clearly seen that performance evaluation criteria (RMSE, NSE and BIAS) are better under Approach 1 for both stations. Results were not better though expected under Approach 2 (with rainfall data as an input layer). Anningkanda rainfall may not affect all the time for the Pitabeddara and Urawa station flows. That could be a reason for that. Therefore, it can be identified that ANN model performance under Approach 1 show better suitability for predicting the streamflow at Pitabeddara and Urawa.

4.3 Model Comparison

The study compared SARIMA and ANN models for forecasting stream flows at Pitabeddara and Urawa stations. SARIMA, tailored for monthly data due to daily flow limitations, was contrasted with daily-focused ANN models. Monthly flows in ANN were derived from daily predictions. Comparative analysis indicated that ANN predictions closely aligned with actual flows at both stations, suggesting superior performance in predicting Nilwala River flows compared to SARIMA. Tables 4.7 and table 4.8 detail the mean and standard deviation variations of the best SARIMA and ANN models from October 2018 to December 2021 for Pitabeddara and Urawa. Figures 4.1 and figure 4.2 depict comparisons between monthly predicted flows of ANN and ARIMA models with observed data for each station.

Table 4.7: Comparison of best SARIMA with ANN model of Pitabeddara station

	Actual flow	ANN	SARIMA
Mean	592.69	611.33	602.37
Standard deviation	398.21	367.12	198.60

Table 4.8: Comparison of best SARIMA with ANN model of Urawa station

	Actual flow	ANN	SARIMA
Mean	83.11	88.57	85.29
Standard deviation	57.14	52.32	32.79

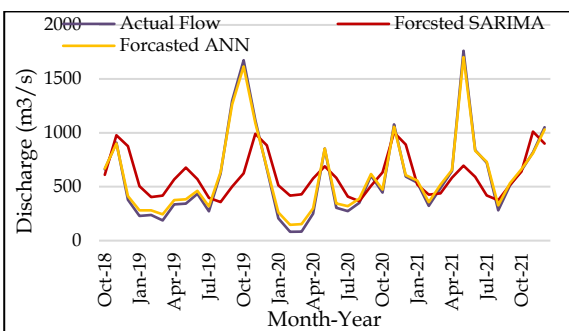


Figure 4.1: Comparison of best SARIMA with ANN model of Pitabeddara station

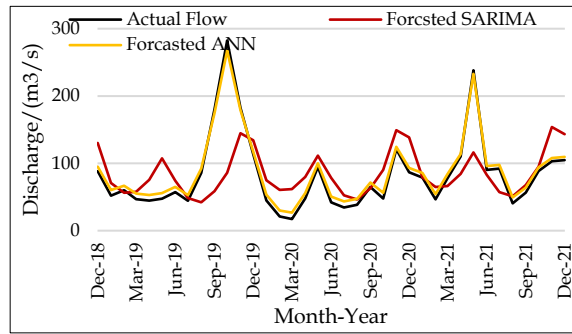


Figure 4.2: Comparison of best SARIMA with ANN model of Urawa station

5. Conclusions

SARIMA (3,0,3)(2,1,1) and SARIMA (1,1,1)(1,1,1) are deemed most suitable for monthly Nilwala River flow predictions at Pitabeddara and Urawa, respectively, proving effective for water estimation but not recommended for flood forecasting. ANN models excel in daily flow prediction, especially with extensive historical data. Despite limited input data, ANN models performed well, demonstrating high effectiveness in predicting Nilwala River flow at Pitabeddara and Urawa. Simple architectures with one hidden layer, containing 5 neurons for Pitabeddara and 9 for Urawa result in optimal predictive performance. The ANN model surpasses SARIMA, particularly in daily forecasting, even with extensive SARIMA training data, highlighting its potential for applicability in water resources and flood estimation studies.

References

Cigizoglu, H.K. (2003) 'Incorporation of ARMA models into flow forecasting by artificial neural networks', *Environmetrics*, 2003, 14: 417-427.

Kisi, O. (2007) 'Streamflow Forecasting Using Different Artificial Neural Network Algorithms', *J. Hydrol. Eng.*, 2007.12:532-539.

Valipour, M., Banihabib, M.E. and Behbahani, S.M.R. (2013) 'Comparison of the ARMA, ARIMA, and the autoregressive artificial neural network models in forecasting the monthly inflow of Dez dam reservoir', *Journal of Hydrology*, [online] 476, pp.433-441.

Modelling Of Hydrodynamic Processes of Membrane Based Treatment System Using Artificial Neural Network

Punchihewa K.G.G., Dissanayake D.M.N.D., and Nanayakkara K.G.N.*

Department of Civil Engineering, Faculty of Engineering, University of Peradeniya, Sri Lanka

* nadeen@eng.pdn.ac.lk

Keywords: Artificial Neural Network, Mean Relative Effects, Partial Dependency Plots

Abstract

This research provides insights into the applicability of Artificial Neural Network (ANN) models for Trans Membrane Pressure (TMP) prediction in membrane-based treatment systems, offering guidance for model improvement and treatment system control. The effects of input parameters on the model's performance are assessed using partial dependency plots (PDPs) and mean relative effects (MREs). The modelling results indicate excellent agreement between input variables and TMP, suggesting the potential omission of 'filtrate temperature' from the input variables based on sensitivity analysis.

1. Introduction

The utilization of computer-based modelling in membrane technology is considered essential, as it presents a powerful tool for understanding, analysing, and predicting complex dynamics of systems. Among these modelling approaches, artificial neural networks (ANNs) have gained significant attention for its ability to effectively capture highly non-linear behaviours. Consequently, this research is focused on developing an ANN model to predict the operational behaviour of a UF membrane-based water treatment unit. Membranes which act as selective barriers in separation, concentration, and purification processes are widely used as highly effective tools in environmental engineering, industrial production, and water management. Even with significant advances in membrane technology, challenges still prevail in maintaining productivity and product quality, especially in dealing with membrane fouling and concentration polarization (Ezugbe O. & Rathilal S, 2020). Employing modelling approaches makes it easier to understand these complex systems offering insights for potential improvements.

1.1 Artificial neural network (ANN)

Artificial Neural Network (ANN) is a computer-based model that mimics the complexity of the human brain and inspired by

the structure and functioning of the biological nervous system. Operating as 'black box' models, ANNs possess the capability to establish correlations between input and output variables, without requiring information about the underlying physical parameters of the process.

ANN is a data-driven model, which establishes its relationships between variables through a learning process. There are several types of ANNs based on their topography and architecture. Among those, back propagation feed forward neural network, commonly referred as multi-layer perceptron (MLP) stands out as prominent choice for function approximation.

Multi-layer Perceptron (MLP)

MLP architecture consists of an input layer, one or more hidden layers, and one output layer, each with a specific number of neurons or nodes.

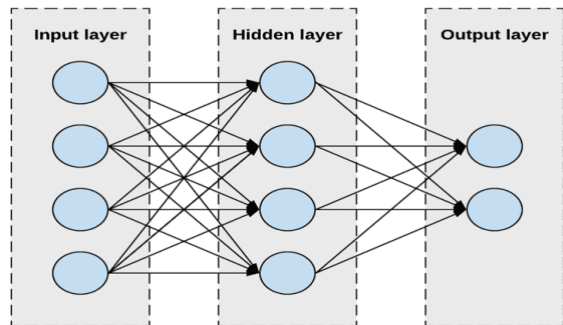


Figure 1: Typical MLP architecture with a single hidden layer (Jawad et al., 2021).

Figure 1 shows a typical MLP architecture in which each connection between neurons is associated with weights and each neuron with a bias value. The feed-forward calculation process is described in the following equation.

$$Y_j = \sum_{i=1}^p \omega_{ji} X_i + b_j \quad (1)$$

Where X_i represents the input to a neuron, p denotes the number of input nodes, ω_{ji} signifies the weight associated with the connection from i^{th} to j^{th} neuron, and b_j is the bias of the j^{th} neuron. Y_j denotes the expected output and it is

passed through an activation function, also known as the transfer function. The transfer function is responsible for introducing nonlinearity into the neural network, determining the transformation of neuron inputs to outputs. During the development of an ANN model, the associated weights and bias values are updated through a back propagation algorithm until a highly accurate network is obtained.

2. Methodology

This study focused on developing an ANN model with the primary objective of predicting transmembrane pressure (TMP) within a UF pre-treatment unit of reverse osmosis (RO) seawater desalination system reported elsewhere (Zhou et al., 2021; Cohen et al., 2021). Values of selected parameters were normalized between 0 and 1 using the min-max normalization technique, ensuring fair treatment of features. The Minimum Redundancy Maximum Relevance (MRMR) method is used as the feature selection technique, employing ‘mutual_info_regression’ in Python to calculate scores for relevance and redundancy and rank the features accordingly. Then, the development of the ANN architecture and model was executed utilizing the TensorFlow machine learning framework, employing a Multilayer Perceptron (MLP) configuration with rectified linear units (ReLU) as the transfer function.

A compiled dataset comprising 100,000 data points was partitioned into subsets, with 80% allocated for training and 20% for testing. Model training employed the Adam optimization algorithm. The performance evaluation of the developed model was conducted using root mean squared error (RMSE), mean absolute error (MAE), and the coefficient of determination (R^2). Additionally, an assessment of the significance of input variables was conducted through sensitivity analysis employing partial dependency plots (PDPs) and mean relative effects (MREs).

3. Results and Discussion

3.1 Input variable selection

Figure 2 shows the MRMR scores obtained for the selected variables. From Figure 2, variables exhibiting the positive MRMR scores were chosen as input variables for the ANN model.

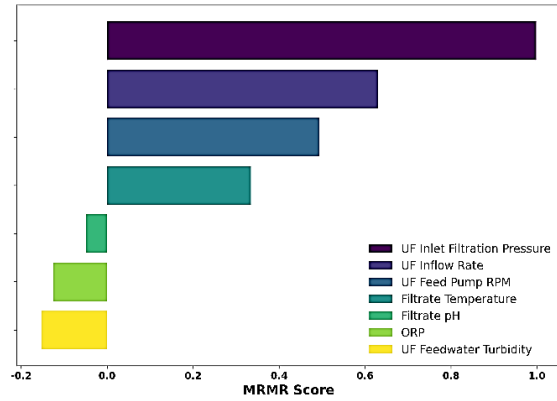


Figure 2: MRMR importance score

3.2 Developed ANN model comparison

Table 1 summarizes the five MLP ANN models developed, each with a unique network architecture.

Table 1: Number of hidden layers and neurons employed in each model architecture

Model	No. of hidden layers	No. of neurons in hidden layers
Model 1	1	81
Model 2	3	71,31,41
Model 3	4	385,449,225,321
Model 4	7	801,673,321,833,225,801,193
Model 5	9	385,193,385,513,321,769,641,641,129

Upon a careful examination of Figure 3, it can be identified that except model 1, remaining four models are well fitted with the actual system. However, a notable concentration of outliers is observed in predictions within the specific range of 150-220 kPa. Also, each figure highlights the scarcity of data points within this range, potentially affecting the model’s comprehensive training and contributing to the observed outliers, resulting in decreased predictive accuracy. On the other hand, as each graph in Figure 3 illustrates, developed models yield higher predictive accuracy within the operating conditions since the data set employed consists of a typical operating data set of the treatment system, where a majority of data points are clustered in the specific operating range as shown in Figure 4.

When comparing five developed models based on the performance metrics shown in Table 2, model 5 emerged as the best model, yielding the highest predictive accuracy with a Mean Absolute Error (MAE) of 1.40 and Root Mean Square Error (RMSE) of 3.56, effectively

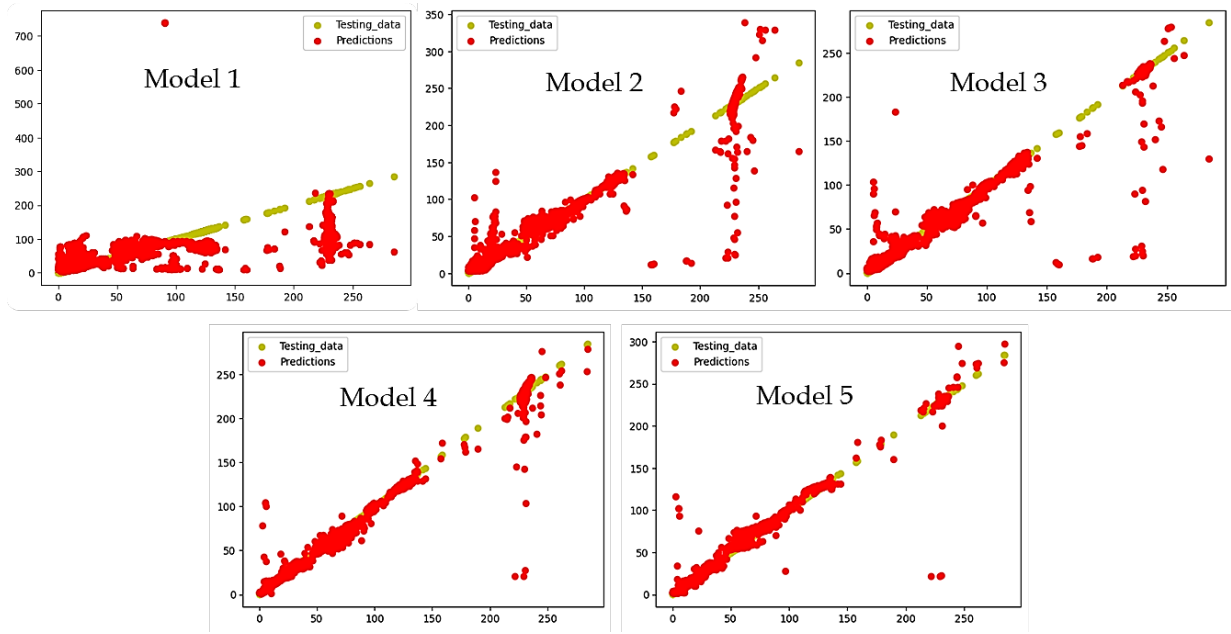


Figure 3: Variation of actual values with model predictions

minimizing the error between predicted and actual values. Furthermore, model 5 exhibits the highest R-squared value of 0.992, signifying a better fit to the testing dataset.

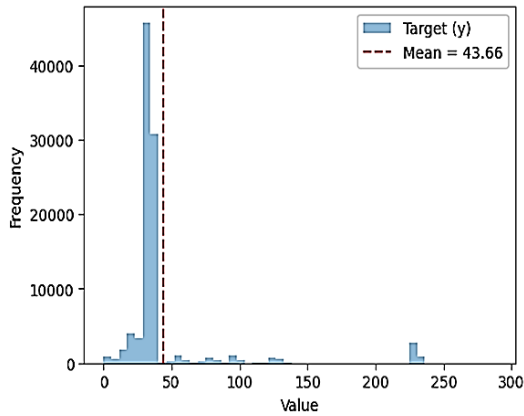


Figure 4: Distribution of TMP values in the dataset

Table 2: Comparison of performance metrics for each model

Model	MAE	MSE	RMSE	R ²
Model 1	9.57	906.12	30.10	0.468
Model 2	2.01	47.21	6.87	0.973
Model 3	1.73	39.31	6.26	0.977
Model 4	1.43	14.67	3.83	0.991
Model 5	1.40	12.68	3.56	0.992

3.3 Partial Dependency Plots (PDPs)

The following figures show PDPs obtained for each input variable in the typical operating

conditions of the UF pre-treatment unit. Observed TMP variation exhibits a complex variation with an obvious upward trend which is evident with the increasing inlet pressure as illustrated in Figure 5. In addition, the figure reveals a decreasing rate of TMP increases beyond an inlet pressure of 240 kPa, suggesting a tendency towards a constant value indicative of a steady state.

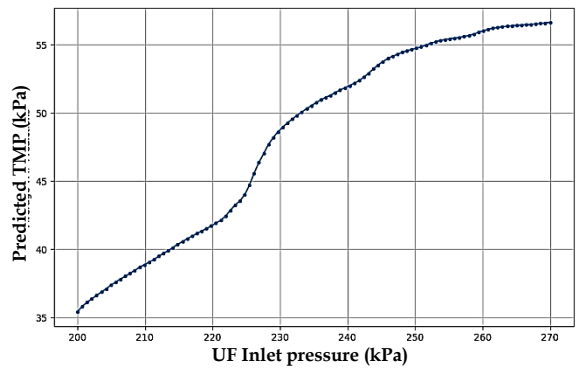


Figure 5: Variation of transmembrane pressure with UF inlet filtration pressure

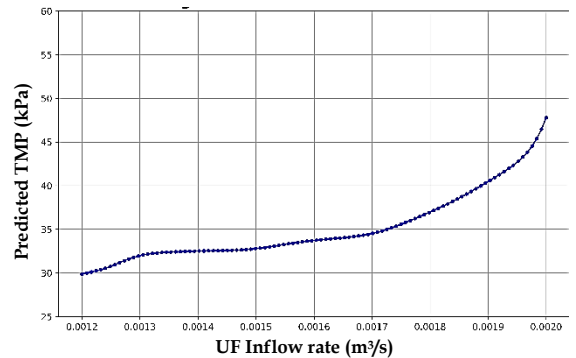


Figure 6: Variation of TMP with UF inflow rate

Similarly, Figure 6 depicts the obvious relationship between predicted TMP and UF inflow rate, showcasing a complex interplay with an increasing trend. Also, both Figure 5 and Figure 6, show variation of TMP values across a significant range indicating a considerable impact on the predicted output. However, when consider the variation of TMP with feed pump RPM and filtrate temperature illustrated in Figure 7 and Figure 8, shows a relatively lesser variation in a smaller range indicating a lesser impact on the predicted output.

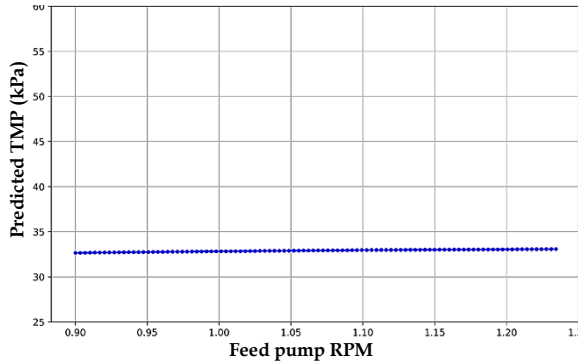


Figure 7: Variation of transmembrane pressure with Feed pump RPM

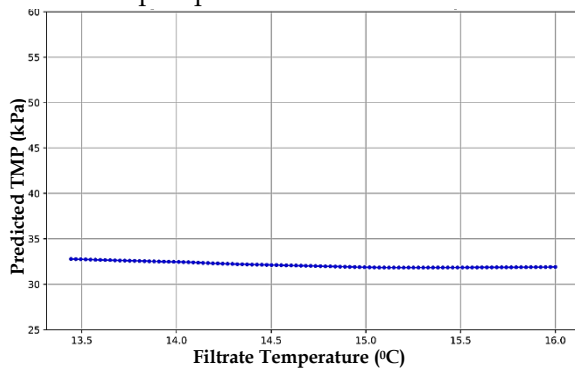


Figure 8: Variation of transmembrane pressure with Filtrate temperature

3.4 Mean Relative Effects (MREs)

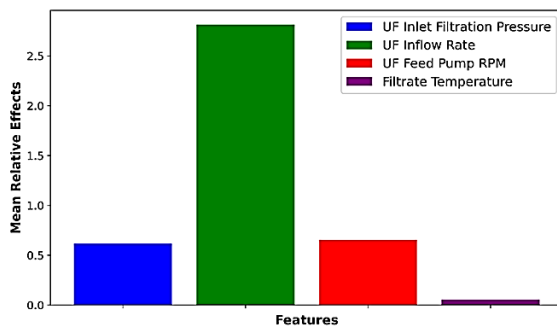


Figure 9: Mean Relative Effects input variable

In Figure 9, the mean relative effects of each input variable are illustrated, determined by the average absolute partial derivative values

resulting from a perturbation of 0.01 (1%). The figure reveals that the UF inlet flow rate exerts the most substantial influence on the model, whereas the filtrate temperature exhibits comparatively minimal impact.

4. Conclusions

Among the developed Multilayer Perceptron (MLP) neural network models, model 5 emerges as the most adept in fitting the system, resulting in a higher predictive accuracy. However, the presence of a notable number of outliers in predictions within a specific range highlights the importance of expanding the training dataset with a larger number of data points exhibiting higher variability. This is essential for achieving a more robustly trained model capable of accurately predicting the desired output across a broader range of values. Furthermore, sensitivity analysis, conducted through Partial Dependency Plots (PDPs) and Mean Relative Effects (MREs), indicates that 'filtrate temperature' exerts minimal influence on the model's predictions. Therefore, in pursuit of a less complex model with enhanced accuracy, it may be possible to consider excluding 'filtrate temperature' from the input variables.

Acknowledgment

The authors acknowledge the final support extended by the Tokyo Cement Company (Lanka) PLC and the University of Peradeniya to conduct the research and the support given by Dr. Damayanthi Herath, Department of Computer Engineering, University of Peradeniya.

References

- Cohen, Y. et al. (2021) 'UF pre-treatment of seawater RO feedwater - performance data', Available at: <https://doi.org/10.5068/D1310B>.
- Jawad, J., Hawari, A.H. and Javaid Zaidi, S. (2021) 'Artificial neural network modeling of wastewater treatment and desalination using membrane processes: A review', *Chemical Engineering Journal*, 419, p. 129540. Available at: <https://doi.org/10.1016/j.cej.2021.129540>.
- Obotey Ezugbe, E. and Rathilal, S. (2020) 'Membrane Technologies in Wastewater Treatment: A Review', *Membranes*, 10(5), p. 89. Available at: <https://doi.org/10.3390/membranes10050089>.
- Zhou, Y., Khan, B., Gu, H., Christofides, P.D. and Cohen, Y. (2021) 'Modeling UF fouling and backwash in seawater RO feedwater treatment using neural networks with evolutionary algorithm and Bayesian binary classification', *Desalination*, 513, p.115129. Available at: <https://doi.org/10.1016/j.desal.2021.115129>.

Hydraulic Modelling of Membrane Filtration Using Computational Fluid Dynamics

Pathirana D.S., Sandaruwan G.P.C., and Nanayakkara K.G.N.*

Department of Civil Engineering, Faculty of Engineering, University of Peradeniya, Sri Lanka

*nadeen@eng.pdn.ac.lk

Keywords: Computational Fluid Dynamics (CFD), Hollow Fiber Membranes, Membrane Modules, Ultrafiltration, Unit-cell meshing

Abstract

This study addresses the significance of membrane filtration in diverse industries, emphasizing its crucial role in ensuring water or effluent treatment's purity, safety, and efficiency. Focused on developing a model for hollow fiber membrane modules (HFMM) using Computational Fluid Dynamics (CFD) techniques, the research aims to simulate and analyze ultrafiltration performance under dead-end filtration. Utilizing ANSYS FLUENT software, the study integrates fundamental fluid dynamics principles, incorporating governing equations and boundary conditions, to explore factors impacting hydraulic performance, including module geometry, operating conditions, and fluid properties. Model validation will be conducted for various inflow turbidity patterns with pre-published data from a desalination experiment done for HFMMs.

1. Introduction

Water scarcity, intensified by climate uncertainties and population growth, necessitates innovative solutions for effective water treatment. The membrane, as a selective barrier, enables water purification by allowing the passage of water molecules while retaining contaminants. This versatile solution, applicable across industries, efficiently overcomes water scarcity challenges and prevents pollution. Computational Fluid Dynamics (CFD), a powerful engineering tool, proves instrumental in membrane purification and hydraulic modelling. By numerically solving fluid motion equations, CFD offers insights, predicts flow patterns, and optimizes designs without extensive physical experiments. Its role in hydraulic engineering enhances accuracy and efficiency, providing cost-effective means to analyse and improve fluid flow systems.

2. Literature Review

Water is a critical resource for the survival of living organisms, with global concerns rising about the availability and quality of freshwater. Zhou et al., (2021) conducted a study on ultrafiltration hollow fiber membrane modules, using a 2D single fiber model with dead-end operation mode and Ansys Fluent software. Their focus was on concentration polarization factors and layer thickness, particularly in seawater. Zhuang et al., (2020) explored effective modes for ultrafiltration hollow fiber membrane modules, employing a 3D single fiber model with dead-end operation mode and Ansys Fluent software, with emphasis on solutions containing large particles. Jian et al., (2020) assessed the overall model performance of forward osmosis hollow fiber membrane modules, using a 2D single fiber model with crossflow operation mode and COMSOL Multiphysics software, concentrating on aqueous NaCl. In a study by Ghidossi et al., (2006), a simplified approach (Eq. 01) utilizing the Darcy equation was proposed to represent the flow mechanism in a hollow fiber ultrafiltration process and calculate the pressure drop.

$$\bar{J} = L_p TMP = \frac{1}{\mu R_m} \tau MP \dots \dots \dots \text{(Eq. 1)}$$

Zhuang et al., (2018) also used the Darcy permeability principle. The resistance value for that was obtained on the basis of the resistance-in-series law, the porous zone merged the membrane and the accumulated cake as shown in Figure 2.1.(Eq. 2)

$$J = \frac{\Delta P}{\mu(R_m + R_f)} \dots \dots \dots \text{(Eq. 2)}$$

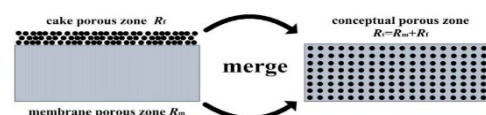


Figure 2. 1: Porous zone (Zhuang et al., 2018)

The steady RANS equation governs all turbulent models, and that governing equation is given below (Eq. 3).

$$(\vec{v} \cdot \vec{v})\vec{v} = -\frac{1}{\rho}\vec{\nabla}p' + \nu\nabla^2\vec{v} \quad (\pi_{ij}, \text{turbulent}) \quad (\text{Eq. 3})$$

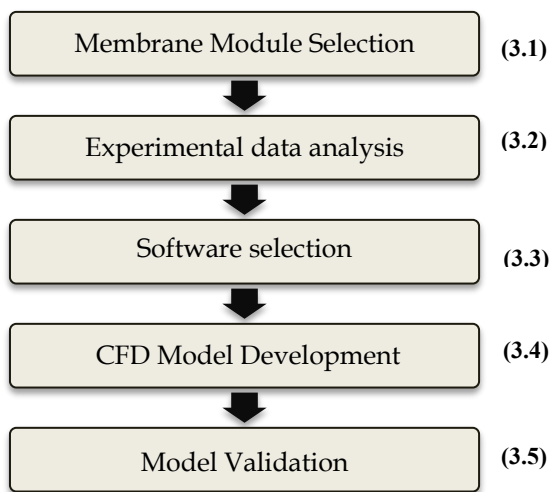
Reynold's stress tensor:

$$\pi_{ij}, \text{turbulent} = - \begin{bmatrix} \overline{u'^2} & \overline{u'v'} & \overline{u'w'} \\ \overline{u'v'} & \overline{v'^2} & \overline{v'w'} \\ \overline{u'w'} & \overline{v'w'} & \overline{w'^2} \end{bmatrix}$$

These research papers contribute to the understanding of membrane module filtration processes and their performance under different conditions providing valuable insights for future research in the field.

3. Methodology

The research was conducted under five major steps as shown in Figure 3.1. CFD model development was again broken down into sub-steps as shown in Figure 3.2.



3.1 Membrane Module Selection

Similar to the experimental research (Zhou et al., 2021) Dizzer® 5000plus Modules with a surface area of 50m² and Polyether sulfone Inge Multibore® Hollow Fiber Membranes (pore size of 0.02 μm) were chosen for the model development.

3.2 Experimental Data Analysis

The pre-published data set from Zhou et al., 2021 research was used as experimental data. Inlet flow rate and outlet pressure were selected as input parameters while inlet pressure was used to calibrate the model. For validation purposes, turbidity values were used.

3.3 Software Selection

The research was conducted using ANSYS FLUENT 2022 R1 software version 22.1.0-10213 and an AMD Ryzen Thread ripper 3960X 24-

Core Processor 3.79GHz and a usable RAM of 128GB 64-bit operating system computer.

3.4 CFD Model Development

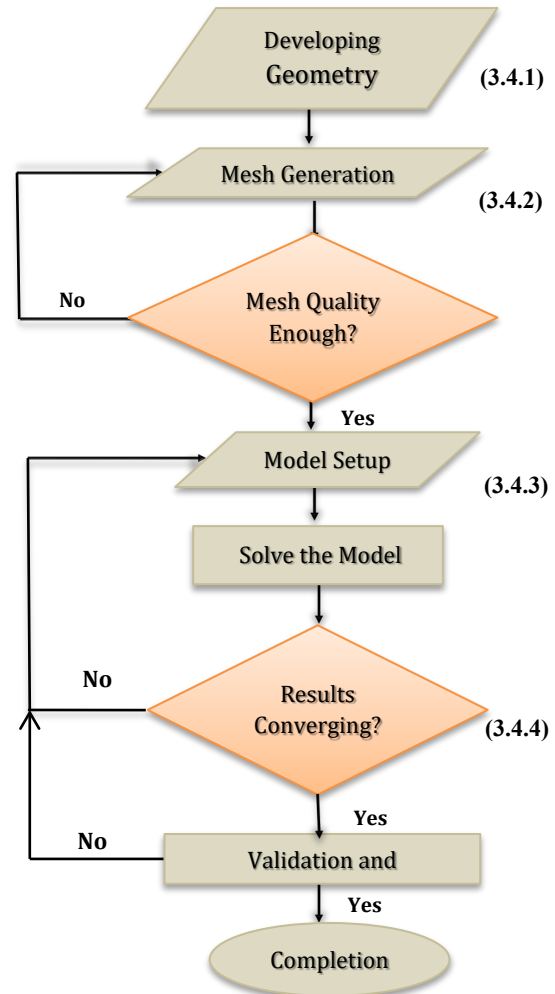


Figure 3.2: CFD model development procedure

The model development was conducted under the sub-steps mentioned in Figure 3.2.

3.4.1 Geometry Development

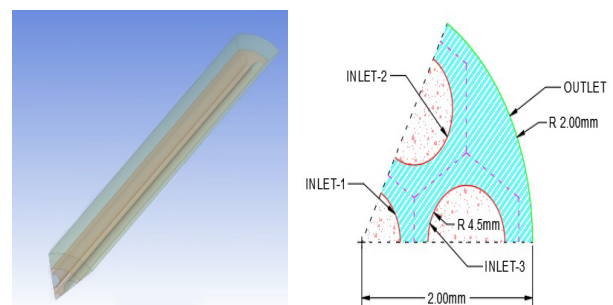


Figure 3.3: Generated geometry of the model (LHS shows the 3D view and the RHS shows the cross-sectional view of the geometry)

3.4.2 Mesh Generation

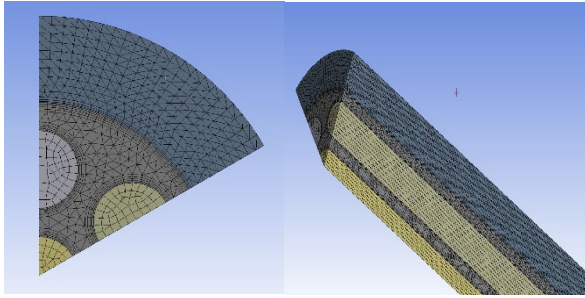


Figure 3.4: Generated mesh of the model
Considering the skewness values, a hybrid mesh with 0.25mm rectangular & triangular cells was chosen as the optimum developed mesh.

3.4.3 Model Setup

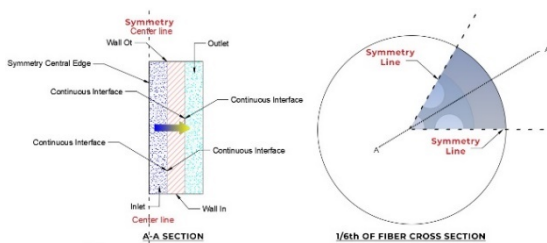


Figure 3.5: Boundary conditions (not to scale)

As shown in Figure 3.5, symmetrical and continuous boundary conditions were applied to the fluid-solid contact surfaces of the developed CFD model.

3.4.4 Results Convergency

The residuals of the 0.25mm mesh models converged on a 10^{-6} scale within 906 iterations (2000 iterations were given).

4. Results and Discussions

4.1 Model Calibration

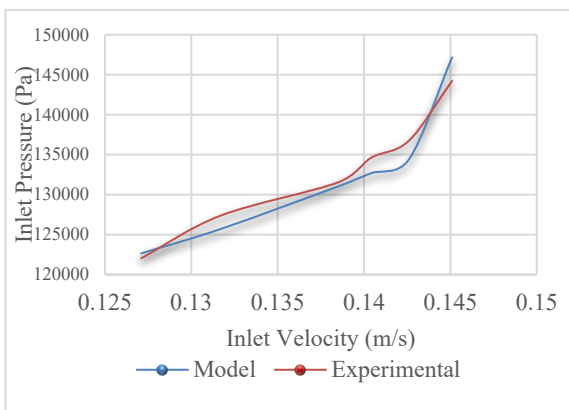


Figure 4.1: Model calibration results

As per the calibration results shown in Figure 4.1, it is proven that the model was calibrated up to more than 97% accuracy by comparing the inlet pressure values of the model and the

experiment which was conducted by Zhou et al., (2021) for the same HFMM arrangement.

4.2 Velocity Variation

As shown in figure 4.2 and 4.3, velocity inside membrane fibres (lumen side) decreases quickly, while the outer side (shell side) exhibits a gradual increase towards the outlet end cap longitudinally. Inlet concentrated force leads to higher seawater velocity, facilitating efficient particle transport to the membrane surface. However, as the flow progresses, velocity variations due to membrane structure, fouling, and concentration polarization may cause uneven distribution and reduced flow rates, affecting overall filtration efficiency.

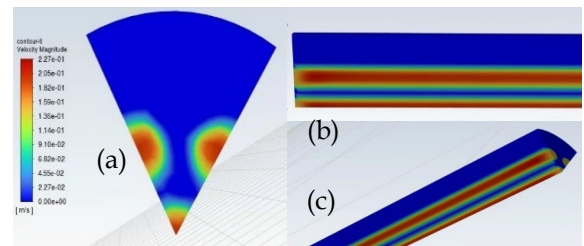


Figure 4.2: Velocity variation in (a) inlet surface; (b) longitudinal direction; (c) 3D view

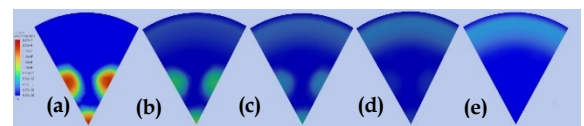


Figure 4.3: Velocity variation along the fibres in (a) inlet (b) 300mm (c) 600mm (d) 900mm (e) end wall from the inlet

4.3 Pressure Variation

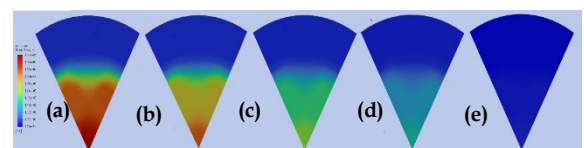


Figure 4.4: Pressure variation along the fibres in (a) inlet (b) 300mm (c) 600mm (d) 900mm (e) end wall from the inlet

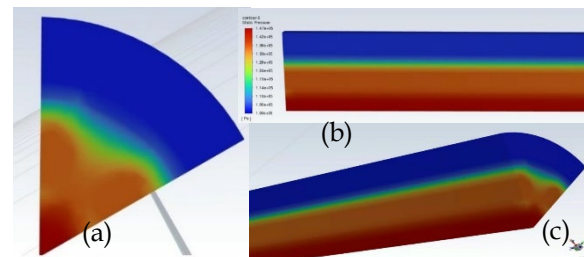


Figure 4.5: Pressure variation in (a) inlet surface; (b) longitudinal direction; (c) 3D view

As the seawater flows through the hollow fiber membrane, the pressure experiences variations

influenced by factors such as membrane fouling, concentration polarization, and the inherent resistance of the membrane material. As shown above, it was observed that the pressure inside the membrane fibres decreases gradually towards the outlet end cap with the longitudinal direction.

4.4 Model Behaviour

As shown in Figure 4.6, it was observed that the feed filtration occurred in a radial direction from the fibers toward the shell side of the membrane.

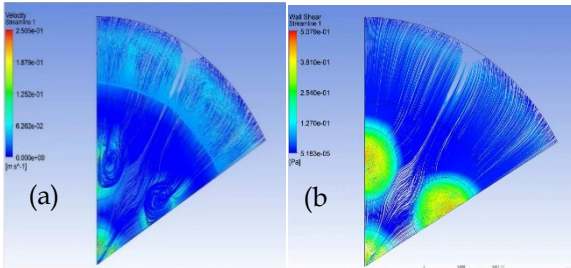


Figure 4.6: model behaviour of (a) velocity (b) wall shear

4.5 Model Validation

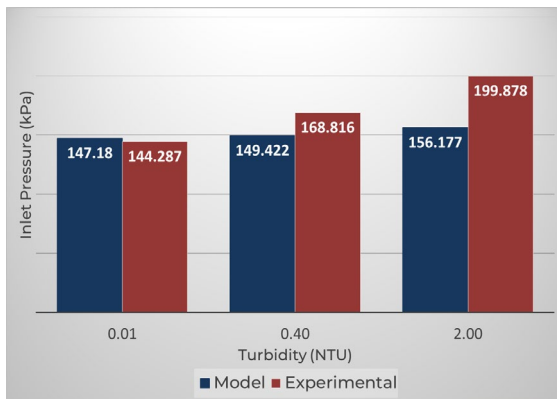


Figure 4.7: Inlet pressure variation for different turbidity conditions

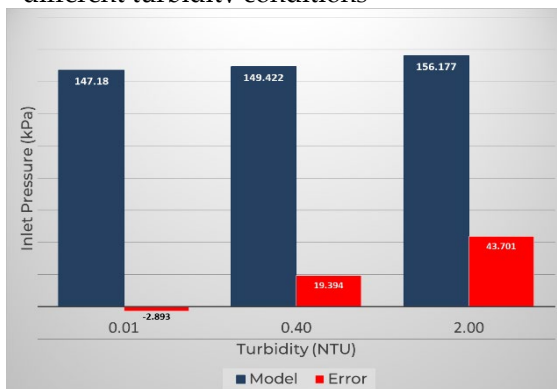


Figure 4.8: error characteristics for different turbidity conditions

As shown in above figures, it was observed that when the turbidity value was increased from 0.01NTU to 2.0 NTU, the difference between the

model and experimental inlet pressure values were increased. Moreover, the error value as well as the error percentage was also increased with the increasement of the turbidity value.

5. Conclusions

The study's findings highlight that a significant portion, specifically over 90%, of filtration in porous media occurs within the initial 300mm of the membrane fiber, diminishing gradually with distance until reaching the end cap. Pressure analysis reveals that the central fiber experiences the highest pressure, leading to lower pressure values in fibers closer to the outer wall. Within a single fiber, the pressure gradient decreases radially from the centroid to the fiber wall. Notably, around 85% of the pressure drop on the lumen side occurs in the initial half of the membrane fiber's distance. Model validation, encompassing various turbidity conditions, demonstrates heightened accuracy for lower turbidity but significant disparities under higher turbidity, indicating limitations in accurately modelling flows through HFMMs in such scenarios. Recommendations include refining the CFD model to address resistance variations, incorporating dynamics of backwash flow for a comprehensive system understanding, and developing an additional model tailored to a diverse experimental dataset to enhance versatility and applicability.

References

- Ghidossi, R., Veyret, D., & Moulin, P. (2006) 'Computational fluid dynamics applied to membranes: State of the art and opportunities', *Chemical Engineering and Processing: Process Intensification*, 45(6), 437-454. Available at: <https://doi.org/10.1016/j.cep.2005.11.002>
- Zhou, Y., Khan, B., Gu, H., Christofides, P. D., & Cohen, Y. (2021) 'Modeling UF fouling and backwash in seawater RO feedwater treatment using neural networks with evolutionary algorithm and Bayesian binary classification', *Desalination*, 513. Available at: <https://doi.org/10.1016/j.desal.2021.115129>
- Zhuang, L., Dai, G. and Xu, Z. (2020) 'CFD study on the performance of hollow fiber ultrafiltration membrane modules with different fiber arrangement', *DESALINATION AND WATER TREATMENT*, 181, pp. 13-27. Available at: <https://doi.org/10.5004/dwt.2020.25147>.

Investigate the Effect of Sustainable Stormwater Management in An Urban Catchment

Abeykoon G.A.M.H.K.*, Dunukara D.A.M.D., and Gunawardana W.C.T.K.

Department of Civil Engineering, Faculty of Engineering, University of Peradeniya, Sri Lanka

*e17002@eng.pdn.ac.lk

Keywords: Best Management Practices (BMPs), Detention ponds, Diversion, Stormwater model, SWMM, Urbanization,

Abstract

Conventional drainage infrastructure in Sri Lanka struggles to manage increasing stormwater due to urbanization, unauthorized construction, and expanding impervious surfaces. This study uses the Storm Water Management Model (SWMM) to assess the current drainage system and evaluate sustainable alternatives, particularly the Mahaiywa sub catchment Kandy. It identifies best management practices (BMPs) like bio-retention cells, rain barrels, and storage ponds to address water quantity issues. Implementation of BMPs resulted in notable reductions in peak flow and increased lag time, with detention ponds proving the most effective. The research suggests that introducing BMPs step-by-step can mitigate flash floods and improve stormwater management in urban areas.

1. Introduction

The study focused on investigating the effect of implementing best management practices in an upstream catchment to effectively reduce and control the peak flow rate and prevent downstream flooding issues. Conducted in the Mahaiyawa sub-catchment of Kandy in Sri Lanka, which had been experiencing frequent flash floods for many years due to high-intensity short-duration rainfalls. The entire catchment area coming to the Mahaiyawa tunnel Drainage canal is shown in Figure 1, can be categorized into four primary sections, each representing distinct drainage paths originating from Udawatta Kele, Asgiriya, Old Matala Road, and Welikanda.

In this research, it is focused on the Udawatta kale sub catchment which is 42% of the entire catchment. The project aimed to identify suitable stormwater management alternatives using Best Management Practices (BMPs) to address water quantity issues in that area. It also involved creating hydraulic models for the selected catchment using SWMM software and

modelling runoff volume variations under different rainfall intensities.



Figure 1: Contribution from Udawatta kele catchment for Mahaiyawa Tunnel canal catchment

2. Literature Review

2.1 Storm Water Best Management Practices

This literature review focuses on identifying appropriate stormwater management alternatives implementing BMPs for a particular urbanized catchment in order to improve challenges with water quality and quantity. BMPs' alternatives in stormwater management are believed to improve the ecological integrity of rivers and streams, reduce flooding and flash flooding in downstream areas (especially in urban areas), reduce sediment transport, and mitigate erosion. Eventually, this makes urban stormwater a useful resource instead of an infliction (Khaniya et al, 2009). Green roofs, rainwater tanks, wetlands, bioswales, pervious pavement, storm-water detention systems, planter boxes, and other related BMPs fall under the category of structural BMPs. Non-structural BMPs include increasing the amount of vegetation in a specific area or region,

enhancing the soil's ability to retain water through modifying properties, and designing structures like buildings and roads with less imperviousness (Iddamalagoda et al., 2022).

3. Methodology

3.1 Study Area

This research study focuses on the stormwater quantity issues in the rapidly growing city of Kandy, Sri Lanka. The study area is located in the Mahaiyawa region, which is part of the Existing drainage canal which carries stormwater into the Mahaweli River. The area experiences flash floods due to the sudden discharge of stormwater flow into the Mhaiyawa Tunnel canal from the Udawtta kale catchment which is approximately 40% urbanized. Furthermore, due to geographic features such as sloppy terrain Udawatta Kele sanctuary. Additionally, the presence of geographic features like sloping mountain terrain in the Udawatta Kele Sanctuary contributes to a reduction in the time of concentration of the flow.

3.2 Data and Data Collection

Overall, this report provides a comprehensive overview of the data collection and analysis process for the SWMM modelling study of the Kandy area. Table 1 shows the various SWMM parameters and data input origins.

Table 1: SWMM Parameters and Relevant Data Extractions

Type	SWMM Parameters	Data Sets
Sub-catchment	Spatial Location, Sub-catchment area, Average slope, Percentage of impervious area	Kandy 5419 GIS data set, 5m×5m resolution DEM, Google Earth's high-resolution satellite imagery,
Conduit	Spatial Location, Cross-section dimensions, Length	Kandy 5419 GIS data set, Field Survey data
Junctions	Spatial Location, Invert level elevations,	Kandy 5419 GIS data set, Field Survey data

Storm Water Outlet	Spatial Location, Invert level elevations,	Kandy 5419 GIS data set, Field Survey data
Rainfall	Time series data for precipitation	IDF curve data for Kandy Katugasthota 2019

3.3 SWMM Model Development

The Stormwater Management Model (SWMM) is a computerized tool extensively utilized for simulating water movement within a watershed. Specifically designed for hydrological analysis, SWMM enables the evaluation of factors like land use modifications, urbanization, and the effectiveness of Best Management Practices (BMPs) in mitigating runoff.

In the SWMM framework, a watershed is subdivided into distinct sub-catchments as illustrated in Figure 2, defined by common attributes such as slope, soil type, and land use. The integration of mountain topography data with watershed and sub-watershed information, along with transportation network data, results in the identification of 46 sub-catchment areas. Each sub-catchment is further segmented into smaller units, encompassing conduits, junctions, and outlets. These components collectively contribute to the simulation of water movement by incorporating variables like precipitation, evaporation, infiltration, runoff, and storage.

SWMM's simulation encompasses the flow of water through conduits, and channels, and the quantification of water stored in catch basins and other storage units. There is a detention pond within Udawatta Kele near the entrance, integrated into the SWMM model. Consideration is given to diverse factors influencing water movement, including land use and the presence of roadways. The model's capability to forecast the hydrological dynamics of a watershed under varying conditions renders it an invaluable asset for effective stormwater runoff management.

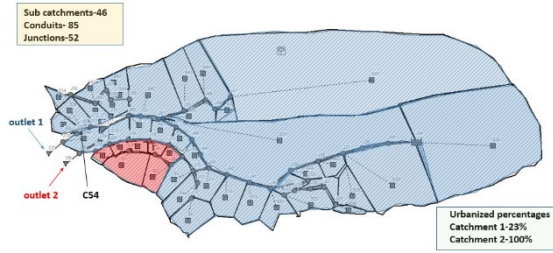


Figure 2: The conceptualized storm-water drainage system, junctions, and the sub-catchments.

The rainfall event during which flow was measured for calibration was considered as rain event 1. The precipitation data obtained for 25-year return periods from IDF curves modelled as event 2. The rain event during which a Flash flood occurred at Mhaiyawa Tunnel on 25th December 2022 was considered as rain event 3.

3.3 Design of Model Development Scenarios

Table 2: Description of Scenarios

Scenario	Remarks
Existing Condition (SC1)	S1 represent the existing state of the drainages.
Only DP (SC2)	Only with detention ponds at appropriate locations were identified during field visits.
Only RB (SC3)	After the installation of only rain barrels for 10% of the population.
Only BR (SC4)	Five bio-retention cells were strategically implemented for the appropriate location identified.
Combination BR + DP (SC5)	Compare the effectiveness of runoff reduction, when used both BR and DP.
Combination BR + RB (SC6)	Compare the effectiveness of runoff reduction, when using both BR and RB.
Combination DP + RB (SC7)	Compare the effectiveness of runoff reduction, when used both DP and RB.
Combination BR +DP +RB (SC8)	Compare the effectiveness of runoff reduction, when used BR, DP and RB.

Combination BR+DP+RB (SC9)	SC8 without implementation Rajan Memorial Ground as a detention pond
Combination BR+DP+RB (S10)	In SC8, proposed two detention ponds equipped with orifices at the bottom

4. Results and Discussions

4.1 Calibration and Validation

A carefully considered drainage channel with a consistent section and significant upper catchment coverage was selected for calibration during the conducted field trips. Accessibility during intense rainfall was a priority. Udawatta Kale rain gauge data was used to calibrate the SWMM model using field data taken on October 9, 2023, and is included in Table 3, guaranteeing precise representation of hydrological dynamics in simulation results.

Table 3: Data collected on 9th October 2023

Time	5.30 pm
Flow depth	13 cm
Conduit width	1.38 m
Velocity of flow	2.486 ms^{-1}
Flowrate through conduit C54	446 ls^{-1}
Rainfall intensity	24 mm/hr

4.2 Results and Discussion

The research involved an examination of runoff in an established setting during three distinct rainfall events. The highest outflow volume was observed during the second rainfall event with a 25-year return period. In the pre-development condition, Outfall 1 experienced flooding, indicating that the conduit leading to the Mhaiyawa Tunnel canal had reached its maximum capacity. Notably, there were no flooded junctions within the study area. Following a thorough analysis of runoff in various sub-catchments, critical sub-catchments were pinpointed by assessing the drainage branches originating from Sri Dhammadassi Mawatha, Lady Torinton Road, Upland Pahala Road, and Dharmashoka Road.

In comparison to SC1, the peak runoff reduction rates for Outfall 1 were 19.31% and 18% for SC8 and SC9, respectively, during Rain Event 2. Conversely, Outfall 2 exhibited a notable 40.47% reduction in peak flow rate for

both SC8 and SC9. The analysis revealed that 77% of the catchment area for Outfall 1 is located within Udawatta Kele Sanctuary, making the implementation of BMPs like rain barrels and bio-retention cells impractical. This accounts for the lower sensitivity of Outfall 1 to BMPs. Moreover, Detention Pond 1 is recommended for water extraction from the valley drainage feeding into the Bandiyawatta drainage canal in order to reduce the runoff contribution from forested areas. A notable difference in peak flow and lag time is observed with the implementation of on-site detention ponds in a bypass arrangement at Rajan Memorial Ground (DP 3) and Ground at Lexington International Primary School (DP 2/Sri Dhammdassi Road). An on-site detention pond functions as a detention facility that comes into action only when required, typically serving as a ground or parking lot under normal conditions. During the initial rain, stormwater is directed to flow in the existing drainage path. As peak discharge occurs, the flow is diverted to selected detention pond sites, which contribute to reduced flow rates in conduits after that detention pond as shown in Figure 3.

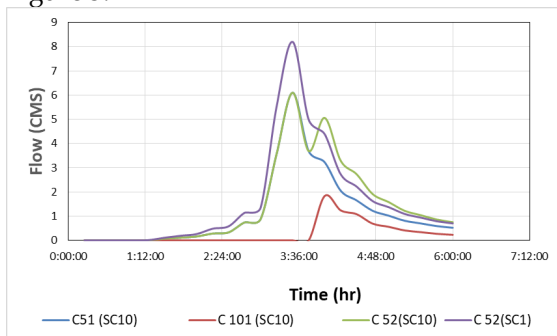


Figure 3: Variation of flow rates in conduits after implementation of diversion structure and orifice for the detention pond 2

Subsequently, after the peak flow in the Mahaiyawa Tunnel subsides, the stored water volume in the detention pond can be discharged.

5. Conclusion

The use of Best Management Practices (BMPs) in upstream sub-catchments significantly reduces Peak flow, effectively managing overflow in the Mahaiyawa Tunnel. Outlet 2, dedicated to urbanized catchments, shows a notable 40% peak flow reduction, indicating

substantial improvement. Scenario 9 emerges as the most practical choice among considered scenarios. Implementing BMPs upstream can prevent costly constructions in existing drainage paths, minimizing expenses, and enhancing flood resilience. These sustainable measures contribute to the development of Sri Lanka, a country in its developmental phase. Further analysis of diverse events can refine outflow predictions, providing accurate data for enhanced suggestions and supporting sustainable development efforts.

References

- Harshani, H.M.D. and Wijesekera, N.T.S. (2011) 'Stormwater management modelling for ungauged watershed in Matara municipality', Engineer: Journal of the Institution of Engineers, Sri Lanka, 44(4).
- Iddamalagoda, I.D.M.P. and Warusavitharana, E. (2022) 'Investigation of application of green infrastructure practices for storm water management in urban areas: a case study of Diyatha Uyana'.
- Khaniya, B., Wanniarachchi, S.S. and Rathnayake, U.S. (2016) 'Sustainable stormwater management system: a conceptual design model for SLIIT, Malabe campus, Sri Lanka', (Vol. 4, pp. 06-2016).
- Pathirana, U.P.L.V., Peiris, M.T.O.V., Jayasinghe, A.B. and Mahanama, P.K.S. (2020) 'Assessment framework to select sustainable storm water management options for urban areas', Assessment, 7(02)
- Rossman, L.A. (2010) 'Modeling low impact development alternatives with SWMM', Journal of Water Management Modeling.

Impact of River Bathymetric Models on River Hydrodynamic Simulations

Banadara W.M.I.J., Hemakumara H.N.S., and Neluwala N.G.P.B.*

Department of Civil Engineering, Faculty of Engineering, University of Peradeniya, Sri Lanka

**pandukaneluwala@eng.pdn.ac.lk*

Keywords: Bathymetric models, Digital Elevation Models, Hydrodynamic modelling

Abstract

This study investigates the impact of different bathymetric models on river hydrodynamics simulations. It involves a thorough review of various bathymetric models, their application in hydrodynamic modeling, and subsequent calibration and validation using field data. The research compares the hydraulic outputs of six Digital Elevation Models (DEMs) and assesses the uncertainty of results from each DEM separately. Findings highlight that the Merit DEM yields superior hydrodynamic simulation results compared to the SRTM DEM. Additionally, DEMs derived from sparse cross-sections and trapezoidal sections demonstrate accurate results, contributing valuable insights to the understanding of bathymetric model choices in river hydrodynamic simulations.

1. Introduction

Accurate river hydrodynamics models are essential for water resource management, flood prediction, and environmental impact assessments. Bathymetric models, depicting riverbed topography, are crucial for generating reliable hydrodynamic simulations, including water levels, velocities, flow rates, and shear stress distribution in rivers. While ground surveys and boat-mounted GPS methods are common for collecting bathymetric data, they are often expensive and impractical for every river. Remote sensing techniques, such as LiDAR and satellite data (e.g., SRTM, ALOS), provide alternatives, but accuracy challenges arise due to turbidity and vegetation issues (Arash et al., 2022).

To address these challenges, estimated bathymetric models, employing simple geometric shapes like trapezoidal sections, offer a practical solution (Saleh et al., 2012). Trapezoidal sections have been identified as providing superior hydrodynamic outputs compared to other shapes.

Hydrodynamic simulations, essential for effective water resource management, can be performed using software like HEC-RAS. Focused on Sri Lanka's Mahaweli River, this research assesses different bathymetric models for the river section between Nawalapitiya and Peradeniya. This study contributes valuable insights into bathymetric model uncertainties and their impact on hydraulic simulations. The results, applicable to regions with similar geomorphological features, are expected to enhance the accuracy of hydraulic predictions and improve water resource management strategies for data-sparse areas.

2. Literature review

The accurate representation of riverbed topography, known as bathymetry, is integral to various hydrologic and hydraulic applications (Dey et al., 2019). In selecting a study area, factors such as reach length and geomorphological features, including meandering and braided characteristics, are crucial considerations (Conner et al., 2013). These features significantly impact simulation outcomes.

Various bathymetric models can be identified in previous studies, but they have used one or two bathymetric models in each study. In this study, six bathymetric models are evaluated. Flow modelling, essential for understanding river dynamics, can be achieved through software like HECRAS (Dey et al., 2019), FastMech (Conner et al., 2013), MIKE11, and MIKE21 (Benjankar et al., 2014). HECRAS employs computational approaches, including diffusion wave and Saint-Venant equations (Arash et al., 2022), to compute flow within a 2D flow area. When considering 1D and 2D modelling, 1D hydrodynamic modelling is used to compare the uncertainty of bathymetric models in river hydrodynamic simulations (Saleh et al., 2013). 2D hydrodynamic modelling

is done to compare the results between 1D and 2D modelling in river hydrodynamic simulations, not for the identify the impact of bathymetry in river hydrodynamic simulation. This study evaluated the uncertainty of the bathymetric model using 2D modelling. Lateral inflow is another factor that needs to be considered in simulation (Arash et al., 2022). While many studies focus on steady-state flow simulations, but in this study, simulation is done in unsteady state conditions. As the 2D modelling creates an additional consistency in results rather than the 1D Modelling (Arash et al., 2022).

3. Methodology

The study was centered on a 35 km river section between the Nawalapitiya and Peradeniya water depth gauge stations in the Mahaweli river, encompassing straight and bend sections shown in Figure 1. HEC-RAS 6.3.1 version software is utilized as the modelling tool. Bathymetric model creation is a crucial aspect of this study. Three major input DEMs, including surveyed DEM, SRTM DEM, and Merit DEM, are employed, and three additional DEMs are generated using Ras Mapper.

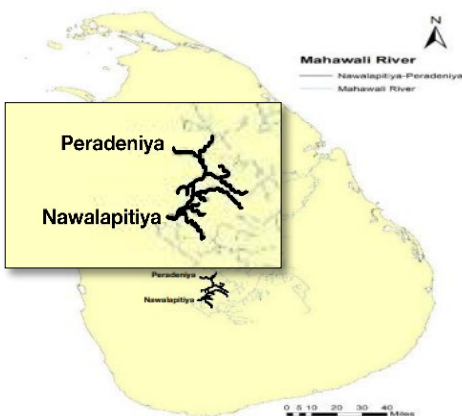


Figure 1: Study area.

The process involves extracting river cross sections at 200 m intervals from the surveyed DEM, creating river bathymetry through interpolation in Ras-mapper, and merging it with the Merit DEM (M1). Randomly extracted cross sections, based on the longitudinal slope variation, are used to create another new DEM by merging with Merit DEM (M2). These randomly obtained cross sections are transformed into trapezoidal sections, forming the basis for creating river bathymetry and yet another new DEM by merging with Merit DEM (M3). In total, six separate DEMs are crafted for the simulation process.

In flow modelling, the initial phase focuses on calibrating and validating Manning's coefficient for accuracy. The surveyed DEM is pivotal in establishing a 2D flow area through Ras Mapper, incorporating three break lines with varying cell spaces (30 m at the river center, 100 m at the riverbank, and 200 m away). Upstream and downstream conditions are defined by the flood hydrograph at Nawalapitiya and normal depth at Peradeniya. Inflows include Kotmale spill flow and Kotmale power flow. Calibration for the flood event of 02/08/2022 to 09/08/2022 involves adjusting Manning's coefficients, while validation for the event from 30/10/2022 to 07/11/2022 utilizes the obtained Manning's coefficients.

Subsequently, the simulation is executed for the six DEMs separately, employing the same 2D flow area, Manning's coefficients, and flood event 02/08/2022. The flow at the Peradeniya gauge and water surface elevation at Meewathura are extracted as results and compared with observed data at these locations. The comparative analysis employs Root Mean Square Error (RMSE) and Mean Absolute Error (MAE) as metrics, providing a statistical evaluation of results variation among different DEMs. And cross-section details also get at different stations to compare the DEMs..

4. Results and Discussion

4.1 Calibration results

The best match model result is shown in figure 2.

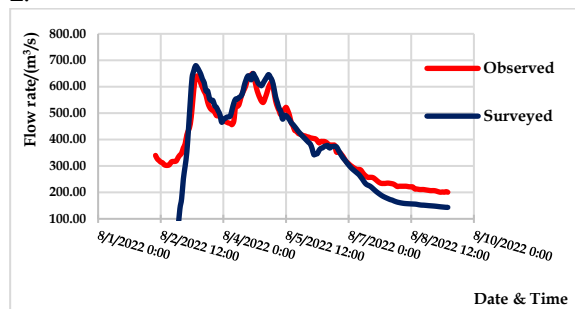


Figure 2: Calibration results.

To obtain this model, the calibration process has carried out by changing the manning's coefficient using the surveyed DEM. Effective rainfall which contributes to runoff after abstraction losses was found as 85% during the calibration. The Root Mean Square Error (RMSE) value is 41.1m³/s.

The validation is done with the same condition for another event to validate the obtained Manning’s coefficients. Which got a reasonable RMSE of $36.4\text{m}^3/\text{s}$.

4.2 Cross-section comparison

The study compares different bathymetric models for the Mahaweli River, revealing variations in channel shapes, particularly at the left riverbank. The surveyed DEM yields the most accurate representation but may experience reduced accuracy over time. Vegetation near the riverbank contributes to a gap between surveyed DEM and other satellite derived DEMs. Trapezoidal sections, particularly M1, closely resemble surveyed DEM cross-sections, making them suitable for simulation in data-sparse regions. However, models M2 and M3, which linearly interpolate depth, exhibit significant differences in channel depth compared to surveyed DEMs, emphasizing their limitations in capturing sudden changes in longitudinal slope.

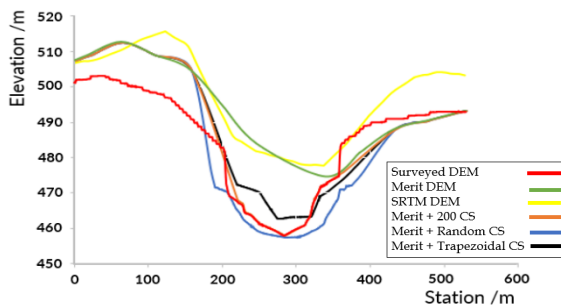


Figure 3: Comparison of cross section from different DEMs

4.3 Discharge comparison at Peradeniya

4.3.1. Surveied DEM, Merit DEM, and SRTM DEM

Figure 4 shows the, initial starting time to receive a flow to Peradeniya.

Surveied DEM < Merit DEM < SRTM DEM
From 04/08/2022 to 05/08/2022, Merit DEM and SRTM DEM discharge values show lower discharge than observed discharge. SRTM DEM discharge values are lower than Merit DEM discharge values. From 05/08/2022 to 09/08/2022, Merit DEM discharge values and SRTM DEM discharge values are nearly same as well as match slightly with the observed discharge values.

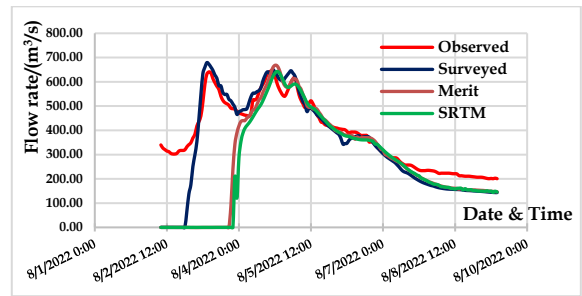


Figure 4: Discharge comparison between Surveied DEM, Merit DEM and SRTM DEM

4.3.2. Surveied DEM with M1 and M2

Figure 5 shows, the initial starting time to receive a flow to Peradeniya varied as follows, $M2 < \text{Surveied DEM}$ and $M1$

$M1$ and $M2$ give much similar results with observed values. But the $M1$ curve is not smooth. There is a small rapid fluctuation in the $M1$ curve. $M1$ and $M2$ discharge results are much better than the surveyed DEM discharge values. $M2$ results are better than the surveyed DEM results.

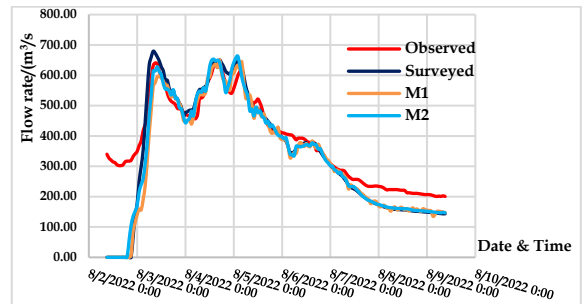


Figure 5: Discharge comparison between Surveied DEM, M1 and M2

4.3.3. Surveied DEM, M2 and M3

The initial starting time to receive a flow to Peradeniya are same in $M2$ and $M3$, as shown in below Figure 6. $M2$ and $M3$ give much similar results. But there are a lot of small fluctuations in the $M3$ curve.

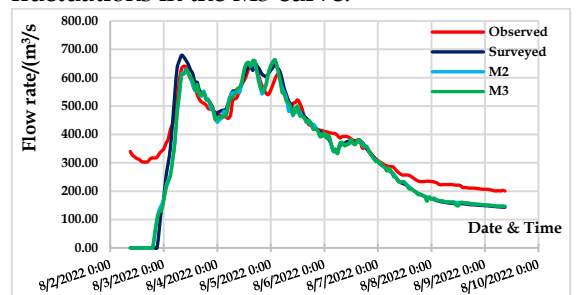


Figure 6: Discharge comparison between Surveied DEM, M2, and M3

According to the RMSE, Mean Absolute Error, and the NSE values shown in Table 1, it can be

considered that M2 and M3 DEMs show precise results similar to the surveyed DEM analysis.

Table 1: Statistical comparison between bathymetric models output data and observed data for the 02/08/2022 to 09/08/2022 flood event.

Bathymetric model	RMSE (m ³ /s)	MAE (m ³ /s)	NSE
Surveyed DEM	41.1	33.8	0.88
Merit DEM	42.8	34.1	0.83
SRTM	43.8	35.1	0.63
M1	40.4	31.9	0.83
M2	40.2	32.5	0.87
M3	40.1	32.2	0.87

4.4 WSE comparison at Meewatura

According to Figure 7, M2 and M3 give closer results to the observed WSE values. M2 and M3 results are much better than the surveyed DEM results. SRTM and Merit DEM results have a huge difference from observed values.

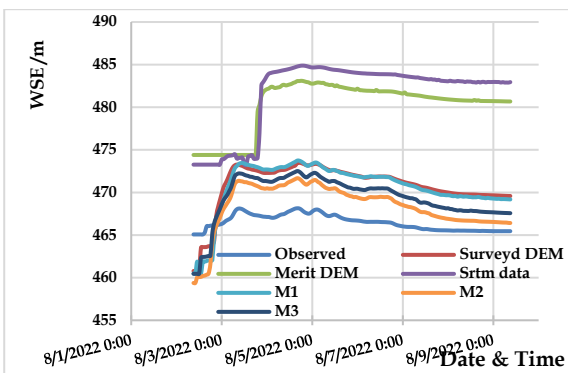


Figure 7: WSE comparison at Meewatura from different bathymetric model simulation results.

Table 2 shows, the RMSE and MAE values of water surface elevation at Meewatura plant and that values concluded that M3 and M2 gives much better result similar to observed values.

Table 2: Statistical comparison between bathymetric models output data and observed data for the 02/08/2022 to 09/08/2022 flood event.

Bathymetric model	RMSE (m)	MAE (m)	Correlation Coe.
Surveyed DEM	4.8	4.8	0.71
Merit DEM	14.1	13.7	0.11
SRTM	15.7	15.1	0.04
M1	4.5	4.7	0.71
M2	2.8	2.6	0.81
M3	3.5	3.4	0.81

5. Conclusions

In the conducted simulation process, all bathymetric models consistently yield reliable results over time. These findings are recommended for rivers with flow rates ranging between 150-700 m³/s. Notably, M2 and M3 demonstrate a quicker initiation of flow at Peradeniya compared to the surveyed DEM, attributed to the failure of HECRAS interpolation in capturing sudden changes in the longitudinal slope. Among Satellite DEMs, Merit DEM is preferable over SRTM DEM for these simulations. The combination of M2 and M3 proves to be the most suitable, providing highly accurate results in data-sparse regions. Additionally, trapezoidal sections emerge as a viable choice for cross-sections in such regions. These insights contribute to the optimization of hydrodynamic simulations in river systems.

References

- Arash, A.M. and Yasi, M. (2022) 'The assessment for selection and correction of RS -based DEMs and 1D and 2D HEC-RAS models for flood mapping in different river types', *Journal of Flood Risk Management*. Available at: <https://doi.org/10.1111/jfr.1271>.
- Benjankar, R., Tonina, D. and McKean, J. (2014) 'One-dimensional and two-dimensional hydrodynamic modeling derived flow properties: impacts on aquatic habitat quality predictions', *Earth Surface Processes and Landforms*, 40(3), pp.340-356. Available at: <https://doi.org/10.1002/esp.3637>.
- Conner, J.T. and Tonina, D. (2013) 'Effect of cross-section interpolated bathymetry on 2D hydrodynamic model results in a large river', *Earth Surface Processes and Landforms*, 39(4), pp.463-475. Available at: <https://doi.org/10.1002/esp.3458>.
- Dey, S., Saksena, S. and Merwade, V. (2019) 'Assessing the effect of different bathymetric models on hydraulic simulation of rivers in data sparse regions', *Journal of Hydrology*, 575, pp.838-851. Available at: <https://doi.org/10.1016/j.jhydrol.2019.05.085>.
- Saleh, F., Ducharme, A., Flipo, N., Oudin, L. and Ledoux, E. (2013) 'Impact of river bed morphology on discharge and water levels simulated by a 1D Saint-Venant hydraulic model at regional scale', *Journal of Hydrology*, 476, pp.169-177. Available at: <https://doi.org/10.1016/j.jhydrol.2012.1>

Rainfall Trend Analysis in Mi-Oya River Basin

Wickramaratne L.T.*, Hasaranga H.J.S. and De Silva M.M.G.T.

Department of Civil Engineering, Faculty of Engineering, University of Peradeniya, Sri Lanka

* e17391@eng.pdn.ac.lk

Keywords: Rainfall, Trend analysis, Mi-oya basin

Abstract

The Mi-Oya River basin is one of the flood prone river basins in Sri Lanka, which is nestled in the North-Western province. Recently the region has grappled with recurring major floods, notably in 2014, 2016, and 2019, prompting inquiries into the relationship between rainfall patterns and these events. There exists a notable gap in comprehensive rainfall trend analysis tailored for Mi-Oya River basin. Hence, this research tried to bridge this knowledge gap by conducting a meticulous analysis of historical rainfall data within the Mi-Oya River basin to identify daily, seasonal, and annual trends. Missing data completion, and consistency checking were done to ensure the quality of observed data. Mann-Kendall method with Sen's slope and the ITA method with ITS method, are employed for the analysis. The objective of using two methods, one numerical and one graphical, is to compare the results, leveraging the unique features that each method offers. The results can be used to identify rainfall patterns within the area, which can be instrumental in effective agriculture and water resource management. Overall, this study provides valuable insights into rainfall trends in the Mi-Oya River basin, offering a foundation for evidence-based decision-making in various sectors dependent on reliable supporting information.

1. Introduction

The Mi-Oya River basin is one of the flood prone river basins in Sri Lanka, which is nestled in the North-Western province and spanning three districts, as shown in Figure 1.1.

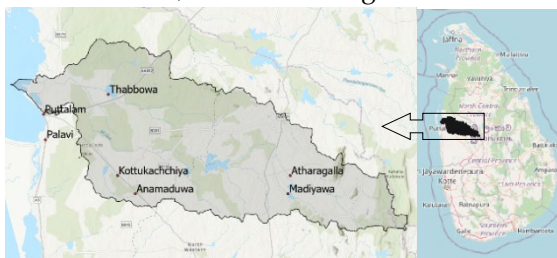


Figure 1.1: Mi-Oya River basin and Spatial variation of the stations

A larger portion of the basin belongs to the Puttalam district and it is rich with numerous reservoirs including Inginimitiya, Thabdowna, Halmilla, and Maha Wewa.

However, recently the region has grappled with recurring major floods, notably in 2014, 2016, and 2019, prompting inquiries into the relationship between rainfall patterns and these events. Despite the documented floods, there exists a notable gap in comprehensive rainfall trend analysis tailored for the Mi-Oya River basin. Hence, this research tried to bridge this knowledge gap by conducting a meticulous analysis of historical rainfall data within the Mi-Oya River basin.

The aim of this study is to investigate the variations in rainfall patterns and trends in the Mi-Oya River basin. The insights gained from this analysis can be instrumental in enhancing the understanding of the role of rainfall trends in frequent flooding, thereby contributing to the formulation of effective flood management strategies and disaster preparedness plans.

This study did not concise only one technique and used the Mann-Kendall method with Sen's slope and the Innovative Trend Analysis (ITA) method with Innovative Trend Slope (ITS) to ensure a thorough and unbiased approach. This diversity aims to yield a robust and reliable set of results, providing a holistic understanding of rainfall patterns in the Mi-Oya River basin.

The implications of this study could extend beyond academic curiosity, offering valuable insights for decision-making in water resource management, agricultural planning, and disaster mitigation. By unraveling the intricacies of rainfall trends, this research contributes to the resilience and sustainable development of the Mi-Oya River basin and its surrounding regions.

2. Literature Review

2.1 Data Processing

In the context of data processing, the emphasis lies on ensuring the reliability of data. Two primary processes, missing data analysis and consistency checking, play pivotal roles in enhancing the quality of input data.

The missing data analysis component addresses the significance of accurate and reliable data in research. Various methods, such as multiple imputation, arithmetic mean method, normal ratio method, and IDW method, are employed based on the percentage of available missing data. Case studies, like Das (2021) utilizing multiple imputations for 1% missing data, highlight the applicability of specific methods depending on data characteristics. Consistency checking followed missing data analysis, involving the verification of internal coherence within the dataset. The double mass curve method, as demonstrated by Kabi Raj (2016), serves as a robust tool to identify and rectify inconsistencies effectively. This step ensures the dataset's integrity before proceeding with further analysis.

3.1 Rainfall Trend Analysis

In rainfall trend analysis, the Mann-Kendall method detects the presence of trends as discussed by K. Raj (2016), while Sen's slope provides information about the trend's magnitude or rate of change. Simultaneously, the ITA method, as discussed by J. Das (2021), offers advanced data visualization and a comprehensive approach to trend identification. The ITA method's unique ability to discern trends associated with different precipitation levels enhances its applicability. A number of studies, including Nisansala, Abeysingha et al (2017), and Raj (2016), showcase the application of the Mann-Kendall method while Gedafaw (2018) discussed about ITA method in different geographical regions and time periods. Moreover, comparisons between Mann-Kendall, Sen's slope, and ITA methods, as illustrated by Kisi and Ay (2019) underscore the advantages of employing multiple methods for a more robust analysis.

3. Methodology

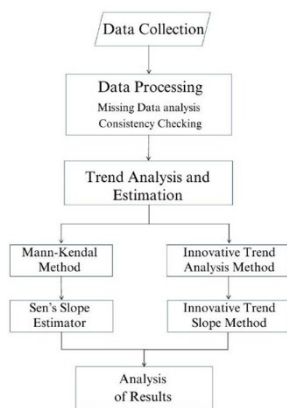


Figure 3.10: Methodology Chart

The methodology employed in this study encompasses a comprehensive approach to analyse rainfall trends over a 30-year period (1990-2019) in the Mi-Oya River basin. The initial phase involved the careful selection of rainfall gauging stations. Initially, 14 numbers of rain gauging stations were identified, and ultimately refined the list to seven stations based on the data availability and consistency. The Inverse Distance Weighted (IDW) interpolation procedure was applied to address missing data issues when the missing percentage is high. However, the Multiple Imputation technique was employed for the missing data amount less than 10%. Consistency checking was performed using the Double Mass Curve and the results are shown in the figure 3.2.

With the satisfaction of consistency, rainfall trend analysis was executed using both the Mann-Kendall method with Sen's slope estimator and the ITA method with the ITS method.

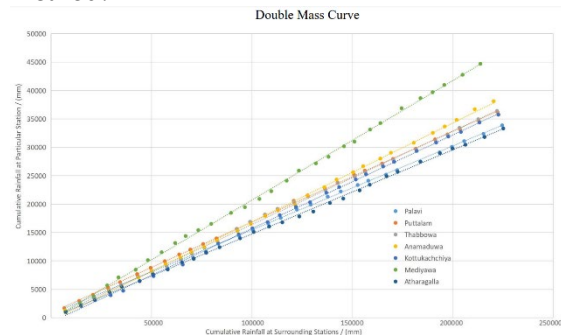


Figure 3.2: Double Mass Curve

The Mann-Kendall method involved a sequence of equations to identify trends, calculate Sen's slope, and generate results. R Studio software was used for this purpose. The ITA method with ITS, a graphical approach, utilized Excel for slope calculations and graphical representations.

3.1 Mann-Kendall Method and Sens' Slope

The Mann-Kendall method with Sens's slope estimator involves a sequence of equations outlined in Equations 3.1 to 3.4. The process begins with Equation 3.1 and progresses through subsequent equations, constituting the procedural steps of the Mann-Kendall method.

$$sgn(X_j - X_i) = \begin{cases} +1 & \text{if } (X_j - X_i) > 0 \\ 0 & \text{if } (X_j - X_i) = 0 \\ -1 & \text{if } (X_j - X_i) < 0 \end{cases} \quad \text{Equation 3.1}$$

$$S = \sum_{i=1}^{n-1} \sum_{j=i+1}^n sgn(X_j - X_i) \quad \text{Equation 3.2}$$

$$Var(S) = \frac{n(n-1)(2n+5) - \sum_{i=1}^n t_i(i-1)(2i+5)}{18} \quad \text{Equation 3.3}$$

$$z = \begin{cases} \frac{S-1}{\sqrt{\text{Var}(S)}} & \text{if } S > 0 \\ 0 & \text{if } S = 0 \\ \frac{S+1}{\sqrt{\text{Var}(S)}} & \text{if } S < 0 \end{cases} \quad \text{Equation 3.4}$$

$$Q = \text{Median} \left(\frac{X_j - X_k}{j - k} \right) \text{ here } j > k \quad \text{Equation 3.5}$$

Once the trend is identified, the magnitude of the trend is determined using Sen’s slope estimator, as per Equation 3.5. In this equation, Q is computed as the median of the expression $((X_j - X_k) / (j - k))$, where j is greater than k. This Sen’s slope estimator is instrumental in quantifying the strength and direction of the trend observed in the data.

3.2 ITA method and ITA Slope method

The ITA method, coupled with the ITS method, presents a graphical approach for trend analysis, designed to draw ITA graphs without relying on sophisticated software tools.

The method initiates by selecting the time series, and arranging it arranged in ascending order. Subsequently, the time series is divided into two equal sub-series. A scatter graph is then plotted one sub-series against the other, with the first half preferably placed on the horizontal axis (Figure 3.3).

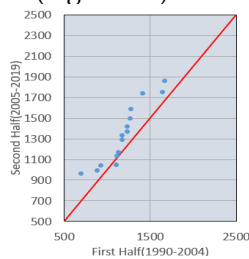


Figure 3.3: ITA Graph

This scatter graph is meticulously adjusted to maintain equal lengths on both horizontal and vertical axes, ensuring a consistent scale. Finally, a 1:1 straight line is drawn on the graph, providing a baseline for further analysis.

Similar to Sen’s slope estimator in the Mann-Kendall method, the ITS is employed to quantify the magnitude of the trend, as expressed in Equation 3.6.

$$B = \frac{1}{n} \sum_{i=1}^n \frac{10(x_j - x_k)}{\bar{x}} \quad \text{Equation 3.6}$$

B=Sens’ slope

n =Number years considered

xj =Rainfall in the second half

xk=Rainfall in the first half

4. Results and Discussion

The results include the temporal and spatial variations of monthly seasonal and annual rainfall trends. Table 4.1 outlines monthly, seasonal, and annual Sens's slope values. Coastal stations (Palavi and Puttalam), exhibit declining trends, while inland stations (Mediyawa and Anamaduwa) display highest increasing trends in annual and seasonal rainfalls. The annual rainfall shows an overall increase for all stations except Puttalam, suggesting a consistent upward trend in annual rainfall across most monitoring stations.

Table 4.1: Sen’s slope estimations

Month	Puttalam	Palavi	Thabowa	Anamaduwa	Mediyawa	Atharagala	Kottukachchiya
January	-1	-1	0	-1	-1	-1	0
February	1	1	1	1	1	0	0
March	0	0	1	1	2	1	2
April	1	0	1	1	1	2	-1
May	-4	-2	-2	-1	0	-1	-2
June	0	0	0	1	0	0	1
July	0	0	0	0	0	0	-1
August	0	0	0	1	0	0	1
September	1	1	0	1	3	0	0
October	-2	0	-2	0	1	1	-4
November	1	-1	-1	0	1	-1	3
December	1	2	1	3	2	1	4
Annual	-1	0	5	11	8	4	11
South West	-3	-2	-1	4	0	-2	0
North East	-1	1	3	1	1	-2	4

Table 4.2: ITA slope estimations

Month	Puttalam	Palavi	Thabowa	Anamaduwa	Mediyawa	Atharagala	Kottukachchiya
January	-1	-1	2	-1	0	-2	0
February	1	0	2	2	-2	3	-5
March	2	3	4	3	3	4	5
April	0	-1	-1	-1	0	1	-2
May	-2	-2	0	0	0	-1	0
June	-2	-1	-1	1	-1	-3	0
July	-4	-2	-1	0	-2	-3	-1
August	9	12	7	7	2	3	8
September	2	1	-1	0	2	-1	0
October	0	2	0	1	1	1	1
November	0	0	0	0	1	0	1
December	1	2	0	3	1	1	4
Annual	0	0	0	1	1	0	1
South West	-1	-1	1	1	-1	-1	1
North East	0	0	0	-2	0	0	1

Spatial variation of annual and seasonal rainfall in coastal areas confirms a significant decreasing trend (Figure 4.1).

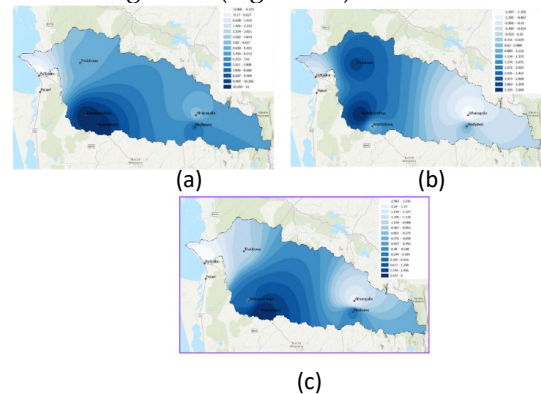


Figure 4.1: (a) Spatial variation of annual Sens’ slope values (b) Spatial variation of Sens’ slope values for North-East monsoon (c) Spatial variation of Sens’ slope values for South-West monsoon

Supporting to Mann-Kendall method with Sen’s slope estimator, as shown in Table 4.2, the ITA method with ITS evidenced that the

Coastal stations (Palavi, Puttalam), experienced a decrease in rainfall trend.

The ITA graphs (Figure 4.2) reveal an increasing trend for almost all the stations, emphasizing the method's effectiveness in identifying upward trends.

The alteration in the North-Eastern monsoon period proposed by monthly analysis suggests a shift in the inter-monsoon period, potentially influenced by long-term climate changes.

Furthermore, the ITA method reveals monotonic patterns indicating consistent upward trends in the mid-years across various stations.

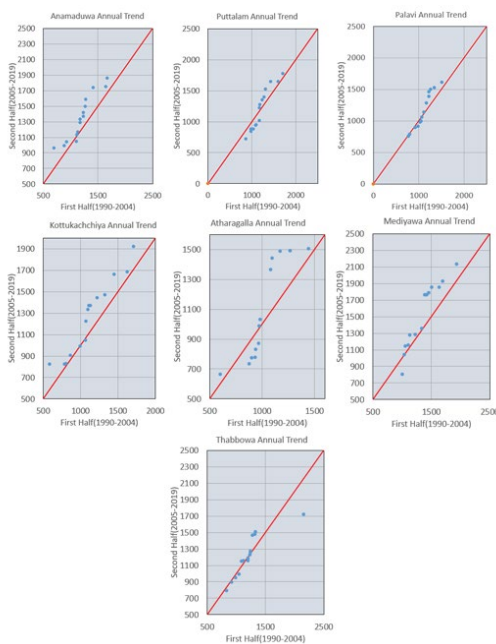


Figure 4.2: ITA graphs for annual trends

The comparison of both methods underscores their agreement on key findings. Both methods detect a consistent annual increase across monitoring stations, with coastal areas exhibiting decreasing trends and inland stations showing a notable increase. Additionally, a rising trend in the North-Eastern monsoon is identified by both methods, while the South-Western monsoon's impact on the study area is relatively insignificant, indicating a reducing trend.

5. Conclusions

In conclusion, this research has yielded significant findings regarding the long-term trends in monthly, seasonal, and annual rainfall within the Mi-Oya River basin. The analysis, employing the Mann-Kendall method and the ITA method, focused on precipitation data from eight monitoring stations. The results reveal

consistent upward trends in annual rainfall across the majority of monitoring stations, emphasizing a general increase over the 30-year period. Importantly, the proximity to coastal areas demonstrates a substantial decreasing trend in observed rainfall, highlighting the influence of geographical location on precipitation patterns. Examination of monthly trends indicates specific months with increasing or decreasing patterns, providing a detailed understanding of the temporal variations in rainfall. The extension of the North East monsoon duration up to March and the shift in the first inter-monsoon period to April-May, along with a reduction in the South West monsoon period by one month (June-September), signifies notable changes in the climatic patterns within the basin.

To enhance the reliability and applicability of this research, recommendations include expanding the number of monitoring stations, extending the time period, and incorporating a wider geographical range of stations. These recommendations aim to bolster the robustness and overall quality of the study, ensuring its relevance for future research endeavours and policy considerations in the Mi-Oya River basin

References

- Caloiero, T. (2019) 'Evaluation of rainfall trends in the South Island of New Zealand through the innovative trend analysis (ITA).', *Theoretical and Applied Climatology*, 139(1-2),
- Caloiero, T., Coscarelli, R. and Ferrari, E. (2019) 'Assessment of seasonal and annual rainfall trend in Calabria (southern Italy) with the ITA method', *Journal of Hydro informatics*, 22(4),
- Malik, A., Kumar, A., Guhathakurta, P. and Kisi, O. (2019) 'Spatial-temporal trend analysis of seasonal and annual rainfall (1966–2015) using innovative trend analysis method with significance test', *Arabian Journal of Geosciences*, 12(10). 4
- Mohammad Arab Amiri and Gocić, M. (2021) 'Innovative trend analysis of annual precipitation in Serbia during 1946–2019', *Environmental Earth Sciences*, 80(23).
- Nisansala, W.D.S., Abeysingha, N.S., Islam, A. and Bandara, A.M.K.R. (2019) 'Recent rainfall trend over Sri Lanka (1987–2017)', *International Journal of Climatology*, 40(7), pp.3417–3435.
- Seenu, P Z., and Jayakumar, K V., (2021) 'Comparative study of innovative trend analysis technique with Mann-Kendall tests for extreme rainfall', *Arabian Journal of Geosciences*, 14(7).

Estimation of Water Level Using Satellite Data

Nawoda J.M.I., Madumalsha A.A.D.C., and Neluwala N.G.P.B.*

Department of Civil Engineering, Faculty of Engineering, University of Peradeniya, Sri Lanka

** pandukaneluwala@eng.pdn.ac.lk*

Keywords: ICESat-2, Water level estimation, Satellite altimetry

Abstract

The accurate estimation of reservoir water levels is highly essential for effective management and planning of water resources. This study leverages ICESat-2 satellite altimetry to construct a water level time series for 10 prominent Sri Lankan reservoirs over a five-year period. The evaluation of water elevation data from six reservoirs, validated against in-situ gauge measurements, reveals consistent trends. Despite slight overestimations by the satellite-derived elevation values, particularly notable at the Kothmale and Udawalawa reservoirs, a robust correlation coefficient of 0.99 underscores a strong linear relationship with in-situ gauge data. However, a discrepancy in data records, attributed to the smaller size of Sri Lankan reservoirs, prompts further exploration of factors influencing these variations. The study emphasizes the evolving nature of remote sensing and calls for continued research to enhance the accuracy and applicability of satellite-derived elevation data in reservoir monitoring and management. This research contributes to the broader understanding of satellite applications in water resource management.

1. Introduction

Reservoirs are essential for local water supply, agriculture, and ecosystem preservation, with Sri Lanka hosting many crucial reservoirs. To advance scientific studies and water resources management, creating a comprehensive, publicly accessible reservoir dataset is imperative, especially in the face of climate warming and a growing human population. However, limited in situ water level data in remote areas poses challenges to resource management.

Traditionally, water levels were manually gauged, but this method has limitations, prompting exploration of ground-based remote sensing techniques like radar or laser altimeters. Satellite altimetry techniques, particularly using ICESat-2, offer a modern

approach to water level estimation, although challenges arise in large-scale lake studies. In this study, ICESat-2 ATL13 products are employed to assess water elevations in 10 Sri Lankan reservoirs, focusing on smaller dimensions often overlooked in past research.

Utilizing in situ data from these reservoirs enhances data quality, providing valuable references to validate existing satellite datasets. The developed code can be applied for specific applications or regions, contributing to effective reservoir management, hydrological modelling, and environmental assessments at the catchment level. The study aimed to estimate water levels in medium-sized reservoirs using satellite data. Its objectives were to identify accurate satellite data for measuring water elevation, evaluate the accuracy of satellite data in predicting water levels, and analyse monthly water levels and seasonal fluctuations.

2. Literature review

2.1 Satellite based water level estimation methods

To overcome limitations in traditional water level estimation methods, the satellite altimetry technique proves valuable. There are two main types of satellite altimetry: radar satellite altimetry and laser satellite altimetry (An et al., 2022). Satellite radar/laser altimetry is a promising technique for directly detecting water levels of open water bodies from space. Satellite altimeters transmit a series of pulses toward the terrestrial surface in the nadir direction and receive the echo reflected by the surface. The two-way travel time of radar or laser is measured and used to calculate the distance between the satellite and the target surface, called "range" (Garkoti & Kundapura, 2021). Through repeated measurements over time, satellite altimetry generates a time series of water level data, facilitating monitoring of changes. Satellite altimetry boasts global coverage, the ability to provide long-term data

records, and the capacity to measure large water bodies.

Traditional radar altimeter sensors (e.g., Topex/Poseidon, Jason, ENVISAT, ERS, CryoSat-2, Sentinel-3, and Sentinel-6) have large footprints (hundreds of meters to a few kilometres). While crucial in many aspects, they struggle to measure water levels in small lakes and reservoirs less than 1 km² due to land interference (Shen et al., 2023).

2.2 ICESat-2 satellite

ICESat-2, a NASA spacecraft, is dedicated to measuring Earth's elevation, including water bodies and ice surfaces. Equipped with the Advanced Topographic Laser Altimeter System (ATLAS), While its main scientific goals focus on monitoring polar glaciers, sea ice, and forests, the technology is also applicable for monitoring inland waters. Featuring six beams arranged in three pairs, the system offers broader global coverage compared to its predecessor. The cross-track interval between beam pairs is approximately 3 km. Each pair consists of a strong and weak beam positioned 90 meters apart on either side of the reference ground track. Additionally, the system boasts a small footprint of around 17 meters. (Zhang et al., 2019). ICESat-2 transmits laser pulses and precisely measures the time it takes for the pulses to reflect back (Calmant et al., 2008). This process allows the spacecraft to generate highly accurate elevation data. Unlike traditional radar altimeter sensors, which face challenges in measuring water levels of small water bodies (<1 km²), ICESat-2 overcomes this limitation. With smaller footprints (a few tens of centimetres)

3. Methodology

In this study, water level time series for 10 main Sri Lankan reservoirs spanning the past five years have been constructed. To identify accurate satellite data sets for future research, a comprehensive review of previous studies was conducted. Based on the analysis of these studies, it is observed that ICESat-2 demonstrates higher accuracy in water level estimation, although it has a temporal resolution of 91 days, limiting its ability to capture only seasonal variations. All available ICESat-2 ATL13 products were collected from the National Snow and Ice Data Centre to obtain water elevations of reservoirs.

To ensure data reliability, an initial filtering process was implemented, focusing on four key quality flags in the ICESat-2 ATL13 products. Data points with "qf_bckgrd" equal to 6, indicating the largest background photon density and typically captured at midday with low signal-to-noise ratio, were removed to mitigate outliers. Entries with "qf_bias_em" >2 or <-2, representing the highest electromagnetic bias and potential elevation errors, were discarded. Similarly, data flagged with "qf_bias_fit" >2 or <-2, associated with significant elevation bias, were eliminated. Entries with "stdev_water_surf" larger than 2, indicative of an extremely large significant wave height, were also excluded.

Then water bodies for this study were selected. Shapefiles were created for the specific water bodies under study, allowing the masking of ICESat-2 ATL13 products to obtain elevation data only for the designated areas. The study employed WGS84 ellipsoidal heights (h), EGM2008 orthometric heights (H), and geoid heights (N) along the track. Opting for orthometric heights with respect to the EGM2008 geoid addressed the instability issue associated with ellipsoidal heights, providing a more reliable measure of water levels. The results for all reservoirs were based on this chosen vertical datum, ensuring a consistent and accurate assessment across the study.

$$H = h_{alt} - h_{range} - N \quad (1)$$

According to equation (1) H is the water body height, H_{alt} is the distance from the satellite to the reference ellipsoid, h_{range} is the distance between the altimeter and the water body and N is the geoid height from the reference ellipsoid.

Finally, the outlier removal process was done for elevation data. Outliers in the river surface remained evident after initial data filtering. Therefore, IQR method were adopted to remove the outliers of each ground track for each observation time. Finally, the remaining observations were used to calculate the average water levels for each observation time.

Next for the data validation process in situ, gauge data of reservoirs that obtained from Mahaweli authority were used. Comparisons between daily averaged water levels derived from ATL13 products and in situ, data of 6 reservoirs were performed to validate our produced water level results. The accuracy and

correlation of the water level estimation were verified through calculations of root mean square error (RMSE) and correlation coefficient (r), demonstrating robust validation between observed and gauge values.

4. Results and Discussion

Also results of water elevation data of 6 reservoirs were evaluated using gauge data of them. Table 1 shows the data validation of that reservoirs with their gauge data.

Table 1: Summary of the water level time series of validated reservoirs with their gauge data.

Reservoir	Date	Satellite Data(m)	Gauge Data(m)
Kothmale	10/23/2019	86.018	85.710
	12/24/2019	88.828	88.460
	1/1/2020	88.827	88.420
	6/22/2020	84.651	84.250
	12/29/2020	83.814	83.220
	6/20/2021	88.428	88.050
	10/18/2021	87.470	86.950
	9/18/2022	83.538	83.070
Victoria	12/25/2018	432.951	432.810
	3/23/2020	428.845	428.600
	12/29/2020	430.687	430.490
	3/22/2021	429.730	429.670
	9/19/2021	430.789	430.640
Randenigala	3/26/2019	230.098	229.740
	12/24/2019	231.141	230.750
	6/20/2021	229.473	229.040
	9/19/2021	230.280	229.980
	3/20/2022	223.638	223.130
	6/19/2022	222.596	222.220
Rantambe	9/18/2022	226.257	225.860
	12/24/2019	152.195	151.830
	6/20/2021	150.699	150.450
	10/18/2021	150.185	149.890
Kala Wawa	1/3/2019	129.136	128.781
	4/4/2019	127.678	127.284
	4/1/2020	127.514	127.05
	7/1/2020	129.000	128.61
	9/29/2020	125.782	125.242
	6/29/2021	128.631	128.202
	6/27/2022	128.423	128.034
	3/27/2023	129.140	128.799
Udawalawa	10/23/2019	86.018	85.710
	12/24/2019	88.828	88.460
	1/1/2020	88.827	88.420
	6/22/2020	84.651	84.250
	12/29/2020	83.814	83.220
	6/20/2021	88.428	88.050
	10/18/2021	87.470	86.950
	9/18/2022	83.538	83.070

The success of the research was assessed for six reservoirs by calculating the root mean square error (RMSE) and correlation coefficient as part

of the individual data validation process. Figure 1 show the comparison of ICESat-2 water elevation data with is situ gauge data.

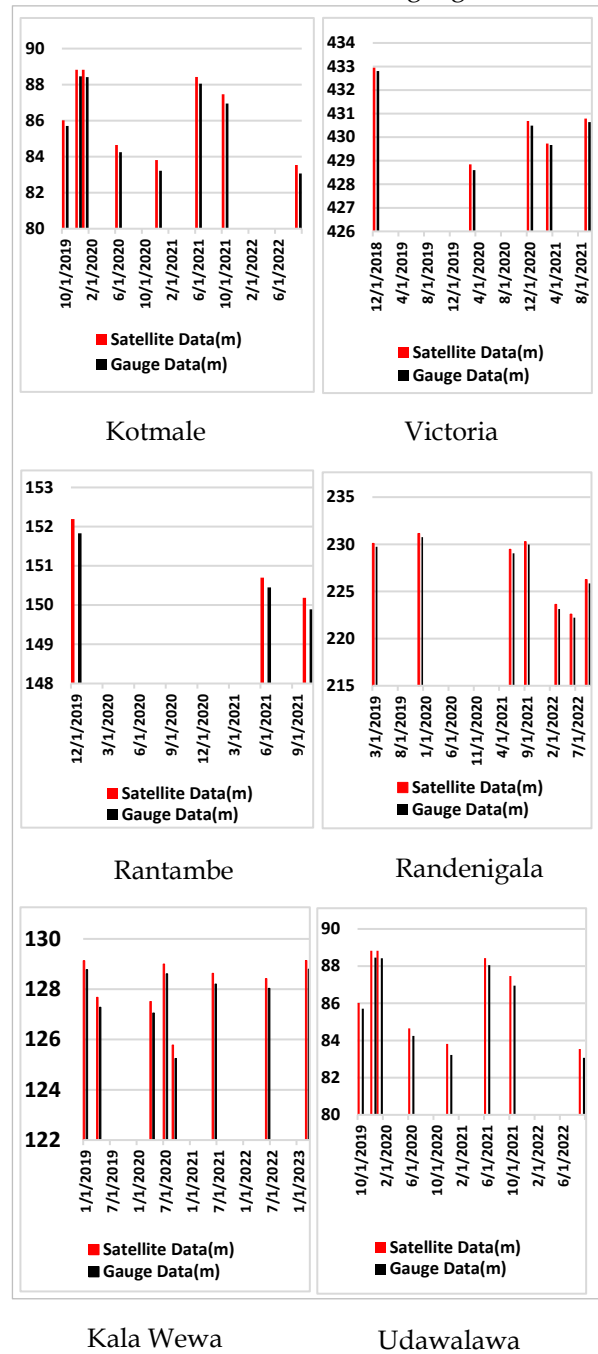


Figure 1: Reservoirs water elevation data obtained from ICESat-2 and in-situ gauge data

When considering the number of observations for each reservoir, they exhibit relatively lower values compared to other global reservoirs. Table 2 presents the number of observations for each reservoir along with the root mean square error and correlation coefficient.

Table 2: Comparison of observations, root mean square Error, and Correlation coefficients among studied reservoirs

Reservoir	Number of observations	RMSE (m)	Correlation coefficient
Kotmale	6	0.43	0.99
Victoria	5	0.42	0.99
Randenigala	7	0.40	0.99
Rantambe	3	0.31	0.99
Kala Wewa	8	0.42	0.99
Udawalawa	8	0.44	0.99

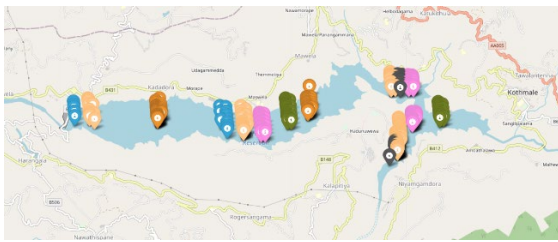


Figure 2: Kotmale reservoir water elevation data obtained from ICESat-2 and location of altimeter footprints (different colours represent different dates)

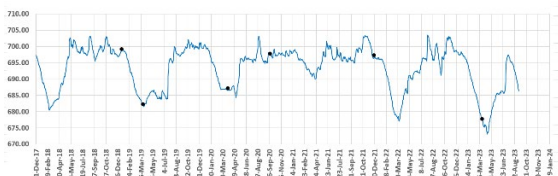


Figure 3: The validation result of Kotmale reservoir, the gauge water level (blue line) and altimetric water level (Black dots) are shown.

Furthermore, our investigation revealed a disparity in data records captured by the ICESat-2 satellite, with a notably lower quantity of measurements recorded. Among the reservoirs studied, Kala Wawa reservoir and Udawalawa reservoir stood out with the maximum number of readings at 8 measurement data records. This discrepancy in data acquisition can be attributed to the relatively smaller size of Sri Lankan reservoirs in comparison to other reservoirs previously investigated in the literature.

5. Conclusions

This study sought to assess the accuracy of satellite-derived elevation values compared to in-situ gauge data across 6 reservoirs. Our findings reveal a consistent trend wherein the satellite-derived elevation values consistently register slightly higher than the corresponding in-situ gauge data readings. Notably, the maximum deviation was observed at the

Kothmale reservoir, reaching 0.7 meters, while the highest Root Mean Square Error (RMSE) was recorded at the Udawalawa reservoir, with a value of 0.44 meters.

Despite these variations, it is noteworthy that the correlation coefficient remained consistently high at 0.99 across all reservoirs validated. This suggests a strong linear relationship between the satellite-derived and in-situ gauge data, emphasizing the reliability of the former in capturing elevation trends.

In light of these findings, it is evident that the observed discrepancies in elevation values are not uniform across reservoirs, and the choice of satellite data source may influence the accuracy of results. As the field of remote sensing continues to evolve, further research is warranted to enhance this understanding of the factors contributing to these variations, ultimately refining the applicability of satellite-derived elevation data in reservoir monitoring and management.

References

An, Z., Chen, P., Tang, F., Yang, X., Wang, R. and Wang, Z. (2022) ‘Evaluating the Performance of Seven Ongoing Satellite Altimetry Missions for Measuring Inland Water Levels of the Great Lakes’, *Sensors*, 22(24), p. 9718. Available at: <https://doi.org/10.3390/s22249718>.

Calmant, S., Seyler, F. and Cretaux, J.F. (2008) ‘Monitoring Continental Surface Waters by Satellite Altimetry’, *Surveys in Geophysics*, 29(4-5), pp. 247-269. Available at: <https://doi.org/10.1007/s10712-008-9051-1>.

Garkoti, A. and Kundapura, S. (2021) ‘Deriving water level and discharge estimation using satellite altimetry for Krishna River, Karnataka’, *Remote Sensing Applications: Society and Environment*, 22, p. 100487. Available at: <https://doi.org/10.1016/j.rsase.2021.100487>.

Musa, Z.N., Popescu, I. and Mynett, A. (2015) ‘A review of applications of satellite SAR, optical, altimetry and DEM data for surface water modelling, mapping and parameter estimation’, *Hydrology and Earth System Sciences*, 19(9), pp. 3755-3769. Available at: <https://doi.org/10.5194/hess-19-3755-2015>.

Shen, Y., Liu, D., Jiang, L., Nielsen, K., Yin, J., Liu, J. and Bauer-Gottwein, P. (2022) ‘High-resolution water level and storage variation datasets for 338 reservoirs in China during 2010-2020’. Available at: <https://doi.org/10.5194/essd-2021-470>.

Xu, N., Zheng, H., Ma, Y., Yang, J., Liu, X. and Wang, X. (2021) ‘Global Estimation and Assessment of Monthly Lake/Reservoir Water Level Changes Using ICESat-2

Identification of the Most Critical Parameter for Wastewater Treatment Using Stoat Software

Wijewickrama W.S.C., Wimalarathne P.G.S.N., and Rathnayake R.M.L.D.*

Department of Civil Engineering, Faculty of Engineering, University of Peradeniya, Sri Lanka

* *lashithar@eng.pdn.ac.lk*

Keywords: Dynamic simulation, Sensitivity analysis, STOAT, Wastewater treatment,

Abstract

Dynamic simulation tools like STOAT enhance wastewater treatment plant (WWTP) performance by improving risk management and reducing costs, time, and energy consumption. STOAT, a dynamic simulation modelling software, helps engineers evaluate various treatment processes, making it a valuable tool for operational optimization. This study employed STOAT to conduct a sensitivity analysis on Kurunegala and Ekala WWTPs, aiming to identify critical parameters influencing performance while avoiding costly and time-consuming manual procedures. The research focused on offering solutions for improved wastewater treatment processes and future implementations, highlighting STOAT's role in effective wastewater management. In the study, wastewater treatment processes at Kurunegala and Ekala WWTPs were modelled using BOD (ASAL) models. Model calibration ensured the validity and reliability of the results, followed by sensitivity analysis to assess the impact of parameter variations on system performance. The sensitivity analysis for Ekala WWTP indicated that variations in flow rate, return activated sludge (RAS), and the kinetic coefficient K_{Lamin} significantly influenced key water quality indicators like BOD, TSS, NH_4^+ , and NO_3^- . For Kurunegala WWTP, similar variations highlighted the importance of balancing nitrification and denitrification processes to achieve desired nutrient levels in the effluent. These findings underscore the need for precise parameter management and the use of dynamic simulation tools like STOAT for optimizing WWTP performance.

1. Introduction

Wastewater treatment is crucial for public health, biodiversity preservation, and effective water management, with biological treatment, particularly the activated sludge process, employing various advanced processes each with its advantages and limitations (Gao et al., 2016). Dynamic simulation tools have become

instrumental in optimising wastewater treatment plant (WWTP) performance, enhancing risk management, and reducing cost, time, and energy consumption. STOAT, a versatile, dynamic simulation modelling software, evaluates various treatment processes, aiding engineers in scenario assessment and operational optimisation (Minhaj et al., 2020). With increasing global demand, dynamic simulation modelling is essential for predicting and understanding system behaviour over time. STOAT, a dynamic wastewater treatment modelling software by WRc, is globally recognised for simulating over 40 processes, uniquely based on BOD and COD models (Akuma, Hundie, & Bullo, 2022).

The Jababeka Industrial Estate (KIJ) research assessed Jababeka 1 WWTP's removal efficiency and operating parameters using STOAT software. With BOD, COD, and TSS removal rates meeting standards, the analysis emphasised the significant impact of discharge, underlining its importance in operational and maintenance strategies (Minhaj et al., 2020).

In this study, STOAT was employed to conduct a Sensitivity Analysis on Kurunegala and Ekala WWTPs, as this WWTP is to be upgraded future for septage treatment. This study was conducted to identify critical parameters influencing performance and bypassing time-consuming manual and experimental procedures, which can be costly. The findings aim to offer solutions for improved wastewater treatment processes and future implementations while underscoring STOAT's role in effective and efficient wastewater management practices.

2. Methodology

The identification of the most critical parameter for wastewater treatment using STOAT software was undertaken in a research study that involved two different WWTPs: the Kurunegala sewage treatment plant and the Ekala waste treatment plant. The study's implementation process was detailed

sequentially in the methodology. The wastewater treatment processes at these plants were modelled and simulated to distinguish the ultimate outcomes of the study.

2.2 Modelling Using STOAT Software

Using BOD (ASAL) models has considered both models for two WWTPs in this simulation context rather than taking COD (IWAQ) models. For Kurunegala, WWTP ASAL 1A has been selected considering the two-stage activated sludge process. Since the stage-activated sludge process is considered for the Ekala WWTP ASAL 5A model has been selected for the study.

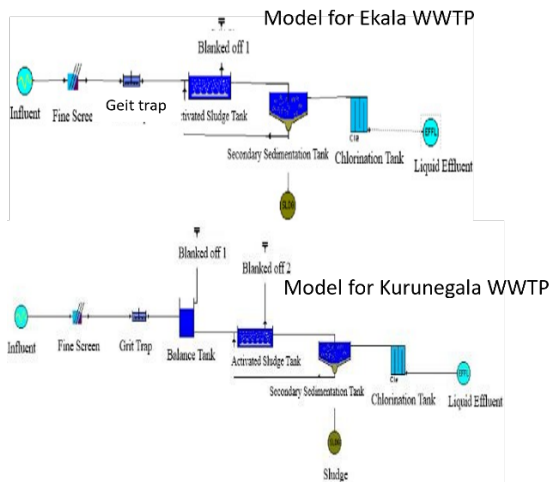


Figure 1: Images of models of Ekala (top) and Kurunegala (bottom) WWTPs

In the Ekala sewage treatment plant, fine screen, grit chamber, anoxic tank, anaerobic tank, aerobic tank, secondary sedimentation tank, and disinfection unit are the key unit process arrangements using data given in the STOAT manual (Figure 1).

In Kurunegala WWTP, the STOAT model included the fine screen, grit chamber, equalization tank, primary sedimentation tank, activated sludge system with pre-denitrification, and secondary sedimentation tank.

2.3 Sampling Procedure and Laboratory Tests

At the Kurunegala sewage treatment plant, samples were collected from five locations, representing influent wastewater, various treatment stages, and effluent quality. Over two days and four sampling sessions, biological oxygen demand (BOD), Ammonium (NH_4^+), Nitrate (NO_3^-), total suspended solids (TSS), Phosphate (PO_4^{3-}), and Mixed Liquor Suspended Solids (MLSS) were quantitatively measured for the STOAT model. Similarly, the

Ekala wastewater treatment plant underwent sampling at five locations, with laboratory tests focusing on BOD, Ammonia, TSS, MLSS, and Phosphate (PO_4^{3-}) due to its three-stage activated sludge process.

2.4 Model Validation

As the initial step, model calibration was done to make the model, giving the model effluent values as close as possible to the actual test results for sample effluent values by varying the input values and conditions constrained to actual WWTP running parameters. To ensure the validity and reliability of the results, the model was run with another data set for model validation.

2.5 Conducting of sensitivity analysis

Sensitivity analysis assesses the impact of parameter variations on a mathematical model or system performance by quantifying the uncertainty in the simulation model output relative to its input. The sensitivity index is crucial in STOAT modelling, indicating the parameters that substantially influence modelling results. The sensitivity index is calculated using a specific formula or equation 1.

$$\text{Sensitivity Index} = \frac{\left(\frac{O' - O}{O}\right)}{\left(\frac{P' - P}{P}\right)} \quad (1)$$

Where,

O' - Output after parameter change

O - Actual output parameter

P' - Parameter after change

P - Initial parameter value

For the analysis flow (influent discharge), return activated sludge flow (R.A.S.), sludge wastage flow (S.W.F.), oxygen transfer coefficient in aerobic tank of activated sludge ($K_L \text{amin}$) and MLSS recycle flow (M.R.F.) has been selected as the parameters which were varied by small increments; by increasing by 5% and by decreasing 5% separately and individually for each parameter, assessing how each case has affected the overall treatment. Sensitivity in the index for each case has been derived to arrive at final conclusions.

3. Results and Discussion

3.1 Model validation

The STOAT models for the Kurunegala and Ekala wastewater treatment plants were calibrated and validated based on samples that were analysed and information received from the wastewater treatment facilities. The summary of validation is depicted in Figure 2.

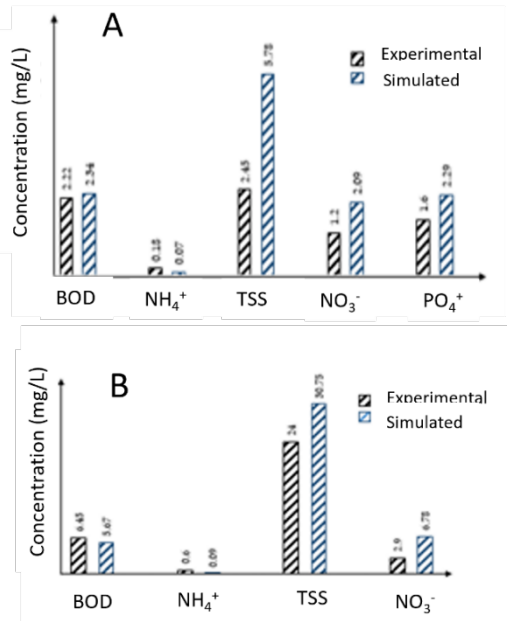


Figure 2: Model calibration data (A) for Ekala WWTP and (B) for Kurunegala WWTP

The provided data in Figure 2 compares experimental and simulated results for the Ekala and Kurunegala WWTP, measuring key parameters such as BOD, NH₄⁺, TSS, NO₃⁻ and PO₄³⁻. For Ekala WWTP, the experimental and simulated values for BOD, NH₄⁺, TSS, NO₃⁻ and PO₄³⁻ are 2.22 and 2.34, 0.15 and 0.07, 2.48 and 5.78, 1.2 and 2.09, and 1.6 and 2.29 respectively. For Kurunegala WWTP, the corresponding values are 6.45 and 5.67, 0.6 and 0.09, 14 and 19.97, 2.9 and 6.79 respectively. These results show that WWTPs effectively reduce BOD and NH₄⁺ levels, indicating efficient removal of organic matter and nitrification. Although the simulated TSS values are slightly higher than the experimental ones, they remain within a manageable range. The NO₃⁻ and PO₄³⁻ levels are within acceptable limits, demonstrating effective nitrification and phosphate removal. Overall, the experimental and simulated results align well with wastewater treatment guidelines, indicating that the model used is accurate and suitable for further analysis and optimisation of the WWTPs.

3.2 Sensitivity Analysis for Ekala Wastewater Treatment Plant

The sensitivity index for the Ekala plant was calculated by considering the BOD, TSS, NH₄⁺, NO₃⁻, and PO₄³⁻, and Table 1 shows the calculated values. The provided data illustrates the impact of variations in operational parameters on key water quality indicators in a wastewater treatment process, specifically focusing on BOD, NH₄⁺, NO₃⁻, and PO₄³⁻.

Examining the changes in these parameters with a $\pm 5\%$ variation in several operational factors offers valuable insights into process dynamics and potential optimisation strategies.

Firstly, it's observed that flow rate variations (Flow) substantially influence BOD, TSS, and NH₄⁺, with these parameters showing proportional changes in response to alterations in flow. This suggests that adjustments in flow rate can directly impact the wastewater's organic load, suspended solids content, and the concentration of ammonium.

Secondly, the data highlights the significance of return-activated sludge (RAS) in influencing BOD, TSS, and NH₄⁺. A reduction in RAS results in decreased removal of organic matter and suspended solids, leading to elevated levels of BOD and TSS. Conversely, an increase in RAS enhances treatment efficiency by reducing these parameters.

Moreover, the coefficient KL_{amin} exhibits pronounced effects on all parameters, particularly BOD, TSS, NH₄⁺, and NO₃⁻. This underscores the importance of fine-tuning process kinetics and mass transfer rates to optimise treatment performance. Notably, the substantial increase in NO₃⁻ with a +5% variation in KL_{amin} suggests enhanced nitrification, which may positively impact nitrogen removal efficiency.

However, it's worth noting that phosphate concentrations remain unaffected by variations in the operational parameters considered in the dataset. This indicates a relative insensitivity of phosphate removal processes to changes in flow rate, return activated sludge, and kinetic coefficients, highlighting the need for targeted interventions to address phosphate removal if required.

3.3 Sensitivity Analysis for Kurunegala Sewage Treatment Plant

The sensitivity index for the Kurunegala WWTP plant was calculated considering the BOD, TSS, NH₄⁺, and NO₃⁻, and Table 2 shows the calculated values.

The provided data presents variations in key water quality parameters BOD, TSS, NH₄⁺, and NO₃⁻ in response to $\pm 5\%$ changes in operational parameters within a wastewater treatment process. These variations highlight the intricate relationship between operational conditions and treatment performance. Notably, changes in flow rate (Flow), RAS, and

the kinetic coefficient K_{Lamin} significantly impact BOD and TSS concentrations, indicating their crucial roles in organic matter and solids removal. Moreover, variations in NH_4^+ and NO_3^- concentrations suggest balancing nitrification and denitrification processes to achieve desired nutrient levels in the effluent. Although Supernatant Waste Flow (S.W.F.) and Mixed Liquor Recycle Flow (M.R.F.) exhibit relatively smaller effects on water quality indicators, they still contribute to overall process dynamics. These findings underscore the importance of optimising operational parameters to enhance treatment efficiency, minimize pollutant discharge, and ensure regulatory compliance in wastewater treatment systems

4.0 Conclusions

The analysis conducted on the Ekala and Kurunegala wastewater treatment plants revealed the intricate relationship between operational parameters and key water quality indicators, including BOD, TSS, NH_4^+ , NO_3^- , and PO_4^{3-} . Variations in flow rate, return activated sludge (RAS), and the kinetic coefficient K_{Lamin} significantly influenced treatment performance, emphasising the need for precise parameter management. While flow rate adjustments directly impacted organic load and suspended solids content, RAS optimisation was crucial in enhancing removal efficiency. Fine-tuning K_{Lamin} coefficients proved essential for efficient nutrient removal, particularly for BOD, TSS, NH_4^+ , and NO_3^- . Despite the insensitivity of phosphate removal processes to operational variations, targeted interventions may be necessary. Overall, the

findings underscored the importance of optimising operational parameters to ensure regulatory compliance and achieve efficient wastewater treatment, highlighting the significance of employing software tools like STOAT for process optimisation.

References

Akuma, D.A., Hundie, K.B. and Bullo, T.A. (2022) 'Performance improvement of textile wastewater treatment plant design by STOAT model simulation', *Environmental Health Engineering and Management*, 9(3), pp. 213–221. Available at: <https://doi.org/10.34172/EHEM.2022.22>.

Crini, G. and Lichtfouse, E. (2019) 'Advantages and disadvantages of techniques used for wastewater treatment', *Environmental Chemistry Letters*, 17(1), pp. 145–155. Available at: <https://doi.org/10.1007/s10311-018-0785-9>.

Gao, Y.N., Liu, X.Z., Zhang, R.X., Shan, J.J., Sun, M.Q., Zong, Z.X., Li, C.W. and Wang, X.Z. (2016) 'Operation and management of Liaoning wastewater treatment plants by STOAT Simulation', *MATEC Web of Conferences* (Vol. 63, p. 04019) EDP Sciences. Available at: <https://doi.org/10.1051/mateconf/20166304019>.

Minhaj, P.G.O., Pratama, M.A., Adityosulindro, S. and Hartono, D.M. (2020) 'Modelling performance of industrial park wastewater treatment plant by STOAT software', *E3S Web of Conferences* (Vol. 211, p. 02018), EDP Sciences. Available at: <https://doi.org/10.1051/e3sconf/202021102018>.

Table 1: Results of sensitivity analysis for Ekala WWTP

Parameter	BOD		TSS		NH_4^+		NO_3^-		PO_4^{3-}	
	+5%	-5%	+5%	-5%	+5%	-5%	+5%	-5%	+5%	-5%
Flow (m^3/hr)	0.622	0.622	0.422	0.422	0	0	0.867	0.867	0	0
RAS (m^3/hr)	0.178	0.089	0.141	0.175	0	0	0.157	0.236	0	0
S.W.F. (m^3/hr)	0.356	0.356	0.042	0.035	0	0	0	0	0	0
K_{Lamin} (mg/l)	0.222	1.111	0.018	0.053	64	980	0.197	3.708	0	0
M.R.F. (m^3/hr)	0	0	0	0	0	0	0.028	0	0	0

Table 2: Results of sensitivity analysis for Kurunegala WWTP

Parameter	BOD		TSS		NH_4^+		NO_3^-	
	+5%	-5%	+5%	-5%	+5%	-5%	+5%	-5%
Flow (m^3/hr)	3.297	0.942	0.992	2.025	17.491	0	4.012	2.142
RAS (m^3/hr)	2.825	1.560	1.063	2.079	2.694	4.996	3.153	3.229
S.W.F. (m^3/hr)	0.165	0.262	0.205	0.094	0.500	0.250	0.310	0.306
K_{Lamin} (mg/l)	1.060	1.060	0.755	0.755	1.250	1.250	1.548	1.531
M.R.F. (m^3/hr)	0.004	0.004	0.003	0.003	0.005	0.005	0.004	0.007

Sponsored By



DEPARTMENT OF CIVIL ENGINEERING
FACULTY OF ENGINEERING
UNIVERSITY OF PERADENIYA
SRI LANKA



9 773021 673003